University of Glasgow

Polarimetric Terahertz Imaging Systems based on tailored Metasurface Optics

Thomas Stephan Nowack

Submitted in fulfilment of the requirements for the Degree of

Doctor of Philosophy (PhD) by Research

James Watt School of Engineering

College of Science and Engineering

University of Glasgow

September 2022

Acknowledgements

I would like to thank all those who have supported me during the challenging yet fulfilling period of this PhD.

First and foremost, I would like to thank my personal supervisor Prof. David R. S. Cumming, who entrusted me with the opportunity for this PhD position and continuously supported me with his experience and advise. I would further like to thank Prof. Edward Wasige for his relentless efforts to initiate and lead the TeraApps project (Marie Skłodowska-Curie grant agreement No. 765426), as well as for his personal support as my co-supervisor. I feel truly privileged and grateful to have been a part of the European Union's TeraApps project, which not only provided exceptional financial means to support my research but also access to a network of brilliant academics and companies that both widened and deepened my knowledge on terahertz technologies beyond my own research during several meetings. Special thanks go to my fellow early-stage researchers (ESR), whose friendship became especially important during the difficult and isolated period of the COVID-19 pandemic.

Furthermore, I would like to thank my colleagues of the Microsystems Technology group (MST) who helped me settle in at the University of Glasgow and feel at home. Thanks to James Paul Grant for his counselling and discussions on potential research directions, as well as his superb introduction to cleanroom processing. Thanks to Yash Diptesh Shah for the fruitful discussions on the outline of laser experiments and manuscript drafting. Thanks to Ivonne Escorcia Carranza for her introduction to using the terahertz laser and the continuous support that enabled the obtained experimental results, as well as to Vincenzo Pusino for his professional feedback upon diverse discussions. Thanks to Mitchell Guy Kenney for his help in getting started with FDTD simulation software.

I would furthermore like to thank the staff of the James Watt Nanofabrication Centre for their support in device fabrication and maintaining the infrastructure that was crucial to this publication. Special gratitude goes to Corrie Farmer for his relentless efforts in developing and optimising fabrication and dry etch recipes on a world-class level.

Last but not least, my greatest gratitude goes to my parents and brother, whose support and care I could always count on, as well as to my beloved Dominika and our dogs Pati and Willy, who made even the hardest of days feel special and fulfilling.

Thanks to all of you,

Thomas

Author's Statement of Originality

I certify that the thesis presented here for examination for a PhD degree of the University of Glasgow is solely my own work other than where I have clearly indicated that it is the work of others (in which case the extent of any work carried out jointly by me and any other person is clearly identified in it) and that the thesis has not been edited by a third party beyond what is permitted by the University's PGR Code of Practice. The copyright of this thesis rests with the author. No quotation from it is permitted without full acknowledgement. I declare that the thesis does not include work forming part of a thesis presented successfully for another degree. I declare that this thesis has been produced in accordance with the University of Glasgow's Code of Good Practice in Research. I acknowledge that if any issues are raised regarding good research practice based on review of the thesis, the examination may be postponed pending the outcome of any investigation of the issues.

Thomas Stephan Nowack

Abstract

Terahertz radiation has long been highly anticipated for a wide range of advanced imaging applications due to a range of special inherent properties. Spectral fingerprints of many molecules within the terahertz spectrum offer prospects for spectroscopic imaging, while the low energetic impact and biocompatibility of terahertz photons raise prospects for biomedical and security imaging. Furthermore, the high achievable resolution in the sub-millimetre range together with high transparency for common packaging materials are opening applications in non-destructive testing and (agri-food) production control. However, common obstacles for all these applications are found in the limited signal strength of terahertz sources, the high (thermal) noise levels of (uncooled) detectors, and the lossy optical components in-between. Terahertz setups are thus typically somewhat limited in their complexity and imaging capabilities as a result of this low signal-to-noise ratio (SNR).

This thesis aims to alleviate the SNR constraints of terahertz setups by developing metasurface optics that provides polarimetric imaging capabilities in an ultra-compact, efficient and easy to integrate format. The state of polarisation is expected to be particularly suited as a contrast channel since it is robust to both low-light-level conditions and common sources of noise, such as unpolarised background radiation, white noise, and thermally-induced noise. Furthermore, the state of polarisation can provide important additional information on the images sample and its microstructure. To demonstrate this concept within two prototype setups, four major research objectives were addressed in this thesis:

First, a methodology to design all-dielectric metasurface optics from individual anisotropic meta-pillars to their collective response based on simulations was developed and successfully tested. Such metasurface optics showed unparalleled capabilities in manipulating both the transmitted phase and polarisation front into well-defined shapes that can be tailored to their intended application.

In a second step, a method for the monolithic fabrication of the metasurface designs into low-cost silicon substrates was developed based on a single photolithography step that included an optimised Bosch etch. The presented fabrication technique raises the prospect of mass-production and included the reliable quantification of fabrication tolerances to achieve process control over the dry etch, as well as the well-founded estimation of associated optical performance deviations.

The third research objective aimed to demonstrate beam forming metasurface optics that created a non-diffracting Bessel beam with a polarisation profile that varied in all three spatial dimensions in a well-defined manner. The utility of such 3D-polarised probe beams to measure a sample's refractive index or polarisation-dependent behaviour was explored in theory and confirmed with both simulations and laser experiments. Polarimetric imaging experiments employing the metasurface to illuminate a resolution target and composite sample showed a remarkable resolution of $\leq 1.5\ \lambda_0$ and the ability to identify electrically conductive carbon fibres (measured diameter: 5.1 µm $\pm$ 1.4 µm) based on their polarisation signature, respectively.

Finally, a beam analysing metasurface was developed to precisely determine the incident state-of-polarisation within a single image. A sophisticated measurement methodology including an initial calibration ensured a robust, reliable and accurate operation with an averaged measurement accuracy of 92.1 % $\pm$ 4.2 % for the incident state of polarisation obtained from 64 measurements.

This thesis thus demonstrates the benefits offered by metasurface optics to create compact optical setups with advanced capabilities for sensing and imaging applications in NDT, as well as the validity of the strategy to utilise the state of polarisation as a contrast channel that remains robust to low-light conditions and the low SNR often encountered at terahertz frequencies. Beyond the presented results, much potential remains to extend the capabilities of both the presented metasurface optics and the optical setups.

Outcomes of the Research Activity

Peer-reviewed Publications in International Journals

[1] **Thomas S. Nowack,** Yash D. Shah, Ivonne Escorcia, James P. Grant, Mitchell Kenney, Vincenzo Pusino, Daniele Faccio, Edward Wasige, and David R. S. Cumming, "Terahertz polarimetry with a monolithic metasurface" Opt. Letters 47, 4199-4202 (2022).

[2] Yash D. Shah, Adetunmise C. Dada, James P. Grant, David R. S. Cumming, Charles Altuzarra, **Thomas S. Nowack**, Ashley Lyons, Matteo Clerici, and Daniele Faccio, "An all-dielectric metasurface polarimeter" ACS Photonics (in print) (2022)

Manuscripts Submitted to Peer-reviewed International Journals

[3] **Thomas S. Nowack,** Yash D. Shah, James P. Grant, Ivonne Escorcia Carranza, Mitchell G. Kenney, Daniele Faccio, Edward Wasige, and David R. S. Cumming, "Metasurface Optics with on-axis Polarisation Control for Terahertz Sensing Applications" submitted to IEEE Transactions on Terahertz Science and Technology on 21.12.22.

Oral Presentations

1. **Thomas S. Nowack,** Mitchell Kenney, James P. Grant, Danni Hao and David R.S. Cumming. "Nanostructured Ultra-lightweight Lenses for Earth Observation". Presented at 'Centre for earth observation instrumentation (CEOI) technology showcase'. 24 June 2021. Online Conference.

2. **Thomas S. Nowack,** and David R.S. Cumming. "Metasurfaces as platform for highly integrated terahertz optic". Presented at 'European Microwave Week'. 07 April 2022. ExCel, London, United Kingdom.

3. **Thomas S. Nowack,** Yash D. Shah, Ivonne Escorcia, James Grant, Mitchell Kenney, and David R.S. Cumming. "Advanced Terahertz imaging systems based on tailored metasurface optics". Presented at 'International School on Terahertz photonics and electronics'. 11 May 2022. Sala Azzurra, Scuola Normale Superiore, Pisa, Italy.

Poster Presentations

1. **Thomas S. Nowack** and D.R.S. Cumming. "Terahertz imaging with extended functionality by tailored optical metasurfaces". Poster presented at '29th International Travelling Summer School (ITSS) on Microwaves and Lightwaves'. 13 July 2019. Casino building, Goethe University Frankfurt am Main, Frankfurt am Main, Germany.

International Workshops and Summer Schools

1. 'TeraApps Transferrable Skills Training'. 23-24 January 2019. PGR Training Room, University of Glasgow, Glasgow, United Kingdom.

2. 'General Assembly and Annual Conference of the Marie Curie Alumni Association (MSCAA)'. 24-25 February 2019. University of Vienna, Vienna, Austria.

3. 'TeraApps MSCA ITN – Introductory course on Terahertz technology and applications'. 11-12 April 2019. Bushy House, National Physical Laboratory (NPL), Teddington, United Kingdom.

4. 'Joint ITN CELTA & TeraApps Summer School and 29th International Travelling Summer School (ITSS) on Microwaves and Lightwaves'. 13-19 July 2019. Casino building, Goethe University Frankfurt am Main, Frankfurt am Main, Germany.

5. 'TeraApps MSCA ITN – 2nd Transferrable Skills Course'. 12-13 February 2020. Keysight, Leuven, Belgium.

6. 'International School on Terahertz photonics and electronics'. 8-14 May 2022. Sala Azzurra, Scuola Normale Superiore, Pisa, Italy.

Table of Contents

List of Acronyms

AC	Alternating current
ALD	Atomic layer deposition
ARDE	Aspect ratio dependent etching
BPF	Bandpass filter
CIE	Commission internationale de l' éclairage (International Commission on Illumination)
COVID-19	Coronavirus disease of 2019
CW	Continuous wave
DC	Direct current
DNA	Deoxyribonucleic acid
DoAP	Division-of-aperture polarimeter
DOP	Degree of Polarisation
DRIE	Deep reactive ion etching
ESR	Early-stage researcher (PhD student within TeraApps project)
FIR	Far infrared (alternative term for the terahertz spectrum)
FIRL	Far infrared laser (source of monochromatic terahertz radiation)
FOV	Field of view
HEPA	High-efficiency particulate air
HDPE	High-density polyethylene
HWP	Half-wave plate (linear retarder with retardance of π)
IAD	Ion angular distribution (upon dry etching)
ICP	Inductively coupled plasma
IR	Infrared radiation
LR	Long range (design type of bi-axicon metasurface used for imaging applications)
LVB	Longitudinal vector beam
MSP	Metasurface polarimeter
NDT	Non-destructive testing
NEP	Noise-equivalent power
OAM	Orbital Angular Momentum
OPB	Orthogonal polarisation basis
PAC	Photoactive compound (Active component in photoresist)
PCA	Photoconductive antenna
PE	Polarisation Ellipse
PML	Perfectly matched layer
PTFE	Polytetrafluoroethylene
QCL	Quantum-cascade laser
QWP	Quarter-wave plate (linear retarder with retardance of $\pi/2$)
RI	Refractive index (of an optical medium)
RIU	Refractive Index Unit
SAM	Spin-angular Momentum (handedness of polarisation)
SE	Secondary electrons (imaged within a Scanning Electron Microscope)
SEM	Scanning Electron Microscopy
SLM	Spatial light modulator
SNR	Signal-to-noise ratio
SoP	State of Polarisation
SR	Short range (design type of bi-axicon metasurface used for sensing applications)
SRR	Split-ring resonator
TeraApps	Doctoral Training Network in Terahertz Technologies for Imaging, Radar and Communication Applications: https://www.gla.ac.uk/research/az/teraapps/aboutus/
THz-TDS	Terahertz time-domain spectroscopy
TPX	Polymethylpentene
TVVB	Transverse vector vortex beam
USAF	United States Air Force
WGP	Wire grid polariser
WLI	White light interferometry

Chapter 1 : Introduction to the Research Project

1.1 Overview and Background

The terahertz spectrum, loosely defined within the wavelength range from 10 μm to 3 mm (or 30 THz to 0.1 THz, respectively) [4], represents one of the last portions of electromagnetic radiation that still remains technologically challenging to exploit. Terahertz radiation is hence often disregarded for industrial applications despite the immense potential behind its unique properties. Nonetheless, the scientific quest to "fill the terahertz gap" has only intensified in recent years as technological advances within the adjacent microwave and infrared regions were optimised to extend ever deeper into the terahertz realm, spearheaded by hybrid approaches [5] that aim to work around intrinsic obstacles rather than attempting to diminish them.

In particular, the advent of metasurface optics – artificial 2D assemblies of sub-wavelength structures that are meticulously optimised towards their target optical function – was quickly adopted in terahertz research to overcome the limited product range and quality of commercially available terahertz optics, while extending equipment capabilities with completely new and exotic effects, such as negative refraction, magnetic resonances and tuneable transmission.

However, latest developments towards anisotropic and dielectric metasurfaces that allow for the versatile manipulation of the state of polarisation (SoP) with high efficiency, respectively have been thus far challenging to scale towards the terahertz spectrum due to challenges in their fabrication. Consequently, metasurfaces made up of split-ring resonators (SRR) that utilise plasmonic effects of lossy metallic layers remained the predominant subject of investigation at terahertz frequencies until recently.

This work aims to overcome the beforementioned shortcomings by developing an adaptable, all-dielectric metasurface platform that enables the design of complex polarising optics in a highly integrated and efficient format. The metasurface optics is optimised to demonstrate viable applications in non-destructive testing (NDT), sensing and polarimetric imaging by exploiting the SoP as a versatile information channel. The SoP was studied in depth since it was found to be particularly robust to unpolarised sources of noise, such as thermal heating and background radiation, which typically limit terahertz equipment's operation due to a low signal-to noise ratio (SNR).

This chapter will provide an introduction to this thesis by first discussing the current state of technology in terms of applications within the terahertz spectrum, outline the strategy and

objectives identified to advance the capabilities for terahertz imaging and discuss the wider significance for the field, as well as the limitations of the approach adopted in this research.

1.2 Technological Prospects and Challenges of the Terahertz Spectrum

Terahertz imaging [6, 7] is a major opportunity for applications such as security [8-11] or bio-medical imaging [12-14], astronomy [15-17] and NDT [18-22]. Spectroscopy is also well advanced [23-25], offering the potential for spectroscopic imaging [14, 17, 18, 26], albeit mostly in slow point-by-point scanning setups. Terahertz radiation is non-ionising, hence suitable for human body imaging [9, 13], delivers sub-millimetre resolution [18-22] and offers plentiful molecular absorption bands [23-26]. Furthermore, many industrial materials including polymers [19, 20], cardboard [10, 11] and textiles [8, 9] are relatively transparent so that obscured objects can be safely imaged.

Whilst many advances have been made in developing suitable technologies to operate in the terahertz band, there is still considerable scope for improvement [4, 5]. Notably, the lack of compact high-power sources and sensitive detectors remain limiting factors for many applications [7]. One reason for this is the low energy of terahertz photons in the range of 0.4 meV - 124 meV, that is comparable to the thermal energy at room temperature ($k_bT \approx 25$ meV). Consequently, high thermal noise and charge carrier generation leads to severe performance degradation, especially for semiconductor-based devices [5, 27]. Suitable cooling technologies are expensive and bulky thus bolometric detection is widely used for large pixel-arrays at room temperature, despite the high noise floor [6]. The performance of terahertz imaging systems is further compromised by losses arising from unwanted reflections [28, 29], atmospheric and material absorption [17, 29] and misalignment between individual optical components. Instruments that are designed to be compact are prone to the formation of standing waves between constituent components that further deteriorate the performance as a result of unwanted interference [28]. As a consequence of low power sources, lossy optics and low sensitivity detectors, terahertz systems typically suffer from a low signal-to-noise ratio (SNR) [12] that severely limits the complexity of imaging systems. Consequently, new avenues to improve the performance of optical components while limiting system complexity are needed, ideally complemented by strategies that bypass low intensity levels by employing alternate mechanisms to generate image contrast.

1.3 Metasurface-based Polarimetry for Terahertz Imaging

One promising strategy to overcome the noise limitation of terahertz systems by decreasing optical losses is to develop efficient and highly integrated optical components that achieve compact systems with advanced function despite the underlying limitations of the source and detector [5, 7]. Metasurface-based optics is such a solution that can compress the function of several traditional components into a single layer [30-32], eliminating the problems associated with reflections, unwanted diffraction and interference occurring between such components. Rigorous optimisation by simulation and precise fabrication using lithography typically result in high transmission (≥80 %), even for complex optical functions [30-33]. Reducing the number of lossy components and simplifying the construction of imaging systems leads to improved overall SNR, thereby unlocking the potential for advanced imaging techniques that would otherwise remain unfeasible.

Polarimetric imaging is such an advanced imaging technique that can provide important sample information beyond intensity-based images, which constitutes a valuable extension in particular for NDT application. Especially beneficial in the terahertz regime is that non-polarised sources of radiation, such as thermal noise and background radiation, can be filtered out when analysing for the polarimetric contrast of images and sceneries, resulting in a certain degree of robustness of polarimetric information to the mentioned sources of noise. Even though the state of polarisation (SoP) is a well-known property of light that can carry information on a wide range of observable effects, its generation and measurement remain complex and often require multiple moving components. Consequently, reports on polarimetric terahertz imaging are scarce and mostly limited to incomplete observations of only two orthogonal linear polarisations [34-38]. However, many material classes that particularly rely on NDT characterisation, such as composite materials or materials with micro-crystalline domains or inclusions, would greatly benefit from a more substantial and complete polarimetric characterisation with both high resolution and acquisition speed.

Fortunately, dielectric metasurfaces with anisotropic elemental structures have been proven an exceptionally compact, efficient and versatile platform to manipulate the SoP into complex shapes, which can be exploited in beam forming and beam analysing optics for application in polarimetry. As a consequence, anisotropic metasurface optics is uniquely suited to simultaneously overcome both the signal-to-noise limitations frequently encountered in complex terahertz systems as well as the complexity problems associated

with polarimetric imaging, thereby paving the way towards applications exploiting polarimetric terahertz imaging. Figure 1.1 aims to illustrate these complementary benefits of combining terahertz imaging with metasurface optics and polarimetric NDT capabilities.

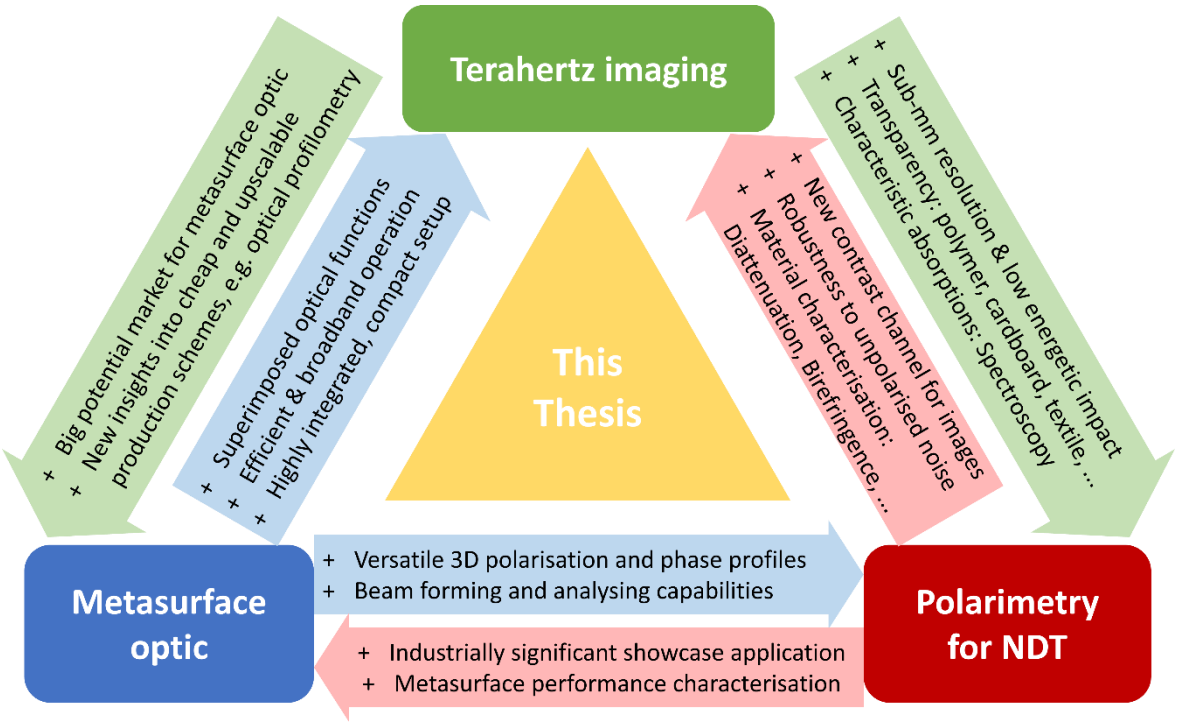

Figure 1.1: Schematic outlining the benefits of combining terahertz imaging with metasurface optics and polarimetric capabilities. These three scientific disciplines complement each other's technological capabilities in a mutually beneficial manner that paves the way towards applications in NDT and quality assurance imaging.

1.4 Research Objectives of this Thesis

This PhD position was part of the "Doctoral Training Network in Terahertz Technologies for Imaging, Radar and Communication Applications" (TeraApps), an innovative training network of the European Union's Marie-Skłodowska-Curie Action that aimed to advance terahertz technologies on a broad scale within 15 individual PhD scholarships. Within this frame, this specific work aimed to explore novel systems for terahertz imaging to demonstrate industrially feasible applications, as stated in "work package 5 – terahertz demonstrator systems" of the underlying TeraApps funding agreement. To achieve this, several research objectives were outlined as listed below in Table 1.1.

Table 1.1: List of research objectives including the reference to their reported Section.

Research Objective	Reported in
Identification of potential gaps in research on terahertz imaging and formulation of research goals	Chapter 1
Review of literature on terahertz imaging, metasurface optics, structured light with Bessel beams and polarimetry	Chapter 2
FDTD simulations to optimise the design of elemental meta-pillar	Section 3.2
Algorithm to arrange individual meta-pillars into metasurface with desired optical function	Section 3.3
Setting up simulations to gauge the collective response of the designed metasurfaces	Section 3.4
Identification and optimisation of a cheap fabrication sequence	Section 4.1 and 4.2
Design and fabrication of Cr-photomask with metasurface designs	Sections 3.3, 5.2 and 6.2
Metrology to assess the physical tolerances of fabricated metasurfaces	Sections 4.3 and 4.4
Model to gauge impact of fabrication tolerances on optical performance	Sections 4.3 and 4.4
Novel concepts and setup design for polarimetric sensing and imaging applications using metasurface optics	Chapter 3, Chapter 5 and Chapter 6
Collective simulations and analytical model development to describe beam forming Bessel metasurface	Section 5.2
Design and construction of polarimetric imaging setup employing the beam forming Bessel metasurface	Section 5.3
Experimental data acquisition and analysis algorithms for the beam forming Bessel metasurface applied for polarimetric terahertz imaging and sensing	Section 5.3
Interpretation of obtained results, discussion and outline of future work	Section 5.4 and 5.5
Publication of the work involving the Bessel metasurface in high-impact peer-reviewed scientific journal (TBA)	Section Peer-reviewed Publications
Collective simulations of the beam analysing polarimeter metasurface	Section 6.2
Design and construction of test setup to gauge the operation of the beam analysing polarimeter metasurface	Section 6.3
Experimental data acquisition and development of automated analysis algorithms, incl. setup calibration	Section 6.4
Interpretation of results, discussion and outline of avenues for future work	Section 6.4 and 6.5
Publication of the work involving the polarimeter metasurface in a renowned peer-reviewed scientific journal (Optics Letters)	Section Peer-reviewed Publications

1.5 Thesis Outline

Chapter 1 aimed to give a brief introduction to the technological challenges hampering practical applications within the terahertz spectrum and motivate the need for tailored optics that add advanced imaging functionalities while simplifying the setup. The objectives of this thesis were defined with a clear research strategy to advance terahertz capabilities towards application in NDT and polarimetric imaging.

Chapter 2 provides a theoretical background on the four core topics fundamental to this research project, including respective reviews on previously reported work. These core topics are applications and technologies within the terahertz spectrum, the polarisation of light and polarimetry, structured light based on Bessel-type beams, and the advent of metasurfaces as ultra-compact and efficient functional optics.

Chapter 3 will present the fundamental design, optimisation simulations and algorithmic assembly of the developed anisotropic metasurface platform from elemental structures to their intended collective operation.

Chapter 4 describes the fabrication technique that was developed to produce the designed metasurfaces. Special focus is put on a single-step monolithic fabrication into cheap and widely available silicon substrates, including the quantification of fabrication tolerances and the modelling of resulting performance deviations.

Chapter 5 presents the first type of metasurface optimised to generate a Bessel-type beam with controlled longitudinal polarisation. This metasurface was integrated as beam forming optics into a polarimetric microscope to demonstrate applications in NDT, polarimetric imaging and material characterisation within the terahertz spectrum.

Chapter 6 presents the second type of metasurface that was optimised to integrate the entire functionality of a beam analysing division-of-aperture polarimeter (DoAP) into a single optical layer with high efficiency and prospects for a broad operational bandwidth. Experimental tests certified accurate, reproducible and robust SoP measurements from a single image based on automated calibration and analysis algorithms.

Chapter 7 concludes this thesis by summarising key findings and discussing them in terms of novelty, performance and significance compared to previous work. Limitations of designs and experiments are discussed to outline promising avenues for future work. The chapter finishes with concluding remarks on the encompassing TeraApps project, the impact of the COVID-19 pandemic and a brief account to the author’s efforts towards the award of a PhD.

Chapter 2 : Theoretical Background and Literature Review

2.1 Introduction

This chapter aims to provide a brief introduction to the fundamental physics and principles necessary to understand and interpret the scientific results that will be presented in the subsequent chapters of this dissertation. Furthermore, brief reviews on the scientific literature will be presented for the four core topics of this thesis to underline the current capabilities, challenges, research gaps and strategies to advance each respective field. These four core topics underlying the presented thesis are discussed in respective sections.

Section 2.2 presents the terahertz spectrum with its unique properties and infers its prospects and challenges for imaging applications. The current state of available optical components and setups is discussed with their commonly encountered limiting factors and deficiencies, after which a literature review on diverse imaging applications at terahertz frequencies will highlight strategies to overcome or bypass these challenges.

Section 2.3 introduces the theory behind the state of polarisation and its unique interactions with matter. An application-oriented review on polarimetry and polarimetric imaging will discuss how different polarisations can be used to measure important polarisation-dependent properties of a sample.

Section 2.4 discusses how the field of metasurface optics developed in recent years, highlighting general scientific and technological breakthroughs. Special focus is put on anisotropic metasurfaces that can manipulate the state of polarisation with excellent precision and design versatility. An in-depth review on metasurface optics developed to operate within the terahertz spectrum will highlight the importance of metasurfaces to advance the field of terahertz imaging while pointing out current shortcomings compared to other spectral regions.

Finally, Section 2.5 discusses recent studies on structured light based on Bessel-like beams that can exhibit well-designed polarisation profiles in 3 dimensions and argues for their potential application as beam forming optics.

The chapter will conclude in Section 2.6 with a summary of the presented topics that highlights how their combination offers cumulative benefits that help overcome individual limitations.

2.2 The Terahertz Spectrum and its Application to Imaging

2.2.1 Special Properties of Terahertz Radiation

Electromagnetic radiation with terahertz frequencies, ν_{THz}, in the range of ca. 0.1 THz to 30 THz [4] boasts a wide range of intriguing and promising properties which will be summarised in this section.

Arguably the most defining property of terahertz radiation is the comparably low photon energy $E_{ph}(\nu_{THz})$ of ca. 0.4 meV to 125 meV, which entails several consequences in practice that can be exploited in many applications.

The thermal energy of cold matter with temperature T of ca. 2.7 K to 400 K [39], which includes interstellar clouds [17, 40, 41] or the ambient conditions on earth, is within the range of terahertz photons, e.g. $E_T(300\ K) \approx 25$ meV. Matter within this temperature range will therefore emit a significant amount of blackbody radiation with terahertz frequency according to Planck's radiation law, with the peak wavelength $\lambda_{peak} = b/T$ given by Wien's displacement law ($b \approx 2898\ \mu m \cdot K$) [42]. A striking 98 % of all photons that have been emitted since the big bang are estimated to reside in the terahertz spectrum [43], underlining the omnipresence and significance of terahertz radiation. First endeavours to utilise terahertz[1] radiation were thus focussed around astronomic imaging [17, 40, 41], with prominent examples including the Herschel Space Observatory [44] and the Event Horizon Telescope [45]. On the other hand, terrestrial applications involving terahertz radiation typically suffer from this very same blackbody emission around room-temperature as it often causes significant thermal noise within imaging setups or performance degradations within bandgap-based semiconductor devices, e.g. high noise equivalent power (NEP) [5, 27].

The energy of terahertz photons is furthermore overlapping with a rich set of intra-molecular, inter-molecular and electronic excitations i.e., rotational, (collective) vibrational or plasmonic modes, respectively [25, 46, 47]. Spectroscopy has thus developed into an established and mature application of terahertz radiation [48, 49] with diverse sub-categories in material characterisation [23, 25, 50, 51], chemical identification [52-55], remote sensing [56-58] and many more [59, 60]. The downside of absorption is that strong atmospheric absorption bands, particularly caused by oxygen and water vapour often restrict long-range

[1] Terahertz radiation is often also named far infrared (FIR) radiation, especially in astronomy.

applications to so-called atmospheric windows [56, 61]. Although a range of industrially important material classes are famously transparent - or at least translucent – to terahertz radiation [49], i.e. non-polar polymers [19, 20], cardboard [10, 11] and textiles [8, 9], there are nevertheless a lot of widely used materials with strong absorption bands [49], as will be discussed in detail in Section 2.2.2. All this typically results in comparably strong attenuation of terahertz signals under ambient conditions in addition to the high noise floor caused by thermal terahertz radiation. As a result, almost all terrestrial terahertz applications rely on active illumination of the sample with a source of terahertz radiation.

Another beneficial consequence of the low energy of terahertz photons is their non-ionising, low-impact interaction with sensitive biological samples, rendering terahertz radiation a less harmful alternative to X-rays or UV light. Diverse applications in bio-chemical spectroscopy and bio-medical imaging have been pursued, e.g. studies on the recognition and characterisation of macro-molecules such as proteins and deoxyribonucleic acid (DNA) [59, 60] or cancerous tissue [62, 63]. Furthermore, agricultural applications are under investigation e.g., monitoring water content in leaves [26, 64]. However, the penetration depth of terahertz radiation is limited to a few mm at most in these applications due to extremely strong attenuation in organic matter i.e., due to water absorption [65, 66].

Last but not least, the short wavelength of terahertz radiation allows for a high imaging resolution ($\approx \lambda/2$) within the industrially important sub-mm range [18-22]. In combination with the aforementioned high degree of transparency for some industrially important material classes and the biocompatibility of terahertz radiation, several applications in NDT, quality assurance imaging and security imaging have emerged [8-11, 18-22]. Terahertz radiation therefore allows for a higher image resolution compared to the use of microwaves ($\nu_{MW} < \nu_{THz}$) with far less radiation damage compared to ionising X-rays ($\nu_{XR} > \nu_{THz}$) while still being a non-contact technique, as opposed to ultrasonic testing [22].

As this brief summary has pointed out, terahertz radiation combines a rich set of unique properties that have vast potential for a plethora of applications. Yet the very same properties often simultaneously cause difficulties in their practical exploitation and implementation. In the next Section 2.2.2, I will discuss the current state of the technological development of the terahertz spectrum in terms of optical devices, components and setups while pointing out commonly encountered limitations and obstacles.

2.2.2 Optical Technologies and Components Operating at Terahertz Frequencies

Any optical setup used in the far-field configuration can in principle be divided into three fundamental parts [67]:

1. The source of electromagnetic radiation, which defines the emitted wavefront in terms of intensity, wavelength incl. bandwidth, polarisation and other beam parameters such as divergence, beam shape, beam diameter etc. Even for passive imaging, a source is strictly needed e.g., the sun or intrinsic blackbody radiation.
2. The detector that measures the incident intensity per time interval (frame rate) with a sensitivity that depends on the wavelength - and in some cases also on the SoP. Detectors typically integrate the intensity over a large active area, whereas cameras have a sensor that is subdivided into arrays of small pixels to obtain a 2-dimensional image from the locally differing incident light.
3. Optical components in between the source and detector that provide beam forming and shaping functionality such as collimation, focussing or splitting of the intensity profile, or a modulation of the light's properties such as wavelength (e.g., bandpass filter, chromatic dispersion) and polarisation (e.g., wave retarder, polarisers). As such, optical components ultimately aim to overcome the limitations of source and detector technologies and extend the capabilities and functionalities of the optical setup.

This section aims to provide a brief, practice-oriented overview on the state-of-the-art of these three optical technologies within the terahertz spectrum, and justify the choices made within this work. For a complete and elaborate discussion of all available source and detection technologies operating within the terahertz spectrum, the author refers to these excellent review articles [4-7, 65], whereas optical components and materials typically used within the terahertz spectrum are summarised in [68-71].

In general, high-power generation and sensitive detection of terahertz radiation remain limiting factors for many applications [7]. Both terahertz source and detection technologies can be roughly divided into a photonic approach and an electronic approach [5, 61], which seek to extend the technological capabilities of existing optical and microwave technologies, respectively, ever deeper into the terahertz spectrum. Accordingly, photonic terahertz technologies tend to work favourably at the higher frequency end of the terahertz spectrum above 1 THz, whereas electronic technologies typically operate best at lower frequencies in the range of 0.1-1 THz [5].

Figure 2.1 summarises the most prominent terahertz source technologies as a function of operational frequency and (averaged) output power. It is apparent that virtually all source technologies retain a low (averaged) output power in the sub-W to nW range throughout most of the terahertz spectrum i.e., between ca. 0.3 THz and 3 THz. Despite steady progress made in recent years, most notably for quantum-cascade laser (QCL) [27, 72-78] and resonant tunnelling diodes (RTD) [7, 79], the general problem of limited available source power at terahertz frequencies is unlikely to fundamentally change in the near future [4].

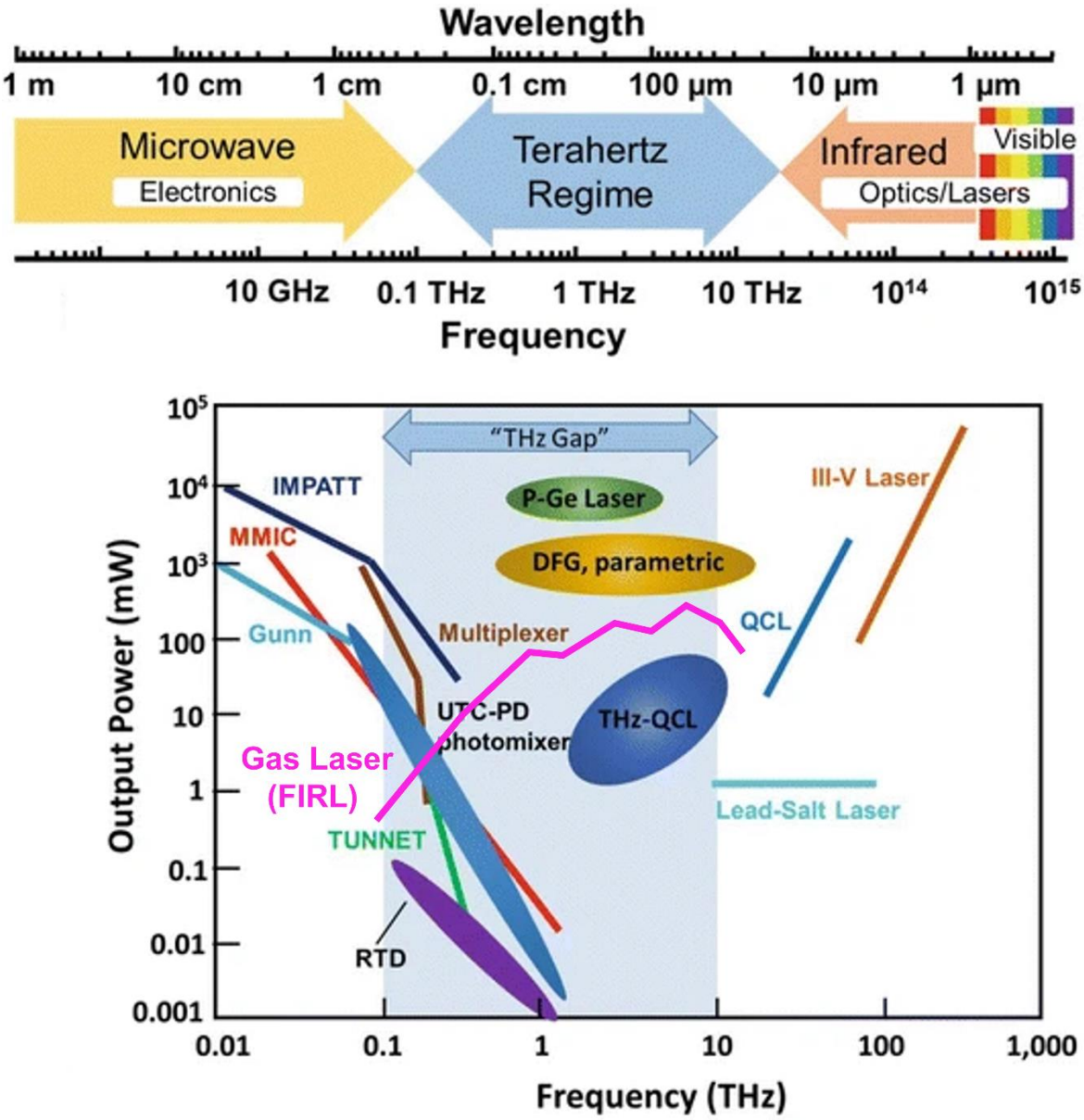

Figure 2.1: Summary of the performance of diverse terahertz source technologies in terms of operational frequency and (averaged) output power. Adapted from [80] and [81].

Aside from output power, there are many other important source metrics to consider when selecting the best suited terahertz source for a specific application. These considerations include, but are not limited to, the setup's costs, complexity (e.g., cooling), size, the output beam's shape, polarisation, coherence length, or the emitted wavelength characteristics such as the bandwidth, phase noise and tunability.

In this project, the terahertz source that was used was needed to allow reliable optical characterisation of the metasurface-based polarisation optics that were developed, as well as the subsequent demonstration of imaging and sensing applications. For this task, an ideal source should deliver a collimated beam of highly coherent and polarised radiation with low phase noise that evenly illuminates the active area of the metasurface i.e., large beam diameter of ~10 mm-30 mm. Furthermore, a monochromatic wavelength at the centre of the terahertz spectrum would simplify initial data analysis due to the absence of dispersive effects and demonstrate the ability of the new optics to advance imaging applications at the heart of the terahertz spectrum, respectively. Finally, a high output power would ensure that even complex setups, sub-optimal configurations or strongly scattering samples will still result in a sufficiently strong measurement signal. As with most research aiming towards a proof of principle, aspects such as costs, size or upscalability were of secondary importance. An optically pumped gas laser, also known as far infrared laser (FIRL), was hence chosen as ideal source for this work.

Despite being an old technology that was first demonstration in 1964 [82], FIRL still represent an excellent solution when high output power above 100 mW and high frequency between 0.15 - 6 THz are paramount, although QCLs advanced to even surpassed these output powers in recent years, i.e. in pulsed mode operation [74]. Operation of a FIRL is possible in both pulsed (broadband) or continuous wave (monochromatic) mode. Other striking features are a long coherence length, stable phase front and low beam divergence. The clear downside of FIRL are their large size and power consumption, as well as limited emission wavelengths restricted to the emissive lines of the employed gas molecules i.e., methanol, ammonia, etc. However, recent efforts show promising results in overcoming these issues by increasing compactness, efficiency and tuneable bandwidth [83-86].

Terahertz detection technologies have matured considerably within the last decade, with an ever-expanding choice of commercial detectors and focal plane arrays targeting applications in terahertz imaging [87-89]. Although optimal performance at terahertz frequencies necessitates (cryogenic) cooling of the sensor to decrease the dark count and thermal noise,

most commercial products target (semi-)industrial applications with focus on optimising room temperature operation due to vastly reduced setup costs and complexity [6]. Table 2.1 summarises the most developed room temperature detector and camera technologies. For a more elaborate review, the author refers to [7, 81, 90, 91].

Table 2.1: Established terahertz detectors and cameras operating at room temperature. Table adapted from [6].

Detector Type	**Detection Principle**	**NEP [pW/$\sqrt{Hz}$]**	**2D pixel array possible?**	**Reported in**
Thermal				
Microbolometer	Resistive change by thermal excitation	~10–100	Yes, commercial	[92-94]
Pyroelectric detector	Polarisation change by thermal excitation of a pyroelectric crystal	~10–1000	Yes, commercial	[95-97]
Golay cell	Pressure change by thermal excitation of an encapsulated gas	~100–1000	No	[98]
Optically triggered				
Photoconductive antenna (PCA)	Ultrafast photoexcitation of charge carriers in a semiconductor gap	$1.81 \cdot 10^{-3}$ - 0.1 [99], 0.8 [100]	Possible, but uncommon	[101-107]
Electro-optic sampling	Birefringence-induced by THz pulse in nonlinear media	~1 [108], $1.5 \cdot 10^{4}$ [109]	Possible, but uncommon	[110-114]
Air-based coherent detection	THz field-induced second harmonic (TFISH) in plasma gas	SNR: 95-185 [115]	No	[116, 117]
Mixer				
Schottky-barrier diode	High-frequency detection enabled by fast switching speeds in metal/semiconductor junction	~10–100	Yes	[118, 119]
Plasmonic detector				
Field-effect transistor	Plasmonic excitation of electronic charge densities in transistor channels	~10–100	Yes, commercial	[120-122]

A microbolometer-based camera was found to best match the application requirements. First of all, microbolometer exhibit a low NEP over a broad detection bandwidth that covers most of the terahertz spectrum [93], yet can be adapted to exclusively detect customised wavelength using a bandpass filter and/or an anti-reflective coating. Crucially, the pixel

design ensures a polarisation-independent detection sensitivity, which greatly simplifies polarimetric experiments. Furthermore, the sensor array covers a sufficiently large active area (13.44 mm x 10.08 mm) with a high resolution (384 x 288 pixel) and operation at video-rate (25 fps). It shall be mentioned that a pyroelectric camera would also match these conditions in principle yet at a significantly higher price.

To this day, commercially available optical components operating at terahertz frequencies are mostly confined to reflective or refractive optics. Setups that employ broadband sources, such as the terahertz time-domain spectrometers (THz-TDS), typically employ gold-coated parabolic mirrors to collimate and focus terahertz radiation with minimal dispersion, but such optics are quite bulky, challenging to align and limited to manipulations of the phase front, i.e. no controllable alteration of the SoP via birefringence or diattenuation [123, 124]. On the other hand, the quality and performance of refractive optics is currently limited by the optical characteristics of materials at terahertz frequencies [49, 71]. Most dielectric materials possess absorption bands within the terahertz spectrum that originate from many different effects i.e., plasmonic absorption of free electrons, phonon absorption of lattice modes, vibronic/rotational excitations in polar materials or disorder-induced absorption within amorphous materials [49]. Furthermore, significant scattering losses are encountered for porous materials or rough surfaces [49]. Consequently, only a few materials are deemed viable for refractive terahertz optics, most importantly polymethylpentene (TPX), (high-density) polyethylene (HDPE), tsurupica (also known as picarin), polytetrafluoroethylene (PTFE), single-crystalline quartz and intrinsic silicon [125]. Polymer-based terahertz optics is comparably cheap with reasonably low dispersion, but such components are also subject to quality variations caused by locally varying density and impurities within the polymer, as well as subject to potential (thermal) deformation and scratching. On the other hand, crystalline materials such as quartz and high-resistivity silicon are expensive due to their intricate production from bulk crystals but offer superior and more uniform performance. Another consideration is the refractive index (RI) n_M of the materials. The low RI of polymer-based optics ($\sim$ 1.5 RIU [125]) severely restricts the achievable numerical aperture $NA = n_M \sin\theta$ and requires strongly curved lens surfaces, whereas the high RI of silicon ($\sim$ 3.418 RIU [126]) results in high reflective losses of $\approx$45 % for untreated silicon-air interfaces, compared to 10-20 % for polymers-air interfaces [125]. In combination with coherent terahertz sources, such reflections often lead to detrimental standing wave effects both within and between constituent components, which further deteriorates the setup's

performance as a result of unwanted interference [28]. Furthermore, diffractive effects become significant since the wavelength becomes comparable to the lens thickness, especially at low terahertz frequencies in low index materials.

The overall consequence of low source power, detectors with high thermal noise and optics of mediocre quality is that terahertz imaging setups typically exhibit lower SNR compared to respective setups at other spectral ranges i.e., microwave, infrared or visible spectrum. One strategy to overcome this problem is to develop novel optical components tailored to simplify their surrounding setup and thereby achieve useful system function despite the underlying limitations of the sources and detectors [5, 7]. Such systems relying on novel components have the potential to deliver terahertz systems that meet the demands of robust, reproducible and reliable performance, which shall be explored within this thesis.

2.2.3 Review on Terahertz Imaging

Ever since the first image was recorded within the terahertz spectrum using a FIRL in 1976 [127], there has been a great deal of work carried out to explore imaging capabilities that take advantage of the unique properties of terahertz radiation [5, 6, 65, 128, 129].

Arguably the most mature and widespread optical setup employing terahertz radiation is the THz-TDS that was pioneered by Hu et al. in 1995 [130]. It is therefore no surprise that a large portion of work demonstrating imaging applications within the terahertz spectrum has been conducted using THz-TDS as well [18, 49, 66, 131-141], driven in particular by its compelling capabilities beyond simple intensity-only contrast [6, 49, 142]. Most importantly, the pulsed nature of the terahertz signal enables the derivation of spectral information by applying the Fourier transform, thereby allowing for spectroscopic imaging [66, 131-135, 143, 144]. Thus far, targeted applications include the identification and quantification of molecular substances [17, 135, 141, 145], molar fractions in pharmaceutical tablets [144], the detection of illicit drugs and explosives [55, 132, 134] and the characterisation of electronically active materials and structures [23, 25, 51]. Furthermore, the time-resolved signal detection allows for the coherent measurement of phase information, which can be used to measure a material's RI [48, 70, 136, 146], to obtain phase contrast images [136, 139, 141, 147-152] and ultimately for tomographic 3D imaging [18, 136, 151-154]. The comparably weak signal power obtained with PCAs (see Figure 2.1) are somewhat offset by the coherent detection scheme that relies on a probe beam propagating within a delay line and lock-in amplification in order to achieve good SNR [142].

However, imaging based on the THz-TDS setup also comes with several disadvantages and limitations. TDS-based imaging setups typically employ a single-pixel detector that requires slow lateral scanning of the sample (point-by-point image acquisition) [133], which vastly limits both the achievable frame-rate and imaged area. Recent demonstrations involving computational or compressive imaging techniques with single-pixel detectors might prove beneficial but require complex image acquisition and data analysis methodologies [137, 139, 155]. In general, the coherent detection scheme dictates the use of a pair of complementary source and detector that are typically connected by a delay line (except for the asynchronous optical sampling technique [156, 157]), which renders the technique incompatible with most other source or detection technologies and thereby for long-range or large field of view (FOV) applications [158]. As such, THz-TDS is a stand-alone technology that usually does not combine favourably with other terahertz technologies or components.

In contrast to this, a lot of highly anticipated terahertz applications require an approach based on exchangeable and individually optimised components within modular imaging setups. For instance, imaging of packaged goods or hidden objects requires video-rate operation with a large FOV that can only be achieved by a focal plane array with high resolution [151, 159-161] e.g., using a micro-bolometer camera. Furthermore, passive or long-range imaging for astronomic [15-17] or security applications [147, 151, 160, 162-165] often requires sophisticated optical configurations based on transmissive elements that are optimised towards their function and image sensor, e.g. magnification, holographic interference, polarisation analysis, etc. On the other hand, through-the-wall imaging and NDT of buried defects are both examples that rely on strong illumination with a powerful source rather than spectral information. The technological advancements in terms of optical components and modular setups would also benefit several other optical applications closely related to imaging, most notably remote sensing and high-speed wireless data transmission at terahertz frequencies. None of these applications would be feasible using a THz-TDS setup.

Interestingly, only few terahertz setups have been reported to explore the state of polarisation (SoP) as information channel [38]. Apart from THz-TDS setups that individually analyse two orthogonal linear SoPs [34-36], notable reports on polarimetric terahertz imaging were based on compact interferometric [166-168] or reflective [28] setup geometries and sophisticated custom-build ellipsometers [28, 169].

Consequently, an approach to tailor highly integrated and specialised terahertz optics that can control the transmitted polarisation profile would open up a wide range of novel applications for terahertz imaging.

2.3 Polarisation of Light and its Role in Imaging

2.3.1 Theoretical Description of Polarisation

Electromagnetic radiation can be regarded as transverse wave with the propagation direction and both the oscillating electric field vector and the oscillating magnetic field vector all perpendicular to each other, as described by Maxwell's equations [170-172]. In this illustrative format, the wavelength λ_0 in vacuum constitutes the travelled distance upon one full oscillation period $\lambda_0 = c_0/\nu$, which will be reduced by the experienced RI $n = c_0/\mathrm{v}_n$ to $\lambda_n = \lambda_0/n$ within an optically dense medium of propagation speed v_n compared to the speed of light in vacuum c_0.

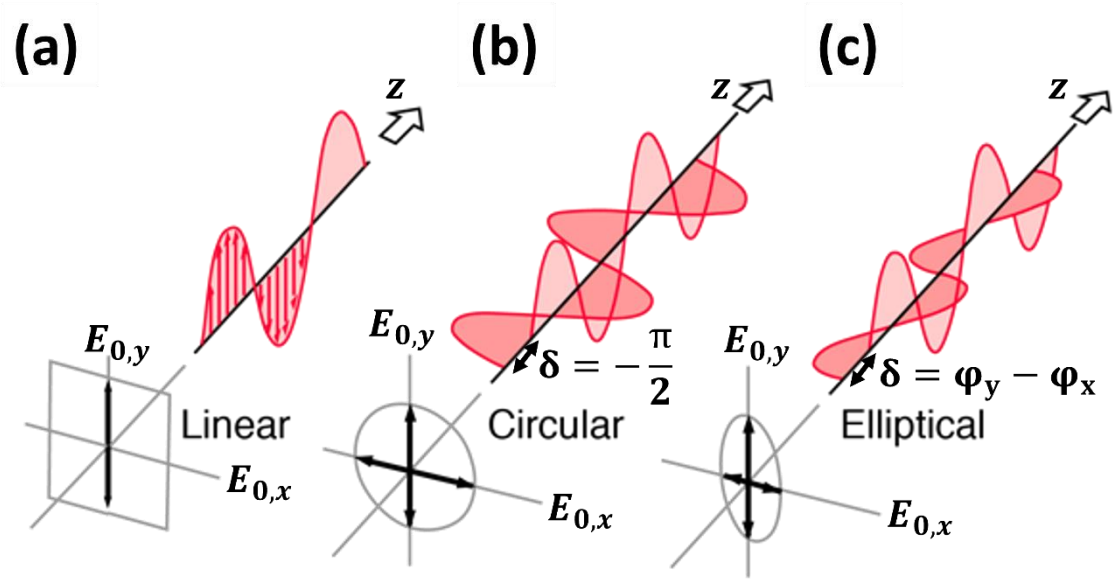

Figure 2.2: Illustration of the spatio-temporal oscillation of the electric field vector $\vec{E}(x, y)$ of electromagnetic radiation upon propagation along the z axis. (a) shows linearly polarised light, (b) circularly polarised light and (c) elliptically polarised light. Illustration adapted from [173].

The macroscopic state of polarisation (SoP) of light describes therefore the time-averaged spatial oscillation of the electric field vector $\vec{E}(x,y)$ relative to the wave's propagation direction z, which is fully described by the E-field components in x- and y-direction, $E_{0,x}$ and $E_{0,y}$, and the relative phase shift $\delta = (\varphi_y - \varphi_x)$ between them, as shown schematically in Figure 2.2 (a)-(c) for linearly polarised, circularly polarised and elliptically polarised light, respectively. The magnetic field vector $\vec{B}(x,y)$ is traditionally omitted since it can be reconstructed from knowledge of the propagation direction and electric field vector due to their orthogonality relation [170-172].

The SoP is consequently a fundamental property of light with extensive implications in the field of optics, yet often neglected in every-day life. The reason for this is that many common sources of light such as the sun, candles or even light-emitting diodes (LED) emit unpolarised light that consists of equal amounts of each SoP. Furthermore, most polarisation-dependent material interactions remain hidden to the human eye that cannot distinguish different SoPs (with exception of Haidinger brushes [174, 175]), unlike bees [176] or the mantis shrimp [177]. Nevertheless, the SoP and its analysis in the field of polarimetry is of indispensable importance to describe, probe and measure a wide range of important phenomena and material characteristics, as will be discussed in Section 2.3.2.

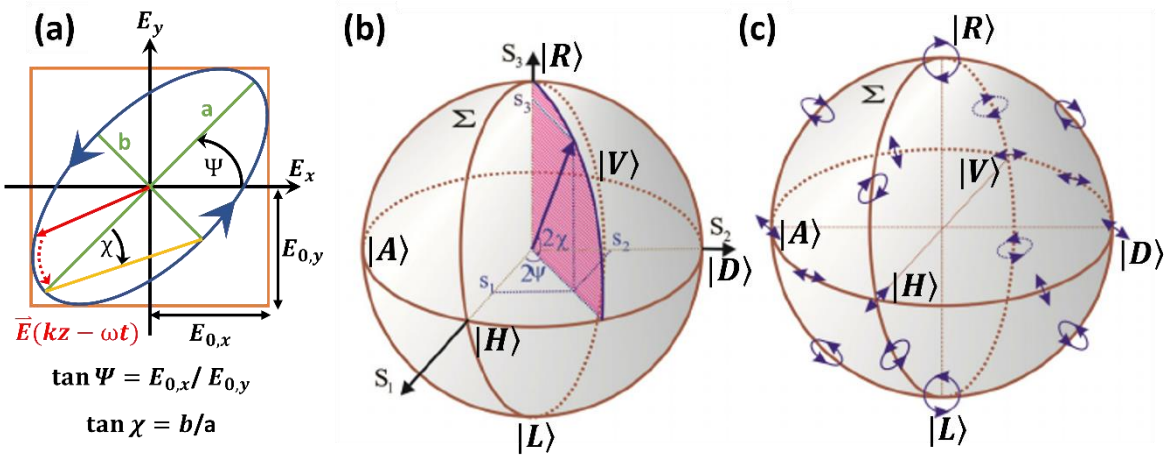

Figure 2.3: (a) A detailed schematic of the polarisation ellipse (blue) along which the electric field vector (red arrow) oscillates, highlighting important parameters, i.e. the characteristic angles, Ψ and χ. (b) Illustration of the Poincare sphere spanned by azimuth angle 2Ψ and latitude angle 2χ including (c) small insets of the local PE (blue symbols). (b), (c) adapted from [178].

The polarisation ellipse (PE) illustrated in Figure 2.3 (a) is sufficient to describe any possible SoP via its characteristic angles, namely the orientation angle, $\Psi \in [-\pi/2\,;\,\pi/2]$, of the PE's major axis a and the ellipticity angle, $\chi \in [-\pi/4;\,\pi/4]$, spanning between minor axis b and the major axes a of the PE, respectively. All SoPs and polarisation transformations can be illustrated on the Poincare sphere as locations and paths, respectively. As shown in Figure 2.3 (b), (c), the Poincare sphere is intuitively connected to the PE via its azimuth (2Ψ) and latitude (2χ) angles in a spherical coordinate system, which are simply twice the characteristic angles of the PE. The three cartesian coordinates constitute the normalised Stokes parameter S_1-S_3 that will be introduced at the end of this Section, with S_0 being the sphere's radius that is typically normalised. This work employs the Poincare sphere to depict the simulated and measured SoPs in Chapter 5 and Chapter 6.

Table 2.2 summarises the diverse descriptive notations that are introduced in this section for the six most prominent SoPs, often referred to as the degenerate SoPs.

Table 2.2: The six degenerate states of polarisations with their different notations commonly used in the field of polarimetry.

Linguistic Name	**Ket Notation**	**Jones Vector**	**Stokes Vector (Mueller calculus)**	**Characteristic Angles of the Polarisation Ellipse (Ψ, χ)**
Horizontal Linear	$\|\mathrm{H}\rangle$	$\begin{pmatrix}1\\0\end{pmatrix}$	$(1 \quad 1 \quad 0 \quad 0)^T$	(0, 0)
Vertical Linear	$\|\mathrm{V}\rangle$	$\begin{pmatrix}0\\1\end{pmatrix}$	$(1 \quad -1 \quad 0 \quad 0)^T$	(π/2, 0)
Diagonal Linear (+45°)	$\|\mathrm{D}\rangle$	$\frac{1}{\sqrt{2}}\begin{pmatrix}1\\1\end{pmatrix}$	$(1 \quad 0 \quad 1 \quad 0)^T$	(π/4, 0)
Anti-diagonal Linear (-45°)	$\|\mathrm{A}\rangle$	$\frac{1}{\sqrt{2}}\begin{pmatrix}1\\-1\end{pmatrix}$	$(1 \quad 0 \quad -1 \quad 0)^T$	(3π/4, 0)
Right-handed Circular	$\|\mathrm{R}\rangle$	$\frac{1}{\sqrt{2}}\begin{pmatrix}1\\i\end{pmatrix}$	$(1 \quad 0 \quad 0 \quad 1)^T$	(0, π/4)
Left-handed Circular	$\|\mathrm{L}\rangle$	$\frac{1}{\sqrt{2}}\begin{pmatrix}1\\-i\end{pmatrix}$	$(1 \quad 0 \quad 0 \quad -1)^T$	(0, -π/4)

The (normalised) Jones vector $\vec{J}$ offers a simple description of the SoP and is fully defined according to Eq. (2.1) by the two transversal E-field amplitudes $\mathrm{E}_{0,\mathrm{x}}$, $\mathrm{E}_{0,\mathrm{y}}$ oriented along the x- and y-axis, respectively, and the relative phase shift $\delta = (\varphi_\mathrm{y} - \varphi_\mathrm{x})$ between them [179] shown in Figure 2.2, with i being the imaginary unit and φ_x, φ_y being the absolute phase of

the x- and y-polarised light components, respectively. The wave vector $k = 2\pi/\lambda$ and angular frequency $\omega = 2\pi \cdot \nu$ are hereby constant, which is why their exponential term is commonly omitted.

$$\vec{J} = \begin{pmatrix} \boldsymbol{E_{0,x} \cdot \exp(i\,\varphi_x)} \\ \boldsymbol{E_{0,y} \cdot \exp(i\,\varphi_y)} \end{pmatrix} \boldsymbol{exp(i(kz - \omega t))} = \begin{pmatrix} \boldsymbol{E_{0,x}} \\ \boldsymbol{E_{0,y} \cdot \exp\,(i\,\delta)} \end{pmatrix} \qquad \textbf{(2.1)}$$

Optical components that alter the SoP are expressed as 2×2 Jones matrices, commonly denoted with A, that are multiplied with the incident Jones vector, e.g. $\vec{J}_D$ for incident diagonally polarised light, to result in the Jones vector of the altered SoP behind the optics, denoted as $\vec{J}_{out}$, as exemplified in Eq. (2.2).

$$\vec{\boldsymbol{J}}_{\boldsymbol{out}} = \boldsymbol{A_{HWP}} \cdot \vec{\boldsymbol{J}}_{\boldsymbol{D}} = \begin{bmatrix} \boldsymbol{1} & \boldsymbol{0} \\ \boldsymbol{0} & \boldsymbol{-1} \end{bmatrix} \cdot \left(\frac{\boldsymbol{1}}{\sqrt{\boldsymbol{2}}} \begin{pmatrix} \boldsymbol{1} \\ \boldsymbol{1} \end{pmatrix} \right) = \frac{\boldsymbol{1}}{\sqrt{\boldsymbol{2}}} \begin{pmatrix} \boldsymbol{1} \\ \boldsymbol{-1} \end{pmatrix} = \vec{\boldsymbol{J}}_{\boldsymbol{A}} \qquad \textbf{(2.2)}$$

In this specific case, the reader can verify with Table 2.2 that incident diagonally polarised light $\vec{J}_D$ was transformed by a horizontally oriented linear retarder $A_{HWP} = \begin{bmatrix} \boldsymbol{1} & \boldsymbol{0} \\ \boldsymbol{0} & \boldsymbol{-1} \end{bmatrix}$ with retardance $\Delta = \pi$, commonly referred to as "half-wave plate (HWP)", into its orthogonal anti-diagonal state $\vec{J}_A$.

To obtain a more general description of a linear half-wave retarder $A_{HWP}(\theta)$ at a random transverse rotation angle θ with respect to the horizontal plane upon normal incidence, one can employ the rotation matrix $R(\theta)$ of Eq. (2.3) to obtain the expression of Eq. (2.4).

$$\boldsymbol{R(\theta)} = \begin{bmatrix} \boldsymbol{\cos\theta} & \boldsymbol{\sin\theta} \\ \boldsymbol{-\sin\theta} & \boldsymbol{\cos\theta} \end{bmatrix} \qquad \textbf{(2.3)}$$

$$\boldsymbol{A_{HWP}(\theta) = R(-\theta)\, A_{HWP}\, R(\theta)} = \begin{bmatrix} \boldsymbol{\cos^2\theta - \sin^2\theta} & \boldsymbol{2\cos\theta\sin\theta} \\ \boldsymbol{2\cos\theta\sin\theta} & \boldsymbol{\sin^2\theta - \cos^2\theta} \end{bmatrix} \qquad \textbf{(2.4)}$$

Using the expression of Eq. (2.4) for an arbitrarily oriented half-wave plate, one can predict the general impact of this optical element on incident circularly polarised light in Eq. (2.5) for incident $\vec{J}_R$ polarised light (see Appendix A for the step-by-step derivation).

$$\vec{\boldsymbol{J}}_{\boldsymbol{out}} = \boldsymbol{A_{HWP}(\theta)} \cdot \vec{\boldsymbol{J}}_{\boldsymbol{R}} = \vec{\boldsymbol{J}}_{\boldsymbol{L}} \cdot \underbrace{\boldsymbol{exp(i\,2\theta)}}_{:=\boldsymbol{\varphi_g(\theta)}} \qquad \textbf{(2.5)}$$

The reader can verify that the respective result for incident $\vec{J}_L$ polarised light is $\vec{J}_R \cdot exp(-i\,2\theta)$. From this result, one can draw the following conclusions:

1. Circularly polarised light passing through a HWP will be converted to its orthogonal circular state with inverted handedness irrespective of the orientation angle θ.

2. A phase term $\varphi_g(\theta) = \pm 2\theta$ is observed that depends on the HWP's orientation angle θ and exhibits an inverted sign for circular light with inverted handedness.

The orientation-dependent phase term $\varphi_g(\theta)$ is known in literature as geometric phase or Pancharatnam-Berry phase [180] and constitutes an important finding for polarimetry. Geometric phase is an intrinsic phenomenon encountered upon polarisation transformations that is fundamental to a dedicated branch of metasurfaces and optical components, as will be discussed further in Section 2.4. From this short study it is apparent that Jones calculus is a powerful tool when the exact phases of coherent light components are important. Hence, Jones calculus will be employed to describe the polarisation-dependent phase encoding presented in Section 3.3 that utilises (among others) the phenomenon of geometric phase, and for the description of the polarisation-beating in Section 5.2.1. However, one crucial drawback of Jones calculus is its inability to take account for unpolarised or partially polarised light, in which cases Mueller calculus must be employed.

Mueller calculus utilises differently polarised intensity components rather than complex-valued electric fields, therefore sacrificing information on the phase for a more intuitive description of the SoP based on easily measurable metrics. The SoP is described by the Stokes vector $\vec{S} = (S_0 \quad S_1 \quad S_2 \quad S_3)^T$, whose individual parameters S_0-S_3 represent:

- $S_0 \in [0, 1]$: The total (polarised) intensity of the beam (power)
- $S_1 \in [-1, 1]$: The prevalence of the $|\mathrm{H}\rangle$ (+1) over the $|\mathrm{V}\rangle$ (-1) polarised component
- $S_2 \in [-1, 1]$: The prevalence of the $|\mathrm{D}\rangle$ (+1) over the $|\mathrm{A}\rangle$ (-1) polarised component
- $S_3 \in [-1, 1]$: The prevalence of the $|\mathrm{R}\rangle$ (+1) over the $|\mathrm{L}\rangle$ (-1) polarised component

The degree of polarisation $DOP \in [0, 1]$ can be calculated in Eq. (2.6) and subsequently be used to extract the fully polarised component $\vec{S}_{pol}$ from partially polarised light $\vec{S}_{pp}$ according to Eq. (2.7), using $\vec{S}_{unp} = (1 \quad 0 \quad 0 \quad 0)^T$ as unpolarised component [179].

$$\boldsymbol{DOP = \frac{\sqrt{S_1{}^2 + S_2{}^2 + S_3{}^2}}{S_0}} \tag{2.6}$$

$$\boldsymbol{\vec{S}_{pol} = \frac{1}{DOP} \cdot \vec{S}_{pp} + \left(1 - \frac{1}{DOP}\right) \cdot \vec{S}_{unp}} \tag{2.7}$$

Transformations between different SoPs caused by optical components are described via cascaded matrix multiplication with the respective 4×4 Mueller Matrices M_e of each optical element e [181]. This work employed Mueller calculus to describe the generation of arbitrary SoPs and analysis of measured polarimetric data as detailed in Sections 5.3.3 and 6.3.2.

2.3.2 Polarisation-dependent Light-Matter Interactions

As introduced in the previous section, different SoPs represent different spatial distributions of the electric and magnetic field vectors of propagating light. Optical anisotropy of materials refers to a range of polarisation-dependent material characteristics that originate from a spatially differing distribution of atoms, electrons, ions or interfaces - including associated electric or magnetic fields - throughout certain materials. The interaction of light with an anisotropic material depends thereby on the relative alignment between the light's field vectors with the material's internal fields and components, giving rise to polarisation-dependent material characteristics. Polarimetry is dedicated to probing such anisotropic materials with different incident SoPs and measuring the material's optical response to infer conclusions on the material's internal structure. Figure 2.4 gives a non-exhaustive collection of the most important polarisation-dependent material properties.

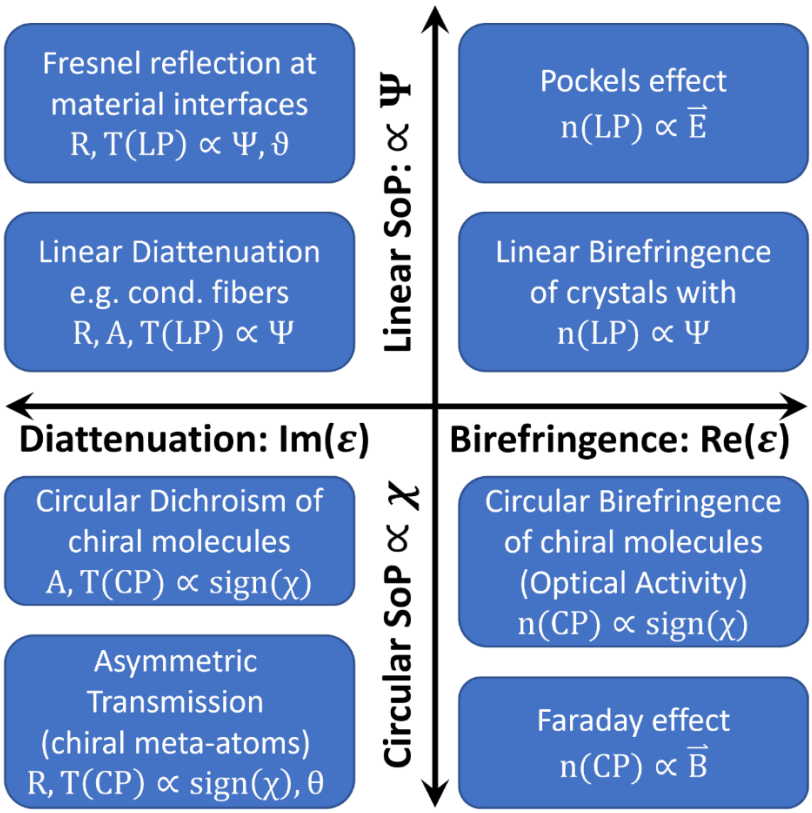

Figure 2.4: Non-exhaustive collection of polarisation-dependent material interactions and effects that alter the transmitted (T), reflected (R) or absorbed (A) SoP as function of the PE's orientation angle Ψ or ellipticity angle χ.

A first distinction can be made regarding the two orthogonal SoPs that experience the anisotropy of physical parameters, called eigen polarisations, which are either the two circular ($\propto \chi$) or two linear SoPs ($\propto \Psi$). The material's internal structure and geometry is typically linked to the type of anisotropy e.g., chiral or helical structures and molecules cause circular anisotropy, while linear structures and molecules cause linear anisotropy.

In a second distinction, the two fundamental types of polarisation-dependent material interactions in a non-magnetic medium ($\mu_r \approx 1$) can be identified as birefringence and diattenuation, for which the real part $\varepsilon'(\omega)$ and imaginary part $\varepsilon''(\omega)$ of the complex dielectric function $\varepsilon(\omega) = \varepsilon'(\omega) + i\,\varepsilon''(\omega)$ are polarisation-dependent tensors, respectively [182]. The real part $\varepsilon'(\omega)$ is thereby linked to the medium's RI $n(\omega) \approx \sqrt{\varepsilon'(\omega)}$, whereas the imaginary part constitutes the associated dielectric losses $L(\omega) \propto \varepsilon''(\omega)$ upon transmission $T(\omega) = \big(1 - L(\omega)\big)$.

Linear birefringence $\boldsymbol{\zeta_{lin}}$ is characterised by differing refractive indices $n_o \neq n_e$ along the ordinary (subscript o) and extraordinary (subscript e) axes, with the retardance Δ representing the accumulated optical phase difference through the material of thickness, t, according to Eq. (2.8).

$$\boldsymbol{\Delta = \underbrace{(n_e - n_o)}_{\zeta_{lin}} \cdot t} \qquad \textbf{(2.8)}$$

Wave retarders employed as polarisation optics are typically thinned to a thickness that results in a retardance of either $\Delta = \pi/2$ (QWP) or $\Delta = \pi$ (HWP). Birefringence can have several sources of origin, some of which are intrinsic to the material while others are controllable via extrinsic parameters. In crystalline structures, intrinsic birefringence originates from a differing density of atoms, ions or charges along different crystal directions. However, birefringent behaviour can also be caused by an external structuring, mechanic stress or an electric field, known as form birefringence [183, 184], stress-induced birefringence [32, 185-187] and the Pockels effect [188], respectively.

Linear diattenuation on the other hand describes the effect that two linear eigen-polarisations (linear OPB) exhibit deviating transmission $T(\Psi) = \big(1 - L(\Psi)\big)$ through a material, depending on the SoP's orientation angle Ψ relative to the OPB. The extinction ratio $T_\parallel/T_\perp$ compares the light's intensity that is polarised along the transmission axis $T_\parallel$ to the light polarised along the extinction axis $T_\perp$. Depending on whether the extinct SoP ($L(\Psi)$) is absorbed (Absorbance A) or reflected (Reflectance R), one can further distinguish between absorptive polarisers based on dichroism e.g., polaroid polarising filter, and beam-splitting

polarisers based on form-dependent reflection e.g., wire grid polariser (WGP). Any (electrically conductive) fibre whose diameter and length are larger and smaller than $\lambda/2$, respectively, will exhibit linear diattenuation [36].

Linearly polarised Fresnel transmission/reflection under non-normal angles of incidence $\vartheta > 0$ according to the Fresnel equations constitutes another common source of linearly polarised light, even if the light source itself is unpolarised. This polarising effect can be observed from the interface of any two media with differing optical density ($n_1 \neq n_2$) and is used in a wide range of applications, e.g. to measure a material's RI [189], for Brewster windows [83], to gauge angles of reflective areas upon remote sensing [190], etc.

Circular birefringence differs from linear birefringence solely in that the eigen polarisations are circular SoPs i.e., Eq. (2.8) holds true for $\boldsymbol{\zeta_{circ}} = (\boldsymbol{n_R} - \boldsymbol{n_L})$. Historically, this effect was first observed in aqueous solutions of chiral molecules such as sugars, for which a rotation of linearly polarised light $\Delta\Psi$ was observed depending on the ratio of the two enantiomers[2]. The Faraday effect replicates this observation with an extrinsically tuneable format by applying a colinear magnetic field $\vec{B}(z)$.

Circular Dichroism describes different absorption coefficients for orthogonal circular SoPs and is often encountered for chiral molecules and structures. An entire branch of spectroscopic material characterisation has been developed to exploit circular dichroism [191] to study the secondary structure of proteins [192], DNA [193] and small molecules [194], as well as the relative ratio of enantiomers [195].

Circular diattenuation is less frequently observed with only a few naturally occurring examples related to complex biological structures [177, 196]. However, recent developments in the field of metasurface science based on geometric phase were able to achieve **asymmetric transmission/reflection of circularly polarised light** using artificial meta-atoms exhibiting structural birefringence that were rotated in-plane by θ [197-200].

To conclude this section, the author wants to emphasise that there are a myriad of additional polarisation-dependent material interactions and effects that have not been presented. However, these unmentioned effects are not fundamental to understand the presented work and were hence outwith the scope of this thesis. The author refers to [201] for a more extensive theoretical description of polarisation-dependent effects.

---

[2] D: dextrorotatory, (+), clockwise; or L: laevorotatory, (-), counter-clockwise)

2.3.3 Review on Polarimetry and Polarimetric Imaging

Polarisation-dependent effects and material interactions can be either independent of the light's wavelength, subject to dispersion or confined to a specific spectral range e.g., Fresnel reflection, linear birefringence and dichroic absorption bands of a material, respectively. Consequently, this review will start off with polarimetric applications that exist throughout most of the electromagnetic spectrum before focussing on polarimetric imaging at terahertz frequencies in particular.

Three often overlapping applications of polarimetric imaging [202] are found in (atmospheric) remote imaging [203-210], astronomic imaging [211-215] and target detection [209, 210, 216-219]. Each application utilises (some parameter of) the SoP as contrast channel that provides either additional information on the scenery or robustness to both the imaging medium. For example, earth observation applications based on synthetic-aperture radars exploit polarimetric signatures to distinguish water bodies (Fresnel reflection) from vegetation (depolarisation upon scattering) and concrete/asphalt (e.g. single bounce reflection) [207, 208]. Compared to intensity-only contrast, polarimetric information is more robust within highly scattering media [217] such as haze (aerosol particles) [210], precipitation and fog [206, 218] or cosmic clouds [45, 215], and under adverse lighting conditions [219, 220].

Similar effects can be used for contrast enhancement in target detection applications to highlight objects that are often concealed behind clouds, haze, vegetation or camouflage [210, 219]. Polarimetry provides crucial additional information on the shape, orientation and roughness of flat, angled objects [216], thereby complementing spectral contrast that depends mostly on the object's material chemistry [202].

Nevertheless, polarimetry also has many applications in material identification and characterisation, often in a combined spectropolarimeter [221-224]. Most notable techniques are (imaging) ellipsometry [28, 225-228], faraday rotation spectroscopy [229-232], circular dichroism spectroscopy [191-195, 233, 234] and birefringence imaging of microstructures within biological matter [235-237] or composite materials [187, 238, 239].

However, respective setups and applications of polarimetric imaging at terahertz frequencies have been thus far hindered by technological shortcomings of terahertz source power, detector sensitivity and quality of optical terahertz components - as previously discussed in Section 2.2.2. As a result, terahertz polarimetry and polarimetric imaging was mostly confined to established THz-TDS modified to split the beam into two orthogonally linear

polarised detection channel [34, 36, 169, 239]. Despite THz-TDS being a mature technology that allows for time-of-flight analysis to generate 3D profiles, it often requires slow point-by-point scanning of the sample to generate images and a second beam path for the probe beam, as discussed previously in Section 2.2.3. A few notable exceptions succeeded in realising well-designed alternative setups for polarimetric terahertz imaging based on compact interferometric [166-168] or reflective [28] geometries. Nevertheless, more sophisticated and versatile systems with multiple adaptable imaging modes - comparable to a polarising microscope - require either more extensive optical trains or advanced optics with tailored polarisation characteristics, especially in transmission geometry. To demonstrate such a polarimetric imaging capabilities at terahertz frequencies, this work focusses on tailoring advanced optics towards their intended function as ultra-compact and efficient optics within a polarimetric terahertz microscope. For this role, anisotropic metasurface optics was identified as prime contender, as will be discussed in the next Section 2.4.

2.4 Metasurface Optics

2.4.1 Brief Introduction to Metasurface Optics

Metamaterials received their name from the Greek word ‘meta’ meaning ‘after/beyond’ and describe artificial materials that are structured in up to three spatial dimensions to achieve a tailored optical, mechanical, thermodynamic, acoustic or other function that extends beyond the capabilities of naturally occurring materials [240]. All metamaterials are composed of periodic arrays of small unit cells that contain an elemental structure within their centre, which is called ‘meta-atom’ in reference to natural atoms that make up the unit cells of natural crystals.

‘Metasurface optics’ is used here to describe flat 2-dimensional arrays of meta-atoms - comparable to the 2D crystal structure of graphene - that are designed towards a specific predefined optical response to incident light [241]. An important feature distinguishing metamaterial optics from photonic crystals is the sub-wavelength nature of both the meta-atoms and unit cells, which ensures the absence of diffractive effects and the validity of the effective medium approach [242-244]. Furthermore, strong light confinement will occur inside and immediately around the meta-atoms for both metallic/plasmonic [245] and dielectric [31] structures. This light confinement ensures a strong (often resonant) and efficient interaction between the incident wave and the meta-atoms while restricting parasitic

crosstalk between neighbouring unit cells [31, 245]. Crucially, such interaction and thereby the transmitted wave properties can be controlled individually at each lattice point via the meta-atom's geometry, as detailed in Section 2.4.2. Thus far, control over virtually all wavefront properties has been achieved with metasurfaces, namely the amplitude [246-249], phase [30, 31, 197, 246-254], polarisation [30, 31, 197, 249-254], orbital angular momentum [31, 197, 250] and even the wavelength via dispersion-engineering [255-259] and higher harmonic generation [260-262].

Giving a brief account to the historic development of metasurface optics and its underlying physics, one can consider wire grid polariser [244] and phase gratings [263-265] with sub-wavelength spacing as early examples of a 1-dimensionally structured optical metasurface that exhibits anisotropy of the transmitted amplitude and phase, respectively. The 1D anisotropy of elemental structures thus induces the different transmitted amplitude and phase for linearly polarised light oriented parallel or perpendicularly to the subwavelength structures.

Nevertheless, the advent of optical metasurfaces as a scientific field started with split-ring resonators (SRR), which are composed of a dielectric substrate with a thin metallic layer that is structured into well-defined rings that include one or several gaps, as shown in Figure 2.5 (a), (b). Whereas most naturally occurring materials are non-magnetic ($\mu_r = \mu/\mu_0 \approx 1$), SRR exhibit a designable magnetic resonance for incident light that can lead to strong and even negative permeabilities $|\mu_r| \gg 1$ around the resonance frequency [240, 266, 267]. Electrically coupled LC resonator are complementary resonant meta-atoms that achieve correspondingly strong and/or negative permittivity $|\varepsilon_r| \gg 1$ [268]. Negative values for both electromagnetic properties $\mu_r, \varepsilon_r < 0$ led to the experimental demonstration of negative refraction in left-handed materials with $n = \sqrt{\varepsilon_r \mu_r}$ [269-273], as shown in Figure 2.5 (c), (d).

Extending plasmonic-based metasurfaces towards the infrared spectrum with V-shaped antennas, Yu et al. [274] famously described a generalisation of Snell's law of refraction in Eq. (2.9**)** to account for the abrupt phase discontinuity encountered at the interface with 2D metasurfaces, as shown in in Figure 2.5 (e), (f).

$$\boldsymbol{n_t \sin\theta_t - n_i \sin\theta_i = \frac{\lambda_0}{2\pi} \cdot \frac{d\varphi}{dx}} \qquad \textbf{(2.9)}$$

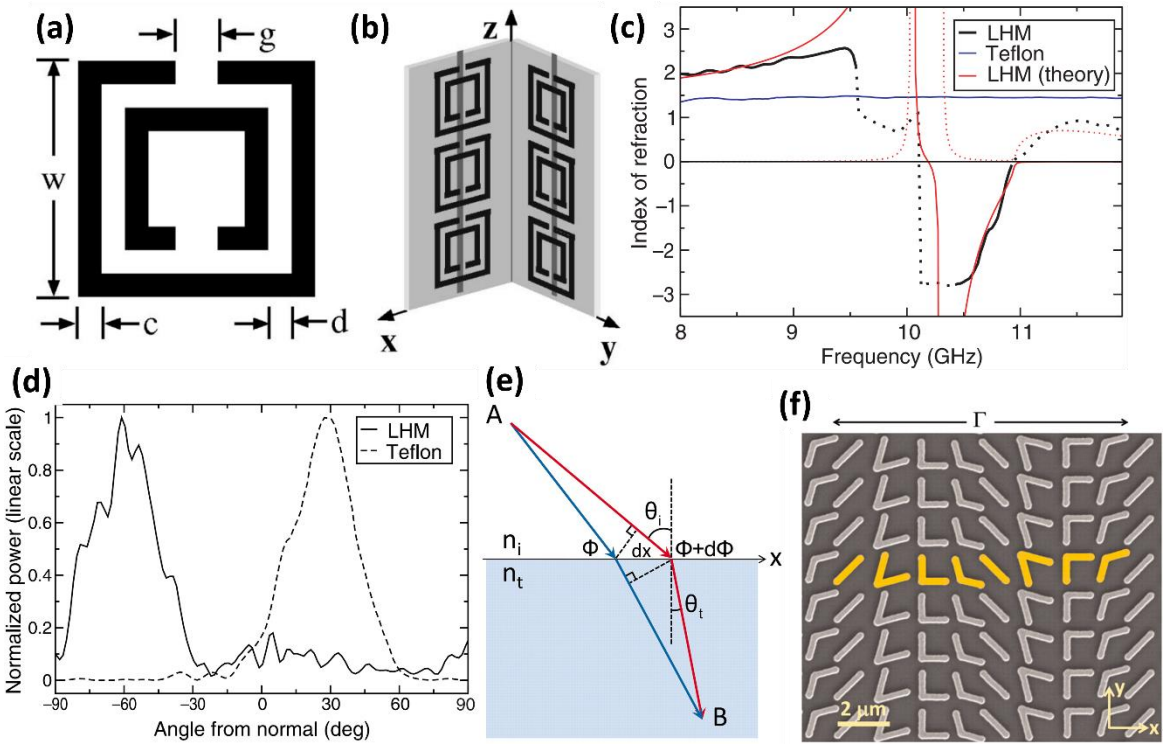

Figure 2.5: Illustration of (a) the geometric parameter and (b) spatial arrangement of a metamaterial based on SRR [269]. (c) Negative refraction with (d) a negative RI around its resonance frequency can be observed for such a SRR-based metasurface [270]. (e) Illustration of the generalised Snell's law of refraction developed to desribe phase discontinuities at the metasurface interface with (f) the structure based on V-shaped anetnnas that was employed to verify its validity [274]. (a), (b) Adapted from [269], (c), (d) adapted from [270], (e), (f) adapted from [274].

Besides the two angles $\theta_{i/t}$ of incidence (subscript i) and transmission (subscript t), and the refractive indices of both respective media $n_{i/t}$, one can identify a new term $d\varphi/dx$ that describes the spatial phase discontinuity $d\varphi$ along the in-plane direction dx. This means that an in-plane (2D) phase gradient can be approximated discretely at each unit cell with differently phase-shifting meta-atoms to steer the transmitted or reflected beams in virtually any direction. One meta-atom at a time, the phase function of classic optical components such as (spherical) lenses, diffraction gratings, axicons, etc. can be implemented by metasurface optics.

However, one major drawback of plasmonic-based metasurfaces are their considerable metallic losses, which imposes limits on the signal strength and overall device efficiency [275] despite recent progress based on intricate design [2, 276]. To address this issue,

lossless dielectric-based metasurfaces moved into the spotlight of the metasurface community due to having high overall efficiencies, typically above 80 % [31, 277]. Operational mechanisms of dielectric-based metasurfaces range from non-resonant metasurfaces based on propagation phase [263, 278, 279], geometric phase [198, 280-283] or their combination [30, 31, 249, 284], to Huygens metasurfaces based on simultaneous electric and magnetic Mie resonances [184, 254, 285] and bound states in continuum [286-288] for non-linear optics. Section 2.4.2 will discuss the underlying physics of propagation phase and geometric phase in detail since the metasurface optics presented in this work was based on a combination of these effects.

To conclude this section, the general key advantages of metasurface optics over their classic counterparts based on refractive and diffractive effects are summarised below:

- **Complexity of optical functions:** Since metasurface optics is optimised point-by-point with subwavelength resolution, it can efficiently and accurately carry complex 2D profiles of the wave's phase, amplitude and polarisation profiles. Superpositions of multiple optical functions can be realised by simply adding up the Fourier transforms of the respective phase functions into a single metasurface layer [289]. As such, a single metasurface can effectively replace multiple refractive elements and greatly simplify the layout and alignment of setups.
- **Performance:** Metasurface optics have reached or even surpassed the efficiency levels of established optics, with transmission efficiencies well above 80 % up to nearly 100 % at most spectral ranges. Further advantages such as the absence of spherical aberration [290], the capability to control chromatic aberration [255, 291] and realise high numerical aperture lenses [283, 292] often render metasurface optics superior to their refractive or diffractive counterparts in terms performance.
- **Versatility/Adaptability:** Once the design and fabrication methodology have been optimised, new metasurface designs with different optical function are straightforward to implement by slight alterations within the underlying design steps. New phase functions are implemented by adapting the code assembling individual meta-atoms, whose geometries can be recycled from previous parametric optimisations while the fabrication methodology remains basically the same for each different optical component. Consequently, metasurface optics is a highly adaptable platform that allows for rapid prototyping and extensions of functionalities.

- **Integrability:** A metasurface optics is basically an ultra-compact 2D optical layer with sub-wavelength thickness that can be directly integrated on to any desired substrate [293], optical element [294] or even the image sensor [276]. The negligible weight and spatial extent renders metasurface optics ideal for satellite optics.
- **Upscalability:** Most metasurface optics with sub-mm structure sizes draw upon lithographic production, which is already industrialised and ready for upscaling. As such, the first start-up already began to mass-produce and industrialise metasurface optics in consumer products [295]. For larger structure sizes, laser writing [296] and 3D-printing [297-299] techniques are promising routes towards cheap and up-scalable fabrication.

2.4.2 Controlling Polarisation and Phase with Anisotropic Metasurfaces

The metasurface optics developed within this thesis was based on dielectric meta-atoms, henceforth named meta-pillars, which utilise the propagation phase φ_p obtained upon transmission. Each meta-pillar can therefore be regarded as a truncated waveguide with low quality factor resonances that scatter transmitted light in a well-defined manner [279]. Let us consider the sub-wavelength unit cell of Figure 2.6 (a) (square of side length s) with its square meta-pillars of width W and height H. Assuming off-resonant (thereby broadband) operation and validity of the effective medium approach [242-244], one can simply approximate the obtained propagation phase φ_p upon transmission with Eq. (2.10) [263, 279]. The effective refractive index $n_{eff}(n_0, W)$ thus depends on the intrinsic refractive index of the meta-pillar's material n_0 and the relative fill-factor FF of the unit cell with pillar material, which is given by the ratio of volume occupied by the meta-pillar ($H \cdot W^2$) to the entire unit cell volume ($H \cdot s^2$), see Eq. (2.11).

$$\boldsymbol{\varphi_p = \frac{2\pi}{\lambda_0} \cdot H \cdot n_{eff}(n_0, FF)} \tag{2.10}$$

$$\boldsymbol{n_{eff}(n_0, W) = 1 + (n_0 - 1)\underbrace{\frac{W^2}{s^2}}_{FF}} \tag{2.11}$$

Consequently, the effective RI $n_{eff}(W)$ and thereby the obtained propagation phase $\varphi_p(W)$ can be controlled via the pillar width W as shown in Figure 2.6 (b), with all other parameters being design constants. Figure 2.6 (c) illustrates this dependence $n_{eff} \propto W$ by showing the x-z cross-section of the propagating electric field distribution for a (left) small and (right)

large pillar width, exhibiting slower propagation for the wider pillar due to its larger effective RI. Furthermore, the electric field is highly confined inside the meta-pillars and shows negligible crosstalk between them [31, 245]. The independence of the pillar's transmitted propagation phase $\varphi_p(W, x, y)$ from their surrounding pillars at each lattice point (x, y) allows us to approximate any two dimensional phase functions $\varphi_{optics}(x, y)$ of optical components such as lenses, axicons, Q-plates, etc. by simply placing locally optimised meta-pillars at each lattice point, as described in detail in Section 3.3. In order to achieve this, the span of meta-pillar dimensions $[W_{min};\ W_{max}]$ must be able to cover the full period of phase shifts $\Delta\varphi_p = \left|\varphi_p(W_{max}) - \varphi_p(W_{min})\right| \geq 2\pi$. From this relation and Eq. (2.11), one can approximate the span of effective refractive indices Δn_{eff} in Eq. (2.12) and thereby the lower limit for the structure height H_{LL} in Eq. (2.13).

$$\boldsymbol{\Delta n_{eff} = n_{eff}(W_{max}) - n_{eff}(W_{min})} \qquad \textbf{(2.12)}$$

$$\boldsymbol{H_{LL} \geq \frac{\lambda_0}{\Delta n_{eff}}} \qquad \textbf{(2.13)}$$

The above discussion described isotropic metasurfaces with meta-pillars of equal widths $W = W_x \equiv W_y$ in x- and y-direction on a square lattice but can be easily adapted to any other 2D lattice. The hexagonal dense lattice is often employed due to its higher packing density with the nearest neighbour distance D_0 and fill factor of $FF = \frac{W^2}{{D_0}^2\sqrt{3}/2}$. Importantly, such isotropic metasurfaces can control the transmitted phase front but fail to alter the transmitted SoP.

A commonly employed strategy to gain control over the transmitted polarisation profile $SoP(x, y)$ in addition to the phase profile is to employ meta-pillars with in-plane dimensions that are varied independently in x- and y-direction ($W_x \neq W_y$) [300]. Such anisotropic meta-pillars take advantage of form birefringence [184, 301], which in principle splits up Eq. (2.11) into two (nearly) independent equations $n_{eff,x}(W_x)$ and $n_{eff,y}(W_y)$ for x- and y-polarised incident light, respectively. It is intuitive to understand that independent adjustments of W_x and W_y therefore allow for independent control over the respective phase profiles $\varphi_{p,x}(W_x, x, y)$ and $\varphi_{p,y}(W_y, x, y)$ imposed on transmitted x- and y-polarised light, respectively. Furthermore, in-plane rotation of all meta-pillars by the angle θ extends this independent control to any orthogonal pair of linear polarisations with orientation angles $\Psi_1 = \theta, \Psi_2 = \theta + 90°$.

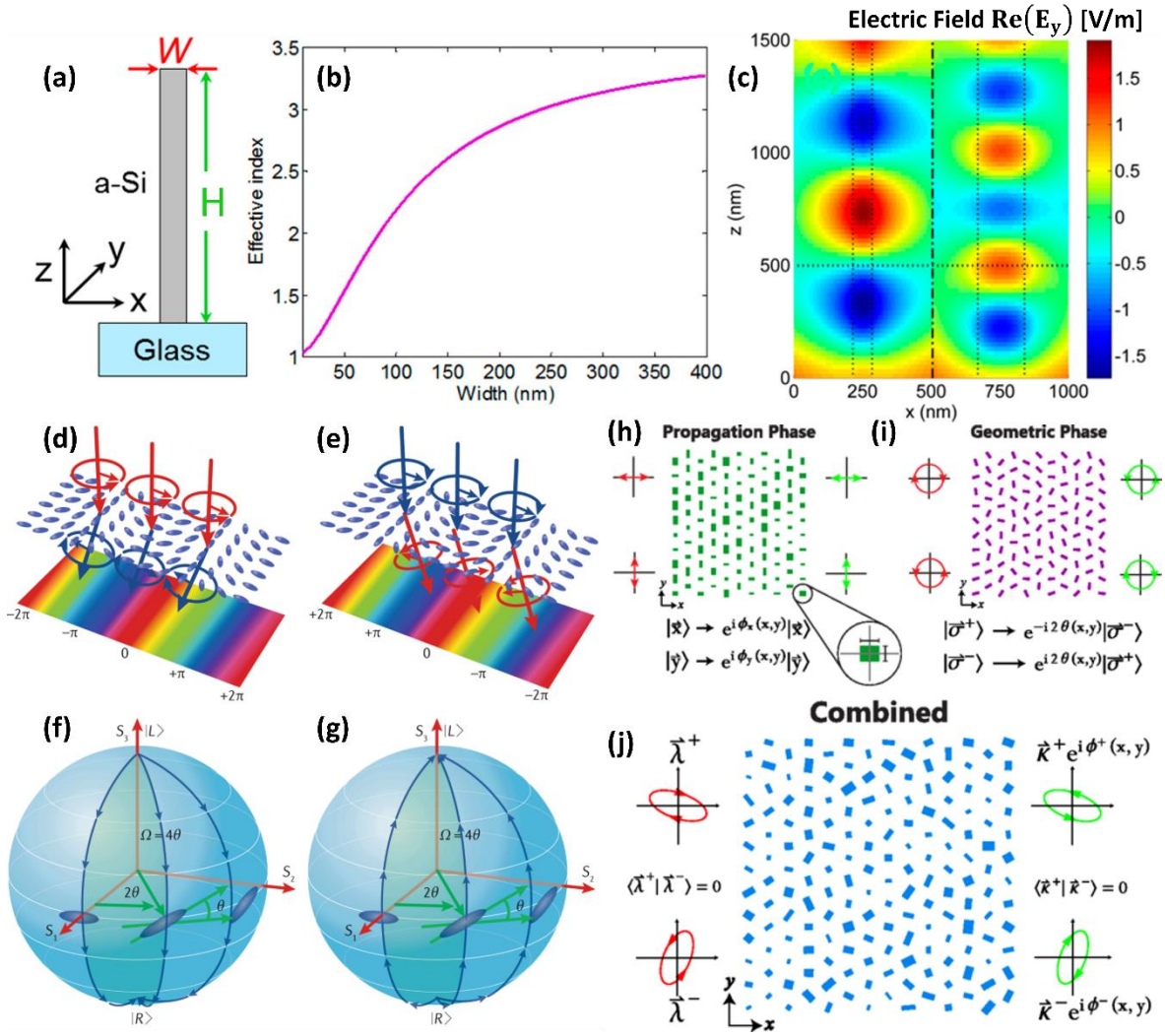

Figure 2.6: (a) A dielectric meta-pillar of Height H exhibits (b) an effective RI $n_{eff}(W)$ that depends on the pillar's width W. (c) The electric field distribution $Re(E_y)$ in x-z cross-section through the meta-pillar (propagation direction z) clearly shows strong light confinement within the pillars with a slower light propagation for the pillar with larger width W, resulting in a phase difference between them behind the pillar. A diffraction grating based meta-pillars that act as HWP exploits the geometric phase $\varphi_g(\theta)$ to achieve opposite diffraction angles for incident (d) $|L\rangle$ and (e) $|R\rangle$ polarised light. This geometric phase effect can be illustrated on the Poincare sphere for (d) $|L\rangle$ and (e) $|R\rangle$ polarised light. (a)-(c) Adapted from [263], (d)-(g) adapted from [302].

However, independent control of orthogonal SoPs with spin-angular momentum (handedness of circular component) requires more intricate design. Hasman et al. pioneered work to exploit the geometric (Pancharatnam-Berry) phase acquired upon conversions of the

incident polarisation [252, 265, 303]. As previously demonstrated in Eq. (2.5) (see Appendix A for the step-by-step derivation) and briefly discussed in Section 2.3.1, a HWP will always convert the circularly polarised component of incident light into its opposite handedness, including a geometric phase term $\varphi_g(\theta) = \pm 2\theta$ that depends only on the in-plane rotation angle θ of the HWP and the handedness of the incident circular light (+ for $|R\rangle$, - for $|L\rangle$).

This effect can be exploited by designing a birefringent meta-pillar as HWP with $\varphi_{p,x} = \varphi_{p,y} + \pi$ and then simply rotating these meta-pillars individually at each lattice point (x, y) throughout the metasurface to achieve the desired phase function $\varphi_g(\theta, x, y)$, as illustrated in Figure 2.6 (d), (f). Such metasurface optics based on geometric (Pancharatnam-Berry) phase have been widely studied in literature [304-306]. However, the phase profiles experienced by orthogonal circularly polarised components are opposite in their sign, but not independent. As shown in Figure 2.6 (d)-(g), a diffraction grating based on geometric phase will diffract light of orthogonal handedness into different directions, but with the same diffraction angle. Similarly, a metasurface based on geometric phase that is designed as focussing lens for one circular SoP will automatically be a defocussing lens for the orthogonal circular component [307, 308].

Arbabi et al. were the first to demonstrate a dielectric metasurface that overcame this limitation and achieved a truly independent choice of two different phase profiles imprinted on to the two orthogonal circular SoPs ($|R\rangle$ and $|L\rangle$) [31]. Their work combined the principles of propagation phase and geometric phase within anisotropic meta-pillars whose lateral dimensions W_x, W_y were varied independently in addition to the in-plane rotation of pillars by the angle θ. This mechanism, also known as spin-decoupled phase control [304], was quickly generalised by Balthasar Mueller et al. to enable independent phase profiles on to any orthogonal SoPs with spin-angular momentum, i.e. elliptically polarised light [30]. Figure 2.7 illustrates this principle, while a detailed explanation on the underlying calculations based on the Jones formalism can be found in the supplement of [309] with its practical implementation discussed in Section 3.3.

In conclusion, metasurface optics has come a long way in offering independent control over the transmitted polarisation and phase profiles, boasting capabilities for wavefront engineering and complex polarisation transformations that are unmatched by any other technology [310]. As such, metasurface optics represents a revolution in polarising optics, which shall be exploited for polarimetric terahertz applications within this thesis.

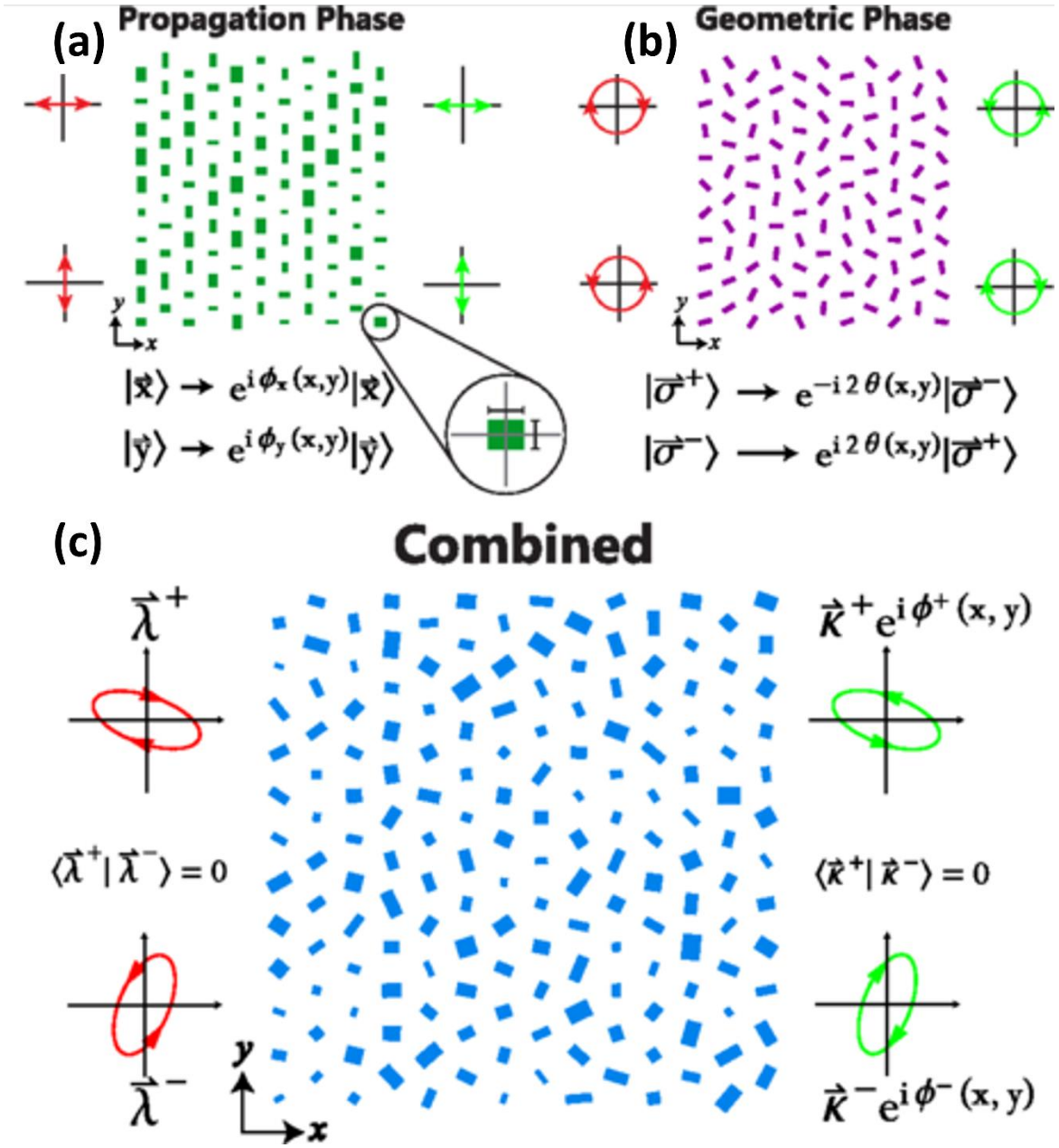

Figure 2.7: Illustration of different physical mechanisms for locally controlled phase acquisition of meta-pillars to implement arbitrary 2D profiles of the tranmitted phase and SoP. (a) Anisortopic pillars with independently varied pillar widths W_x, W_y exploit sturctural birefringence to acquire independent amounts of propagation phase along the two meta-pillar axes for respective linearly polarised light. (b) Geometric phase $\varphi_g(\theta) = \pm 2\theta$ can encode two phase profiles of opposite sign on to the circular SoPs using one pillar-dimension with birefringence of π (HWP) that are locally rotated by θ. (c) By clever combination of both effects, one can imprint independent phase funtions on to arbitrary elliptical SoPs, as will be described in Section 3.3. (a)-(c) adapted from [30].

2.4.3 Review on Dielectric Metasurface Optics at Terahertz Frequencies

As introduced in the previous section, dielectric-based metasurfaces employ 3-dimensional meta-pillars that have to be accurately produced from high-quality dielectric material by either additive or subtractive patterning techniques. Crucially, all operational mechanisms rely on structure dimensions that are scaled relative to the operational wavelength, e. g. Eq. (2.13). To operate within the terahertz spectrum, one therefore requires meta-pillars with structure dimensions i.e., pillar height H, in the range of tens to hundreds of micrometres, which is challenging to fabricate. Presumably for this reason, only a handful of experimental demonstrations of dielectric metasurface optics targeting wavefront manipulation in the terahertz spectrum have been reported when this PhD project started in October 2018 [305, 311-315], with only the Zhang et al. [313] demonstrating two independent phase functions for orthogonal $|H\rangle$ and $|V\rangle$ polarisations. Since then, interest in dielectric-based metasurface optics has been growing rapidly within the terahertz spectrum, with many demonstrations of (auto- [316]) focussing optics such as spherical [281, 299, 305, 313-315, 317-326] and axicon lenses [298, 299, 311-313, 317], albeit only a few take advantage of the polarisation-altering capabilities of anisotropic metasurfaces [281, 305, 311, 313, 318, 319, 323, 325]. Other demonstrated applications of polarising meta-optics include Q-plates [304, 311-313, 327], broadband wave plates [328-330], tuneable polarisation rotators [331-333] and asymmetric transmission [198, 334-338], to name a few. Notable non-polarising metasurface optics in the terahertz spectrum entail dielectric absorber [339-344], spectral bandpass filter [345], (broadband) anti-reflective layer [313, 330] and many more. It is worth noting that the majority of publications employ high-resistivity silicon as dielectric material [198, 199, 304, 305, 312, 313, 315, 317, 320, 321, 323, 324, 329, 331, 334, 338, 340, 346, 347] due to its favourable material properties at terahertz frequencies.

However, most demonstrations thus far of metasurface optics were restricted to presenting a specific metasurface design and confirming its intended operation, with relatively little work demonstrating the integration and use of metasurface optics in practical instruments. Furthermore, the ability to independently control two orthogonal polarisations has thus far only been presented as a scientific investigation rather than an opportunity to engineer novel beam forming and beam analysing optics within the terahertz spectrum, e. g. for polarimetry. This work has therefore aimed to advance the potential of metasurface optics operating at terahertz frequencies towards their tailored applications. Non-diffracting Bessel beams

therefore constitute a unique and versatile design platform for metasurface optics to alter the SoP in three spatial dimensions, as will be discussed in the next Section 2.5.

2.5 Non-diffracting Bessel Beams

2.5.1 Theoretical Background of Bessel Beams

The main objective of imaging optics is to set the intensity, phase and polarisation profiles that illuminate the imaged object and subsequently re-focus or collimate the altered beam on to the image plane for its recording and analysis. The vast majority of focussing and collimating optics employs spherical lenses, which impose the 2D parabolic phase profile of Eq. (2.14) on to the incoming wavefront to focus all intensity into a single (ellipsoidal) focal point at the focal length f behind the lens, as shown in Figure 2.8 (a). The transverse cross-section exhibits a radially symmetric Gaussian-distributed intensity profile with up to diffraction-limited waist radius $w_g(f)$ at the point of tightest focus, see Eq. (2.15). The focus is roughly maintained within $\sqrt{2}\, w_g(f)$ along the confocal length of z_g (twice the Rayleigh length z_R [348]) as shown and Eq. (2.16), respectively, with the incident beam diameter D_0. The waist radius of the Gaussian centre $w_g(z)$ can then be described at any axial distance z according to Eq. (2.17).

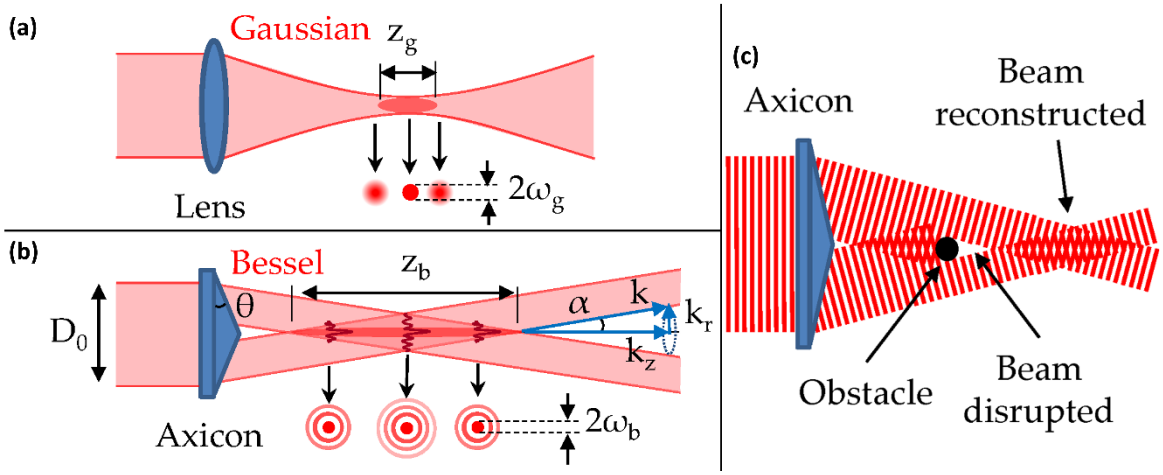

Figure 2.8: Schematics of the axial profiles of (a) a Gaussian beam focussed by a spherical lens and (b) a Bessel beam created by a conical axicon lens. (c) Illustration of the self-reconstructing capabilities of a Bessel beam after encountering small obstructions. Adapted from [349].

$$\boldsymbol{\varphi_g(x,y) = \frac{2\pi}{\lambda}\left(f - \sqrt{[f^2 + x^2 + y^2]}\right)} \quad \textbf{(2.14)}$$

$$\boldsymbol{w_g(f) = \frac{4\lambda}{\pi} \cdot \frac{f}{D_0}} \quad \textbf{(2.15)}$$

$$\boldsymbol{z_g = 2\, z_R = \frac{2\pi}{\lambda} {w_g}^2} \quad \textbf{(2.16)}$$

$$\boldsymbol{w_g(z) = w_g \sqrt{1 + \left(\frac{z}{z_R}\right)^2}} \quad \textbf{(2.17)}$$

Although spherical lenses are the predominant beam forming optics [253, 290, 305, 318, 321], their counterpart based on conical axicon lenses with phase profile given by Eq. (2.18) [350] offer several appealing advantages [351, 352]. The radial period of the axicon's phase profile, g, is thus connected to the axicon's base angle θ and RI n_A via the diffraction angle $\alpha = \sin^{-1}(n_A - \theta) - \theta = \sin^{-1}(\lambda_0/g)$ between the propagation direction and optical axis [353].

As shown in Figure 2.8 (b), the Bessel beams[3] generated by such an axicon phase entail an extended non-diffracting region within which the transverse intensity profile follows the Bessel function of the first kind $J_l(x, y)$ with order l [354]. Most importantly, the central lobe of this transverse Bessel profile exhibits a waist diameter w_b that remains constant over a large axial propagation distance z_b according to Eq. (2.19) and Eq. (2.20), respectively, with the diffraction angle α of the diffracted light given by the radial and axial wave vectors k_r, k_z in Eq. (2.21) [348, 349]. Each point $z_t = \frac{r \cdot d}{\lambda}$ on the optical axis is therefore the focal point of a narrow ring with radius r on the axicon. The concentric side-lobes constitute a reservoir for intensity, SoP and optical orbital angular momentum (OAM) that is fed into the central lobe further down the optical axis z [355, 356].

The needle-shaped focal line (central lobe) simplifies the alignment and retention of focus over considerable distances enabling applications such as light-sheet microscopy [355-357].

[3] Strictly speaking, true Bessel beams are spatially unbound and would hence entail an infinite amount of energy. However, experimental demonstrations of Bessel-Gauss beams with an incident plane wave bound to D_0 are a good approximation to the theory of Bessel beams. In this work, experimentally observed Bessel-Gauss beams are therefore referred to as 'Bessel beam' for simplicity without significant loss of accuracy.

$$\boldsymbol{\varphi_b(\mathrm{x},\mathrm{y}) = \varphi_b(r) = 2\pi \cdot \underbrace{\sqrt{x^2 + y^2}}_{:=|r|} \cdot g^{-1}} \quad \textbf{(2.18)}$$

$$\boldsymbol{w_b = 2.405 \cdot \lambda_0/(2\pi \sin(\alpha))} \quad \textbf{(2.19)}$$

$$\boldsymbol{\mathrm{z_b} = D_0/2 \tan \alpha} \quad \textbf{(2.20)}$$

$$\boldsymbol{\alpha = \arctan\left(\frac{k_r}{k_z}\right) = \arctan\left(\frac{D_0}{z_b}\right)} \quad \textbf{(2.21)}$$

Furthermore, Bessel beams possess self-reconstructing properties after encountering an obstruction, as shown schematically in Figure 2.8 (c) and described by Eq. (2.22), where z_{rec} is the axial distance after which the beam profile obstructed by an aperture of diameter o is reconstructed, and $k = 2\pi/\lambda$ the wave vector [348, 349].

$$\boldsymbol{\mathrm{z_{rec}} \approx \frac{\mathrm{k} \cdot \mathrm{o}}{\mathrm{k_z}} \approx \frac{\mathrm{o}}{\tan \alpha}} \quad \textbf{(2.22)}$$

Bessel beams are therefore broadly considered more robust against perturbations [358, 359]. Another intriguing property is the ability to create higher order Bessel beams that carry orbital angular momentum (OAM) by superimposing the spiral phase $\varphi_{OAM}(\rho)$ shown in Eq. (2.23) with the in-plane polar angle ρ and the topological charge (or order of the Bessel function) l [360, 361].

$$\boldsymbol{\varphi_{OAM}(\rho) = (\pm l \cdot \rho)} \quad \textbf{(2.23)}$$

Such vortex beams and their superpositions have been studied extensively as platform that allows for tailored variations of the SoP both in the transversal and longitudinal plane, which shall be explained in the next Section 2.5.2 [350, 352, 358, 360, 362, 363].

2.5.2 Tailored Transversal and Longitudinal Polarisation Profiles

'Structured light' is a vast and rapidly developing research topic that spans far beyond the concepts and beam types presented in this summary. Several excellent reviews have been published for readers wanting a broader overview [364-368]. This section aims to provide a more focussed and brief theoretical background for the work presented in Chapter 5.

To understand the physics behind the 3-dimensional variations of the SoP that can be achieved using Bessel beams, it is useful to decompose the SoP variation into the transverse x-y plane and the longitudinal z direction [358], as summarised in Table 2.3.

Table 2.3: Summary of (higher order) Bessel beams with different spatial variations of the SoP. The axicon phase functions $\varphi_1(r)$, $\varphi_2(r)$ for two orthogonal polarisations (subscript 1 and 2) are given by Eq. (2.18), whereas the respective OAM is given by Eq. (2.23) with the topologic charges l_1, l_2.

Beam type	**SoP in (x, y)**	**SoP along z**	**Topologic charge**	**Axicon phase fronts $[\Delta\varphi(z)]$**
Scalar Bessel/Vortex beam	Uniform	Uniform	$l_1 = l_2 \in \mathbb{N}_0$	$\varphi_1(r) = \varphi_2(r)$
Transverse Vector Vortex beam	Variant	Uniform	$l_1 = -l_2 \in \mathbb{N}$	$\varphi_1(r) = \varphi_2(r)$
Longitudinal Vector beam	Uniform	Variant	$l_1 = l_2 \in \mathbb{N}_0$	$\varphi_1(r) \neq \varphi_2(r)$
3D Vector Vortex beam	Variant	Variant	$l_1 = -l_2 \in \mathbb{N}$	$\varphi_1(r) \neq \varphi_2(r)$

The fundamental type of polarised Bessel beams are scalar Bessel beams that exhibit a uniform SoP profile in both the transverse and longitudinal direction, alternatively called scalar vortex beams if carrying OAM ($l \neq 0$), see Figure 2.9 (a). Such scalar Bessel beams are created by illuminating an axicon of isotropic phase profile given in Eq. (2.18) with polarised light - including the spiral phase of Eq. (2.23) in case of vortex beams.

(Transverse) vector vortex beams (TVVB) exhibit an SoP profile that varies within the transverse plane around an optical phase singularity in the centre ($l \neq 0$) [369]. Such TVVB have been known for well over a decade [370], with radially and azimuthally polarised vector beams shown in Figure 2.9 (b) ($l = 1$) being the most prominent examples. TVVBs can be easily generated with a segmented wave plate [371], a Q-plate [369, 372] or based on the superposition of two orthogonally polarised higher order Bessel beams $l_1 = l_2 \neq 0$. As shown in Figure 2.9 (b), radially (top left) and azimuthally (bottom left) polarised TVVB exhibit one full rotation of the linear SoP around the optical singularity of $l_1 = l_2 = \pm 1$, whereas higher order TVVB show respectively more of such phase discontinuities, i.e. two for the 2nd order TVVBs shown at the right side of Figure 2.9 (b) [351, 373].

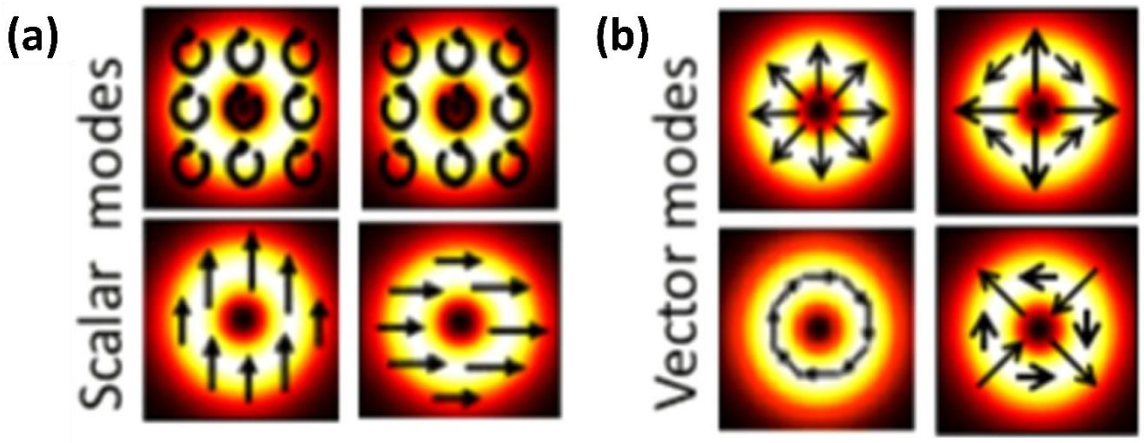

Figure 2.9: Depiction of diverse (a) scalar vortex Bessel beam modes of uniform transverse SoP (black arrows) and (b) vector vortex Bessel beam modes exhibiting a 2D-variant SoP in the transverse plane. The respective spatial intensity profile is depicted by the colour code (white → brightest, black → darkest). Adapted from [351].

Moreno et al. was among the first to demonstrate Bessel beams whose SoP was changing along the propagation direction (z) while remaining constant in each respective transverse plane [350], which will henceforth be called 'longitudinal vector beams' (LVB). Such LVB shown in Figure 2.10 are generated by superposition of two orthogonally polarised Bessel beams B_1, B_2 with different axial wave vectors $k_{z,1} \neq k_{z,2}$ [33]. In practice, this can be implemented by imposing two independent axicon phase profiles $\varphi_1(r)$, $\varphi_2(r)$ of Eq. (2.18) on to two orthogonal SoPs, e. g. $|R\rangle$ and $|L\rangle$. By choosing different grating constants $g_{|R\rangle} \neq g_{|L\rangle}$, a radially growing phase mismatch $\Delta\varphi(r) = \varphi_{|R\rangle}(r) - \varphi_{|L\rangle}(r) \propto r$ can be achieved between the $|R\rangle$ and $|L\rangle$ polarised wavefront. The radial-to-longitunal projection ($z \approx r \cdot g/\lambda$) achieved by the axicon phases results then in a longitudinally varying phase shift $\Delta\varphi(z)$ between the two orthogonally polarised Bessel beams $B_{|R\rangle}$, $B_{|L\rangle}$, which in turn translated into the desired longitudinal variation of the SoP. This longitudinal SoP is oscillating around a circular path on the Poincare sphere, which is equidistant to the underlying orthogonal polarisations of B_1 and B_2, i.e. latitude oscillation for $|H\rangle$ and $|V\rangle$, or azimuth oscillation for $|R\rangle$ and $|L\rangle$ [350, 358].

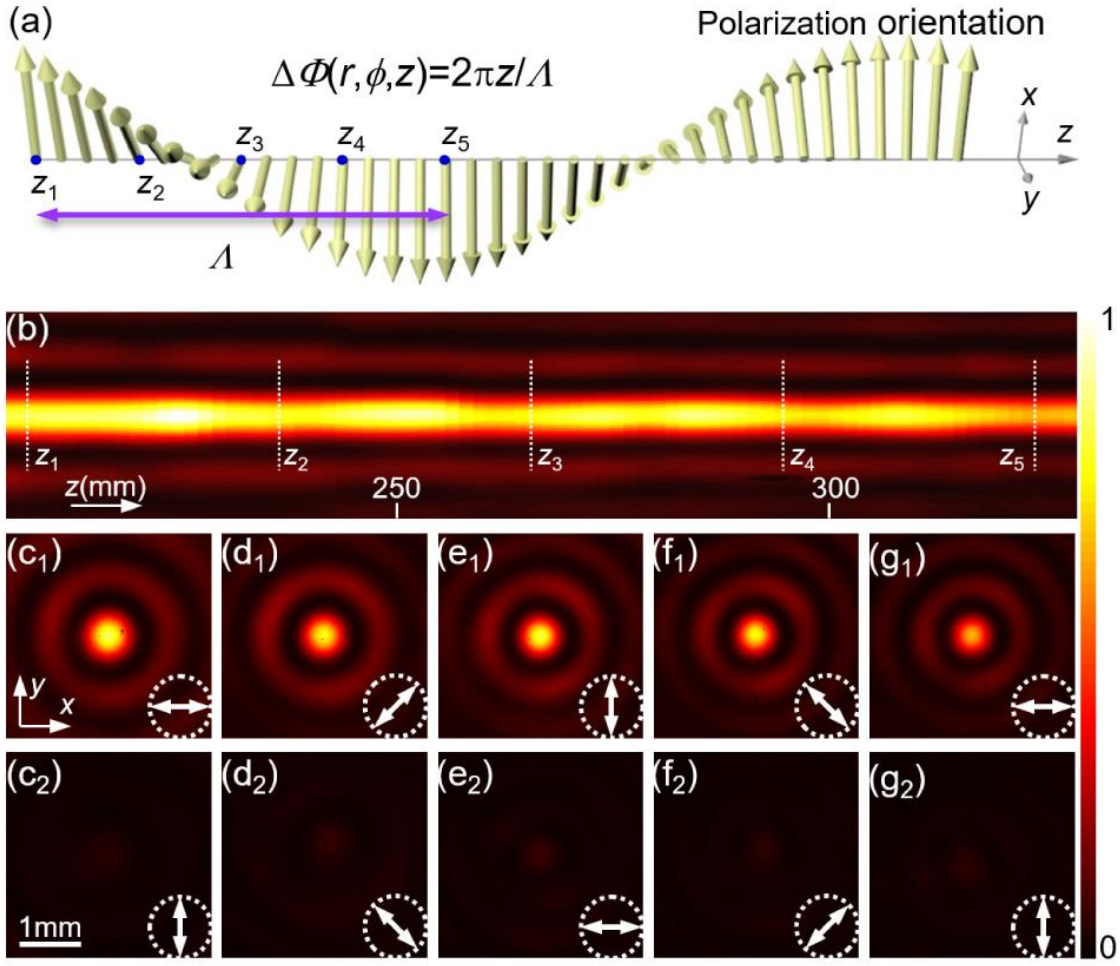

Figure 2.10: Demonstration of a Bessel beam with longitudinal variation of the SoP, consisting of two superimposed $|R\rangle$ and $|L\rangle$ polarised Bessel beams with $k_{z,|R\rangle} \neq k_{z,|L\rangle}$. (a) Schematic illustration of the continuous Λ-periodic rotation of the linear SoP along (b) the non-diffracting focal line. (c1) - (g1) shows the intensity maxima and (c2) - (g2) minima of the transverse plane after a respective polariser (white arrow) for five different z-positions, proving the axial SoP-rotation. Adapted from [358].

Both transverse and longitudinal variations of the SoP can be achieved by combining both previously described effects [352, 363, 374, 375]. Such 3D-vector vortex beams are again based on the superposition of two orthogonally polarised higher order Bessel beams with both $\varphi_1(\mathrm{r}) \neq \varphi_2(\mathrm{r})$ and $l_1 = -l_2 \neq 0$ [358, 360], as shown in Figure 2.11.

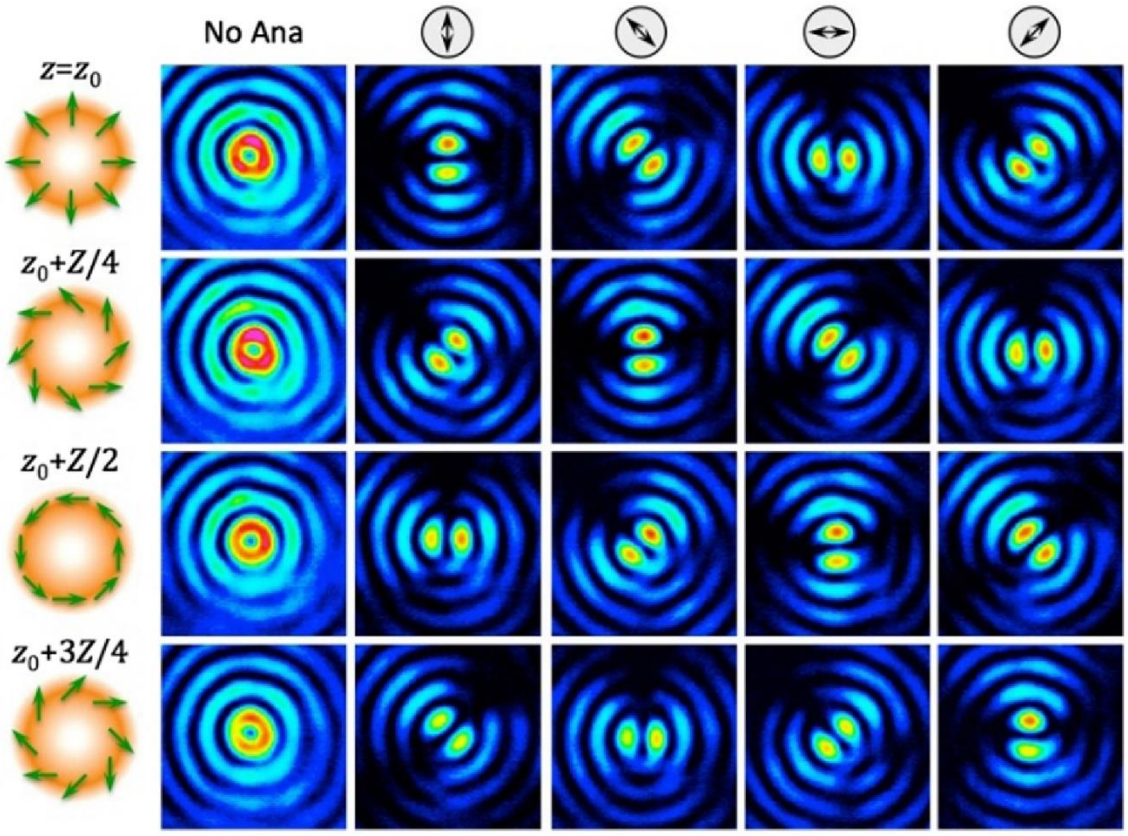

Figure 2.11: First-order (l_1 = 1, l_2 = -1) 3D-vector vortex beam whose transverse SoP profile (left column) varies along the propagation axis z (rows). The pictures from left to right show the transverse intensity profile without and with analyser, the orientation of which is indicated by the symbol above each respective column. Adapted from [360].

At last, it shall be mentioned that focussed radially polarised Bessel beams are even able to generate polarised beams that exhibit a strong linearly polarised component oriented along the propagation direction z [376, 377].

It is clear from this brief background theory that Bessel beams offer a potent and versatile platform to shape the SoP into novel and exotic pattern. Thus far, even polarised Bessel beams that alter their topologic charge upon propagation [360], self-accelerated Bessel beams with tailored trajectories [378] and structured bottle-shaped Bessel beams have been realised [379], to name a few. The following section thus aims to give a non-exhaustive review on important applications of Bessel beams.

2.5.3 Review on Bessel Beams and their Applications

As respective reviews point out [380-382], Bessel beams and their polarisation-variant derivates are highly anticipated as beam forming optics for a wide range of important applications.

Among the earliest reported applications were the prospects for micromanipulation, i.e. optical tweezing and particle trapping based on (higher order) Bessel beams or more complex superpositions thereof [33, 380, 383-389], such as bottle beams [390] or tractor beams [391].

In somewhat related application, Bessel beams are often crucial components in a range of different microscopy techniques. Examples range from their application as excitation beam for the 3D sectioning of samples within light-sheet microscopy [357, 392, 393] to super-resolution microscopy, which utilises either the inherent capabilities of Bessel beams to achieve sub-diffraction limited focusing [380, 394, 395], or employ them as doughnut-shaped de-excitation beam for the stimulated emission depletion (STED) principle that is central to super-resolution fluorescence microscopy [359, 396].

Another long-pursued field of applications for Bessel beams concerns microfabrication and material processing. Bessel beams have been found to have superior characteristics for ultra-fast and precise drilling of micro holes and laser ablation [33, 380, 397-400]. Interestingly, azimuthally polarised (transverse) vector vortex beams have been found to achieve higher drilling speed compared to other polarisation profiles [401], highlighting the benefits of Bessel beam's ability to form complex and versatile polarisation profiles.

Classical and quantum communication constitutes a broad field of application for Bessel beams that has gained a lot of attention over recent years [364, 402-409]. In particular, the OAM carried by Bessel beams offers prospects for signal multiplexing [410] and encryption [411, 412], whereas the directivity of its intensity profile together with non-diffracting and self-healing capabilities renders it an ideal candidate for (optical and 5G/THz) wireless communication links [413-415].

Bessel beams find additional applications in diverse fields, such as spectroscopy [377, 416] and optical sensing e.g. of the RI [33, 417, 418] and polarimetry of materials [419] or advanced beam forming capabilities, e.g. autofocusing beams [316, 420].

In recent years, the capability of metasurfaces to generate Bessel beams with complex intensity and polarisation profiles gained momentum due to the vastly reduced setup complexity required when employing tailored metasurface optics [421].

We can hence conclude that Bessel beams are a powerful and versatile beam forming platform that allows for control over a rich set of optical properties, most prominently OAM and complex (3D) profiles of the SoP. Particularly at terahertz frequencies, several key technologies such as wireless communication, (polarimetric) microscopy or non-destructive material testing have been proven to greatly benefit from the capabilities provided by Bessel beams.

The developments presented here further underline the merit of the strategy to design metasurface-generated Bessel beams with tailored polarisation profiles. These characteristics were deployed as probe beams within a compact and efficient polarimetric imaging microscope operating at terahertz frequencies, as will be presented in Chapter 5.

2.6 Summary of the Chapter

This chapter aimed to provide a well-founded yet brief theoretical background to understand the research conducted in this PhD project, as well as a baseline to evaluate the progress achieved in the completed work when compared to the current state-of-the-art in the literature.

Section 2.2 presented the unique properties of terahertz radiation and outlined the anticipated applications that would take advantage of them. A review on optical components and imaging setups operating within the terahertz regime concluded that progress on industrially viable terahertz applications is currently limited by technological capabilities and the maturity of optical components rather than by lack of potential of the terahertz spectrum or interest therein.

Section 2.3 introduced the theoretical background to understand and describe the state of polarisation as fundamental property of electromagnetic radiation. A brief review outlined the SoP's significance for material characterisation, remote sensing and contrast enhancement within diverse spectral regions before highlighting the apparent lack of efforts to introduce such polarimetric capabilities at terahertz frequencies. One proposition of this thesis is that the SoP is ideally suited to circumvent many challenges encountered for terahertz imaging and even deliver complementary information for the anticipated applications in NDT, security imaging and remote sensing.

The subsequent Section 2.4 provided a short recollection on the booming research concerning optical metasurfaces and summarised the joint advantages that are anticipated

for metasurface optics over its established counterparts i.e., refractive optics. The section concluded with a review on recent efforts to advance imaging capabilities within the terahertz spectrum by design of advanced metasurface optics based on highly efficient dielectric structures with sub-wavelength dimensions.

The last Section 2.5 discussed the physics underlying Bessel beams and derived their special properties, notably the non-diffracting beam profile, self-healing capabilities and formation of optical vortices. Special focus was dedicated to the remarkable capability of structuring the polarisation profiles of Bessel beams in both transverse and longitudinal direction, which renders Bessel beams a versatile platform for beam forming optics in polarimetric applications. The section finally summarised prior work on Bessel beams with focus on their anticipated applications.

Chapter 3 will present the methodology employed for the design and optimisation, using simulation, of the metasurface optics used in this thesis from individual meta-atoms to their assembly into a metasurface in depth. The discussion includes collective simulations that provide a frame of reference to confirm the intended optical operation prior to fabrication.

Chapter 3 : The Anisotropic Metasurface Platform

3.1 Motivation

As introduced in Section 2.4, metasurfaces constitute a revolution in functional optics due to their capability to efficiently convey complex optical functions within a single layer [30-33]. Obtaining respective optical functionality with classical optics typically requires multiple components in a complex setup that is prone to misalignments and standing waves [28] - if it is possible at all.

The majority of metasurface designs are divided into periodically arranged unit cells containing sub-wavelength structures, called meta-atoms, that manipulate the properties of light in a well-defined manner. Every meta-atom across a metasurface can be designed with an individually tailored effect on the transmitted (or reflected) properties of light, namely amplitude including diattenuation, phase shift including birefringence, and polarisation including independent functions for orthogonal SoPs [30, 31, 33, 418, 422]. The transmitted wavefront is formed behind the metasurface as a result of the superposition and interference of light scattered by each individual meta-atom.

This work focuses on dielectric meta-atoms that deliver high and uniform transmission amplitudes since the employed FIRL was already comparably faint in intensity despite being one of the most intense sources of radiation delivering 2.52 THz. Furthermore, it was desirable to encode arbitrary phase shifts independently on to two orthogonal polarisations, requiring an anisotropic geometry for the meta-atoms.

Once enough different meta-atom geometries to evenly cover all transmitted wave properties in the simulations of Section 3.2 were found, it was possible to produce arbitrary optical functions by optimising a spatial combination of these meta-atoms with the algorithm presented in Section 3.3 to obtain the metasurface design. To confirm that the desired optical function will be obtained, a template for collective simulations of large numbers of meta-atoms in the commercial software Lumerical FDTD solutions in Section 3.4 was set up.

It shall be emphasised that the presented meta-atom geometries can be arranged in numerous different spatial configurations to generate virtually any desired optical function. Both metasurface designs of Chapter 5 and Chapter 6 are based on the meta-atom geometries obtained in this section, as well as slightly adapted versions of the pattern generation code and the collective simulation template. Therefore, the anisotropic metasurface design

presented in this chapter can be regarded as a platform that enables quick and flexible creation of tailored polarising optic.

3.2 Optimisation Simulations of Meta-pillars and their Unit Cell

The parameters of the unit cell were chosen with careful consideration.

As dielectric material for both the substrate and meta-pillars, intrinsic silicon (resistivity > 10 kΩcm) was selected due to its high RI of 3.418 RIU [189] and high transparency at the design wavelength λ_0 of 118.8 µm (2.52 THz). A high RI ensures strong light confinement within the meta-pillars, and hence an effective manipulation by the pillar's geometry without significant cross-talk between neighbouring pillars [31]. In the present case, the pillars were separated by air (≈ 1 RIU). Moreover, bulk micromachining techniques such as deep reactive ion etching (DRIE) are well-matured technologies for the microstructuring of silicon [423].

A hexagonal lattice with nearest neighbour distance (D_0) of 40 µm (≈ $\lambda_0/3$) was chosen to provide a dense and even distribution of lattice points with a high spatial resolution of 635 pillars per inch for the encoded phase profiles. This lattice can be divided into three hexagonal sub-lattices, as done in Chapter 6, and still retain its sub-wavelength dimension with a next-nearest neighbour distance (D_1) of 69.3 µm (≈ 0.6 λ_0), or 367 pillars per inch.

The anisotropic pillar geometry was chosen to be rectangular for three major reasons. First of all, rectangular pillars are fully described by 2 vertices within the .gds file format so as to reduce the resulting file size considerably compared to e.g. elliptic pillars that require up to 199 vertices [424]. Beyond this, rectangular pillars are reported to have more efficient and more uniform optical response, e.g. compared to ellipses, see supplement S2 of [30]. Lastly, rectangular pillars are robust to fabrication tolerances upon dry etching. Slight rounding of the vertices affected optical performance insignificantly, while the reduced open space between pillars hindered the detrimental effect ARDE e.g., compared to ellipses.

Simulations of the transmission properties (S-parameters) for a wave propagating from within the substrate (port 1 at z_{min}) through the pillars towards air (port 2 at z_{max}) were conducted using the commercial software CST Studio due its user-friendly "parameter sweep" interface that allowed for the adjustment of the three pillar dimensions within their unit cell shown in Figure 3.1 (a), namely width in x (W_x), width in y (W_y) and height in z (H). The planes dissecting the substrate (white dashed lines) were set to have 'periodic

boundary conditions' in order to include potential cross-talk between neighbouring pillars, whereas the two x-y planes parallel to the substrate at z_{min} and z_{max} were set as "perfectly matched layer (PML)" to absorb the transmitted and reflected waves at port 1 and 2, thereby preventing their reflection back into the simulated space.

Two opposing requirements had to be optimised in a trade-off:

1) **Optical performance:** The transmitted phase-shifts φ_x, φ_y for incident x- and y-polarised light needed to independently span the full phase period from [-π, π]. This required a large range of pillar widths $[Min(W_{x,y}), Max(W_{x,y})]$ and/or a large pillar height (H). In addition, all simulated pillar dimensions shall exhibit a high and uniform transmission T. An in-depth summary and explanation is given by Kruk et al. in [425].
2) **Fabrication tolerances:** Dry-etching the pillars anisotropically into a silicon substrate without an etch-stop layer will lead to *aspect-ratio dependent etch rates* (ARDE), see Section 4.4.2. This detrimental effect becomes more severe for a larger range of pillar width $[Min(W_{x,y}), Max(W_{x,y})]$ and/or a larger pillar height (H). Furthermore, the extreme pillar dimensions were limited to $Min(W_{x,y})$ of 7.5 µm and $Max(W_{x,y})$ of 30 µm to avoid collapsing pillars due to undercutting and low etch rates at narrow trenches ($D_0 - W_{x,y} \geq 10$ µm), respectively.

Figure 3.1 (b) shows the resulting phase shifts φ_x, φ_y for individual pillar geometries (black datapoints) of 100 µm (0.84 λ_0) height (H) with a range of pillar widths spanning [7.5 µm; 30 µm] with 0.5 µm step-size. The colour code around each datapoint represents the pillar's respective aspect ratio (W_x/W_y). It can be clearly seen that the 2D phase plane exhibits two extended regions without black datapoints, representing phase shift combinations φ_x, φ_y that cannot be approximated by any pillar design. Consequently, the simulation results fail to accurately encode two arbitrary phase profiles independently on to the x- and y-polarised components. Furthermore, fabrication trials showed severe spatial etch depth deviations for this large range of pillar widths spanning [7.5 µm; 30 µm].

The simulations of pillar widths spanning [7.5 µm; 30 µm] were rerun with larger pillar heights until 150 µm (1.26 λ_0) was selected as optimum. The resulting phase shifts φ_x, φ_y (black datapoints) in Figure 3.1 (c) successfully cover the entire 2D phase space evenly. The respective transmissions $T_{x,y}$ of these simulated pillars in Figure 3.1 (d) were above 70 %, with a distinct region of even higher transmission (white meshed area).

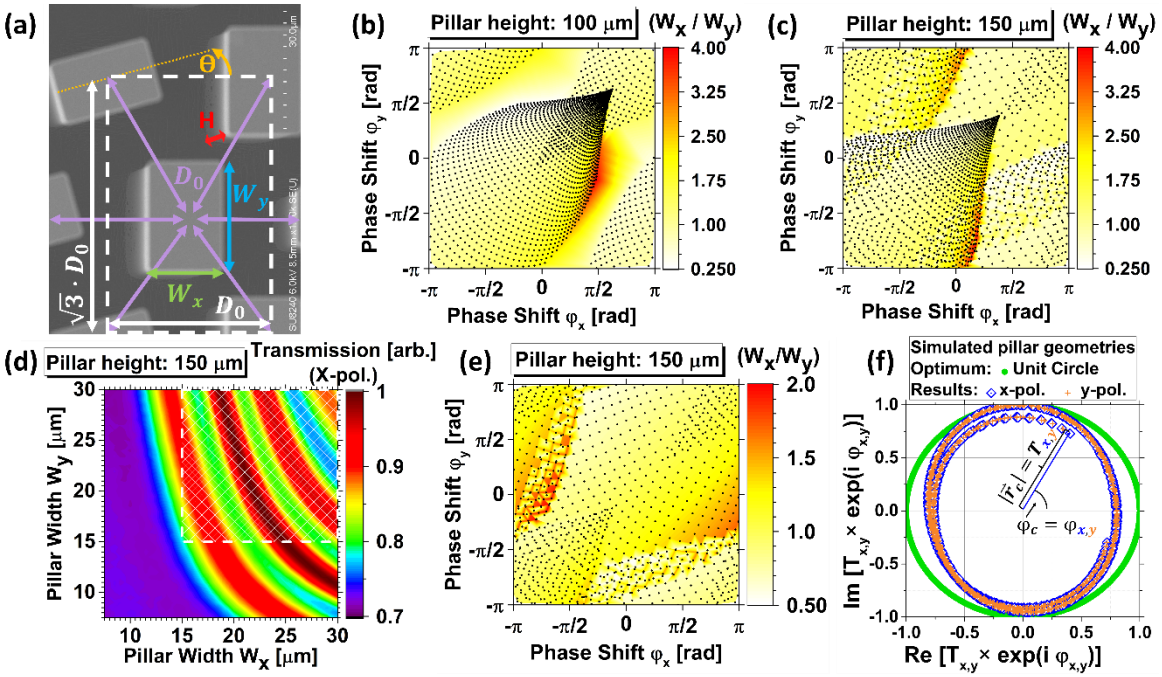

Figure 3.1: (a) Depiction of the unit cell (white dashed box) using the commercial simulation software CST Studio with its parameters: pillar height H, nearest neighbour distance D_0 (40 µm), pillar widths W_x and W_y with 0.5 µm step-size, and the in-plane rotation angle Θ with 1° step-size. (b) Simulation results of the transmitted phase shifts φ_x, φ_y for W_x, W_y in the range [7.5 µm; 30 µm] and a pillar height H of 100 µm (each black datapoint represents the result a different pillar dimension i.e., W_x, W_y). The colour code around each datapoint represents the pillar's respective aspect ratio (W_x/W_y), which should be as low as possible to minimise fabrication tolerances due to ARDE. (c) Respective simulation results of the transmitted phase shifts φ_x, φ_y for a pillar height H of 150 µm (black datapoints) with (d) their respective x-polarised transmission T_x (colour code) for the simulated pillar widths W_x, W_y (respective results for y-polarised light are mirrored around the diagonal line). The highlighted area (white mesh) represents the more efficient range of pillar widths within [15 µm; 30 µm] that was selected for the final design, with (e) the respective phase shifts φ_x, φ_y. (f) Polar plot of the complex transmission for the final design with incident x- and y-polarised light (blue and orange data, respectively). Each datapoint represents a specific pillar geometry W_x, W_y with the respective polar angle and radial distance corresponding to the phase shift and transmission of this pillar. The full phase range (polar angle) was spanned with high and uniform transmission (radial distance) close to the optimum (green unit circle).

This reduced range of pillar widths within [15 µm; 30 µm] was still enough to evenly span the entire 2D phase space as shown in Figure 3.1 (e) and hence selected as final design for our pillars. The polar plot of the complex transmission $T_{x,y} \cdot \exp(i\,\varphi_{x,y})$ of Figure 3.1 (f) demonstrates a good performance of the final pillar design compared to the optimum (green circle), with any pair of phase shifts φ_x, φ_y (corresponding to polar angles) attainable with a high and uniform transmission T_x, T_y (corresponding to radial distance) of 86.9 % $\pm$ 6.4 %. Furthermore, the decreased aspect ratios of these pillars helped to decrease the impact of ARDE on the etch depth to a manageable level.

The selected pillar dimensions ($H = 150\ \mu m$, $W_{x,y} \in [15\ \mu m, 30\ \mu m]$, $\Delta W_{x,y} = 0.5\ \mu m$) are capable of accurately encoding two independent phase profiles on to the x- and y-polarised components of transmitted light with a high and uniform transmission, while limiting the aspect ratio and its associated fabrication tolerances.

To gauge the impact of slight height deviations ΔH caused by ARDE on the optical performance of the selected pillars, the simulations were repeated for a range of different pillar heights encountered in practice (see Section 4.3) while accounting for the associated change of the substrate thickness t_{sub}. Figure 3.2 shows the deviations of the x-polarised transmission $\Delta T_x(\Delta H) = T_x(H) - T_x(H \pm \Delta H)$ caused by height deviations ΔH of $\pm$5 µm and $\pm$10 µm. It can be seen that the transmission efficiency of individual pillar geometries changed by up to $\pm$0.17, or $\pm$17 %, for ΔH of $\pm$10 µm. A respectively smaller height deviation ΔH of $\pm$5 µm resulted in values of $\Delta T_x(\Delta H)$ within $\pm$9.7 %, suggesting a linear relation $\Delta T_x \propto \Delta H$. Strikingly, the averaged transmission efficiency of all pillar dimensions was virtually unaffected by these height deviations. The metasurface can therefore be expected to maintain its overall efficiency within $\pm$10 µm of the intended etch depth of 150 µm despite minor transmission shifts experienced by individual pillar geometries.

The resulting deviations of the transmitted x-polarised phase shift $\Delta\varphi_x(\Delta H) = \varphi_x(H) - \varphi_x(H \pm \Delta H)$ caused by height deviations ΔH of $\pm$5 µm and $\pm$10 µm are depicted in Figure 3.3. Two conclusions can be made from these results:

1. The phase deviation $\Delta\varphi_x(\Delta H)$ changes only gradually with the pillar dimensions W_x, W_y.
2. The phase deviation of each pillar dimension changes in good approximation linearly with the etch depth deviation $\Delta\varphi_x \propto \Delta H$ from -10 µm to $+10$ µm with an average slope of approx. -4.6°/µm.

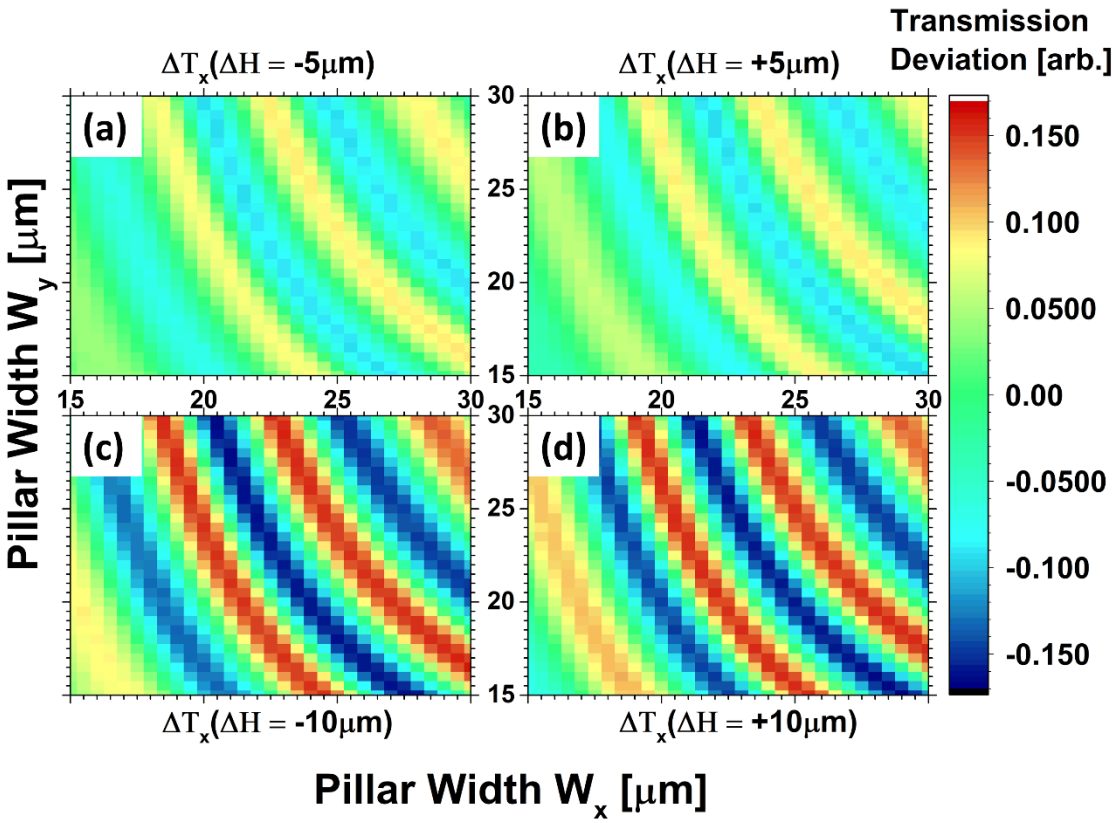

Figure 3.2: (a) Simulation results of the deviations of transmission $\Delta T_x(\Delta H)$ expected for over- and under-etching due to ARDE for ΔH of (a) -5 μm, (b) $+5$ μm, (c) -10 μm and (d) $+10$ μm. The average transmissions at each pillar height were (a) 87.2 % $\pm$ 6.4 %, (b) 87.0 % $\pm$ 6.3 %, (c) 87.3 % $\pm$ 6.4 % and (d) 86.9 % $\pm$ 6.5 %, showing that they were virtually unaffected by the etch depth deviation (86.9 % $\pm$ 6.5 % at 150 μm). Results for y-polarised light $\Delta T_y(\Delta H)$ are obtained by swapping the x- and y-axes.

The linear relation between pillar height (ΔH) and imparted phase shift ($\Delta\varphi_x$) was expected from the theory of propagation phase [263, 279], see Eq.(3.1) with the design wavelength λ_0 and the pillar's effective RI $n_{eff,x,y}$ for x- or y-polarised light, respectively, which can be varied by the pillar widths (W_x, W_y).

$$\Delta\varphi_{x,y} = \frac{2\pi}{\lambda_0}\Delta H \cdot n_{eff,x,y}(W_x, W_y) \qquad (3.1)$$

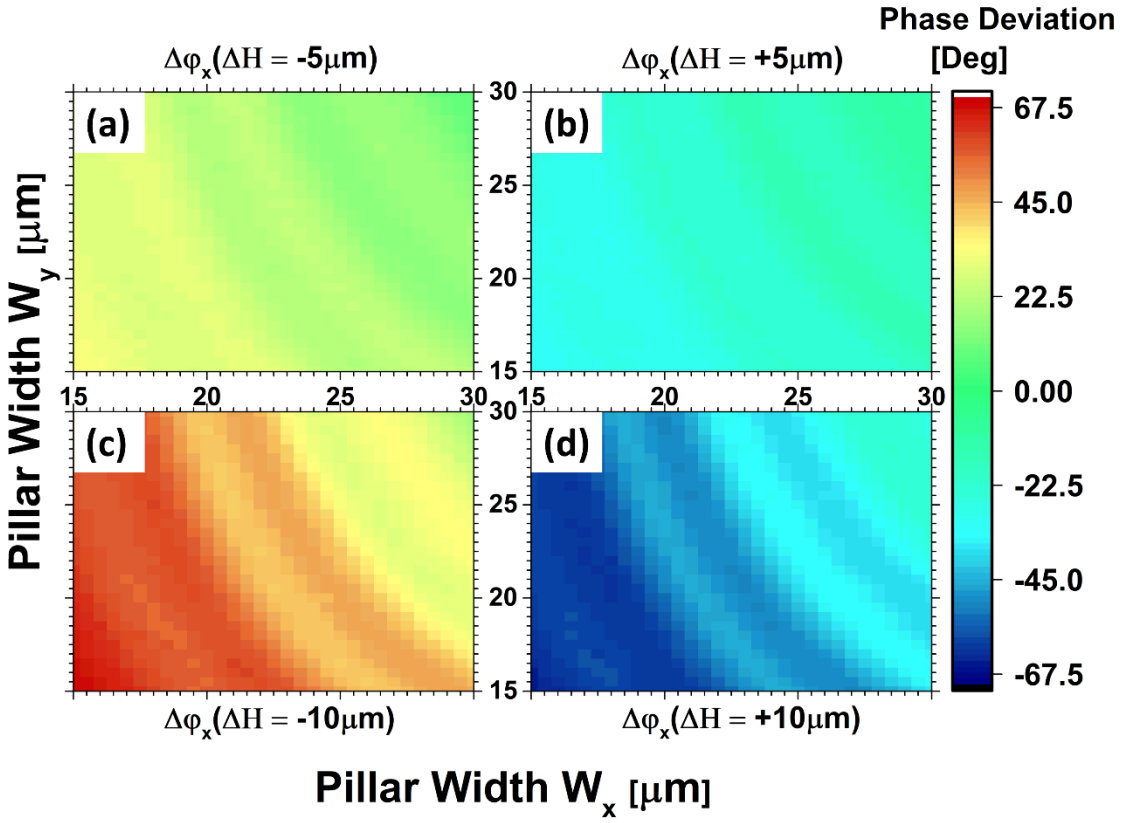

Figure 3.3: (a) Simulation results of the phase deviation $\Delta\varphi_x(\Delta H)$ expected for over- and under-etching due to ARDE for ΔH of (a) -5 μm, (b) $+5$ μm, (c) -10 μm and (d) $+10$ μm. The averaged phase deviation of all design pillars was hereby $22.9° \pm 5.6°$, $-23.0° \pm 5.7°$, $46.1° \pm 11.0°$ *and* $-46° \pm 11.4°$, *respectively. Results for y-polarised light $\Delta\varphi_y(\Delta H)$ are obtained by swapping the x- and y-axes.*

To further explore the linearity of the pillar's phase response to the etch depth deviation, linear fitting was performed with the simulated phase shifts $\varphi_x(H)$ for each pillar dimension (W_x, W_y) at H = [140 µm, 145 µm, 150 µm, 155 µm, 160 µm]. Figure 3.4 shows the slope determined from this fit as a function of pillar geometry, with its correlation coefficient (Pearson's r $\geq$ 0.95) certifying a compellingly linear relation $\varphi_x \propto H$ for each pillar dimension, as expected from Eq. (3.1). Using this slope together with Eq. (3.1) enabled the determination of the effective RI $n_{eff,x,y}(W_x, W_y)$ for transmitted x- or y-polarised light, as well as the pillar's birefringence ($n_{eff,x} - n_{eff,y}$). With the results of this simulation study, a detailed understanding was gained of the operational principle of the unit cell design that makes up the metasurfaces, as well as the data to gauge and quantify the impact of etch depth deviations on the performance of the fabricated metasurfaces.

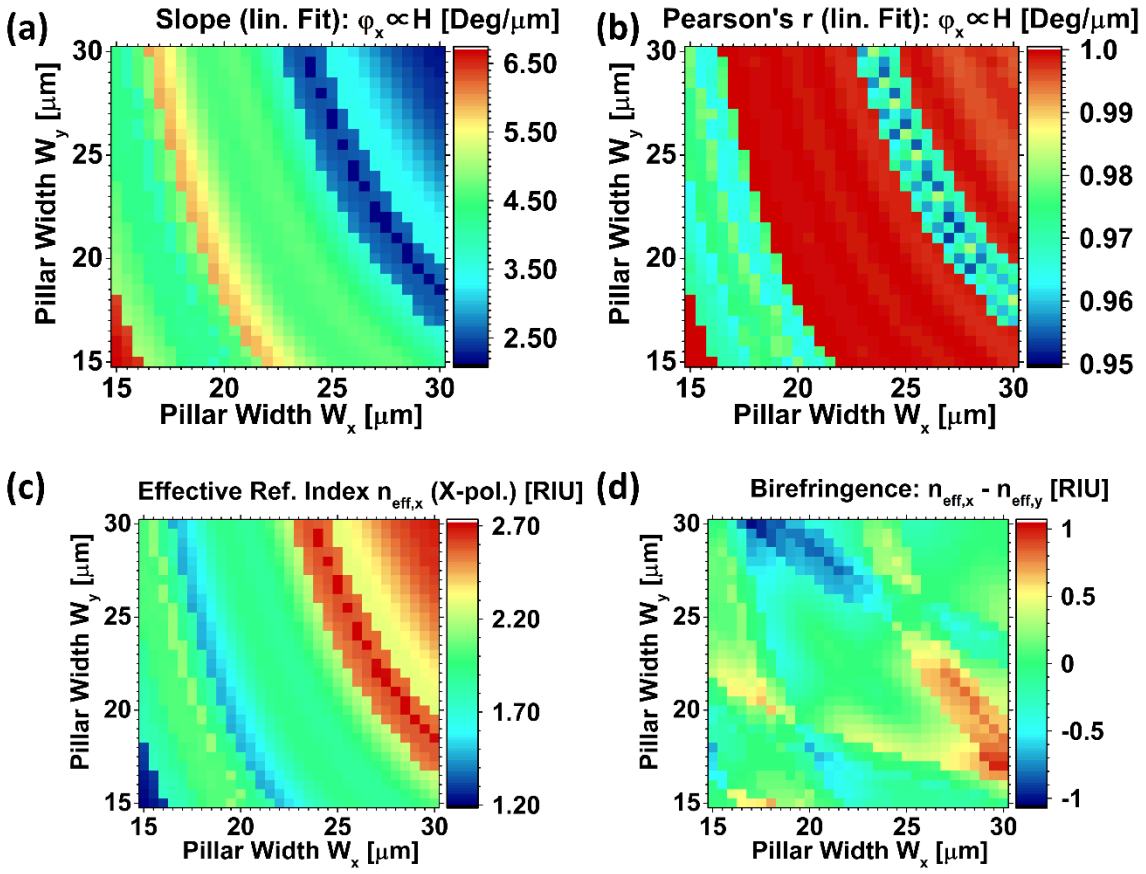

Figure 3.4: For each pillar dimension (W_x, W_y), the simulated phase shifts $\varphi_x(H)$ at H=[140 µm, 145 µm, 150 µm, 155 µm, 160 µm] were linearly fitted to determine the (a) slope with its (b) correlation coefficient (Pearson's r). Using the obtained slope and Eq. (3.1), (c) the effective RI $n_{eff,x}$ of x-polarised light and (d) the birefringence $n_{eff,x} - n_{eff,y}$ can be calculated for each pillar geometry. Respective results for y-polarised light of (a)-(c) are obtained by swapping the x- and y-axes.

The presented design was consequently employed for all metasurfaces (simulations and experiments) presented in this thesis i.e., in Chapter 5 and Chapter 6.

3.3 Pattern Generation – Assembling Meta-Pillars into Metasurfaces

The pattern generation code summarised in Figure 3.5 was written in *python* using the *gdsCAD documentation* [424]. For all metasurfaces presented in this thesis, the code required three initial design parameters:

i) Pattern extent e.g., circular area with R_{MS} of 11 mm, and ii) the two arbitrary phase functions $\varphi_1(x_i, y_i)$, $\varphi_2(x_i, y_i)$ e.g., two different axicons, that are to be imprinted on to iii) the respective OPB e.g., $|R\rangle, |L\rangle$ polarised light. The simulation results of Section 3.2 (($W_x(m)$, $\varphi_x(m)$, $T_x(m)$, $W_y(m)$, $\varphi_y(m)$, $T_y(m)$) for each meta-pillar geometry m were imported into the 'meta-pillar library'. Hexagonal lattice points $l = (x_i, y_i)$ with 40 µm spacing were generated within the pattern extent and - if necessary - divided into their sub-lattices. The algorithm looped over each lattice point l and calculated the phase shifts $\varphi_{aim,x}(l)$, $\varphi_{aim,y}(l)$ to be imposed by the pillar's widths W_x, W_y, as well as the pillar's in-plane rotation angle $\theta_{aim}(l)$ according to Eq. (3.2**)**, Eq. (3.3**)** and Eq. (3.4**)**, respectively.

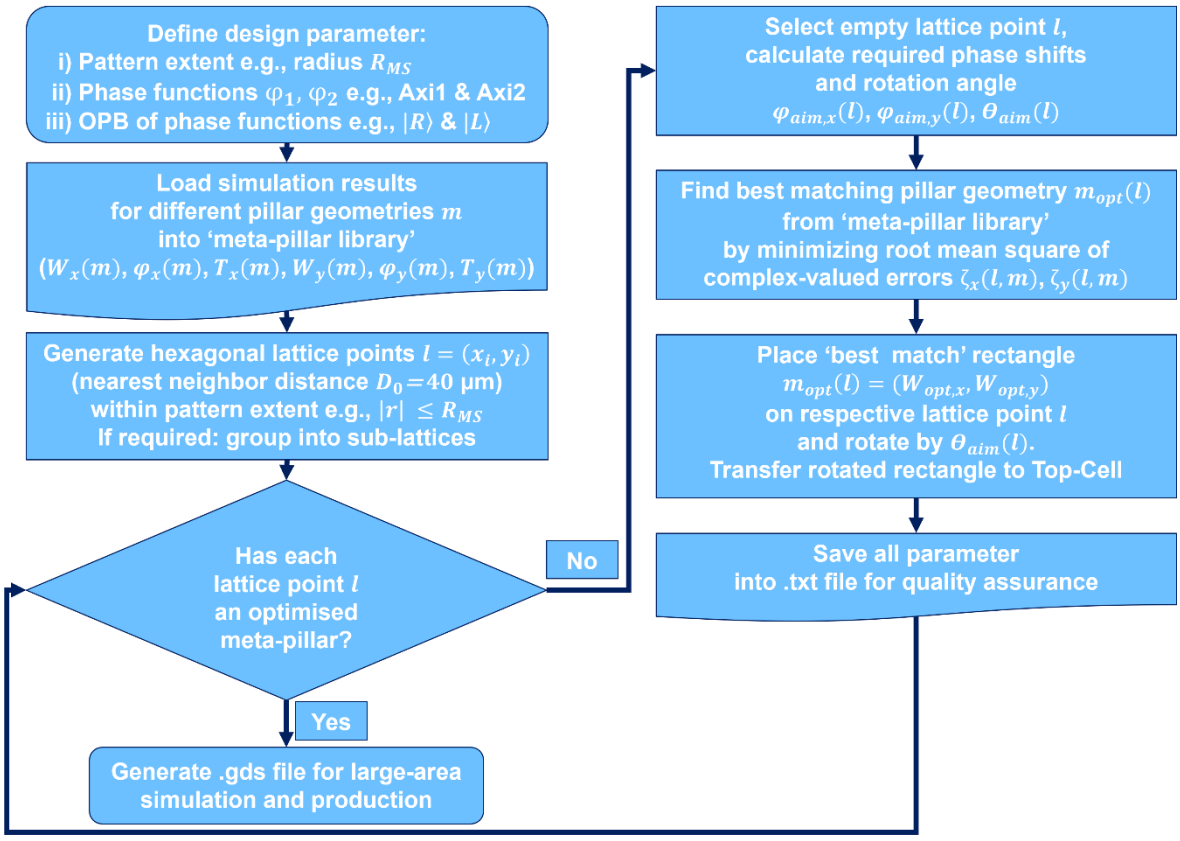

Figure 3.5: Flowchart for the pattern generation algorithm in python utilising the gdsCAD documentation [424].

$$\boldsymbol{\varphi_{aim,x}(l)} = \begin{cases} \boldsymbol{\varphi_1(l)} & \boldsymbol{for\ |H\rangle, |V\rangle, |D\rangle, |A\rangle} \\ \boldsymbol{0.5 \cdot [\varphi_1(l) + \varphi_2(l)]} & \boldsymbol{for\ |R\rangle, |L\rangle} \end{cases} \quad \textbf{(3.2)}$$

$$\boldsymbol{\varphi_{aim,y}(l)} = \begin{cases} \boldsymbol{\varphi_2(l)} & \boldsymbol{for\ |H\rangle, |V\rangle, |D\rangle, |A\rangle} \\ \boldsymbol{0.5 \cdot [\varphi_1(l) + \varphi_2(l)] - \pi} & \boldsymbol{for\ |R\rangle, |L\rangle} \end{cases} \quad \textbf{(3.3)}$$

$$\boldsymbol{\theta_{aim}(l)} = \begin{cases} \boldsymbol{0°(const.)} & \boldsymbol{for\ |H\rangle, |V\rangle} \\ \boldsymbol{45°\ (const.)} & \boldsymbol{for\ |D\rangle, |A\rangle} \\ \boldsymbol{0.25 \cdot [\varphi_1(l) - \varphi_2(l)]} & \boldsymbol{for\ |R\rangle, |L\rangle} \end{cases} \quad \textbf{(3.4)}$$

The equations for independent phase-encoding on to a circular OPB were obtained by solving the Jones Matrix (J), for a spatial arrangement of linearly birefringent meta-pillars, see equation (3.5), with the two arbitrary phase functions $\varphi_{|R>}$, $\varphi_{|L>}$ and their respective Jones vectors $|R\rangle = \frac{1}{\sqrt{2}}\begin{bmatrix} 1 \\ -i \end{bmatrix}$, $|L\rangle = \frac{1}{\sqrt{2}}\begin{bmatrix} 1 \\ i \end{bmatrix}$, as described in detail in the supplement of [309].

$$\mathbf{J} = \mathbf{R}(-\boldsymbol{\theta}) \begin{bmatrix} \mathbf{e}^{\mathbf{i}\boldsymbol{\varphi}_{|\mathbf{R}>}} & \mathbf{0} \\ \mathbf{0} & \mathbf{e}^{\mathbf{i}\boldsymbol{\varphi}_{|\mathbf{L}>}} \end{bmatrix} \mathbf{R}(\boldsymbol{\theta}) \quad \textbf{(3.5)}$$

Still at the same lattice point $l = (x_i, y_i)$, the algorithm then calculated the complex-valued errors $\boldsymbol{\zeta_{x,y}(l,m)}$ for the x- and y-phase functions together with their root-mean square (RMS) $\boldsymbol{\zeta_{RMS}(l,m)}$ according to Eq. (3.6) to (3.8) with the imaginary unit j.

$$\boldsymbol{\zeta_x(l,m)} = \left|\boldsymbol{T_x(m) \cdot exp(j\ \varphi_x(m)) - exp(j\ \varphi_{aim,x}(l))}\right|^2 \quad \textbf{(3.6)}$$

$$\boldsymbol{\zeta_y(l,m)} = \left|\boldsymbol{T_y(m) \cdot exp(j\ \varphi_y(m)) - exp(j\varphi_{aim,y}(l))}\right|^2 \quad \textbf{(3.7)}$$

$$\boldsymbol{\zeta_{RMS}(l,m)} = \sqrt{\frac{\mathbf{1}}{\mathbf{2}} \cdot \left((\boldsymbol{\zeta_x(l,m)})^2 + (\boldsymbol{\zeta_y(l,m)})^2\right)} \quad \textbf{(3.8)}$$

The optimal pillar geometry $m_{opt}(l) = \left(W_{opt,x}(l), W_{opt,y}(l)\right)$ was determined by minimising $\zeta_{\mathrm{RMS}}(l,m)$ of Eq. (3.8) and subsequently placed at its respective lattice point l, rotated by $\Theta_{aim}(l)$ rounded to full degrees. All mentioned parameters were also exported into a .txt file for quality assessment. Once all lattice points had their optimised meta-pillars, an output file (.gds file format) was generated. This file can be imported into Lumerical FDTD solutions for collective simulations or read by computer-aided manufacturing (CAM) software for photomask production.

Figure 3.6 (a) shows the top-view of a metasurface pattern generated with the described methodology and algorithm in which all pillars (blue areas) are rotated by 45° to independently impose two different axicon phase functions on to incident |D⟩ and |A⟩ polarised light. Figure 3.7 (b) and (c) illustrates the two underlying phase functions $\varphi_{opt,x}(l)$ and $\varphi_{opt,y}(l)$ that are imposed by the selected meta-pillars (black points) onto transmitted

|D⟩ and |A⟩ polarised light, respectively. It is apparent that these two phase functions $\varphi_{opt,x}(l)$, $\varphi_{opt,y}(l)$ differ in the radial periodicity of their imposed phase shifts (colour code) as intended.

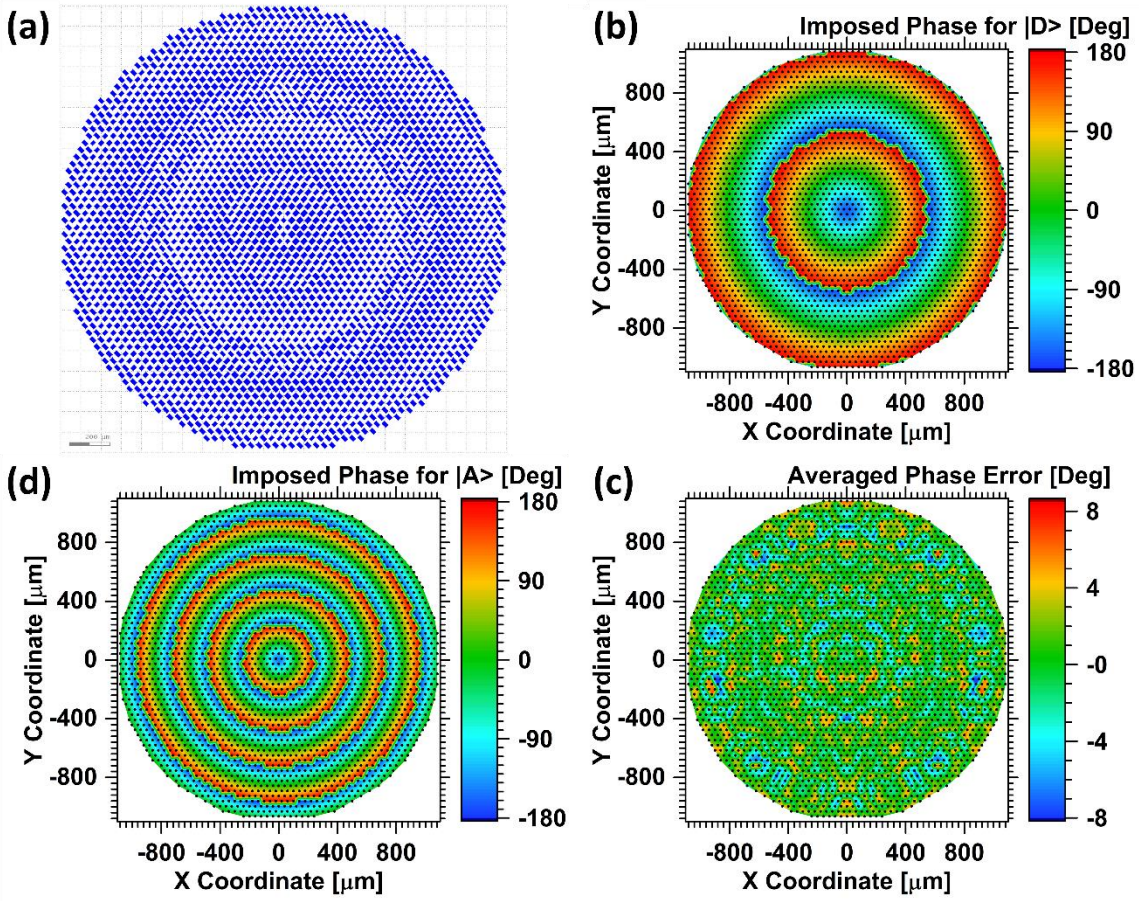

Figure 3.6: (a) Illustration of a metasurface pattern assembled from individual pillars for an exemplary design imposing two different axicon phase functions on to |D⟩ and |A⟩ light using the methodology described in this section with the algorithm of Figure 3.5. (b) The phase shift imposed on to transmitted |D⟩ light (colour code) at each individual pillar (black datapoints) accurately approximates the conical (2D) phase function of an axicon according to Eq. (2.18) with radial phase period g of 540 µm, whereas the same pillars (c) impose a different conical phase function with radial phase period g of 242 µm on to transmitted |A⟩ light. (d) shows the averaged phase error $\left(\left(\varphi_{\mathrm{aim,x}}-\varphi_{\mathrm{opt,x}}\right)+\left(\varphi_{\mathrm{aim,y}}-\varphi_{\mathrm{opt,y}}\right)\right)/2$ *that confirms the remarkably accurate approximation of Eq.* (3.2) *and Eq.* (3.3) *by the chosen pillars, with a global average over all pillars of* $-0.2°\pm 4.3°$.

To gauge the accuracy of the encoded phase functions $\varphi_{opt,x}(l)$, $\varphi_{opt,y}(l)$ with respect to the targeted phase functions $\varphi_{\mathrm{aim,x}}(\mathrm{l})$ and $\varphi_{\mathrm{aim,y}}(\mathrm{l})$, Figure 3.6 (d) show the averaged phase error, calculated as $\left(\left(\varphi_{\mathrm{aim,x}}-\varphi_{\mathrm{opt,x}}\right)+\left(\varphi_{\mathrm{aim,y}}-\varphi_{\mathrm{opt,y}}\right)\right)/2$. These results prove the ability of our approach to simultaneously encode two independent phase functions on to two orthogonal SoPs with a negligible phase error of $-0.2° \pm 4.3°$ averaged over all pillars and both phase profiles.

For the written code employed for pattern generation of the metasurfaces of Chapter 5 and Chapter 6, see Appendix B and C, respectively.

3.4 Collective Simulations of the Metasurface Designs

To confirm that the collective response of a large ensemble of meta-pillars operated according to the intended optical function, collective simulations of metasurfaces with up to 9'060 individual meta-pillars within simulated volumes of up to 4 mm x 4 mm x 7.2 mm were conducted.

For this task, the generated metasurfaces were directly imported from their .gds file into the commercial software Lumerical FDTD solutions. This software is based on a finite-difference time-domain (FDTD) method that numerically solves Maxwell's equations. The FDTD algorithm is widely employed in the field of wave optics, where the feature sizes of objects are in the range of the wavelength e.g., meta-atoms, since it accurately accounts for interference, diffraction, coherence and polarisation effects.

Because all of the metasurfaces developed in this work share the same fundamental design e.g., dielectric materials, meta-pillars, transmission geometry, etc., they also share a fundamental simulation template that is capable of accurately describing the beam shaping functions and polarising effects. The modular user interface of FDTD solutions allows for quick adaptations of the simulation file to new metasurfaces by adding and shifting monitors or by adapting design dimensions.

This section is hence designated to introduce and explain the important modules and parameter of the collective simulation template developed and employed within this thesis. Figure 3.7 shows an exemplary template based on the metasurface polarimeter discussed in Chapter 6 with indication of each module's illustration within the simulation space.

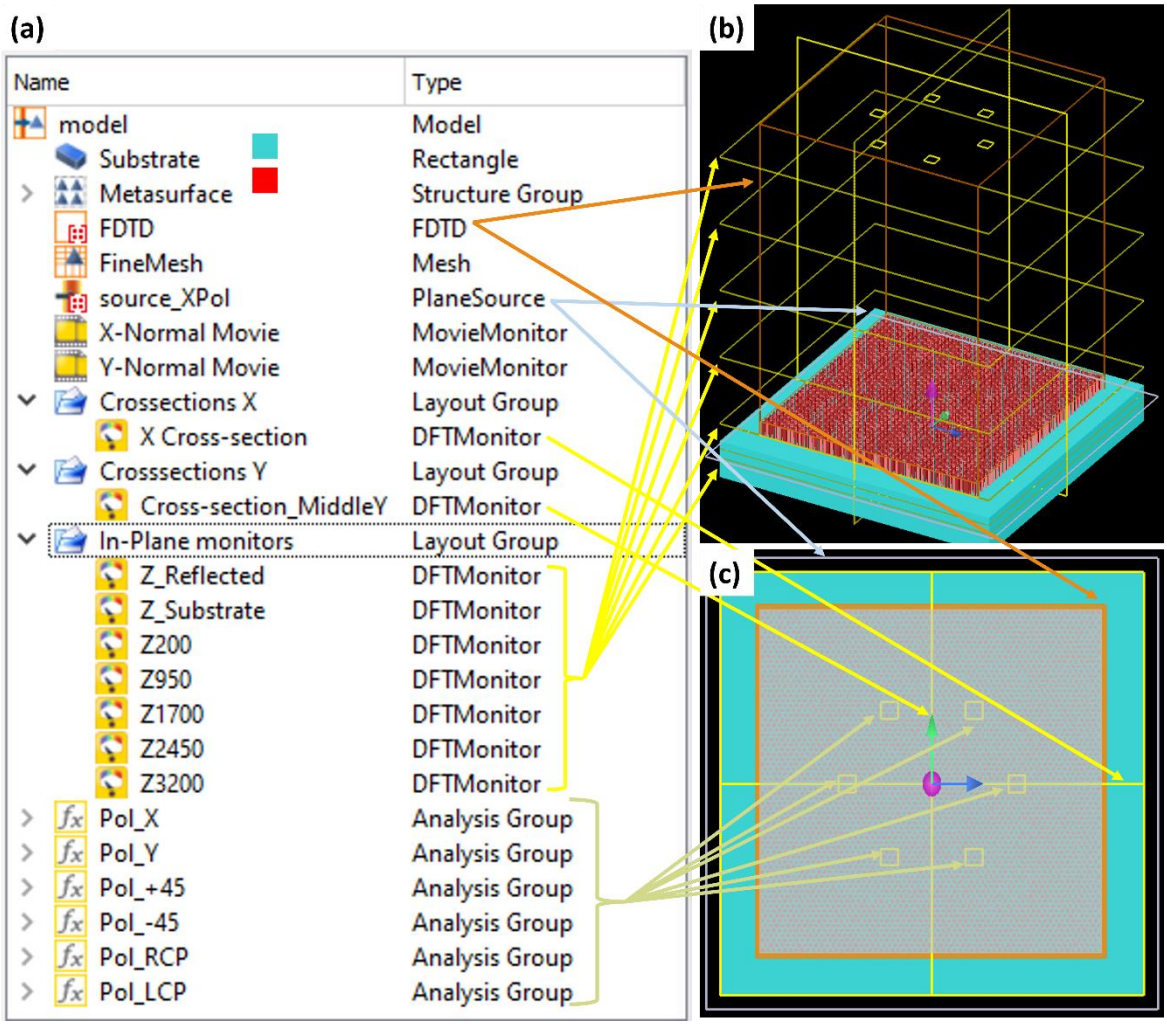

Figure 3.7: Illustration of the setup simulation within the template used in Chapter 6. All simulation modules and monitors are shown and addressed via the (a) technology tree. (b) shows a perspective view of the simulation space, highlighting the 3D nature of the collective simulations of large meta-pillar assemblies. (c) Plan view on to the top of the metasurface (x-y plane) with indication of the different simulation modules and monitors.

Substrate (Material): In this module, the 3-dimensional geometric extent of the substrate is defined, including rotations and the material parameters. The employed material "Silicon_THz" was user-defined as dielectric with RI of 3.4175 RIU (at 2.52 THz) [189, 426]. It is recommended to extend the substrate (cyan) beyond the simulation space (orange square/box) to avoid simulation artefacts originating from edge-effects. Furthermore, the substrate should be sufficiently thick to avoid unwanted near-field effects between the source and substrate-metasurface interface e.g., a few wave cycles ($\lambda_n(3.4175\ RIU) = 34.76\ \mu m$). In the present case, a 200 µm space was left to before the substrate-metasurface interface.

Metasurface (Group): As mentioned before, the metasurface layer can be easily imported (File → Import → GDS...) into a group containing the individual meta-pillars as polygons. In this group element, the 3D position of the layer can be set, as well as the meta-pillars z-span (Height, 150 µm) and material (dielectric with RI of 3.4175 RIU) with the RI of the surrounding medium (air, 1 RIU). In case a circular metasurface shall be simulated, a reflective circular aperture has to be introduced below the metasurface as both the FDTD solver region and source injection plane are restricted to rectangular geometries.

FDTD (solver region): This module defines the spatial extent of the simulation volume (orange boundary) including its meshing and boundary conditions, the maximum simulation time including the auto shutoff condition and other global simulation properties. The maximum simulation time was set to 0.5 ns, simulation temperature to 300 K and the RI of the background to 1 RIU. As mesh settings, "auto non-uniform" was selected with a mesh accuracy setting of 4 and mesh refinement "conformal variant 0". The "dt stability factor" was set to 0.99 and "minimum mesh step setting" to 0.25 µm. All boundary conditions were optimised to "PML" of type "stretched coordinate PML" with "standard" profile, 8 layers, kappa = 2, sigma = 1, polynomial = 3, alpha = 0, alpha polynomial = 1, minimum layers = 8 and maximum layers = 64. Auto shutoff was enabled to end simulations early once the remaining power within the simulation space fell below 10^{-5}.

Mesh override region: This element forced the software to create a finer mesh around the imported metasurface layer including a 5 µm wide buffer. A maximum mesh step of 5 µm was selected for all 3 spatial dimensions.

Optical Source: Depending on the desired incident polarisation, one or two plane wave sources (Bloch/periodic) were employed with propagation direction along the z-axis (forward). The source polarisation can be adapted via the phase shifts and polarisation angles of these two sources. The wavelength was set to start and stop at 118.7 µm and 118.9 µm (2.52 THz), respectively, with "eliminate discontinuities" and "optimise for short pulse" enabled. The injection plane was set inside the substrate, 150 µm, or ca. 4.3 wave circles, below the start of the metasurface layer. Once again, it was recommended to extend the 2D layer beyond the simulation space and substrate area to avoid edge-artefacts. The remaining 50 µm of substrate below this source allowed were used to insert a monitor that evaluated the portion of the E-fields reflected by the substrate-metasurface and metasurface-air interfaces.

Movie Monitor: These monitors were inserted in the x-z and y-z plane to create a short movie showing the temporal progression of the electric field density. Their temporal nature made them particularly useful to observe (multiple internal) reflections and Fabry-Perot effects within the substrate or introduced samples (as in Section 5.2.2).

Frequency-Domain Power Monitor: These monitors were used to record the 2D spatial profile of electric field strength, or optical power. The inferred intensity cross-sections along the x-z and y-z planes, as well as at several axial positions after the metasurface (x-y plane) were vital in the analysis and evaluation of simulation results. Recorded data was the output E- and H-fields along all three coordinates (x, y, z) and the overall output power.

Polarisation Monitor: This 2D analysis group was used to determine the overall state of polarisation passing through them at the target wavelength of 118.8 µm. These monitors played a vital role in confirming and quantifying polarising effects. Their spatial extent was set to 120 µm x 120 µm ($\approx \lambda_0$).

Ring Aperture: In order to simulate circular metasurfaces within the rectangular simulation space, it was necessary to block the light within the excess regions at the vertices. To achieve this, a thin (60 µm) ring aperture consisting of a perfect electric conductor (PEC) was introduced just below the metasurface layer. The intended operation was confirmed without metasurface layer using E-field monitors.

The presented simulation template was of immense benefit to the effective prototyping and performance evaluation of different metasurface designs prior to their lithographic production. The results obtained from these simulations served as benchmark for both the theoretical models developed in this thesis and the experimentally obtained results in Chapter 5 and Chapter 6.

3.5 Summary of the Chapter

In this chapter the fundamental methodology to create versatile metasurface design platform was introduced, which enabled the fast and adaptable development of ultra-compact and highly efficient polarising optics operating at terahertz frequencies.

In Section 3.2 a methodology to predict the optical response of periodic sub-wavelength structures as function of their anisotropic geometry using simulations that sweep the width parameter of rectangular meta-pillars was introduced. The periodic unit cell was optimised to strike a compromise between manufacturability i.e., fabrication tolerances, on the one side

and the targeted optical performance on the other side, including the versatile adaptability of the transmitted phase and polarisation profiles with high transmission efficiency. The resulting pillars can accurately approximate arbitrary points within the entire 2D phase space, thus imposing two independent phase shifts on to transmitted x- and y-polarised light. The confirmed the linear relation between pillar height and transmitted phase shift was then confirmed according to the theory of propagation phase and used this information to gauge the impact of slight variations of the etch depth, which expected from ARDE, on the optical performance.

Section 3.3 presented the developed algorithm to arrange large numbers of these meta-pillars into an optimised 2D metasurface that approximates a user-defined collective response i.e., two independent phase functions imposed on to two orthogonal polarisations. All six degenerate states of polarisation can be independently addressed this way with a high transmission efficiency. It shall be emphasised that the selected phase functions are encoded pillar-by-pillar with a high resolution of 635 pillars per inch. This computer-based "pick and place" approach to phase encoding allows for the straightforward superposition and multiplexing of multiple complex optical functions into a single layer with very high accuracy. As a consequence, a single optimised metasurface can effectively replace extended regions of a setup that would require multiple pieces of classical optics. The system size and associated losses caused by reflection or absorption can be therefore reduced drastically. Performance deterioration from standing waves and interference effects which are prevalent at terahertz frequencies will also be reduced. This makes the presented approach ideally suited to design more compact optical setups with improved signal-to-noise ratios and complex optical functions, which would be difficult to achieve with conventional optical components.

Finally, Section 3.4 introduced the means to test and optimise the collective optical response of the generated metasurfaces with a modular collective simulation template. The function and optimised properties of each module was discussed along with the fundamental operation of the FDTD algorithm.

This chapter hence introduced and developed the tools to create the highly efficient and adaptable polarising optics that are investigated in Chapter 5 and Chapter 6. The following Chapter 4 will present the optimisation of the fabrication methodology, including the metrology to quantify the encountered fabrication tolerances.

Chapter 4 : Fabrication and Quality Assurance

4.1 Fabrication Requirements and Chapter Outline

To produce dielectric metasurfaces with good optical performance that remains close to the simulations of the previous Chapter 3, one must first define the fabrication requirements, identify suitable fabrication techniques and therefrom assess which available fabrication technique appears to be best suited.

The metasurface design of this thesis required the fabrication of meta-pillars with highly accurate lateral structure size (0.5 µm step-size), a large structure height (150 µm) and high sidewall verticality ($\leq \pm 3°$) over large areas (aperture size of up to 4.84 cm^2)[4] into silicon.

Table 4.1: Comparison of prospective fabrication techniques for the metasurface optics designed in Chapter 3 including evaluation of their key metrics.

Design Aspect	**3D Printing [298, 427-429]**	**E-beam litho. & ALD [282, 430]**	**Direct Laser Ablation [423, 431, 432]**	**Focussed Ion beam litho. [433]**	**Photo-litho. & Bosch etch [423, 434, 435]**
Dielectric material	Low ref. index (polymer)	High ref. index (TiO_2 or Si)	High ref. index (Si)	High ref. index (Si)	High ref. index (Si)
Quality of material (roughness, absorption)	Inclusions, material fluctuations	Excellent (low sidewall roughness)	Laser-induced damage	Absorption by implanted ions and carriers	Excellent (wafer grade)
Achievable structure size	Ca. 200 µm	Ca. 40 nm	3 µm - 100 µm ($\propto$ Height)	Ca. 20 nm	Ca. 230 nm
Achievable structure height	3.5 mm (ΔH = 100 µm)	Few µm, (max. is resist thickness)	350 µm, but tapered profile	Few µm to few 100 µm	Several 100 µm
Fabrication tolerances	Medium to high (lateral, height)	Very low ($\pm$ 10 nm)	High (height taper & lateral)	Very low (lateral, height)	Low (taper, etch depth)
Fabrication speed (over mm^2)	Fast to medium (increases in 3D)	Slow along 1D (Height)	Slow (increases in 3D)	Extremely low, (increases in 3D)	Fast, increases in 1D, (Height)

[4] The aperture was 22 mm (square or round), which was twice the 1/e diameter of the FIRL's Gaussian beam.

Table 4.1 provides a non-exhaustive list of potential fabrication techniques for dielectric metasurfaces that have been evaluated against the requirements of this work. The coloured background summarises whether the relevant fabrication requirement is satisfied by the respective fabrication technique (highlighted in green) or not (highlighted in red). As the table shows, most methods comply with only some of the requirements and possess at least one significant flaw. The only method able to meet all requirements is the combination of photolithography and the so-called Bosch silicon etching, and as such it will be central to the remainder of this chapter.

Section 4.2 will give an introduction to the photolithographic processes employed to produce the metasurfaces presented in this work i.e., photolithography and Bosch etching. Commonly experienced production errors and detrimental effects are pointed out together with their respective solution strategies and process parameters. Section 4.3 then presents the optimised process sequence with the exact process parameter as employed for the fabrication of monolithic metasurfaces. Section 4.4 will consider quality assurance of the fabricated metasurfaces by introducing white light interferometry (WLI) and outlining its capability to gain process control over the etch depth through intermediate measurements. A powerful methodology to obtain statistically relevant information on the etch depth will be established that can quantify deviations from ideality. Section 4.5 provides an assessment of the finished metasurfaces using diverse metrology tools. Results obtained from WLI are combined with the simulation results of Section 3.2 to gauge the impact of the observed etch depth deviations on the optical performance of the fabricated metasurfaces. Section 4.6 concludes this chapter by summarising the advantages of the presented monolithic metasurface production over other established fabrication methodologies i.e., the established bilayer structure containing an etch-stop layer.

Last but not least, it shall be emphasised that the sample fabrication, metrology and data analysis presented in this chapter was conducted in its entirety by the PhD candidate of this thesis. Noteworthy support was provided by Corrie Farmer and the staff of the JWNC, who provided standardised recipes for the deposition, patterning and removal of the photoresist, as well as expert advice on the optimisation of the Bosch etch and its execution, respectively.

4.2 Introduction to Photolithographic Patterning

4.2.1 Sample Preconditioning and Handling

Cleanliness lies at the heart of micro- and nanofabrication. This fact is manifested in the sophisticated and extremely costly cleanroom environments, such as the James Watt Nanofabrication Centre, which uphold an artificial atmosphere that is continuously circulated from the ceiling downwards through the floor while being filtered with high-efficiency particulate air (HEPA) filters. This constant airflow is necessary to quickly force any introduced, generated or stirred up particles away from working surfaces towards the HEPA filters. Contrary to common belief, cleanroom suits and face masks are not worn as personal protective equipment against chemicals but intended to reduce particle contamination by the person wearing them.

Even small dust particles can create unwanted ‘pin hole’ or extensive ‘comet streak’ defects within the deposited photoresist layer, thereby locally masking areas that were supposed to be etched away. It is therefore crucial for the quality and yield of processed samples to actively avoid and remove particle contamination whenever possible e.g., by moving slowly next to the samples, by wearing cleanroom gear, by avoiding to lean over samples, by keeping samples within clean and de-dusted carrier boxes, by blowing off particles with gaseous nitrogen before each process step, etc.

Chemical contaminations, such as grease, salts and organic residues, can be even more detrimental as they alter the surface chemistry of the substrate and consequently cause poor wetting or adhesion of the resist layer. Handling the substrate with cleaned tweezers that exclusively touch the far edges of the substrate is hence advisable.

An extensive initial cleaning procedure was essential to the successful and reproducible deposition of the photoresist layer. Typically, the substrate is immersed sequentially into a set of different solvents that possess individual solubilities to different chemicals, so using them in sequence should effectively remove any chemical contamination. For example, deionised water removes most salts but not organic residues while acetone shows the opposite behaviour. This cleaning step is often assisted by high temperatures to increase the speed of dissolution and the solubility of chemicals, and/or ultrasonic agitation that helps to mechanically shake off contaminations. When transferring samples from one solvent to the next it is important to spray the next solvent over the surface to avoid drying of the liquid film, which would re-deposits dissolved contaminations. For the same reason, the sample

has to be blow-dried in nitrogen stream at the end of the cleaning process, preferably with a slowly evaporating solvent such as water or iso-propyl alcohol.

Subsequent preconditioning of the substrate surface chemistry to provide good adhesion of the photoresist layer was the next important step. At ambient air, silicon substrates typically possess a thin native oxide layer of ca. 2 nm with functional silanole (Si-OH) and siloxane (Si-O-Si) groups. This polar surface chemistry strongly binds water molecules (hydrophilic) from the ambient humidity, yet poorly interacts with the organic photoresist (lipophobic). Hence, the adsorbed surface water was first removed in a dehydration step, e.g. at elevated temperature in an oven [436], before the primer solution (MCC80-20[5] [437]) converted the substrate surface lipophilic via a surface functionalisation reaction with 1,1,1,3,3,3-hexamethyldisilazane (HDMS) [438]. The cleaned and preconditioned silicon substrates should be immediately coated with the photoresist, as described in the next section.

4.2.2 Photolithography

The term “photolithography” can be loosely translated from Greek as “writing into stone with light” and includes nowadays a multifaceted group of additive and subtractive processing steps that generate microstructures layer-by-layer, such as integrated circuits, optical films, microfluidic channel, etc. Photolithography is arguably the most potent and versatile top-down fabrication technique for feature sizes in the range of tens of micrometres down to a few nanometres, which was driven by the semiconductor industry from the first integrated circuits to modern complementary metal-oxide-semiconductor (CMOS) and fin field-effect transistor technologies.

The photoresist is the centrepiece of photolithography. Photoresists are mixtures of chemicals i.e., solvent, photoactive compound (PAC), sensitiser and additives, which are optimised to respond to a specific exposure with a locally confined (photo-)chemical reaction that changes the solubility in a specific developer solution. Different types of photoresists are established, each having individual advantages for respective process sequences. For example, a high spatial resolution requires thin resist layers (low viscosity ν) with a spatially confined photoreaction (high contrast resist) that is triggered by a short wavelength (diffraction limit). For extreme resolutions in the order of ten nanometres and

[5] Solvent: 1-Methoxy-2-propanol acetate (80 %), Surface Reactant: 1,1,1,3,3,3-hexamethyldisilazane (20 %)

below, electrons are used to expose the resist within electron-beam lithography, which takes advantage of the tuneable de Broglie wavelength of electrons (via their acceleration voltage), thereby allowing for variable resolution. On the other hand, anisotropic etching of high aspect-ratio structures deep into silicon, as employed in this work, requires thick resist layers (high viscosity ν) with strong adhesion and high selectivity towards the etchant over prolonged process times. Requirements on achievable resolutions are more relaxed with a minimum feature size of a few µm and a tolerance of < ± 10%, which are achievable with i-line exposure (365 nm). A photoresist that meets these requirements is SPR220.7 [439], which was consequently employed to fabricate the metasurfaces in this work.

In its core, photolithographic patterning consists of four fundamental process steps that are summarised in Figure 4.1 and will henceforth be explained in detail.

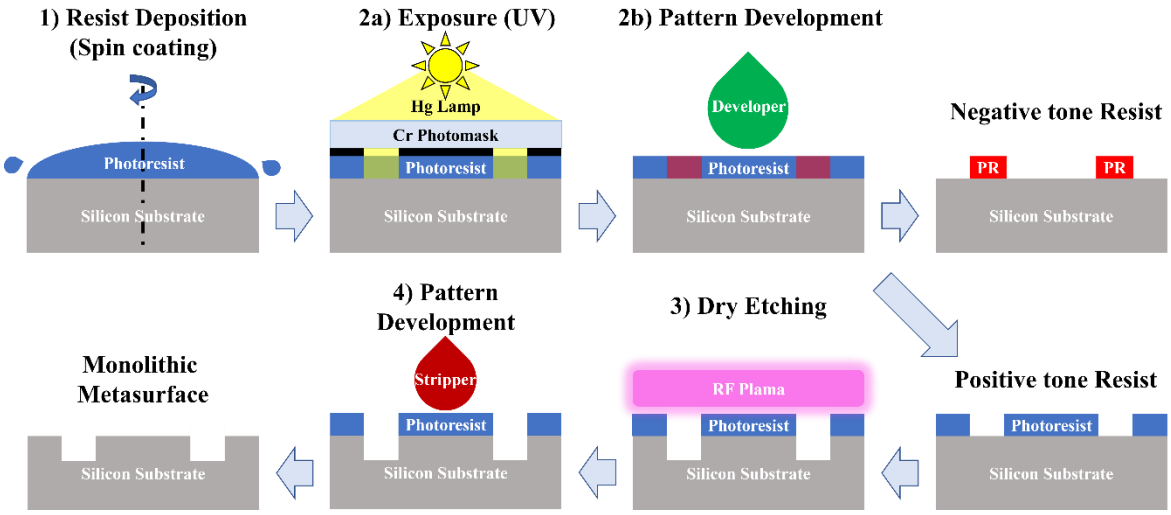

Figure 4.1: Schematic step-by-step illustration of the photolithographic fabrication of a monolithic metasurface via subtractive patterning using plasma-based Bosch etching.

1) Deposition of a uniform photoresist layer: Spin coating

Spin-coating is the established technique to deposit uniform photoresist layers of controllable thickness and high quality, both in lab-scale research and plant-scale manufacturing. The substrate or wafer is hereby fixed on the rotatable sample holder using a moderate vacuum. After the photoresist was applied to the sample surface (static dispense), the sample holder starts to rotate (spin-up), often with a low initial speed (spreading step). The experienced centrifugal force spreads the photoresist evenly over the sample surface, with some excess photoresist being ejected off the sample edges. Once the sample is

accelerated to its intended spin speed ω, excess photoresist is ejected until viscous forces within the photoresist layer start to counteract further thinning (spin off). This step is setting the final film thickness $t_f \propto \nu^{0.4} \cdot \omega^{-0.5}$, which is proportional to the photoresist viscosity ν and the inverse square-root of the spin speed ω [436]. This relation is clearly observed for the photoresist employed in this work, see the $t_f(\omega)$ curves in Figure 4.2.

Resist	SPR220-7.0	SPR220-4.5	SPR220-4.0	SPR220-3.0	SPR220-1.0
Film thickness @ 3000 rpm	7.0 µm	4.5 µm	4.0 µm	3.0 µm	1.2 µm
Viscosity / cSt	390	124	84	49	11.5
Dose (i-line)	470 mJ	380 mJ	350 mJ	310 mJ	160 mJ

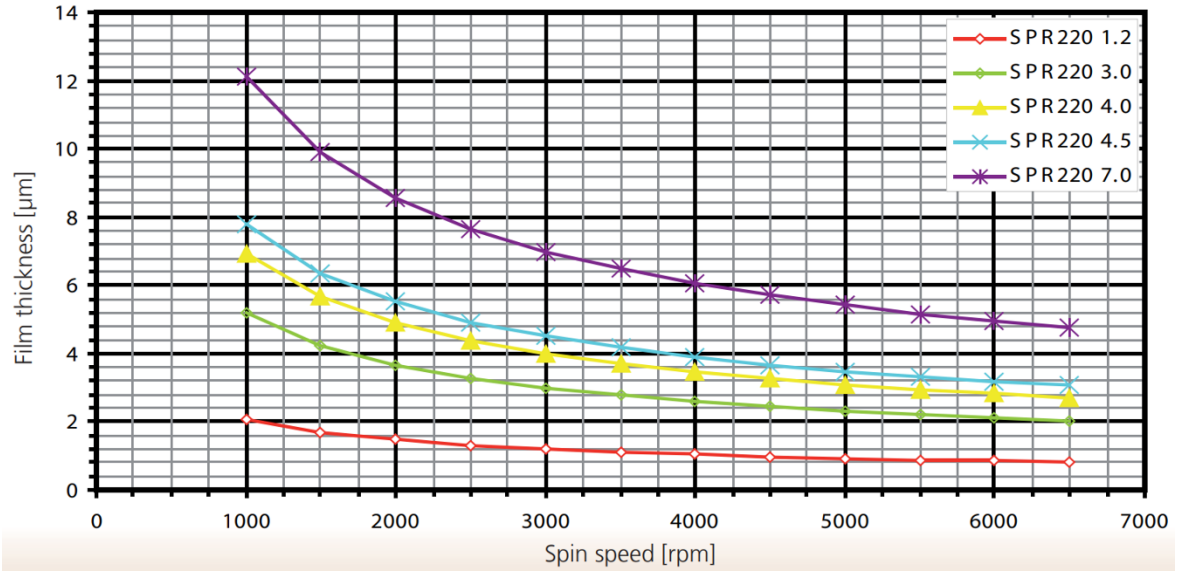

Figure 4.2: Selected photoresist properties of the commercial SPR220-Series photoresist (MEGAPOSIT) employed in this work [439]. The thickness curves for different spin speeds and resist types (viscosity) clearly show decreasing thickness for increasing spin speeds ($t_f \propto \omega^{-0.5}$) and lower resist viscosity ($t_f \propto \nu^{0.4}$). Furthermore, thicker films require a respectively higher exposure dose. Illustration reproduced from the product datasheet [439].

Further resist thinning is driven by solvent evaporation once centrifugal and viscous forces counterbalance. A detrimental artefact commonly observed for high viscosity photoresists is the formation of a thicker deposited layer close to the sample edges compared to the sample center, which is known as ‘edge bead’ in literature [440, 441]. This edge bead hampers hard contact with the photomask upon exposure, leading to a lower pattern resolution with

smeared-out resist walls comparable to proximity lithography. To counter the formation of edge beads, the substrate can be rapidly accelerated to high spin speeds in a short-duration step called kick-off, which throws off remaining resist at the edges while the already dried resist at the sample centre remains unaffected.

2) Pattern generation: Sample treatment, exposure and development

The pattern generation step refers to the structuring of the photoresist layer into the desired 3-dimensional shape that is required for subsequent additive or subtractive processes (pattern transfer). It can be subdivided into three parts, namely sample treatment, exposure and development.

The sample treatment generally aims to support and improve the conditions of the photochemical reaction to achieve a more uniform, precise and reproducible pattern. An initial dehydration delay and soft bake on a hotplate after the photoresist deposition promotes solvent evaporation and densification of the resist layer. This reduces the spacing between diazo-functionalised PAC [442] and sensitiser within SPR220, thereby promoting a more complete photoreaction with higher contrast and sharper structure definition. According to the vendor, rehydration delays before and after exposure are necessary to absorb water molecules, which was essential to complete the photoreaction [443]. Beyond, the post-exposure delay was necessary since gaseous N_2 generated upon exposure [443] has to slowly evaporate to avoid the formation of bubbles, which are commonly observed if the resist is baked right after exposure. This leads the author to believe that the underlying photoreaction of SPR220 is a Wolff rearrangement, in which a hydrophobic diazoketone is converted into a hydrophilic carboxyl group in a two-step reaction[6] [444], see Figure 4.3. This would be in line with SPR200 being a positive tone resist whose exposed areas become soluble in the aqueous developer CD-26 [445], see Figure 4.1. The post-exposure bake is commonly employed to promote diffusion of the products of the photoreaction, thereby smoothening the concentration profile to result in steeper and smoother sidewalls upon development.

[6] Further reaction to form an alkyl group under release of gaseous CO_2 as shown in Figure 4.3 is not expected for SPR220 as the exposed areas would become hydrophobic i.e., insoluble in the aqueous developer CD-26.

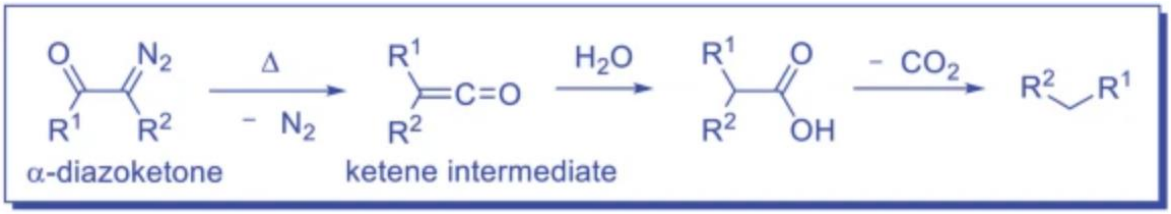

Figure 4.3: Suspected photoreaction of the commercial SPR220-Series photoresist [439] according to the Wolff rearrangement. In a first irreversible step that is activated by exposure to light, the diazoketone-containing PAC is converted into a ketene under release of a N_2 molecule. In the second step involving a nucleophilic attack by a water molecule, this ketene is converted into a highly hydrophilic carboxyl-group (-COOH). The last step forming an alkyl group under CO_2 release is not expected for SPR220 [6]*. Adapted from [446].*

Exposure of the photoresist is commonly achieved through a photomask. The photomasks employed in this work were 2.29 mm thick quartz substrates with a reflective chromium layer of the desired 2D pattern at the substrate-facing side. The minimum feature size was 1 µm with a critical dimension tolerance of $\pm$ 0.15 µm. In addition to the photomask itself, the type and configuration of exposure is critical to the obtainable feature sizes. Projection lithography offers a resolution $R \propto \frac{\lambda_{exp}}{NA}$ [436] down to the diffraction limit, with NA being the numerical aperture of the extensive and expensive projection optics and λ_{exp} being the wavelength of light used for exposure. However, the fabrication requirements of this work allow for much simpler and cheaper exposure in hard contact, with a resolution of down to 0.5 µm using the Karl Suss MicroTec Mask Aligner MA6. Both mask and coated substrate were affixed using vacuum. The lateral alignment process was simplified since the metasurfaces were fabricated in a single-step process, meaning that only rough alignment of the pattern with the substrate extent was necessary. The exposure dose is given by the vendor, see Figure 4.2, usually within a large process window to ensure reproducible results. Finally, the development of the exposed photoresist is, once optimised, typically a straightforward process with reasonably large process window at the structure sizes required in this work. However, attention and strict adherence to safety protocols must be maintained upon immersion of the samples within the developer CD-26 since its active component tetramethylammonium hydroxide strongly affects nerves and muscles upon exposure [445].

3) Pattern transfer: Additive or Subtractive

Once the photoresist layer has been patterned according to the design on the photomask, it can act as a local mask in the pattern transfer step. Most of the processing variability and versatility of photolithographic patterning is encountered at this step, such as (an-)isotropic wet (dry) etching, surface functionalisation or oxidation, ion implantation, electroplating, lift-off and micromolding, to name a few. Complex 3D systems such as transistors and integrated circuits can be built by repeated stripping and reapplying photoresist for the next pattern transfer step, thereby buiding one layer after the other.

4) Resist stripping: Solution- and Plasma-based

Most photoresists can be simply removed by prolonged immersion into a stripper solution, ideally at elevated temperatures and under agitation. In this work, SVC 14 was used to strip the SPR220.7 layers after the Bosch etch [447]. However, the prolonged dry etch in fluorine-containing plasma created an insoluble layer on top of the photoresist, which had to be removed by ashing in oxygen plasma prior to wet-chemical stripping. Plasma-based ashing is an unfavourable alternative to solution-based stripping for the complete resist removal due to long process times, strong substrate heating, harsh oxidative sputtering condition and the inability to remove some ion-based residues inherent to this process. For completeness, it should be mentioned that some negative tone photoresist are permanent and cannot be stripped, such as SU-8 [448].

4.2.3 Deep Reactive Ion Etching into Silicon (Bosch process)

Selective etching of material that is not covered by the photoresist is one of the fundamental subtractive pattern transfer processes involved in microfabrication. A distinction is typically made between wet etching, which uses chemical solutions to provide mostly isotropic etch rates in all directions, and dry etching, which employs a plasma of directed (reactive) ions to etch anisotropically along the surface normal. The vertical, high aspect-ratio surface profiles that can be obtained by dry etching are of great technological importance for applications in micro-electro-mechanical systems (MEMS) [449-452], integrated photonics [453, 454], special (X-ray) optics [435] and many more. The general outline of the setup employed for dry etching in this work (PlasmaPro 100 Estrelas, Oxford Instruments) is summarised together with illustrations of commonly observed etch effects in Figure 4.4.

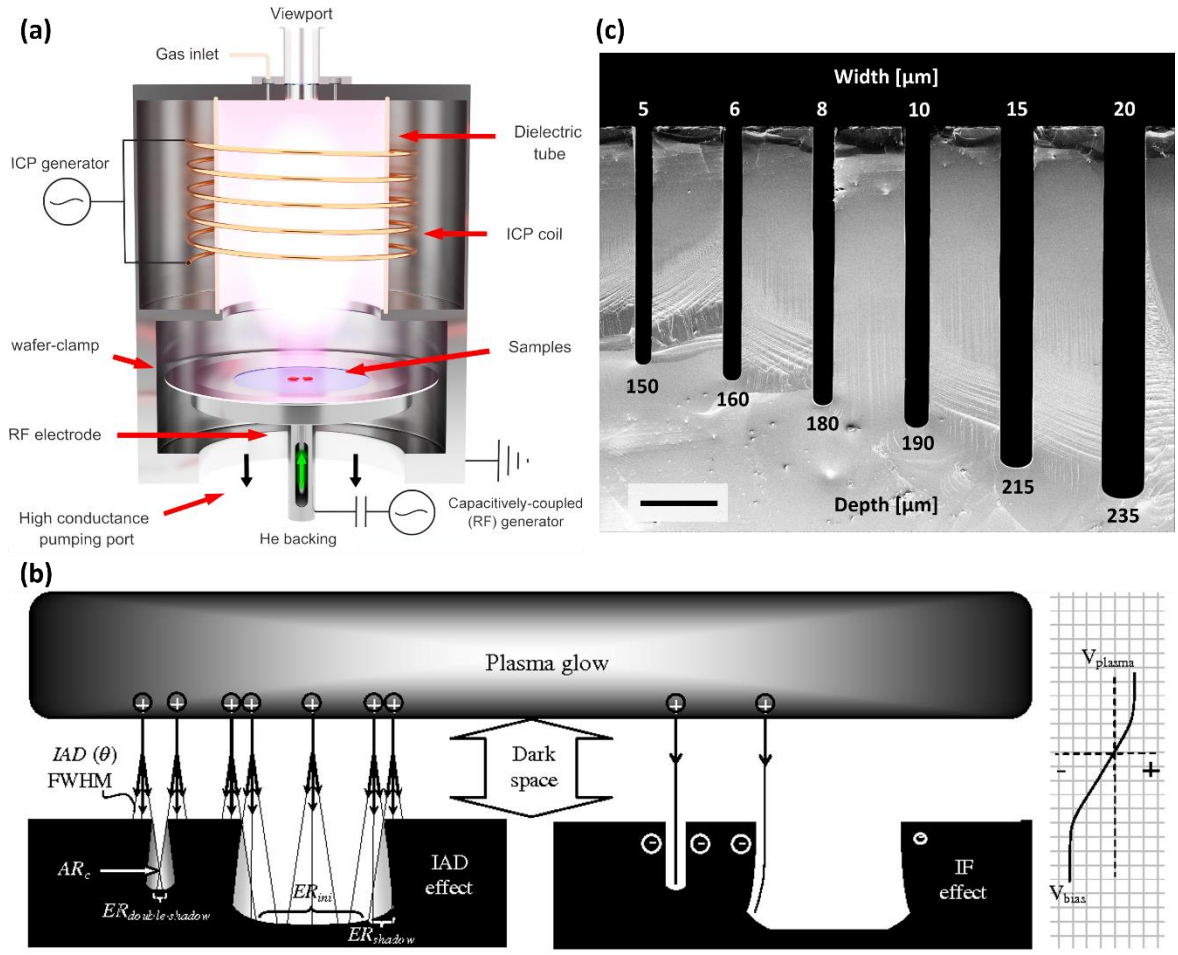

Figure 4.4: (a) Schematic of the process chamber for ICP-DRIE with its important components. (b) Illustration of various factors that cause deviations from ideal, vertical sidewall profiles, such as (left) ion angular distribution (IAD) and (right) image force (IF), which cause negative tapering of the etch profile. (c) The effect of ARDE is manifested in decreasing etch depths (235 µm – 150 µm) for smaller openings (20 µm – 5 µm). Fewer reactive ions reach the etch floor due to shadowing by the top surface (IAD), resulting in slower etch rated and the observed RIE lag. (a) adapted from [455], (b) adapted from [456], (c) adapted from [435].

The sample to be etched is fixed within the vacuum chamber on a holder that is cooled by helium. Cooling is necessary to maintain high etch selectivity between photoresist and silicon and to avoid burning the resist layer. Multiple gas inlets at the top supply the chamber with a well-maintained flow of process gasses and mixtures thereof i.e., O_2, SF_6, C_4F_8, while the chamber is continuously evacuated from the outlet below the sample holder to remove reacted material and gasses. The inductively coupled plasma (ICP) is generated in the upper section of the chamber. The energy to ionise gas molecules is delivered by a strong,

oscillating magnetic field generated by the ICP coils with the ICP power source operating at radio frequency (typically 13.56 MHz). A second, frequency matched power source is capacitively coupled to the sample holder, henceforth called CCP source, to control the electric field between plasma and sample [456].

Within the plasma, electrons move substantially faster than ions due to their drastically lower mass, which results in many electrons reaching the grounded chamber walls and sample holder (RF electrode), thereby leaving behind a net positively charged plasma. The sample holder acts hereby as a capacitor, being a short circuit for the AC field of the ICP generator, yet an open circuit for the DC field built up by the electrons impinging from the plasma. This creates a large DC self-bias, controllable via the CCP source, which attracts the positively charged ions within the plasma towards the sample on the sample holder (cathode). This acceleration of ions towards the sample is the origin of the extremely directional bombardment with ions and in turn the anisotropy of etch rates.

In summary, the ICP source controls the generation and flux of ions and radicals i.e., etch rate, while the CCP source independently controls the acceleration and directionality of ions towards the sample surface i.e., impact energy and ion angular distribution (IAD).

Figure 4.4 (b) illustrates a range of common deviations from a perfectly vertical etch profile. The ions incident to the sample possess a small lateral velocity stemming from collisions within the plasma and dark space, which is described as Gaussian shaped IAD of the incident ions. The IAD's variance (σ^2) can be somewhat controlled by the acceleration voltage towards the sample (CCP source) and the chamber pressure but will never reach perfection i.e., a delta function. As a result, insufficiently protected sidewalls can exhibit a respective negative tapering. Furthermore, the etch floor of small openings is increasingly shadowed by the top surface upon increasing etch depths compared to large openings, leading to decreased ion flux and thereby etch rate, see Figure 4.4 (b), (c). This effect, known as ARDE or RIE lag [435, 456, 457], results in lower etch depths for smaller openings and will be further investigated in Section 4.4 as the fabrication error of main concern to the intended operation of the fabricated metasurfaces. On the other hand, large openings often exhibit an increasingly negative tapering at large etch depth due to the image force effect. As discussed above, the sample holder and the sample are negatively charged. Consequently, positive ions will be attracted towards the negatively charged sidewalls and thereby widen the opening upon increasing etch depths.

The Bosch process addresses the need to inhibit slow lateral etching of the sidewalls in order to achieve – and maintain – excellent sidewall verticality over an etch depth of up to several hundred micrometres [457]. The underlying mechanism is the cyclic repetition of two steps, as shown in Figure 4.5 (a) and (b).

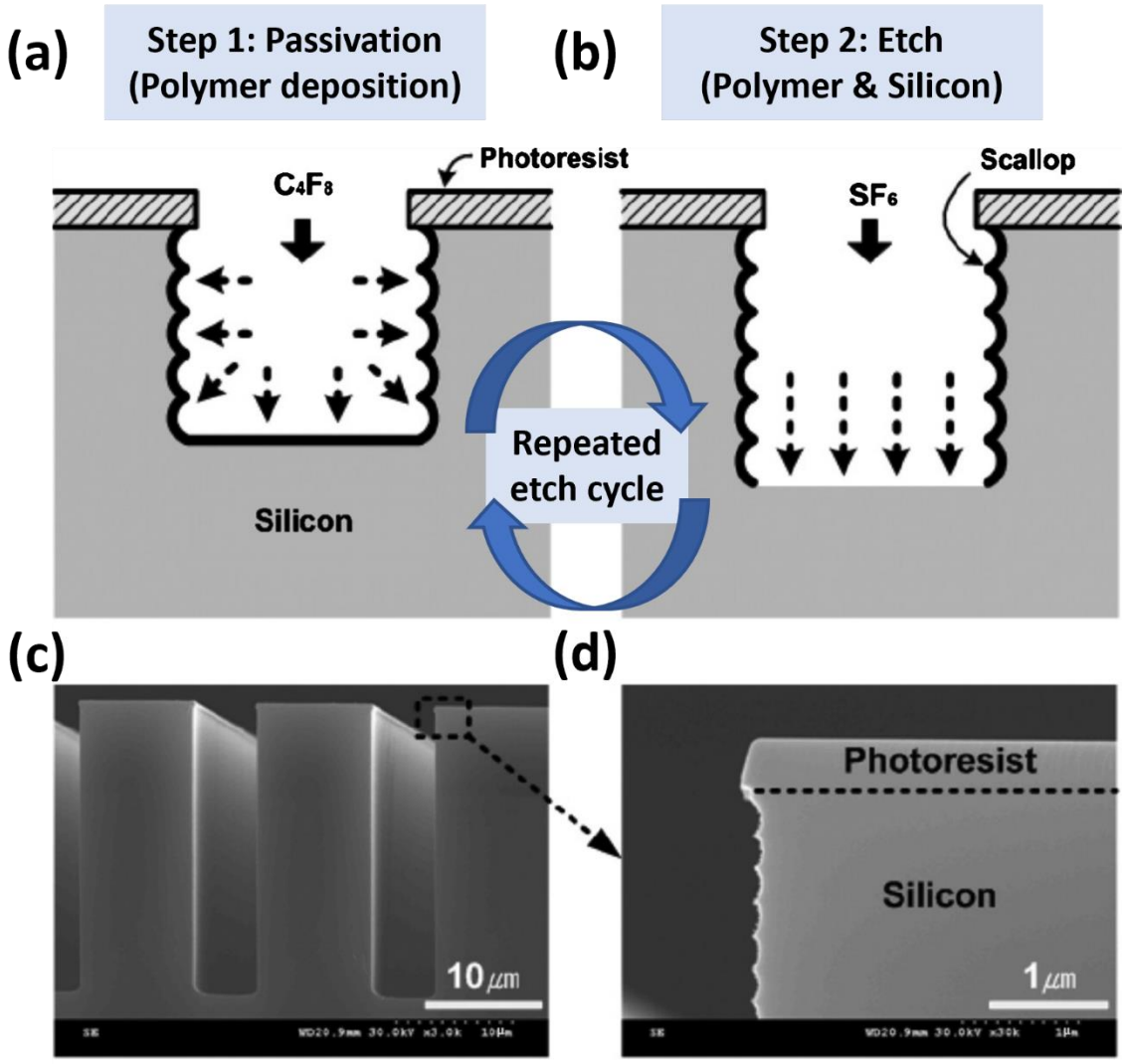

Figure 4.5: The Bosch process employed in this work is a cyclic two-step process consisting of (a) the passivation step, in which a protective fluoropolymer film is isotopically deposited, and (b) the directional etching step, in which fluoropolymer and silicon are removed at the bottom of the etched trenches. The horizontal etch rate at the sidewalls remained too slow to break through the protective polymer film, thereby preventing a negative taper. The resulting (c) deep etch profiles with high sidewall verticality show (d) a scalloping effect at their sidewalls as a result of the cyclic etch process. Adapted from [458].

In the passivation step, C_4F_8 gas chemistry is employed to evenly deposit a protective fluoropolymer over all surfaces, including the sidewalls. The polymer is formed in a free radical polymerisation sustained from plasma-generated radicals. Crucially, this polymer is chemically inert to the etchant and forms a dense film.

The subsequent etch step employs predominantly SF_6, which is partially split into free fluorine $F\cdot$ and heavier SF_x ($x \leq 5$) radicals and ions. The SF_x ions act mostly by sputtering the fluoropolymer and silicon surface via ion bombardment due to their high impulse upon impact. The high directionality of these ions means that fluoropolymer is mostly removed at the top surface (photoresist) and etch floor, leaving the fluoropolymer at the sidewalls relatively unaffected. Consequently, the protective fluoropolymer will be completely removed at the etch floor after a certain etch time [459, 460], leaving the exposed silicon to adsorb and react with fluorine radicals and ions according to Eq. (4.1).

$$\mathbf{Si_{(s)} + 4F_{(g)} \rightarrow SiF_{4\,(g)}} \qquad \textbf{(4.1)}$$

The formed SiF_4 is a gaseous molecule that desorbs away from the etched surface and is ultimately evacuated from the etch chamber. Notably, the etch reaction of Eq. (4.1) itself is isotropic for unprotected silicon surfaces. This leads to a rounded volume of etched material in each cycle that results in slight scalloping of the sidewall profile, see Figure 4.5 (d). The periodicity and lateral extend of these scallops are typically in the sub-micrometre range, thereby insignificant compared to the operating wavelength of the metasurfaces (118.8 µm). At last, it shall be pointed out that all mentioned process parameter i.e., the mixture of process gases and individual flow rates, ICP and CCP power, durations of deposition and etch step, etc., have to be precisely optimised and continuously adapted to achieve and maintain a good etch profile with high sidewall verticality over large etch depths.

4.3 Optimised Process Sequence

Inexpensive and readily available intrinsic silicon (high resistivity > 10’000 Ωcm) was used as substrate (25 mm × 25 mm, 535 µm thick) into which the active metasurface layer was etched monolithically in a single-step photolithographic process. The flow-chart in Figure 4.6 shows the sequence of fabrication steps required to realise the silicon metasurfaces. As highlighted in the chart, some fabrication steps could be repeated without losing the substrate (red and yellow arrows), for example in case of an unsatisfactory deposition, exposure or development of the resist film. Beyond this, several feedback-loops

allowed for fine adjustments that ensured close agreement to target specifications i.e., WLI inspection with the option for a follow-up fine etch, as will be discussed in Section 4.4.2.

The substrates were sequentially cleaned for 5 min each in warm acetone (50 °C), ultrasonically agitated acetone (ca. 20 °C), ultrasonically agitated methanol (ca. 20 °C), ultrasonically agitated isopropanol (ca. 20 °C) and ultrasonically agitated de-ionised water (ca. 20 °C) before being blow-dried in a nitrogen stream. The cleaned substrates were then dehydrated in an oven for at least 30 min at 180 °C in order to remove adsorbed water from the silicon surfaces, which improved the adhesion of subsequently applied (organic) resist.

The dehydrated substrates were transferred directly from the oven to the spin coater (model PWM32 Series photo resist spinners, Headway Research Inc.), covered with primer solution (MCC80/20) and soaked for 20 s before the spin program 1 of Appendix D was started. After the first spin program terminated, a 20 s delay was introduced to fill the next pipette with negative tone SPR220.7 photoresist and select program 2 of Appendix D on the spin coater. Then, the photoresist SPR220.7 was applied generously in a circle around the centre of the square substrate, taking good care not to introduce any air bubbles (they can be removed by sucking them back into the pipette). The spin program 2 was started immediately after the substrate was covered with resist and finished with an edge bead removal step.

After the spin program 2 terminated, the coated substrates were delayed for 30 min in a humidity-controlled room to allow for solvent evaporation. In the meantime, two watch glass for each coated substrate were placed in an oven at 90 °C.

The coated substrates were subsequently transferred on to a hotplate at 118 °C for 90 s with vacuum-supported thermal contact for their soft bake, after which they were transferred to the 90 °C warm watch glass to ensure a slow cool down to ambient temperature, thereby avoiding thermal stress in the resist layer. A subsequent rehydration delay of at least 60 min was given in a humidity-controlled room.

The subsequent exposure was conducted through a chromium photomask containing the metasurface pattern (pillar top surface covered with Cr) in hard contact for 22 s at 7.3 mW/cm^2 lamp power (i-line) using a mask aligner (Mask Aligner MA6, Suss MicroTec). Another delay of at least 60 min in a humidity-controlled room was conducted to ensure a completed photochemical reaction within the resist layer, which required rehydration and loss of nitrogen.

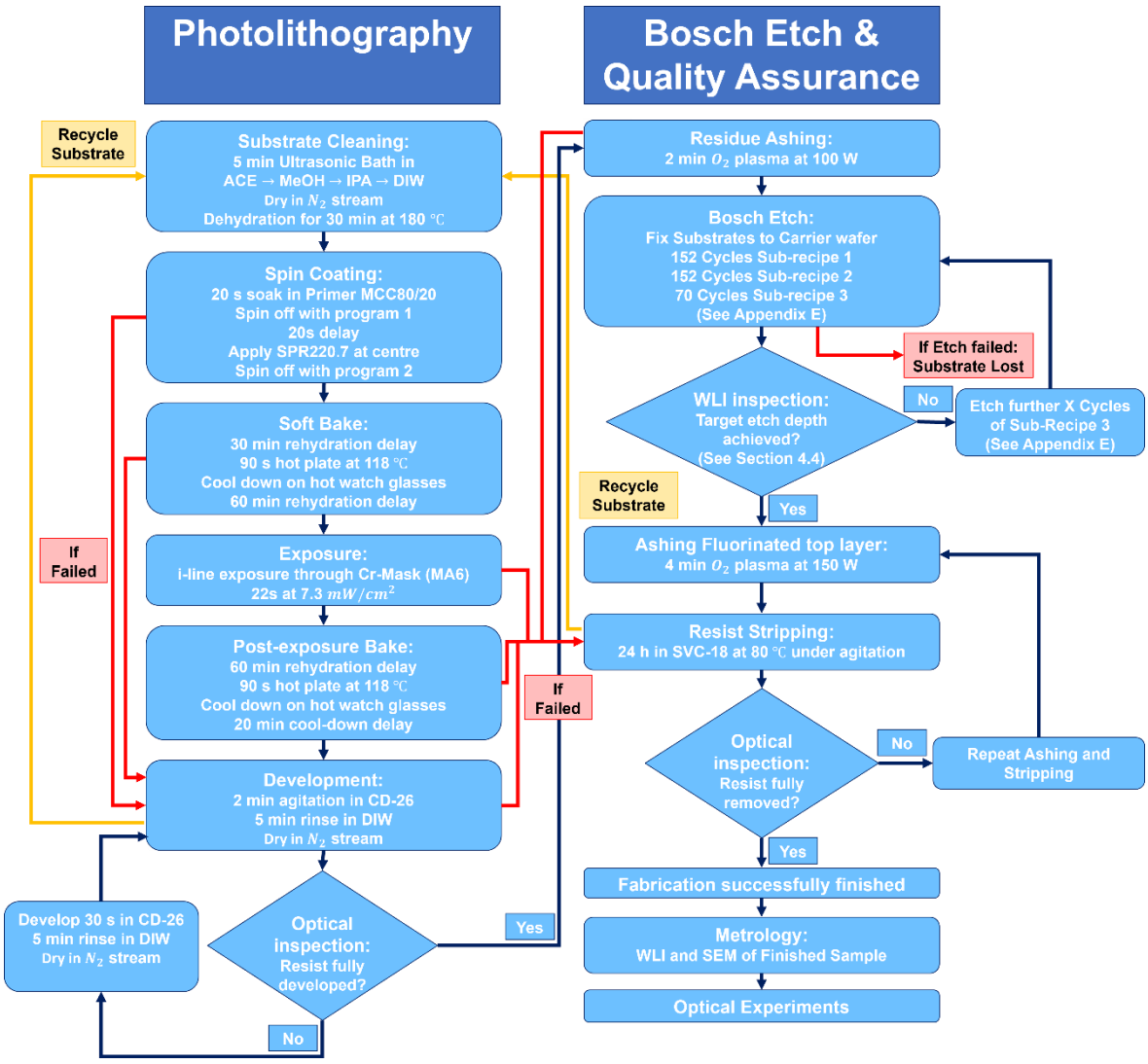

Figure 4.6: Flow-chart of the optimised fabrication sequence including feedback loops and routes to recycle the substrate in case of unsatisfactory quality (red and yellow arrows).

For the subsequent post-exposure bake, the substrates were again transferred on to a hotplate at 118 °C for 90 s with vacuum-supported thermal contact and then slowly cooled down on the second 90 °C warm watch glass.

A further 20 min delay allowed the baked substrates to cool down prior to their development, thereby avoiding thermal shock that can cause resist delamination.

The substrates were developed for 2 min in CD-26 developer under slight agitation, after which they were rinsed in de-ionised water for 5 min and blow-dried in nitrogen stream.

Optical inspection with a microscope ensured that the resist was either fully developed throughout the substrate or developed for further 30s until full development was observed.

Insoluble residues within the developed areas of the substrates were subsequently removed in O_2 plasma for 2 min at 100 W (ET340 RF Asher, PlasmaFab Barrel).

The substrate with developed resist pattern was fixed with up to two other patterned substrates on to the centre of a 6-inch carrier wafer (Si with 5 µm thermal oxide) using Santovac 5 vacuum oil [461] as adhesive. The subsequent ICP-DRIE Bosch process (PlasmaPro 100 Estrelas, Oxford Instruments) employed C_4F_8/SF_6 plasma chemistry [435, 456, 457], with the exact parameters summarised in Appendix E.

As will be described in Section 4.4, the average etch depth could be measured without the need to strip the photoresist, allowing for resubmission of partially etched samples to a final etch run. Once the targeted etch depth of 150 µm ± 5 µm was achieved, the samples were ashed in O_2 plasma for 4 min at 150 W to remove the highly fluorinated top layer of the photoresist, which was insoluble in the SVC-14 stripper solution.

Finally, the samples were stripped overnight (24 h) in SVC-14 at 80 °C under mild agitation until complete resist removal was confirmed with an optical microscope. In case of stubborn residues, further O_2 plasma etching was conducted until the fabricated metasurface was free from resist residue.

The quality of fabricated metasurfaces was then assessed as described in Section 4.5.

4.4 Process Control using White Light Interferometry

In order to develop a fabrication process that would consistently, reliably and repeatably deliver metasurfaces within the dictated specifications, the principles of process control were applied. Process control is a concept in industrial manufacturing that aims to monitor and adjust process variables to achieve and maintain the targeted output specifications. As such, process control systems aim to maintain product quality, improve performance and reduce the loss of material, products and components. The fundamental building block of any control system are control loops, which monitor a single process variable. Together with a developed control model that describes the impact of the monitored process variable on the output specification, a feedback can be given that adjusts the process to deliver the targeted output specification.

This section shows how white light interferometry (WLI) can be utilised within a control loop to achieve process control over the optical performance of the produced metasurfaces, as summarised in the flowchart of Figure 4.7. In the control loop, the etch depth (process

variable) was measured and statistically averaged over large areas using WLI. Knowledge of this process variable allowed for the estimation of the optical performance deviation (phase shift and transmission) by using the simulation results of Section 3.2 within a control model. The acceptable etch range was consequently set to 150 µm ± 5µm (target output). Samples that were not etched deep enough were resubmitted to a fine etch with an adjusted number of remaining Bosch cycles according to the measured etch depth (feedback and adjustment). This enabled the accurate and reproducible fabrication of monolithic metasurfaces while keeping the detrimental effect of ARDE on the optical performance within specified limits.

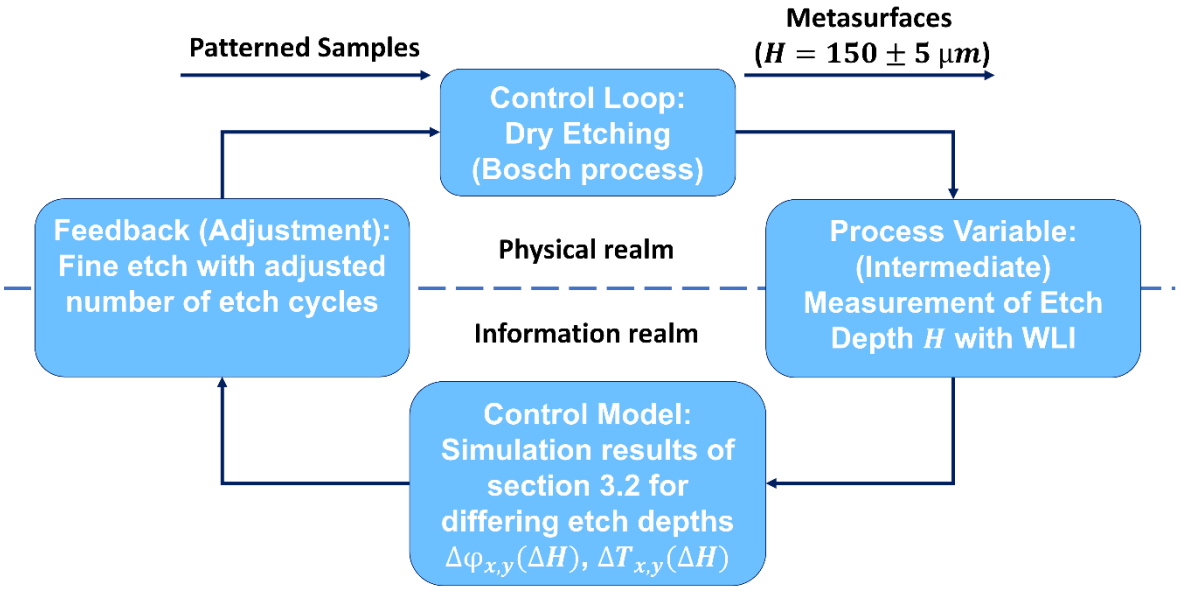

Figure 4.7: Schematic of the process control developed in this section to ensure that the Bosch etch process delivered metasurfaces with good optical performance.

4.4.1 Introduction to White Light Interferometry

The metrology tool employed for the measurement of the metasurface's topology (ContourGT-X 3D Optical Profilometer, Bruker Corp.) was based on WLI. WLI is a non-contact optical method to measure 3D structure with structure heights varying from a few nm to a few cm.

As shown in Figure 4.8 (a), the outline of such a setup is largely similar to a standard optical microscope. A coherent light source is collimated and focussed by the objective lens on to the object plane. Light reflected by the object is recollimated by the objective and imaged

on to the camera sensor by the tube lens in an infinity-corrected configuration i.e., collimated beams are magnified independent of the distance between objective lens and tube lens.

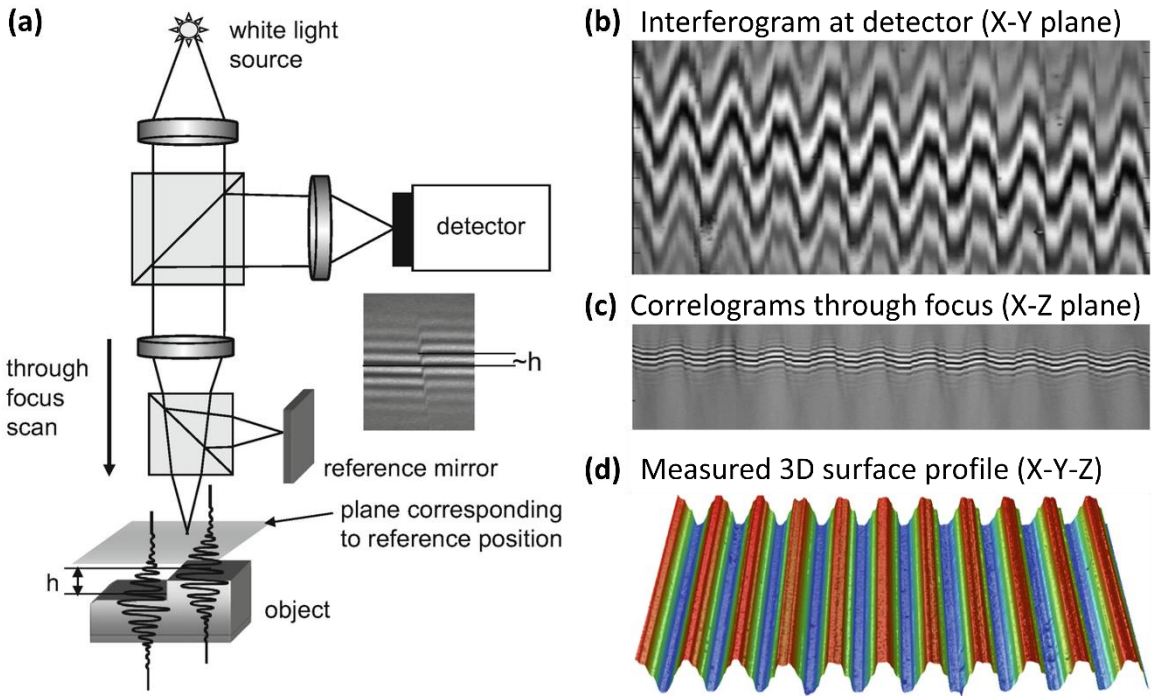

Figure 4.8: (a) Schematic illustration of a 3D optical interferometer based on WLI with Michelson interferometric objective. (b) Intensity pattern of the interference fringes near focus (interferogram) as observed by the image sensor. By scanning the objective along the z-direction, each pixel records (c) a correlogram whose width is given by the source's coherence length. (d) The 3D surface profile is determined pixelwise from the modulation peak position of the correlogram's envelope function. Image data adapted from [462].

The two major differences between WLI compared to a classic microscope are that i) special interferometric objective lenses are used and that ii) the objective lens can be scanned along the optical axis (z-direction) towards the object under investigation with high precision piezoelectric actuators.

Interferometric objective lenses include a beam splitter that introduces a reference beam path in addition to the measurement beam path of a normal microscope, with both beams recombined after they reflect off the object surface and reference mirror, respectively. The superimposed measurement and reference beams only create an interferogram on the camera sensor if the optical path length of both beams differ by less than half the coherence length L_c of the source, see Eq. (4.2). The detected interferogram, see Figure 4.8 (b), contains

spatial information on the object topology that was imprinted on to the phase front of the measurement beam upon reflection.

Consequently, the objective can be scanned along the optical axis (z-direction) to obtain individual correlograms for each pixel that correspond to a certain x-y position on the object. The correlograms, shown in Figure 4.8 (c), describe the detected intensity as a function of the z-coordinate $\mathrm{I}(\mathrm{z})$ according to Eq. (4.3**)** [463].

$$\mathbf{L_c = C\frac{{\lambda_c}^2}{n \cdot \Delta\lambda}} \tag{4.2}$$

$$\mathbf{I(z) = I_0\left(1 + exp\left[-4\left(\frac{(z - z_0)}{L_c}\right)^2\right]cos\left(4\pi\frac{z - z_0}{\lambda_c} - \varphi_0\right)\right)} \tag{4.3}$$

Hereby, λ_c describes the central wavelength, Δλ the spectral bandwidth, n the RI of the surrounding medium and $C \approx 1$ is a constant, while I_0 is the maximum detected intensity and φ_0 is a constant phase gap between the modulation peak position and the central bright fringe of the interference pattern. The modulation peak position is defined as the centre of the envelope function (exponential term in Eq. (4.3**)**) at which the optical path lengths of measurement and reference beams are equal. The z-position of the piezo-actuator that corresponds to this modulation peak position is saved for each pixel into a 3D topology matrix, with rows and columns corresponding to the respective (x, y) positions of the pixels. Figure 4.8 (d) illustrates this 3D topology matrix in the vendor's analysis software *Vision64*. Notably, this metrology technique allowed for fast and accurate data collection over large sample areas since the measured interference signal is not affected by magnification or numerical aperture, but rather by the central wavelength and spectral width. The entire object plane is captured at once for each z-plane, meaning that a large FOV can be measured without affecting the acquisition speed, while the vertical accuracy of the measured z-position is mainly depending on the accuracy of the piezoelectric actuator. The vendor's specifications for lateral and step height accuracy are < 0.38 µm and < 0.75 % (< 1.15 µm at H=150 µm), thereby well within the needs of this work [464].

Crucially, measurements do not require stripping of the resist and even allow for its thickness determination. During the z-scan, two sets of fringes appear at the resist-covered areas. The first fringe stems from the air-resist interface, the second from the mirrored reflection of air-resist interface - not to be mistaken for the resist-silicon interface. The resist thickness is thus half the z-separation between the two sets of fringes. The measured surface profile must be corrected by adding this resist thickness to the resist-covered areas [462].

4.4.2 Etch Depth Deviation – Statistical Analysis and Impact on Performance

As explained in Section 4.2.3, the absence of an etch-stop layer within the monolithic silicon substrates resulted in slight local deviations of the etch depth as a function of the open area between neighbouring pillars, which is known as ARDE [435, 456, 457]. To ensure that the intended etch depth of 150 µm has been achieved and properly assess the impact of the etch depth deviation on the metasurface's optical performance, one must

i) define and measure a statistically relevant average for the etch depth $\bar{H}$ of a metasurface including its standard deviation σ_H (process variable)
ii) gauge the impact on the optical performance caused by deviations from the ideal etch profile (control model).

Additionally, the ability to resubmit a measured sample to a follow-up fine etch is highly desirable to achieve the closed feedback loop shown in Figure 4.7.

Figure 4.9 (a) shows the measured surface profile of the metasurface employed in the imaging experiments of Sections 5.4.4 and 5.4.5 after 152 etch cycles of sub-recipe 1 and 2 each (see Appendix E) with photoresist still atop the rectangular pillars. The measured 3D profile was converted into a histogram over the etch depth to obtain quantitative metrics in Figure 4.9 (b). Two peaks are clearly visible: A very sharp peak at ca. 122.5 µm corresponding to the pillar's top surface (orange areas) and a broader peak at ca. 5.5 µm that corresponded to the etch floor (cyan areas) in Figure 4.9 (a), respectively. The Gaussian shape of the peak can be explained by a curved etch floor stemming from IAD, whereas the pillar surface was expected to be close to a delta function due to the ultra-flat silicon substrate employed. The respective centre peak positions z_{pillar}, z_{floor} and standard deviations σ_{pillar}, σ_{floor} were obtained from Gaussian fit data. The average etch depth $\bar{H}$ and its standard deviation σ_H are consequently obtained with Eq. (4.4**)** and (4.5**)**, respectively.

$$\bar{\mathbf{H}} = \left|\mathbf{z_{pillar}} - \mathbf{Z_{floor}}\right| \tag{4.4}$$

$$\boldsymbol{\sigma_H} = \sqrt{\boldsymbol{\sigma_{pillar}}^2 + \boldsymbol{\sigma_{floor}}^2} \approx \boldsymbol{\sigma_{floor}} \; (\gg \boldsymbol{\sigma_{pillar}}) \tag{4.5}$$

The resist-corrected etch depth in Figure 4.9 was measured to (a), (c) 123.5 µm with a standard deviation of $\pm$ 4.4 µm ($\pm$ 3.6 % of $\bar{H}$) at the central region and (b), (d) 128.0 µm $\pm$ 2.8 µm ($\pm$ 2.2 % of $\bar{H}$) at the edge region of the metasurface. Notably, the edge region exhibited a slightly deeper yet more uniform etch depth, presumably due to loading or heating effects [458] and the more uniform pillar geometries, respectively. An additional 3rd peak was observed at a high depth in (d), which stems from the 100 µm wide opening in (b).

This outer ring (blue area) around the metasurface pattern clearly exhibited the impact of severe ARDE compared to the etch floor of the metasurface pattern.

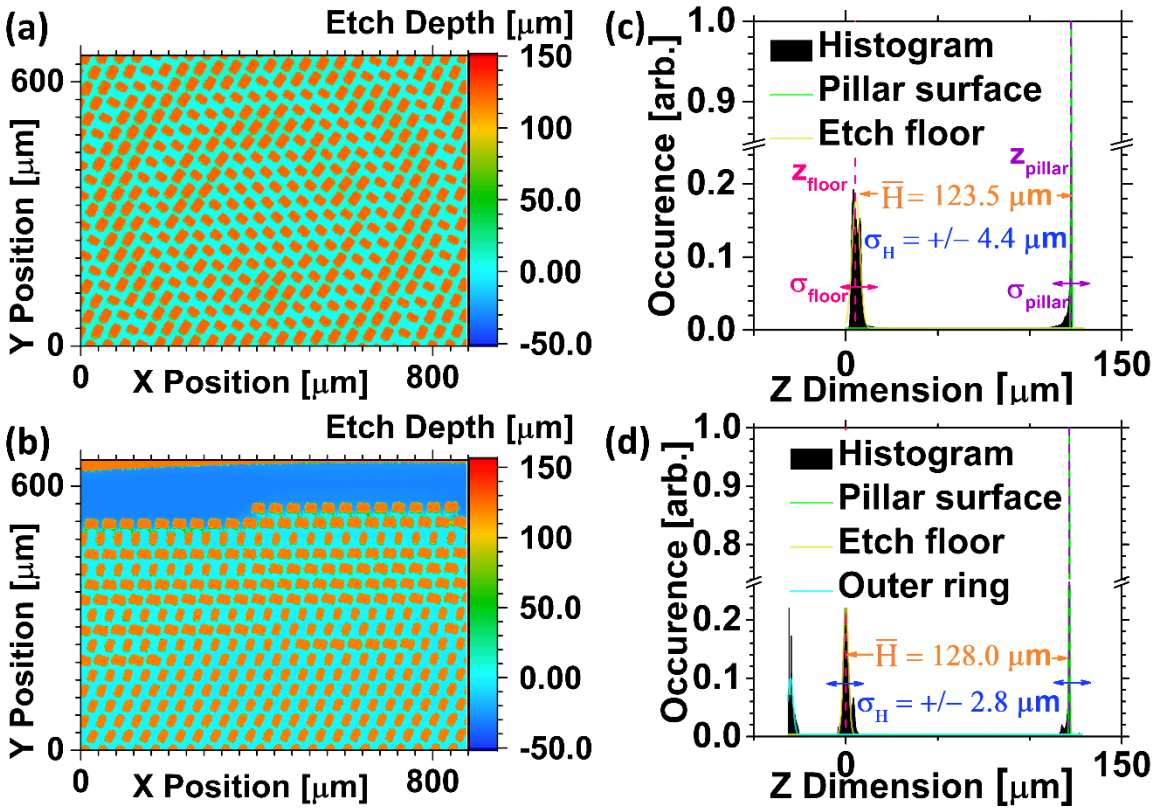

Figure 4.9: 3D surface profiles measured with WLI (a) at the central region and (b) at the edge region of the metasurface after 152 etch cycles of sub-recipe 1 and 2 (see Appendix E). (c), (d) Histograms (1'000 bins) of the etch depths (z-dimension) extracted from the 3D data of (a), (b), respectively.

Overall, the metasurface was found to be insufficiently etched by ca. 24.3 µm and was therefore resubmitted to a follow-up etch of 70 cycles with sub-recipe 3, taking advantage of gained sample information within the feedback loop.

Comparing the results of Figure 4.9 with Figure 4.10, one can see that the additional 70 etch cycles resulted in ca. 22.7 µm increased etch depth, amounting to an average etch rate of ca. 0.32 µm/cycle. The etch depth at the centre (146.0 µm) and edge (150.8 µm) were close to their target (150.0 µm ± 5 µm), while their respective standard deviations increased slightly to ± 5.1 µm (± 3.5 % of $\bar{H}$) and ± 4.6 µm (± 3.1 % of $\bar{H}$). This was expected since the impact of ARDE only increases with the etch depth, thereby leading to a more spread-out peak for the etch floor. It shall be emphasised that the presented measurement methodology

represented a fast, accurate, and clearly defined way to measure the etch depth and its deviations averaged over large, hence statistically meaningful areas. The ability to measure samples without stripping the protective photoresist allowed hereby for a valuable feedback loop of intermediate measurements and informed follow-up etching. Thanks to all this, accurate etch depths within a few percent of their target value were achieved while the detrimental effect of ARDE was confined to $\sigma_H \approx \pm 5$ µm.

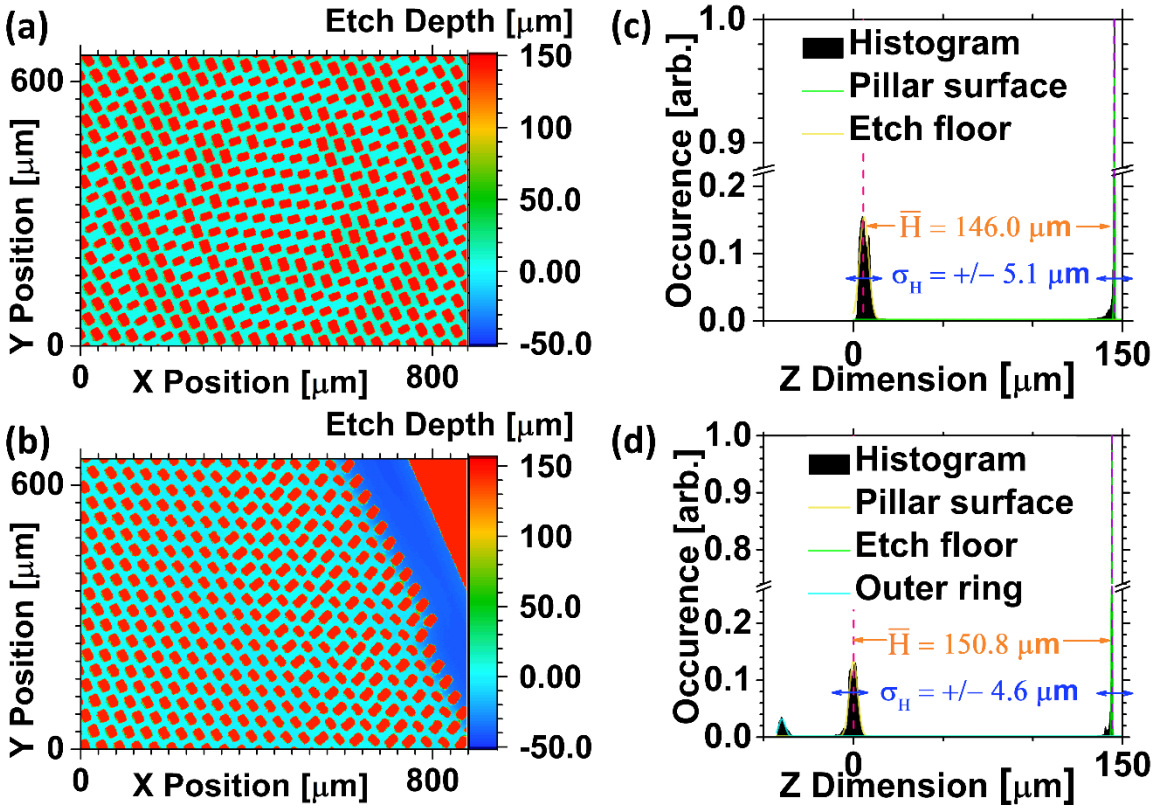

Figure 4.10: Repeated etch depth measurements of Figure 4.9 after additional 70 etch cycles of sub-recipe 3, see Appendix E. (a) 3D topology at the central region and (b) at the edge region of the bi-axicon metasurface employed for polarimetric imaging in Section 5.4.4 and Section 5.4.5. (c), (d) respective histogram (1'000 bins) over the etch depth (z-dimension).

Beyond numerical values, the obtained measurement results allowed for a better understanding of the factors influencing both the formation of ARDE and the spatial distribution of the etch depth deviations. Figure 4.11 (a) shows an adapted version of Figure 4.10 (a) that zoomed in on the etch floor to reveal concentric circular areas that were etched too deep and too shallow in a radially alternating manner. Wherever the radially symmetric phase profiles of Eq. (5.1) required pillars with large diameters and/or rotation angles that

resulted in narrow spacing towards neighbouring pillars, we observed a too shallow etch depth due to ARDE. On the other hand, wherever the pillar diameters were small and/or their edges were parallel to neighbouring pillars, we observed a large spacing between pillars that lead to a too deep etch due to ARDE. It was therefore apparent that this spatial pattern of the etch depth deviation had been distinctly influenced by the spatial distribution of pillar sizes and rotation angles, which in turn was defined by the chosen phase profiles.

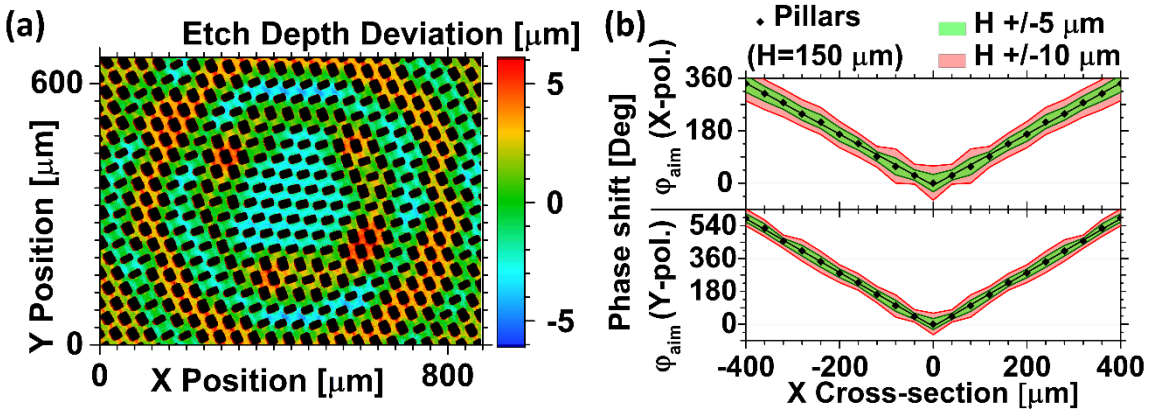

Figure 4.11: (a) Adapted surface profile of Figure 4.10 highlighting the height deviations at the etch floor. By combining results of the etch depth deviation with simulation results of Section 3.2, a control model was created to estimate the impact of the etch deviation on the optical performance of comparable metasurfaces. This is shown for (b) the x cross-section of two axicon phase profiles $\varphi_{aim,x}$, $\varphi_{aim,y}$ (black datapoints incl. linear fit) including respective error bands for the phase deviation caused by a deviating etch depth of $\pm$ 5 µm ($\pm\sigma_H$, green band) and $\pm$10 µm ($\pm 2\sigma_H$, red band) for the metasurface with linear OPB shown in Figure 5.2 (d)-(f) and Figure 5.3 (b), (d).

Knowing the values that are typically encountered for etch depth deviation in practice allowed for the creation of a control model to estimate the impact of these fabrication tolerances on the optical performance. Figure 4.11 (b) shows this by introducing error bands to the x cross-section of the phase profiles corresponding to $\pm\sigma_H$ ($\pm$ 5 µm, green band) and $\pm 2\sigma_H$ ($\pm$10 µm, red band). As discovered previously in Section 3.2, the detrimental impact on the transmitted phase front grows linearly with the etch depth with an average slope of approx. 4.6 °/µm. Consequently, the average phase deviation σ_φ can be estimated to approx. $\mp$23° for $\pm$5 µm, which should still have only limited impact on the optical performance. Hereby, small deviations of the average etch depth $\bar{H}$ from the target value (150 µm) impact

the optical performance more uniformly and less severely than respective values of the etch depth deviation σ_H, while the transmission efficiency was found to be virtually unaffected by either. We can hence conclude that process control over the etch depth of monolithically etched silicon substrates was demonstrated. The quality of all fabricated metasurfaces relevant to this work assessed by WLI are summarised in Section 4.5.1.

4.5 Assessment of Fabricated Structures and Metasurfaces

Once a reliable and repeatable fabrication process was developed, several metrology tools were employed to assess the metasurfaces once the fabrication had been completed and the resist removed. Besides WLI, described in detail in the previous sections, a scanning electron microscope was used to assess the structure definition, the verticality of the sidewall profile and roughness of the etch. Finally, a great amount of information on the fabricated metasurfaces could be gathered even by a mere visual inspection. The next Sections will explore the data obtained on the metasurfaces prior to optical experiments in more detail.

4.5.1 Etch Depth Assessed via White Light Interferometry

The statistics of the etch depth of every metasurface were measured and analysed at both the central and edge regions one more time once the fabrication was completed and the photoresist was stripped, using the same methodology described in the previous Section 4.4.2. These results are summarised in Table 4.2 for the metasurfaces employed in the experiments of Chapter 5 and Chapter 6.

Table 4.2: Summary of the average etch depth and its standard deviation ($\overline{H} \pm \sigma_H$) for the fabricatied metasurfaces selected for optical experiments.

Metasurface	Bi-Axicon OPB: $\|R\rangle, \leftrightarrow \|L\rangle$ Used in Sections 5.4.2 and 5.4.3	Bi-Axicon OPB: $\|R\rangle \leftrightarrow \|L\rangle$ Used in Sections 5.4.4 and 5.4.5	Meta-Polarimeter OPB: $\|R\rangle \leftrightarrow \|L\rangle$, $\|D\rangle \leftrightarrow \|A\rangle$, $\|H\rangle \leftrightarrow \|V\rangle$ Used in Section 6.4
Central region	**143.6 µm ± 3.4 µm**	**148.1 µm ± 4.4 µm**	**148.4 µm ± 4.6 µm**
Edge region	**144.4 µm ± 3.6 µm**	**152.3 µm ± 4.1 µm**	**155.1 µm ± 6.3 µm**

The general trend confirmed a consistently deeper etch at the edge region compared to the sample centre by ca. 0.6 µm to 6.7 µm, which was particularly high for the "Meta-polarimeter" employed in Section 6.4. The average etch depth of the bi-axicon employed for sensing was too shallow by ca. 6.0 µm (- 4 %). However, this resulted in a mostly systematic error on the encoded phase functions since all pillars were too shallow, hence unanimously exerted less phase shift than intended. As discussed in Section 4.4.2, the deviation of the etch depth σ_H and its spatial distribution had a much more significant impact on the phase error since it caused both too much and too little phase shifts depending on the location on the metasurface. Generally, a chaotic and rapidly changing (high spatial frequency) distribution of the phase error (thereby σ_H) was expected to be more detrimental to the device performance than a systematic, continuously distributed one. Hence, the spatial distribution of the etch depth deviation has to be taken into account, see Figure 4.12 and Figure 4.13.

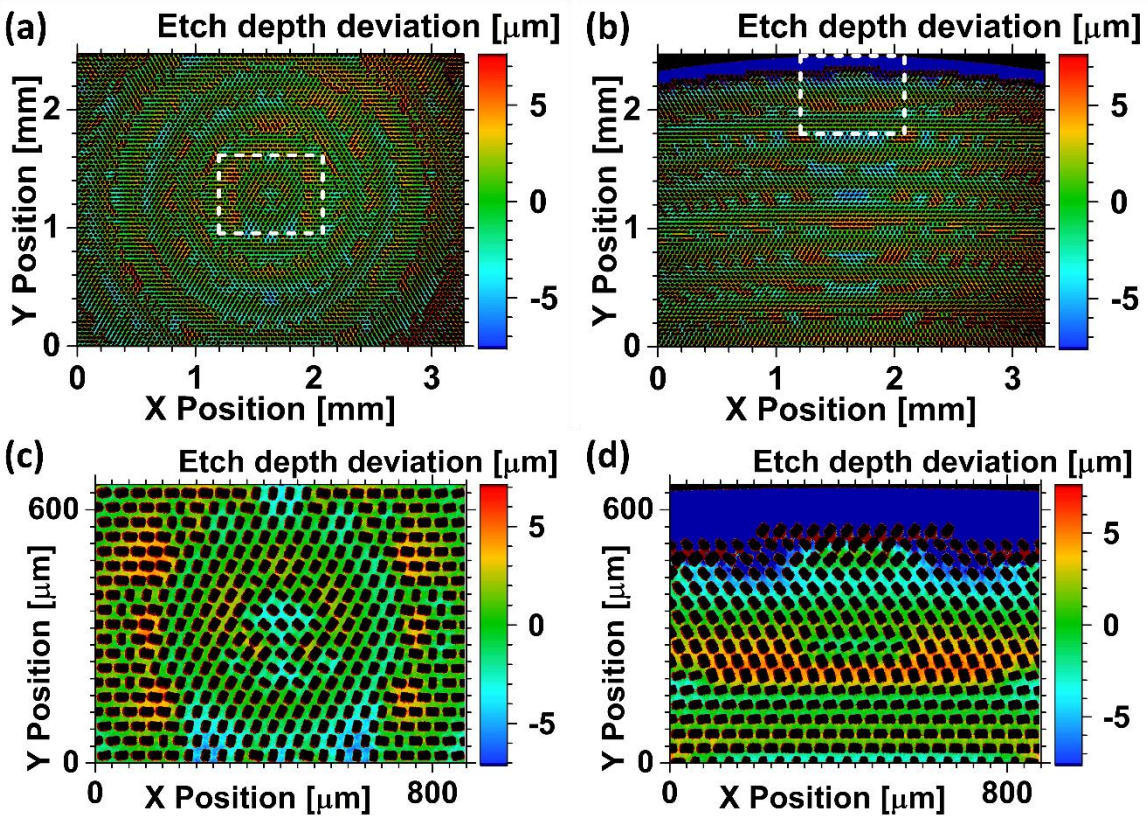

Figure 4.12: 3D surface profiles measured with WLI highlighting the etch depth deviations σ_H (colour code) of the etch floor around pillars (black). (a) Large-area measurement (0.55x) of the central region and (b) at the edge region. The white rectangle in (a), (b) represents the (c), (d) zoomed-in (2x) surface profiles of the two respective regions.

The large area measurements of Figure 4.12 (a), (b) confirmed the centrosymmetric pattern of the etch depth deviation for bi-axicon metasurfaces, which was already observed in Figure 4.11. The constant radial spacing of the depth deviation coincides with the Fresnel zones of the underlying phase profiles, proving their correlation. Interestingly, too deep and too shallow regions were alternating along each centrosymmetric line as the imposed phase shift – thereby pillar's rotation angle θ, see Eq. (3.4) and Eq. (5.1) – remained constant along such concentric paths, see Figure 4.12 (c), (d). The depth deviation is hence uniformly and continuously distributed along the equi-phase lines of the metasurface and should hence impact the optical performance even less than expected.

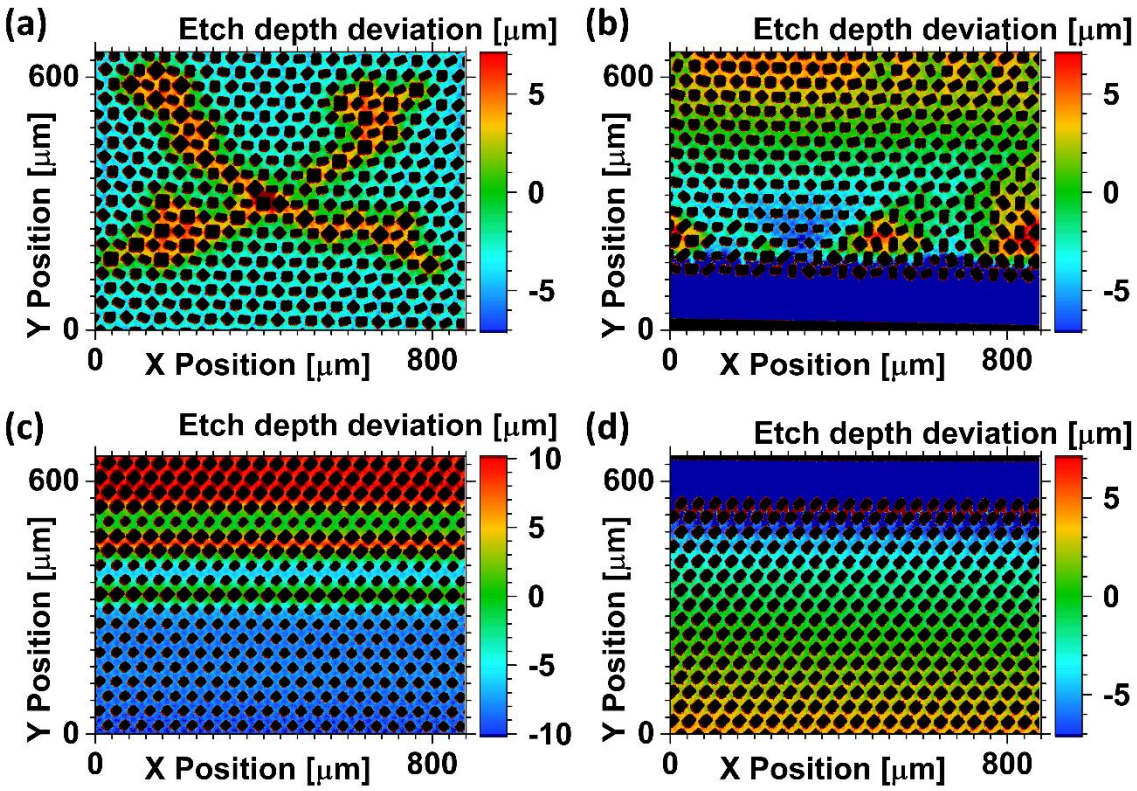

Figure 4.13: 3D surface profiles measured with WLI highlighting the etch depth deviations σ_H (colour code) of the etch floor around pillars (black) for the fabricated metasurface polarimeter. Zoomed-in measurement (2x) of the (a) central region and (b) at the edge region. A different linear-symmetric metasurface without pillar rotation showed more severe etch depth deviations (c) at its centre but not (d) at its edge region.

On the other hand, the metasurface polarimeter in Figure 4.13 (a), (b) showed a more chaotic etch depth deviation as result of its interleaved design (see Section 6.2) that introduced a

high spatial variability of pillar dimensions (W_x, W_y, θ). Nevertheless, the majority of the metasurface is etched rather uniformly, with outliers observed whenever particularly large or small neighbouring pillar dimensions are observed. Consequently, the overall phase error and impact on the optical performance remains generally limited with the occasional exception for individual pillars. This is preferable over designs with low symmetry and slowly changing spatial variability of pillar dimensions (W_x, W_y, θ) e.g., the linearly-symmetric metasurface without pillar rotation shown in Figure 4.13 (c), (d). The deviation of the etch depth is hereby much more pronounced ($\pm$ 10 µm) and divided into distinct areas. We can hence conclude from this analysis that the spatial distribution of the etch depth deviation should further reduce the impact on the transmitted phase profile for both types of metasurfaces presented in this work.

4.5.2 Structure Definition Assessed via Scanning Electron Microscopy

WLI proved excellent at assessing the etch depth variation across a large metasurface. However, it could not provide information on the verticality or the roughness of the etched pillars, for which Scanning Electron Microscopy (SEM) was employed. SEM is an established metrology instrument when structure sizes down to a few nm have to be resolved [465]. Crucially, SEM employs a focussed beam of electrons to generate contrast from the sample interaction as opposed to traditional microscopic techniques, which employ electromagnetic waves. The working principle of SEM can be understood by inspecting Abbe's Eq. (4.6**)**, which describes how the absolute resolution d is limited by the wavelength $\lambda_{0,e}$ and the numerical aperture NA of an optical setup [465]. The wavelength λ_0 is hereby an inherent property for photons, whereas it is a variable described by the de Broglie wavelength $\lambda_e = h/p_e$ for the propagating electron beam, with the Planck constant h and the electron's momentum p_e. The electron gun of an SEM generates and accelerates the electron beam with the acceleration voltage V_a. From equality of electric and kinetic energy, the wavelength of the electron beam can then be shown to be a function of this acceleration voltage V_a in Eq. (4.7**)**, with the electron's mass m_e and its elemental charge e.

$$\boldsymbol{d = 0.612\,\frac{\lambda_{0,e}}{NA}} \tag{4.6}$$

$$\boldsymbol{\lambda_e = \frac{h}{2 \cdot m_e \cdot e \cdot V_a}} \tag{4.7}$$

Consequently, the acceleration voltage of the electron gun is an important parameter to achieve extremely high resolutions. Figure 4.14 describes the general outline of an SEM. The entire setup, including the conductive sample (intrinsic or Au coated), is situated within a high vacuum to minimise scattering of the electrons with gas molecules.

The propagating electron beam is subsequently collimated and focussed by a set of magnetic lenses and apertures in a configuration that is comparable to optical microscopes or the WLI setup of Figure 4.8. However, the electron beam is additionally deflected into a scanning motion to achieve a reasonably large FOV on the sample surface despite the tightly focussed beam with a typical spot size of only 1 - 100 nm [465].

Analytical versatility is granted by a multitude of employable detectors e.g., secondary electron (SE) detector, back-scattered electron (BSE) detector, dark and brightfield detector, energy-dispersive X-ray (EDX) analysis, etc. The images shown within this work employed a SE detector, whose signal is obtained from low-energetic secondary electrons that are set free upon impact of the high-energetic primary electrons (beam) close to the sample surface. Consequently, SE detection was ideally suited for fast, high contrast images of the sample topology, thereby fitting the metrology requirements.

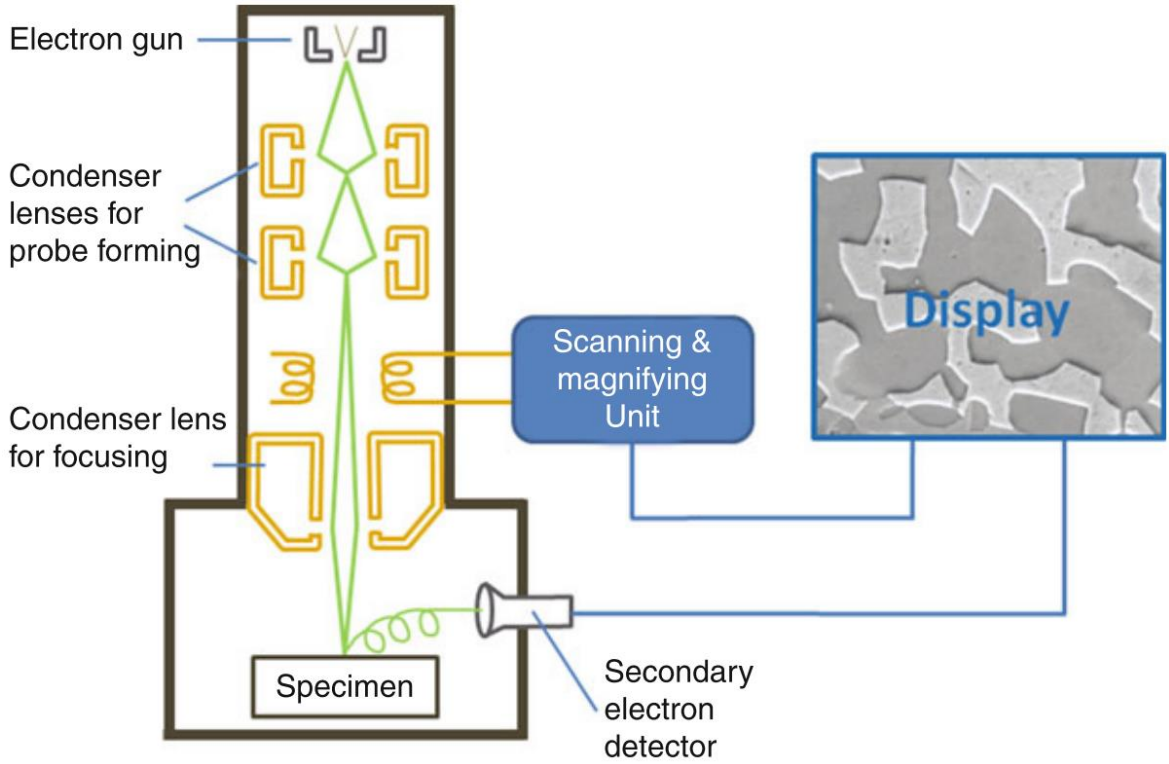

Figure 4.14: Simplified schematic outline of a scanning electron microscope (SEM) with its fundamental components. Illustration reproduced from [466].

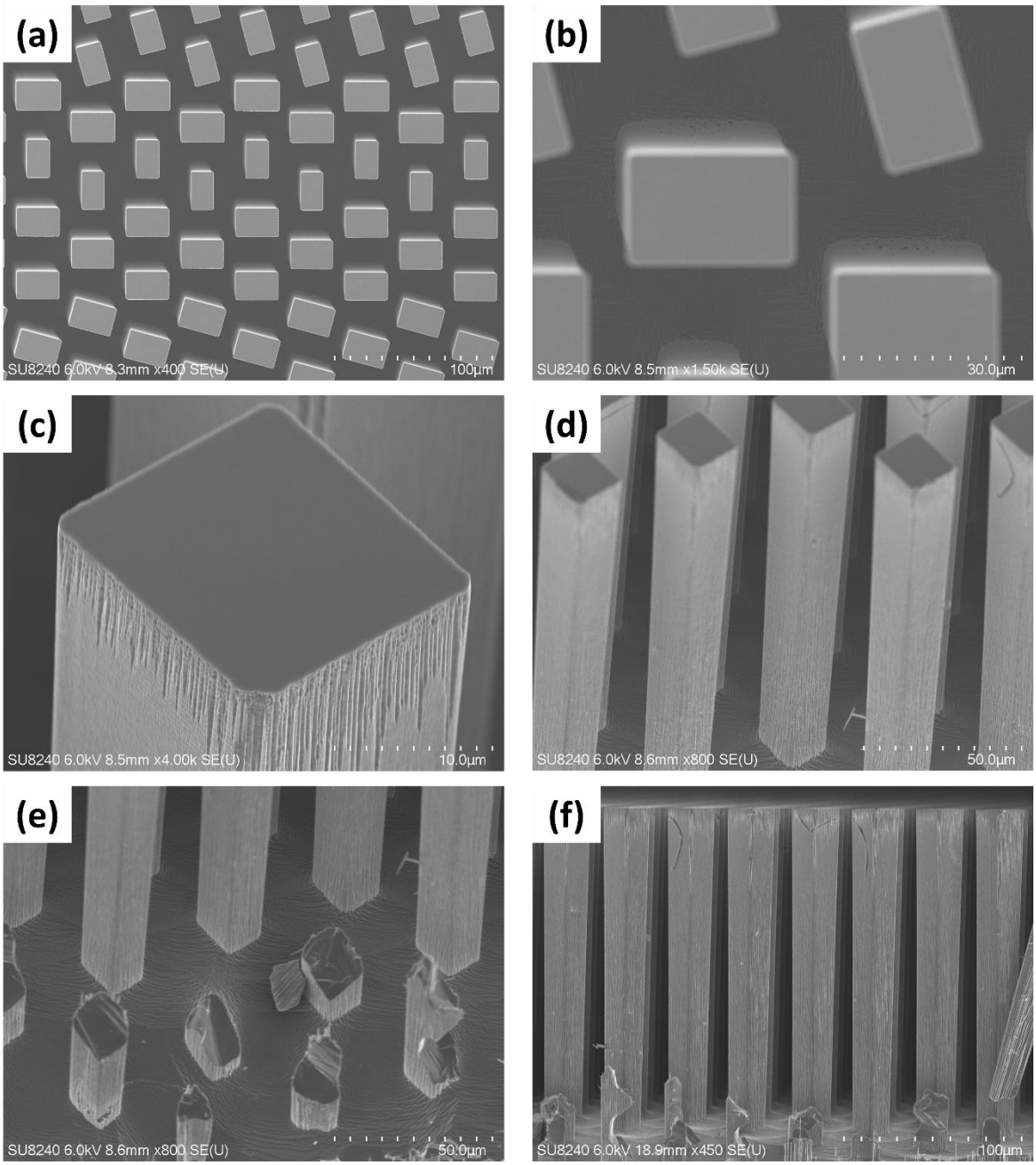

Figure 4.15: SEM images of fabricated metasurfaces. (a) Frontal view of a metasurface showing a clearly defined rectangular pillar structure with sharp edges at (a) low and (b) intermediate magnification. (c) A zoomed-in image of a tilted (60º) metasurface revealed no significant edge-rounding or resist-undercutting effects, and negligible sidewall-scalloping. (d) Increased sidewall roughness is shown at the bottom of the pillars. (e) The etch floor exhibited a curvature as expected. (f) Metasurface imaged in cross-section, revealing a near-perfect sidewall verticality of 88.5º-89.5º (negative slope).

Figure 4.15 (a), (b) shows SEM images of fabricated metasurfaces in frontal view, exhibiting excellent structure definition of the rectangular pillars with sharp vertices that showed no noticeable rounding. No significant resist under-etching at the top surface, nor pronounced sidewall scalloping[7] was observed in angled view (60º), see Figure 4.15 (c), (d), albeit some minor sidewall roughness was observed especially at larger etch depths. A cleaved region allowed for the observation of the etch floor in Figure 4.15 (e), confirming the curvature expected from IAD due to the absence of an etch-stop layer [435, 456, 457], which was also observed with WLI in Section 4.4.2. The sidewall verticality was measured at 90º observation angle to a near-perfect 88.5º-89.5º in Figure 4.15 (f) that remained uniform over the entire 150 µm etch depth.

It can hence be concluded that the obtained high resolution SEM images of the metasurfaces certify an excellent structure definition and sidewall profile, thereby confirming that the employed Bosch process was almost perfectly optimised.

4.5.3 Defect Density Assessed via Visual Inspection

Although optical microscopy was used for the fast inspection of the resist uniformity and assessment of its complete development, it did not provide any additional information compared to WLI, which additionally quantified the depth dimension, or SEM images, which provided higher magnification and resolution. It was thus preferred not to include any optical micrograph for brevity. This section will instead discuss the information that can be derived by a simple visual inspection of the metasurfaces.

Strikingly, the metasurfaces exhibited bright interference colours that were influenced by the illumination and inspection angles, as well as the underlying phase functions i.e., Fresnel zones. Fabrication defects were therefore easily spotted as colour-deviations. Although this might be the simplest metrological technique imaginable, it allowed for the rapid and reliable assessment of medium to large defects over the entire metasurface at once, hence offering the advantages of simplicity, speed and a large FOV.

---

[7] Sidewall scalloping describes the sawtooth pattern of the sidewall caused by the cyclic etch and passivation steps of the Bosch process, which can be seen in Figure 4.5.

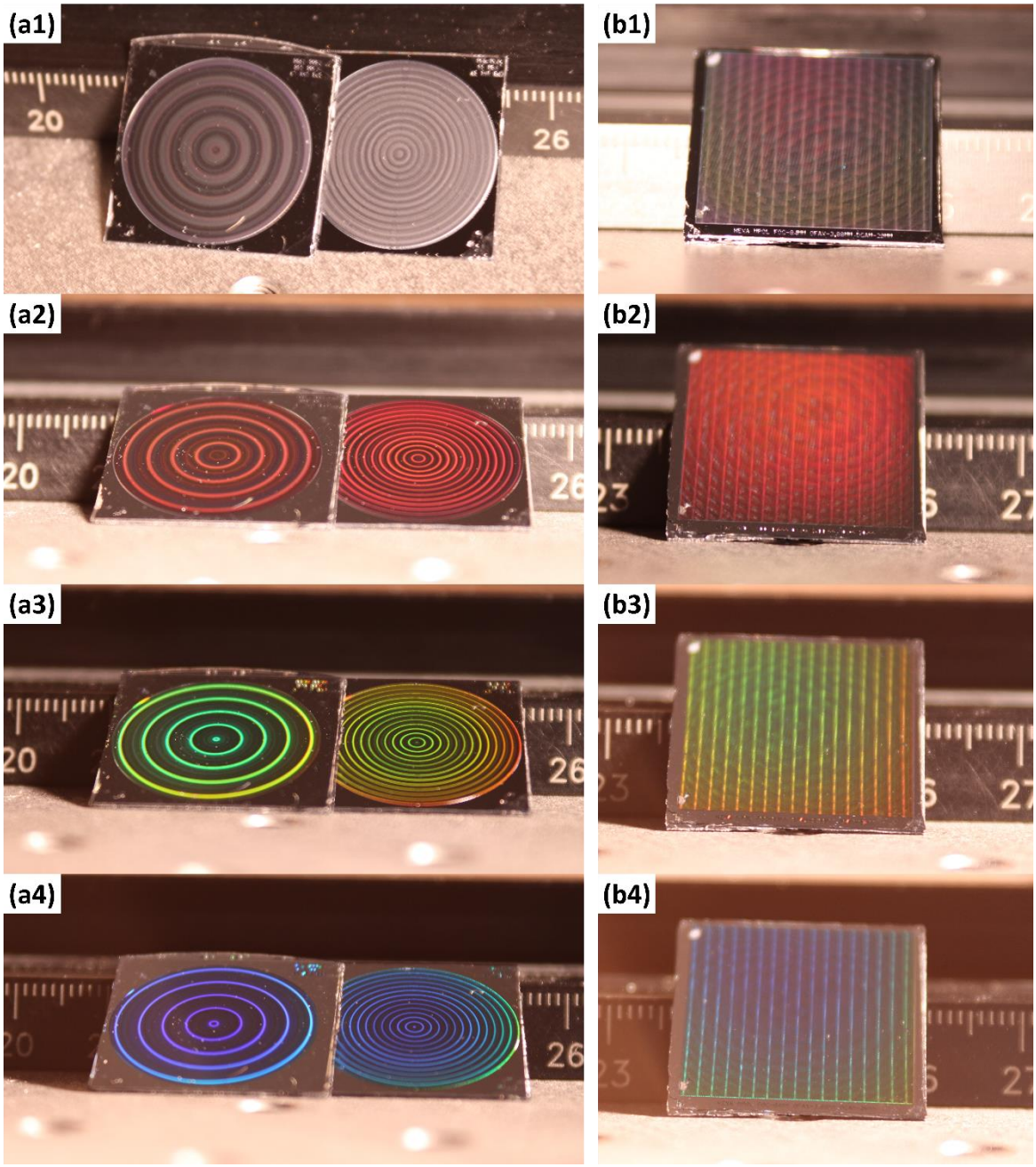

Figure 4.16: Photographs of the fabricated metasurfaces showing interference colours. (a1)-(a4) shows the two metasurfaces employed for (left) polarimetric imaging and (right) polarimetric sensing applications in Chapter 5, whereas (b1)-(b4) shows the metasurface polarimeter developed in Chapter 6. (a1), (b1) The intrinsic silver colour of silicon was observed upon close to normal incidence, which changed to (a2), (b2) red over (a3), (b3) green to (a4), (b4) blue for increasing angles of the incident light (see shadows).

Figure 4.16 shows a selection of images showcasing the described effects for (a1)-(a4) the Bessel metasurfaces used for (left) imaging and (right) sensing applications (Chapter 5) and (b1)-(b4) the metasurface used for polarimetric analysis (Chapter 6). It can be clearly seen that larger incident angles (see shadows) change the appearance from colourless over red to blue interference colours. Besides some insignificant scratches close to the edge caused by tweezer handling, all metasurfaces showed uniform and defect-free active areas albeit with some unavoidable dust-particles that were deposited post-fabrication and can be easily cleaned off. It can hence be concluded that the fabricated metasurfaces were of excellent visual quality with a few minor defects located at the far edges, where they should not have a measurable impact on device performance.

4.6 Conclusion on the Fabrication of Monolithic Metasurfaces

Within this chapter, the fabrication requirements for the previously designed metasurface optics based on monolithic silicon substrates were defined. After careful consideration, photolithographic processing with subsequent plasma-based DRIE was chosen as ideally suited fabrication technique to meet these requirements. The theory and the important parameters of the employed fabrication processes were explained step-by-step to provide the background knowledge necessary to understand the optimised process sequence.

It was then pointed out that the absence of an etch-stop layer meant that ARDE lead to deviations of the etch depth, which were identified as a main cause of concern to the optical performance of the fabricated metasurfaces. In response to this, a process control methodology was developed based WLI to measure the etch depth over a large area. These measurements allowed for statistically relevant quantification of the average etch depth and its standard deviation, as well as the qualitative assessment of the spatial distribution of the mentioned depth deviation. In combination with respective simulation results of Section 3.2, the expectable impact of these depth deviations on the optical performance was shown to be limited and systematic rather than chaotic. The possibility to conduct these measurements even with photoresist on top of the pillars established a feedback loop including the resubmission to fine tune the etching, thereby ensuring that the average etch depth was consistently close to its design value.

SEM inspection found the structure definition and sidewall profile of pillars to be well within the desired, whereas inspection by the naked eye was sufficient to assess the overall quality

and defect density thanks to bright interference colours formed by the metasurfaces. The presented production of high-quality metasurfaces based on a novel monolithic fabrication process included the characterisation and assessment of important fabrication tolerances. The difficulties encountered upon monolithic production compared to a bi-layer substrate with etch stop layer [311] were far outweighed by several key advantages:

1. **Cost effectiveness:** Bi-layer substrates are far more expensive than intrinsic silicon substrates, especially for the thick metasurface layers required at terahertz frequencies. This is due to additional processing steps for bi-layer substrates e.g., prolonged material deposition or thinning of the active silicon layer to the required thickness followed by wafer bonding or gluing to the substrate. Failed fabrication attempts constitute a considerable loss of investment for bi-layer substrates, but not for silicon substrates.

2. **Fabrication tolerances:** While bi-layer substrates avoid etch depth deviations caused by ARDE thanks to their etch stop layer, they still possess height tolerances stemming from the silicon top layer. This top layer must be processed to the required thickness of the metasurface, which introduces thickness tolerances that are comparable to those encountered for monolithic metasurfaces due to ARDE – if not worse. Furthermore, over-etching with an etch stop layer is known to create other detrimental effects at the etch floor, such as lateral under-etching known as footing [467]. This footing effect would most likely impact the device performance more severely due to strong scattering at the substrate-pillar interface and can even lead to catastrophic failure by physical detachment of pillars. Furthermore, different thermal expansion coefficients of substrate and active layer might cause delamination because of the thermal stress at their interface under the high process temperatures encountered upon prolonged etching. Monolithic substrates do not possess such problems.

3. **Optical performance:** Amorphous materials like vacuum-deposited silicon or fused silica cause significant scattering of terahertz radiation, while impurities i.e., in silicon cause significant absorption. Hence, substrates that are intended to be efficient at terahertz frequencies should possess high purity and be monocrystalline e.g., intrinsic silicon and monocrystalline (z-cut) quartz (Qz). Such Si-Qz substrate would exhibit lower reflective losses at the air-substrate interface (transmission air-quartz ca. 70-73 % [125]) compared to monolithic silicon metasurface (transmission air-silicon ca. 46-50 % [125]). However, a simple and cheap anti-reflective coating (e.g., parylene) at the air-substrate interface would overcome this drawback and reach even higher transmission than untreated Si-Qz substrates. Parameter sweep simulations comparable to Section 3.2 were executed to assess the performance of such a Si-Qz metasurface. The Si-Qz metasurface showed a marginally increased and narrowed average transmission of 91.6 % $\pm$ 4.6 % compared to the 86.9 % $\pm$ 6.4 % for a monolithic silicon metasurface. However, this did not take account to expectable detrimental effects like footing. Thus, a comparable or worse performance was expected for bi-layer Si-Qz substrates compared to silicon substrates.

The production methodology presented in this chapter allows hence for an industry-compatible, cost-effective and rapid production of terahertz metasurfaces on to cheap and readily available silicon substrates in a single lithographic step.

Chapter 5 : Beam Forming Metasurfaces for Sensing and Imaging Applications

5.1 Motivation for Beam Forming Polarisation Optics

The Terahertz spectrum has excellent prospects for imaging applications in quality assurance and NDT due to its high achievable resolution in the sub-mm range, low energetic impact (< 40 meV) and high transparency for a range of industrially important material classes such as polymer [19, 20], cardboard [11] and textiles [8, 9], which are opaque to most other spectral ranges. However, more specialised setups that target advanced imaging capabilities - such as the quantification of polarisation-dependent effects - commonly require more extensive and complex optical setups to form the (probe) beam incident on to the sample under test. Such complex optical setups are prone to absorption and alignment losses as well as detrimental standing wave and scattering effects - especially at terahertz frequencies. In combination with typically low source power and low sensitivity with high thermal noise upon bolometric detection at room temperature, one typically finds that a complex setup's signal-to-noise ratio (SNR) falls below the level required for reliable operation. As a result, complex setups such as shown in Figure 5.1 (a) [358] are simply not feasible at terahertz frequencies with an approach based on classic optical components, although the generated probe beam would boast great potential as beam forming optics for the terahertz NDT imaging systems and polarimetric material analysis.

In this context, metasurfaces are a revolutionary development in advanced optics due to their ability to combine the functions of multiple optical components into a single compact and highly efficient optical layer, which depends on intricate and clever design. This section will hence show how the beam forming capability of the yellow highlighted area in Figure 5.1 (a) could be integrated into a single metasurface layer shown in Figure 5.1 (b), thereby reducing the setup's complexity and associated losses and in turn boosting the SNR into a workable range. This metasurface consequently unlocked the application of the generated probe beam for imaging and sensing experiments that would most likely have not been feasible with classic optics. The remainder of this chapter is organised as follows:

The design of the developed beam forming bi-axicon metasurfaces will be introduced and explained in Section 5.2.1 together with an analytical model, both of which will be validated with numerical simulations of a large active area introduced in Section 3.4. Important design

parameters will be discussed with their underlying physics to describe the probe beam's polarisation-dependent interactions with diverse materials, i.e. dielectric, deattenuating and birefringent, thereby outlining its application for material identification and characterisation in sensing mode in Section 5.2.2 and polarimetric imaging mode in Section 5.2.3.

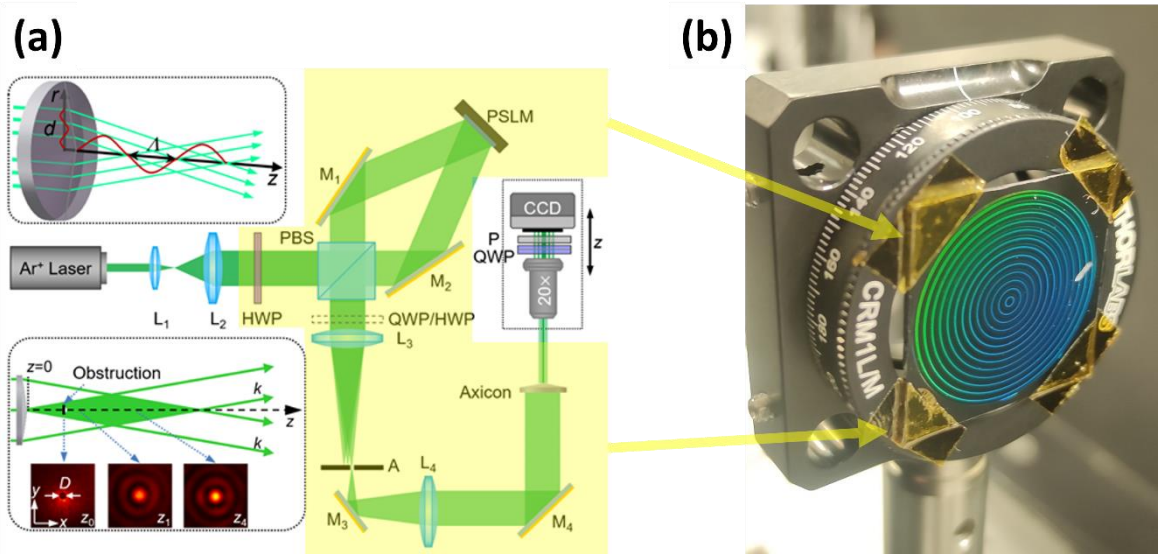

Figure 5.1: (a) Optical assembly of classic components required to generate the Bessel probe beam of interest for NDT applications (adapted from [358]). (b) Metasurface optics developed within this chapter that combined the entire optical function of the yellow highlighted portion of (a) within a single optical layer (showing interference colours).

Section 5.3.1 will present the experimental setup with its measurement and analysis methodology. To this end, a telecentric magnifying objective was designed in Section 5.3.2 which integrated the polarisation analysing capabilities described in Section 5.3.3. A pseudo-colour encoding methodology was developed in Section 5.3.4 to enable the intuitive interpretation of multi-dimensional polarimetric data within a single image.

Experimental results are presented in Section 5.4, specifically the probe beam calibration in Section 5.4.1 with sensing applications of a homogenous sample's diattenuation and RI demonstrated in Sections 5.4.2 and 5.4.3, respectively. Section 5.4.4 gauged the spatial resolution of polarimetric imaging capabilities using the 1951 USAF resolution target for the subsequent imaging of carbon fibres within a polymer matrix in Section 5.4.5, showcasing the characterisation of an industrially-important material class. Finally, Section 5.5 will draw conclusions on the presented results and outline future work.

5.2 Bessel Beam Metasurface – Design, Simulation and Modelling

5.2.1 Encoded Phase Profiles and Resulting Axial Polarisation Beating

The beam forming metasurfaces were optimised to produce an extended focal line - consisting of two orthogonally polarised 0th order Bessel beams - in which the SoP changes linearly as a function of the distance along the propagation axis z_i. The metasurface encoded two spatial phase functions $\varphi_{1,2}(x_i, y_i)$ that were independently excited by a pair of orthogonal polarisations (OPB) [350], as described in Section 3.3. All parameters resulting from these two arbitrary phase functions are subsequently denoted by the subscripts 1 and 2. Both phase functions were implemented as axicons with different radial phase periods ($g_1 > g_2$) according to Eq. (5.1), as previously illustrated in Figure 3.6.

$$\boldsymbol{\varphi_{1,2}(x_i, y_i) = 2\pi \cdot \underbrace{\sqrt{x_i^2 + y_i^2}}_{:=|r|} \cdot \frac{1}{g_{1,2}}} \qquad \textbf{(5.1)}$$

with the radial distance $|r|$ to the centre of the metasurface. The resulting half-cone angles $\alpha_{1,2} = \sin^{-1}(\lambda_0/g_{1,2})$ [350] of the two constituent Bessel beams $B_{1,2}$ and their spatial frequencies along the optical axis $k_{z1,2} = k_0 \cdot \cos(\alpha_{1,2})$ can be calculated from design parameters. This type of metasurface is consequently referred to as "(orthogonal) bi-axicon". Figure 5.2 shows large active area simulations (Lumerical FDTD solutions) of two such metasurfaces with radius R_{MS} of 2 mm and polarisation gratings g_1 and g_2 of 0.4 mm and 0.24 mm that respond to (a)-(c) $|R\rangle$ and $|L\rangle$ or (d)-(f) of $|D\rangle$ and $|A\rangle$ polarised light.

Figure 5.2 (a) and (b) show that both phase functions φ_1 and φ_2 independently generated Bessel beams B_1 or B_2 upon excitation by incident $|L\rangle$ or $|R\rangle$ light, respectively. The axial intensity profiles of B_1 and B_2 exhibit different half-cone angles α_1 and α_2, focal lengths $z_{max1,2} = R_{MS}/\tan\alpha_{1,2}$ and centre-spot sizes $w_{1,2} = 2.405 \cdot \lambda_0/(2\pi\sin(\alpha_{1,2}))$ [348]. The on-axis SoP remained circularly polarised with inverted handedness for both beams B_1, B_2. Upon illuminating the same metasurface with $|H\rangle$ light as shown in Figure 5.2 (c), or any other linear SoP, one can observe a linearly polarised beam centre, the orientation angle ψ of which changes along the propagation direction z_i. In this case, both constituent Bessel beams are excited simultaneously. All superimposed electric fields $E_{x1,2}$ and $E_{y1,2}$ along the focal line are constant and given by the metasurface's OPB i.e., their Jones vector. However, the on-axis phase shift $\delta_{1\leftrightarrow 2}$ between rays of the two constituent Bessel beams B_1 and B_2 grows linearly with the propagation distance z_i according to Eq. (5.2).

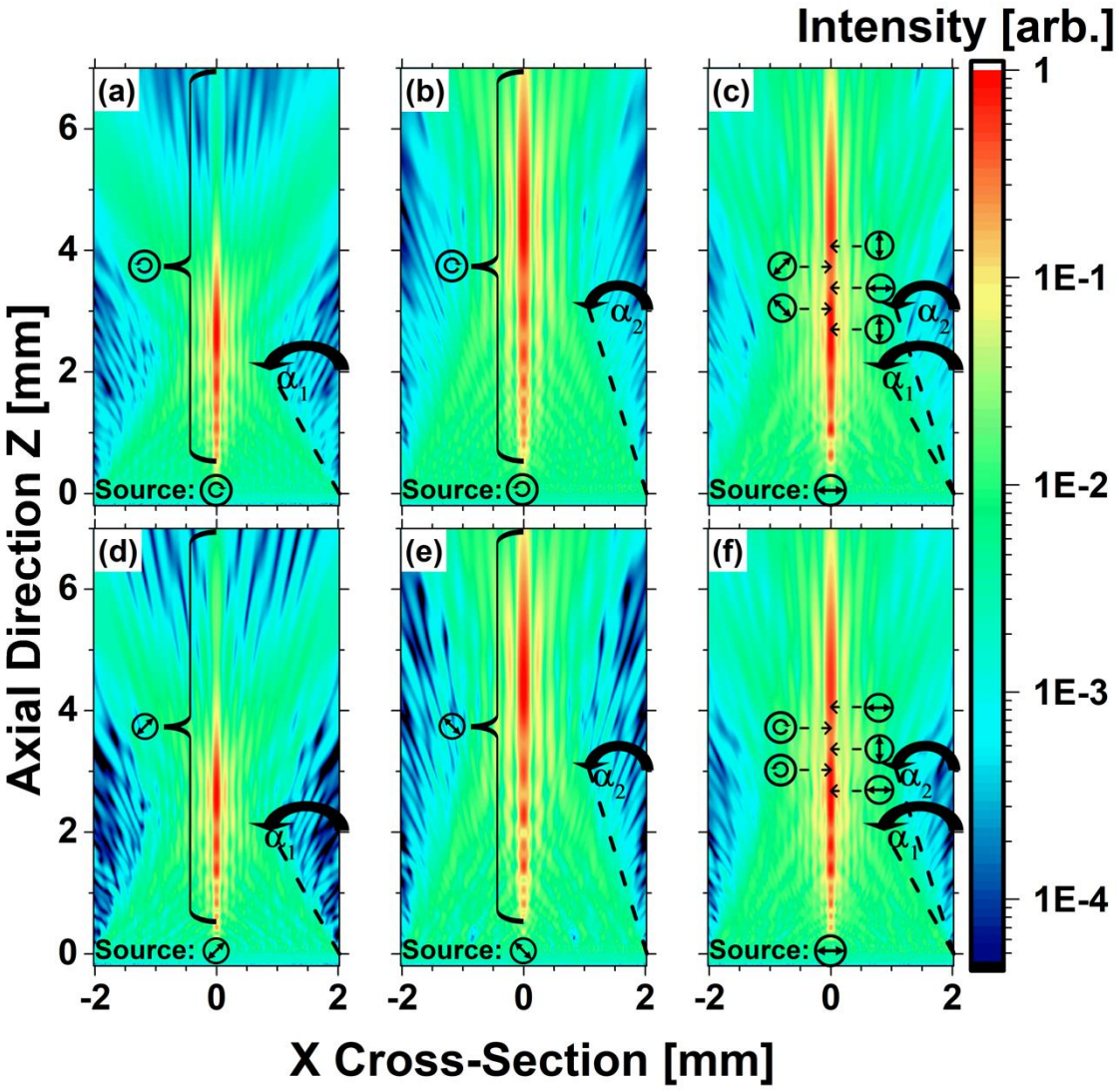

Figure 5.2: Large active area simulations of the x-z intensity profile for two bi-axicon metasurfaces (R_{MS}=2 mm, g_1= 0.4 mm, g_2=0.24 mm) using the simulation template introduced in Section 3.4. The top row shows a bi-axicon with encoded OPB that responds independently to incident (a) $|L\rangle$ and (b) $|R\rangle$ polarised light by forming one of the two fundamental Bessel beams $B_{R,L}$ with inverted handedness. (c) $|H\rangle$ polarised incident light formed a superposition of B_R and B_L beams that resulted in a linearly polarised beam centre with rotating orientation angle $\Psi(z_i)$ along the propagation direction, see Eq. (5.2), with a periodicity described by (5.3). The bottom row shows an analogous bi-axicon metasurface with OPB responding independently to incident (d) $|D\rangle$ and (e) $|A\rangle$ polarised light. (f) Their superposition upon $|H\rangle$ polarised incidence showed comparable polarisation beating yet with a different axial progression of the SoP.

$$\boldsymbol{\delta_{1\leftrightarrow 2}(z_i) = z_i \cdot \left(\underbrace{k_{z1} - k_{z2}}_{:=\Delta k_z} \right)} \quad \textbf{(5.2)}$$

This axially growing phase shift ($\delta_{1\leftrightarrow 2} \propto z_i$) translates therefore into a linearly changing SoP along the focal line with a periodicity Λ_{SoP} given by Eq. (5.3).

$$\boldsymbol{\Lambda_{SoP} = 2\pi(\Delta k_z)^{-1} = \frac{\lambda_0}{\cos\alpha_1 - \cos\alpha_2}} \quad \textbf{(5.3)}$$

Figure 5.2 (d)-(f) shows that an equivalent bi-axicon metasurface with different OPB e.g., |D⟩ and |A⟩ polarisations, composes a similar beam albeit with different axial progression of the SoP. Jones calculus can be used to predict the exact axial SoP with Eq. (5.4) using the Jones vectors $J_{1,2}$ of the two consitituent Bessel Beams $J_{1,2}$ that were chosen via the OPB.

$$\boldsymbol{J_{tot}(z_i) = J_1 + J_2 \cdot exp(i\,\delta_{1\leftrightarrow 2}(z_i))} \quad \textbf{(5.4)}$$

Analytical predictions for the axial SoP progression were compared to the numerical results of the previous simulations to confirm this theoretical model. Figure 5.3 (a) and (b) plots the axial orientation angle $\Psi(z_i)$ and ellipticity angle $\chi(z_i)$ of the PE at the beam centre upon excitation with |H⟩ light, respectively, for both bi-axicons of Figure 5.2 (c) and (f).

It is apparent that the presented theoretical model successfully and accurately describes the observed axial SoP progression for metasurfaces with either OPB (|L⟩ / |R⟩, or |D⟩ / |A⟩). For both OPBs, the observed characteristic angles are found to oscillate along the optical axis with a period Λ_{SoP} of 1.38 mm retrieved from simulations, which is in perfect agreement with the model of Eq. (5.3) and Eq. (5.4).

The deviations observed for the simulation results relative to the model are caused by slight efficiency and intensity differences between the two orthogonal gratings. The steeper half-cone angle $\alpha_1 > \alpha_2$ created a more tightly focused beam centre as per Eq. (2.19) (radius of central lobe $w_{b,1} < w_{b,2}$) with higher intensity collected from a circular area with larger radius $|\vec{r}|$ on the metasurface. This resulted in a slightly imbalanced superposition ($I_1 > I_2$) of the two constituent Bessel beams (B_1 and B_2) with some residual component at the beam centre $I_{res} = I_1 - I_2$. Strikingly, this imbalance affected both the axial orientation angle $\Psi(z_i)$ and ellipticity angle $\chi(z_i)$ equally for the |D⟩ / |A⟩ OPB, whereas the axial orientation angle $\Psi(z_i)$ was mostly unaffected for the |R⟩ / |L⟩ OPB. This observation becomes clear when considering that circular polarisations have no preferred - or defined - orientation angle Ψ that can cause deviations upon imbalance, as opposed to linear polarisations.

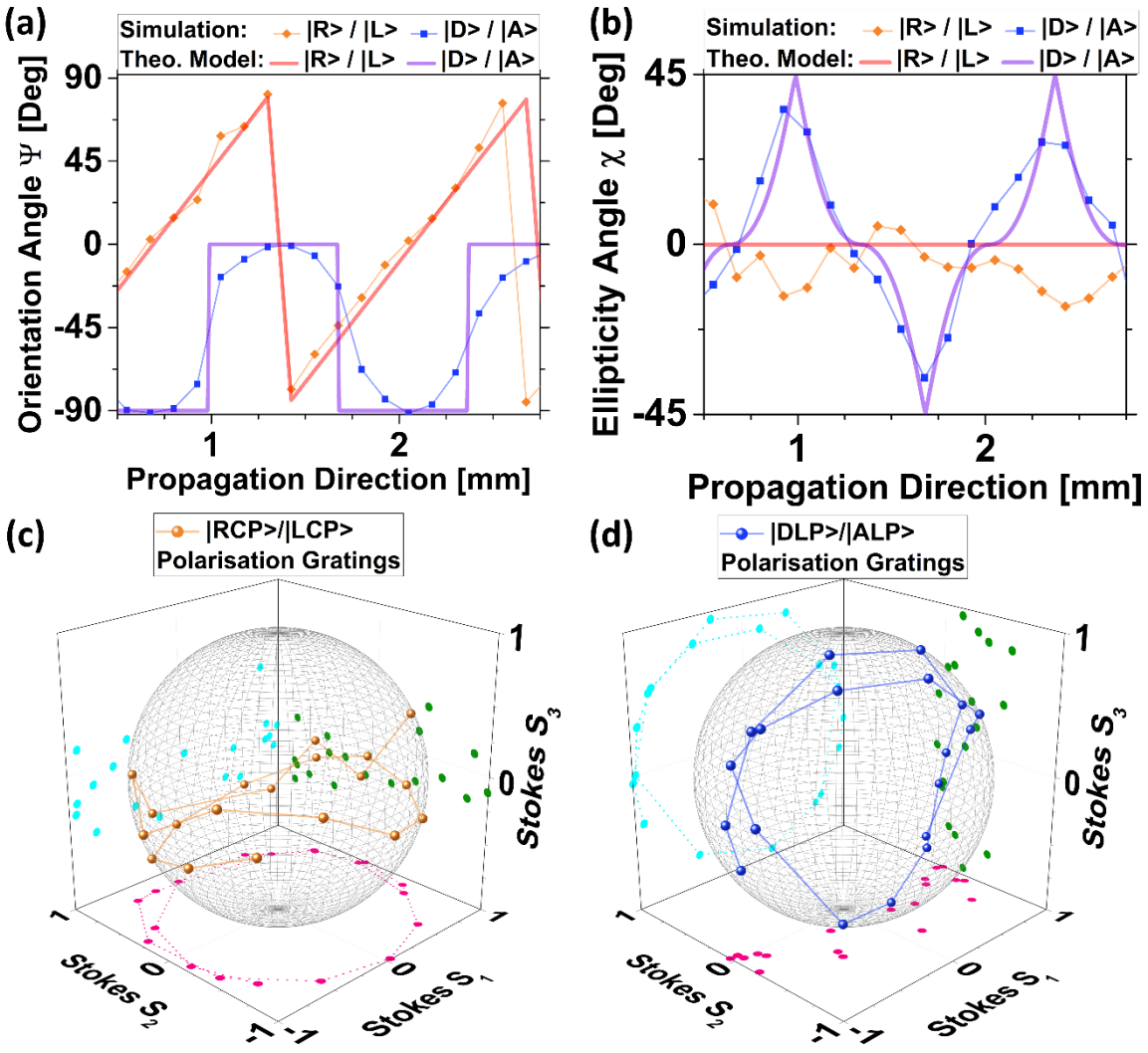

Figure 5.3: Axial polarisation analysis of the collective simulations presented in Figure 5.2 (R_{MS}=2 mm, g_1= 0.4 mm, g_2=0.24 mm). The on-axis characteristic angles of the PE, namely the (a) orientation angle Ψ and (b) ellipticity angle χ, are shown for increasing propagation distances above the metasurfaces (z_i) for both simulated OPB ($|L\rangle$ / $|R\rangle$, and $|D\rangle$ / $|A\rangle$). This SoP progression can alternatively be depicted on the Poincare sphere. (c) shows this for the bi-axicon with $|RCP\rangle/|LCP\rangle$ gratings, while (d) depicts results of the equivalent metasurface based on $|DLP\rangle/|ALP\rangle$ gratings. Both showed a circular path of SoPs in the S_1-S_2 and S_1-S_3 plane, respectively, which was equidistant to their OPB.

Consequently, the orientation angle Ψ is exclusively defined by the superposition of equal circular components ($I_{|R\rangle} \equiv I_{|L\rangle}$) for the |R⟩ / |L⟩ OPB while all intensity deviations I_{res} are concentrated within the ellipticity angle χ. Hence, later experiments employing bi-axicons with |R⟩ / |L⟩ OPB e.g., for RI sensing in Section 5.2.2, will preferentially utilise Ψ as robust "measurement channel" while χ can be used to assess alignment and image quality as a "quality channel".

At last, the axial SoP progression was visually assessed for the two previously presented OPBs on the Poincare sphere in Figure 5.3 (c), (d). In both cases, the SoP oscillation was found to follow a circular path along (c) the equatorial S_1-S_2 plane and (b) the meridian S_1-S_3 plane. These circular paths are exactly equidistant to their respective OPB polarisations (located at $S_3 = \pm 1$ and $S_2 = \pm 1$, respectively), thereby providing a geometric interpretation of the observed SoP oscillation along the optical axis.

In conclusion, one can control the axial SoPs formed along the focal line by choosing the OPB of the metasurface, and the oscillation length Λ_{SoP} by choosing the difference between the two grating periods $\Delta g = g_1 g_2/(g_1 - g_2)$. The metasurfaces presented here will enable various polarimetric applications in sensing and imaging by simply scanning the metasurface along the z-axis with respect to the object under study, as will be shown in Section 5.4.

5.2.2 Sensing Applications - Refractive Index and Polarising Effects

This section explores the physics behind the bi-axicon's capability to measure the RI of a homogeneous sample of known thickness, or vice versa to measure the thickness of a transmissive sample of known RI. To conclude this section, other observable polarisation-dependent effects that are important to material characterisation and NDT are summarised.

Introducing a homogeneous dielectric slab of thickness t and RI n_s into the bi-axicon's beam path will alter the internal half-cone angles $\beta_{1,2} = \arcsin\left[\sin(\alpha_{1,2})/n_s\right]$ of the constituent Bessel beams according to Snell's law, as well as their respective on-axis spatial frequencies according to $k_{n,z1,2}(n_s) = k_0 \cdot n_s \cdot \cos(\beta_{1,2})$. In turn, this leads to altered optical path lengths and thereby a changed on-axis phase shift $\delta_{1\leftrightarrow 2}$ between rays of the two constituent Bessel beams B_1 and B_2 at the detection plane z_i, described by Eq. (5.5).

$$\boldsymbol{\delta_{1\leftrightarrow 2}(z_i, t, n_s) = (z_i - t) \cdot (k_{z1} - k_{z2}) + t \cdot \left(k_{n,z1} - k_{n,z2}\right)} \qquad \textbf{(5.5)}$$

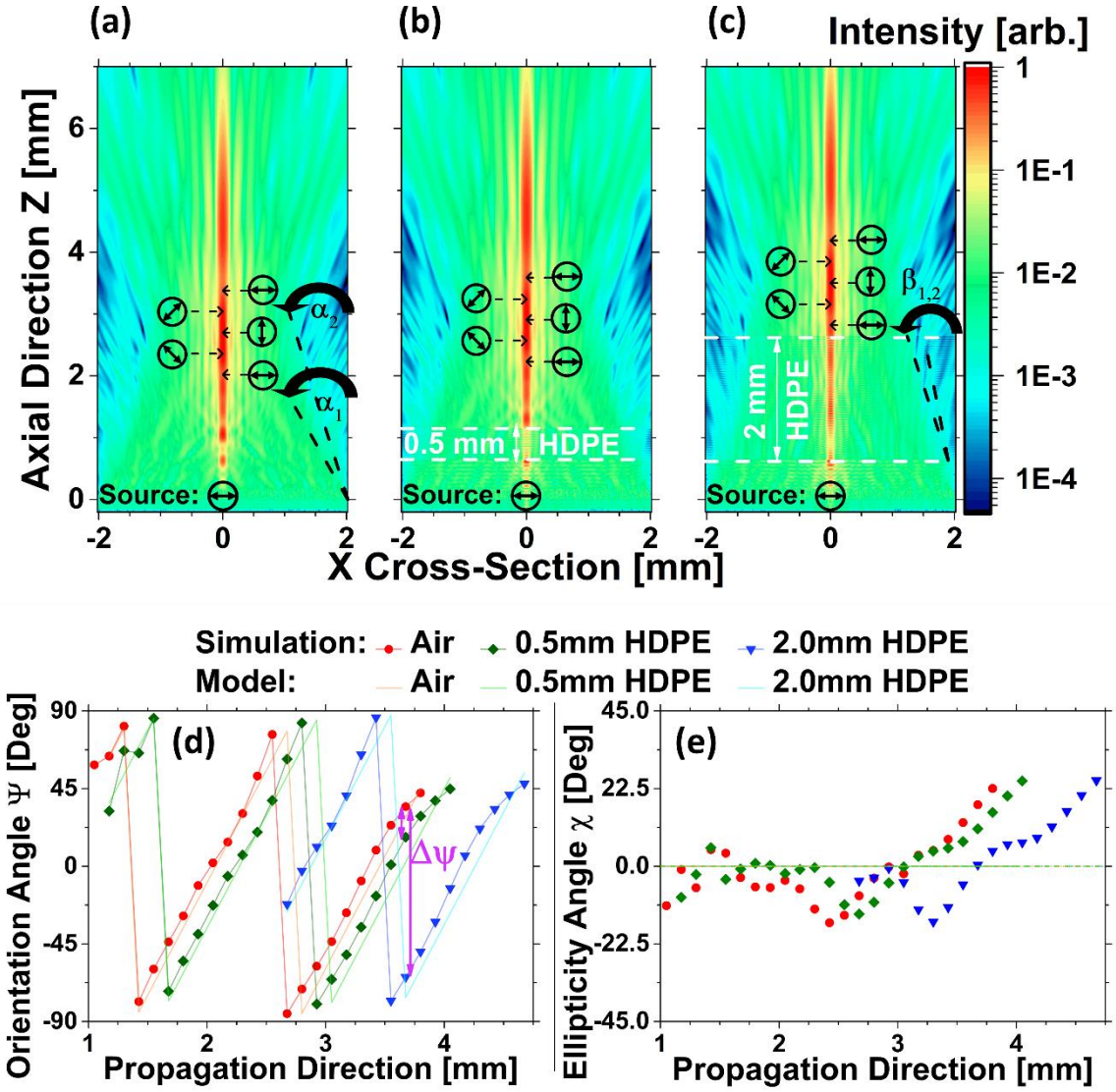

Figure 5.4: Large active area simulations of the x-z intensity profile for bi-axicon metasurface with OPB of $|L\rangle$ / $|R\rangle$ (R_{MS}=2 mm, g_1= 0.4 mm, g_2=0.24 mm) using the simulation template introduced in Section 3.4. Illumination with $|H\rangle$ polarised light formed the previously described superimposed Bessel beam with axially changing polarisation in (a) air and with (b) 0.5 mm or (c) 2.0 mm thick HDPE sample (n_{HDPE}=1.58 RIU [29]) introduced into the beam path between the white dashed lines. (d) The orientation angle $\Psi(z_i)$ of the PE at the beam centre exhibits a clear shift $\Delta\Psi \propto t$ that is proportional to the thickness of the HDPE sample, whereas (e) the ellipticity angle remained close to 0° for all datapoints until the shorter Bessel beam became increasingly faint towards $z_{max}(B_{|L\rangle})$ = 4.1 mm. The theoretical model of Eq. (5.4) and Eq. (5.5) is shown to accurately describe the observed polarisation parameter.

This altered phase shift described by Eq. (5.5) is simply an adapted version of Eq. (5.2) that takes account to the slab's RI n_s and thickness t, to be inserted into Eq. (5.4).

Figure 5.4 confirmed the described behaviour with large active area simulations employing the metasurface with $|L\rangle$ / $|R\rangle$ OPB that was already shown previously in Figure 5.2 (a)-(c) and Figure 5.3 (c). Compared to the undisturbed beam path within air shown in Figure 5.4 (a), one can clearly spot a horizontal standing wave effect between the white dashed lines caused by Fabry-Perot resonances within the 0.5 mm and 2.0 mm thick HDPE sample (n_{HDPE}=1.58 RIU [29]) in (b) and (c), respectively. Furthermore, Figure 5.4 (b), (c) clearly exhibited decreased half-cone angles $\beta_{1,2} < \alpha_{1,2}$ within the sample region that led to axially stretched Bessel beams $B_{1,2}$. After transmission through the sample region, this resulted in an axial displacement of the beams that was proportional to the sample thickness, as indicated by the axial position of the polarisation symbols in Figure 5.4 (a)-(c). This effect becomes more apparent when looking at the characteristic angles of the PE at the beam centre, particularly the orientation angle $\Psi(z_i)$ in Figure 5.4 (d). While the periodicity Λ_{SoP} of 1.38 mm and the general progression of the axial SoP were maintained for all three simulations, there was a distinct shift $\Delta\Psi \propto t$ observed behind the introduced HDPE samples (see green and blue datapoints) compared to the undisturbed beam in air (red datapoints) that remained constant at all scan positions. This shift was accurately described by the analytical model of Eq. (5.5) for both thicknesses using the same value for the RI of 1.58 RIU as in the numerical simulation, thereby confirming the model's validity. The on-axis ellipticity angle $\chi(z_i)$ of the PE in Figure 5.4 (e) remained close to the expected value of 0° until the shorter beam $B_{|L\rangle}$ became increasingly faint towards $z_{max}(B_{|L\rangle})$ = 4.1 mm.

Hence, it can be concluded that the extended analytical model for the on-axis SoP of the presented probe beams accurately described the impact of introducing an optically dense medium with n_s and thickness t on to the observed axial polarisation progression. The comparison between numerical results of large active area simulations and the analytical model showed a remarkably precise agreement, thereby validating the developed model for use in the RI sensing experiments of Section 5.4.3. The RI can be calculated by inverting the analytical model, utilising the measured sample thickness and relative shift $\Delta\Psi$ obtained between a polarimetric calibration measurement and a respective measurement after introduction of the sample into the beam path. Examining Eq. (5.2), Eq. (5.3) and Eq. (5.5), one can see that this shift $\Delta\Psi$ is caused by the difference between the on-axis wave vectors $k_{z1} - k_{z2}$ (or the difference of diffraction angles $\alpha_1 - \alpha_2$). Consequently, the sensitivity of

the bi-axicon's probe beam to the RI of a sample can be controlled via the chosen difference of grating periods Δg and is thereby a design parameter i.e., probe beams with shorter oscillation length Λ_{SoP} can measure the RI more precisely. However, this sensitivity stands in a trade-off with the dynamic measurement range due to the periodicity of the measured shift of the orientation angle $\Delta\Psi \in [-90°; 90°]$ i.e., measured results beyond a certain RI and thickness become ambiguous since $\Delta\Psi = 20°$ cannot be distinguished from $\Delta\Psi = 200°, 380°, ...$ (because of wrapped periodicity). Consequently, the probe beam presented here must be optimised with its respective application in mind to achieve their best performance.

Last but not least, the use of the SoP as measurement channel resulted in a multitude of additional polarisation-dependent material interactions that can be used for material identification and characterisation. The most prominent and widespread interactions were summarised previously in Section 2.2.3 i.e., diattenuation or reflection under the Brewster angle, in which the transmission depends on the incident polarisation, and birefringence, in which different polarisations experience different speed of propagation. These effects can be identified and quantified via their impact on the polarised probe beam, which will be shown experimentally for diattenuation in Section 5.4.2.

5.2.3 Polarimetric Imaging - Image Contrast and Resolution

While sensing experiments allow for the accurate characterisation of homogeneous samples, there are many inhomogeneous (composite) materials with regions of distinctly different physical response to incident polarised light. To fully characterise these industrially important material classes, such as carbon fibre reinforced polymers, one needs to spatially distinguish regions of different composition or orientation using polarisation-dependent interactions to generate image contrast e.g., within a polarimetric imaging configuration.

The most commonly encountered polarisation-dependent material interactions for NDT applications are diattenuation, e.g. anisotropic conductive materials with at least one sub-wavelength dimension such as carbon fibres, and birefringence, which can be either intrinsic to (micro-) crystalline regions or stress-induced [32]. Crucially, the exact identification, characterisation and quantification of such polarisation-dependent effects cannot be achieved with a single incident SoP but requires measurements of the sample's response to several different incident polarisations. For example, a dark sample region upon transmission could be caused by either polarisation-independent absorption or polarisation-dependent

diattenuation (extinction axis aligned to incident SoP). Only observation of the same sample region with different incident polarisation can unambiguously identify the underlying effect e.g., if region still dark with orthogonal SoP → material absorption, if region bright with orthogonal SoP → diattenuation.

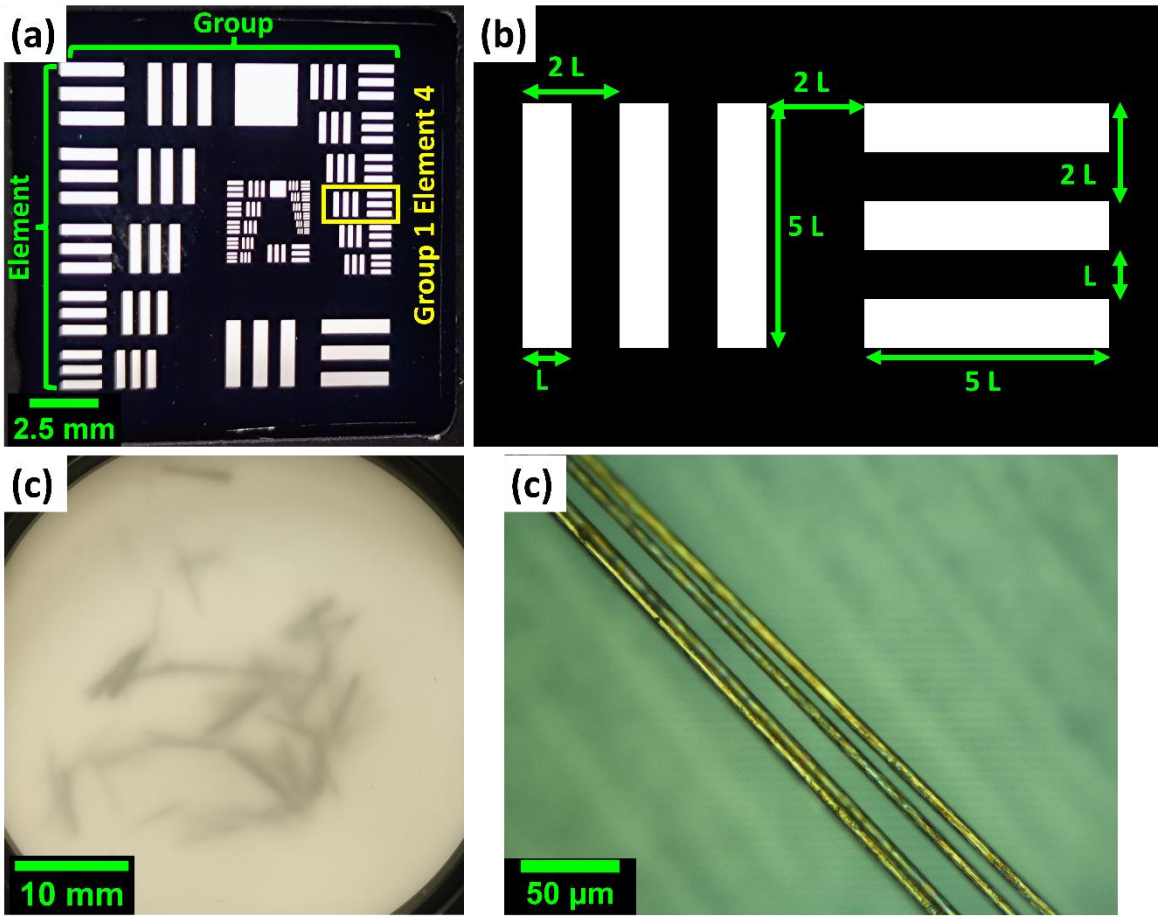

Figure 5.5: The (negative) 1951 USAF resolution test chart consisting of (a) multiple groups and elements of three horizontal and vertical cut-out lines within a metallic film with logarithmically decreasing structure sizes. (b) The equally spaced horizontal and vertical lines follow a common relative design, with the line width L of the smalles element for which 3 lines are still distinguishable representing the minimum resolution of the optical setup. (c) To test applications in NDT of carbon fibre reinforced polymers, a sample with randomly oriented carbon fibres sandwiched between two 0.5 mm thick PTFE slabs has been used. (d) Magnified image of the carbon fibres under an optical microscope exhibiting an average diameter of 5.1 µm ± 1.4 µm of individual fibres with a length of 3-8 mm.

Analogously, the transmitted polarisation of a birefringent material can only be distinguished from a weakly diattenuating material (low extinction ratio) by multiple measurements with different incident SoP (or sample rotation) and analysis of the transmitted intensity (I = const. → birefringence, I = sinusiodally variable → weak diattenuation). This highlights the fact that if one wants to characterise the polarisation-dependent properties of a sample fully and unambiguously, then one must analyse the sample's response to different incident SoPs.

In this context, the bi-axicon's probe beam was ideally suited as beam forming optics for polarimetric imaging applications since different SoPs incident on to the sample were easily achieved by lateral scanning of the metasurface relative to sample and analysing optics. The envisioned NDT prototype for polarimetric imaging required hereby a custom-built magnifying objective, see Section 5.3, since most polarisation-dependent material interactions such as micro-crystallinity or fibres with sub-wavelength thickness are observed at the micro-scale close to the employed wavelength.

An established technique to gauge the achievable image resolution was found with the 1951 USAF resolution test chart shown in Figure 5.5. A commercially available USAF target with cut-out lines within a metallic film (Edmund optics) was used for experiments gauging the minimum achievable image resolution R_{min} (in line pair per mm, i.e. 2w/mm) of the optical setup in Section 5.4.4 according to Eq. (5.6) from the group number G and element number E of the smallest resolvable structures.

$$\mathbf{R_{min} = 2^{\left(G+\frac{E-1}{6}\right)}} \qquad \textbf{(5.6)}$$

To test the setup's capabilities for NDT of composite materials, a sample of carbon fibres sandwiched between two 0.5mm thick PTFE slabs was imaged in Section 5.4.5. The average fibre diameter was determined to 5.1 µm $\pm$ 1.4 µm with a fibre length of ca. 3-8 mm using an optical microscopy in Figure 5.5 (d), thereby having a sub-wavelength dimension perpendicular to the fibre axis but not parallel to it, which should induce diattenuation.

5.3 Experimental Setup and Data Analysis

5.3.1 Outline of the Employed Setup and Measurement Methodology

The setup to use the beamforming bi-axicon metasurfaces for NDT and polarimetric imaging is shown in Figure 5.6. A continuous wave (CW) FIRL (FIRL 295, Edinburgh Instruments) delivered a collimated Gaussian beam (1/e diameter ca. 11 mm) of up to 150 mW at 2.52 THz, which was |H⟩ polarised. A non-polarising beam splitter with power meter in its side arm was introduced to account for fluctuations of the output power between different single-shot images ($I_{ref,n}$ in Section 5.3.3). Subsequently, a pair of wire grid polarisers allowed for dynamic attenuation within the measurement arm by adjusting the angle of WGP 1 while leaving WGP 2 fixed to transmit |H⟩. The custom-build -7.7x telecentric objective introduced in Section 5.3.2 was placed behind the sample with a rotatable QWP, a fixed analyser (|V⟩ transmission) and a bandpass filter integrated in its infinity space. The combination of the QWP and fixed polariser allows for measurement of the SoP [179, 468] as described in Section 5.3.3. The bandpass filter is used to increase the SNR at the terahertz camera (INO MicroXCam-384-THz).

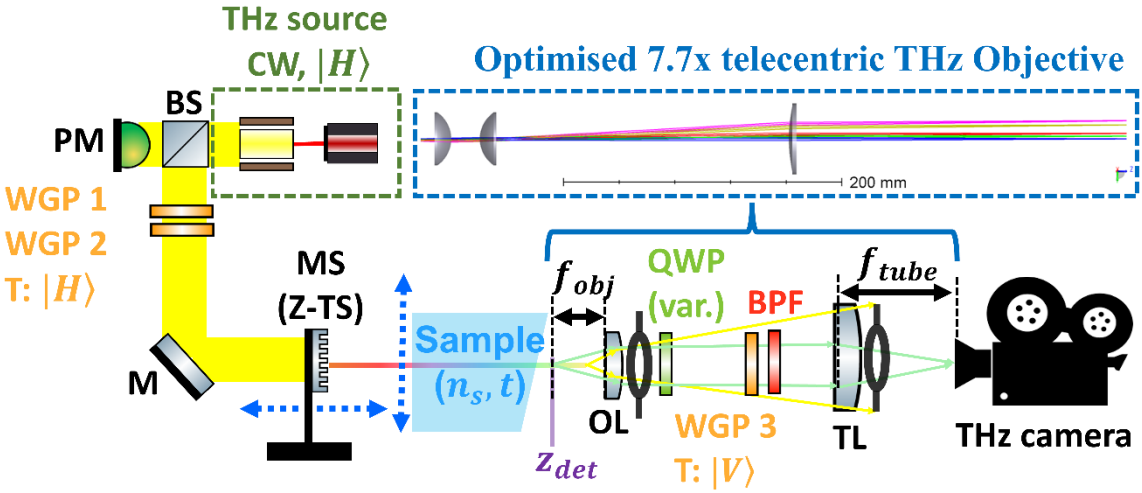

Figure 5.6: Illustration of the setup used for sensing experiments and polarimetric imaging (rotating QWP method, see Section 5.3.3) at 2.52 THz in transmission geometry with an optimised telecentric -7.7x objective (blue box, see Section 5.3.2). BS: non-polarising beam-splitter, PM: power meter, WGP: wire grid polariser, QWP: quarter wave plate, BPF: band pass filter, OL: objective lens, TL: tube lens.

Experiments employing the bi-axicon metasurfaces as beam forming optics used a sequential measurement procedure for the SoP that required only a single rotating QWP followed by a fixed polariser, known as rotating QWP method [179] and detailed in Section 5.3.3. The camera sensor was calibrated and zeroed with blocked beam path before every SoP measurement. Every snapshot image within a SoP measurement was averaged over 60 frames at 50 Hz while the average beam power detected in a reference beam path $I_{ref,n}$ was noted. The QWP was rotated in increments of $\Delta\gamma = 180°/N$ before the next snapshot was taken until all $N = 8$ snapshots had been obtained. Every pixel therefore performed an individual SoP measurement generated from the N constituent intensity measurements with successively increased QWP angle of $\gamma_{n+1} = \gamma_n + \Delta\gamma$ ($\gamma_1 = 0°$).

All 8 snapshot images were imported into a MATLAB script with their respective reference beam powers $I_{ref,n}$. Every individual snapshot n was zeroed columnwise (col) with the minimum raw pixel value $Min\,[I_{raw,n}(col)]$ of each respective column because the employed bolometric sensor showed a column-dependent increase of its dark count over time. Every pixel of a snapshot n was then scaled by a factor accounting for power fluctuation of the reference beam $I_{ref,n}$ relative to the maximum power detected during the SoP measurement $Max[I_{ref,n}]$, as shown in Eq. (5.7).

$$\boldsymbol{I_n(col) = \left(I_{raw,n}(col) - Min\,[I_{raw,n}(col)]\right) \cdot \frac{Max\,[I_{ref,N}]}{I_{ref,n}}} \qquad \textbf{(5.7)}$$

The subsequent polarimetric analysis is presented in Section 5.3.3.

5.3.2 Design of the Custom-built Telecentric Objective

The envisioned imaging system required a magnifying objective to realise sub-mm imaging with good resolution despite the camera's comparably large pixel pitch of 35 µm × 35 µm (INO MicroXcam 384i THz). However, commercially available terahertz objectives are typically targeting wide-angle collection of light on to the camera sensor (M < 1). Furthermore, high prices for commercial objectives render a custom-build magnifying objective from commercial parts viable, especially since further consideration needed to be taken towards integration of the optical components required for polarimetric analysis i.e., QWP, polariser.

In a first step, the requirements for the magnifying objective must be defined. The sensor diagonal of the employed camera is 16.8 mm (384×288 pixel, 4:3 format), or ca. 141 λ_0.

Thus, a magnification of approx. 7.5x would constitute a good trade-off between a high achievable resolution at the image plane and a sufficiently large FOV at the object plane (15 λ_0 × 11.3 λ_0). Furthermore, the absence of perspective parallax error and a constant FOV along the optical axis are highly desirable to limit image distortions, thereby retain uniform structure sizes throughout the image plane and for deviating object distances. At last, the polarisation-analysing components shall be integrated with as little introduced image distortions as possible, with the rotating QWP being of particular concern.

All these conditions can be fulfilled by a telecentric magnifying objective. Telecentricity describes the property of an objective to retain a constant FOV and magnification of $M = f_{tube}/f_{obj}$ both throughout the image plane and for different object/working distances. Furthermore, blurring effects upon defocus are symmetric, allowing for a robust analysis even for slightly defocused images. For example, this means that fibres near the sample surface experience the same magnification as fibres in the sample's bulk, which is a highly desirable property for automated inspection and machine vision. Furthermore, telecentric objectives entail an "infinity space" between objective and tube lens in which ray bundles originating from any point in the object plane propagate as collimated beams. Consequently, optical components introduce minimal image distortions if integrated within this infinity space, making it the ideal location to integrate the required polarisation-analysing components i.e., QWP, WGP, BPF.

The commercial software Zemax OpticStudio was used to design and optimise the outlined -7.7x telecentric objective, see Table 5.1 and Figure 5.7 (a) for the exact design parameter and 3D depiction of the lens arrangement, respectively.

Table 5.1: Input parameter in Zemax OpticStudio for the presented -7.7x telecentric objective. The RI of TPX (ca. 1.46 RIU) at the design wavelength (λ_0 = 118.8µm) was obtained from the lens vendor's webpage (TYDEX) [125].

	Surface Type		Comment	Radius		Thickness		Clear Semi-Dia		Material
0	OBJECT	Standard	Object Plane to ObjLens1 Curved	Infinity		10.000		1.310		
1	(aper)	Standard	ObjLens1: Plano-Curved	Infinity		12.000		19.050	U	TPX_TYDEX_THZ.ZTG
2	(aper)	Standard	ObjLens1 Curved-ObjLens2 Plano	-23.010		20.459		19.050	U	
3	(aper)	Standard	ObjLens2 Curved-Plano	23.010		12.000		19.050	U	TPX_TYDEX_THZ.ZTG
4	(aper)	Standard	ObjLens2 Plano-VarAper	Infinity		8.900		19.050	U	
5	STOP (aper)	Standard	VarAper-TubeLens Curved	Infinity		201.100		1.000	U	
6	(aper)	Standard	TubeLens Curved-to-Plan Surface	111.700		5.500		23.500	U	TPX_TYDEX_THZ.ZTG
7	(aper)	Standard	TubeLens Plan-VarAper	Infinity		0.000		23.500	U	
8	(aper)	Standard	VarAper-Image Plane	Infinity		237.000	V	25.000	U	
9	IMAGE	Standard	Image Sensor	Infinity	C	-		10.080	U	

As objective lens, two plano-convex TPX lenses (TYDEX), each with nominal focal length of 50 mm (40.9 mm simulated at λ_0), were optimised to collimate ray bundles from the object plane (left side) 10 mm in front of the first lens's flat surface. These parallel beams were refocused on to the image plane (right side) by the tube lens - a plano-convex TPX lens (BATOP) with 250 mm nominal focal length (237.7 mm simulated at λ_0).

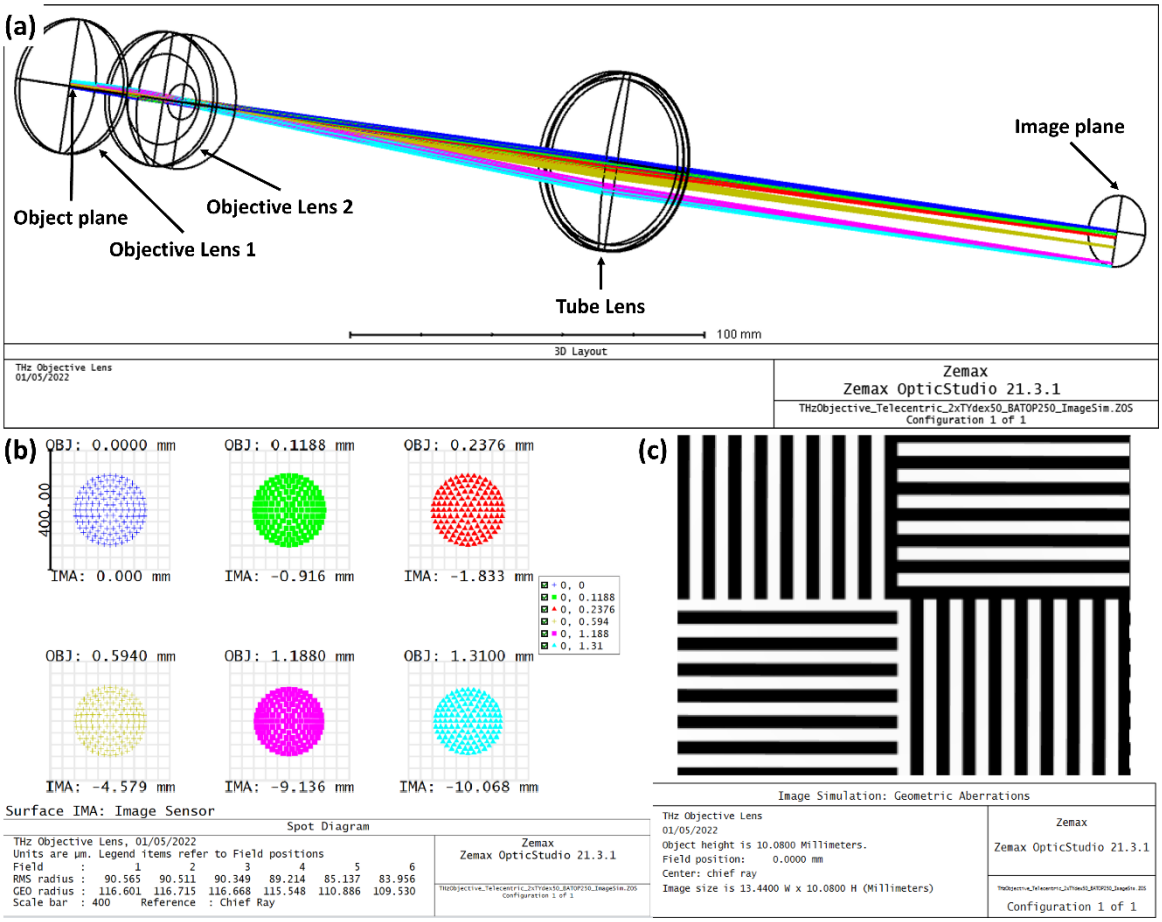

Figure 5.7: Optimised -7.7x telecentric objective employed in the experimental Section 5.4 within the commercial software Zemax OpticStudio (parameters shown in Table 5.1). (a) 3D layout of the optimised magnifying objective employing two plano-convex lenses as objective lens (left) and a tube lens (middle). Ray bundles (coloured lines) originating from different off-axis (y) positions in the object plane (left) are collimated and refocussed on to the image plane (right) with -7.7x magnified spacing. (b) Simulated spot diagrams of these ray bundles show a consistent magnification of the radial offset (IMA/OBJ = -7.7) at the image plane without noticeable distortions. The expected image quality of the "grid of bars" target was (c) simulated at the image plane, showing both high magnification and excellent image quality with no visible distortions (curved lines) or defocus (blurred lines).

Figure 5.7 (b) shows spot diagrams observed at the image plane for six different off-axis (y) positions at the object plane, namely $0 \cdot \lambda_0$, $1 \cdot \lambda_0$, $2 \cdot \lambda_0$, $5 \cdot \lambda_0$, $10 \cdot \lambda_0$ and $11 \cdot \lambda_0$, with the last being the maximum y-displacement that still focussed the centre beam on to the employed image sensor. All six spots retained their circular geometry with evenly spaced rays and RMS spot radius ranging from 90.6 µm to 84.0 µm for increasingly off-axis ray bundles. From the object and image sizes given by the software, the magnification was calculated to -7.7x throughout the entire image plane, which confirmed the required magnification and its uniformity. To better visualise geometric distortions, the "grid of bars" image was simulated after passing through the designed objective, which is shown in Figure 5.7 (c). The results confirm that the designed objective acts as magnifying objective, notably without noticeable image distortion or defocus.

It shall be noted that the presented results do not consider diffractive effects, which are increasingly important as the optics' spatial extend approaches the magnitude of the altered wavelength. While important for low terahertz frequencies, the employed TPX lenses possessed a centre thickness of ca. 101 λ_0 (or 144.4 λ_{TPX}) and 46.3 λ_0 (or 66.2 λ_{TPX}), respectively, thereby rendering them large enough to omit diffractive effects without significant loss of accuracy.

5.3.3 Polarimetric Image Analysis using the Rotating QWP Method

Since the State of polarisation (SoP) is a fundamental property of electromagnetic radiation, there is a rich set of different data acquisition and measurement methodologies established in literature [30, 32, 179, 468]. All of them target the determination of the four Stokes Parameter S_0-S_3 that fully describe the SoP for light propagating in z-direction, with E_{0x}, E_{0y} as maximum amplitudes of the optical field in x- and y-direction and δ the phase shift between them, respectively [179].

$$\boldsymbol{S_0 = {E_{0x}}^2 + {E_{0y}}^2 = \langle I_H \rangle + \langle I_V \rangle = \langle I_D \rangle + \langle I_A \rangle = \langle I_R \rangle + \langle I_L \rangle} \quad \textbf{(5.8)}$$

$$\boldsymbol{S_1 = {E_{0x}}^2 - {E_{0y}}^2 = \langle I_H \rangle - \langle I_V \rangle} \quad \textbf{(5.9)}$$

$$\boldsymbol{S_2 = 2E_{0x}E_{0y}\cos\delta = \langle I_D \rangle - \langle I_A \rangle} \quad \textbf{(5.10)}$$

$$\boldsymbol{S_3 = 2E_{0x}E_{0y}\sin\delta = \langle I_R \rangle - \langle I_L \rangle} \quad \textbf{(5.11)}$$

The right sides of Eq. (5.8) to Eq. (5.11) link the Stokes parameter to observable intensities with $\langle I_i \rangle$ denoting the average intensity over a measurement time much larger than the one optical cycle. The respective subscripts represent the measured SoP, i.e. horizontal H, vertical V, diagonal D, anti-diagonal A, right-circular R and left-circular L [468]. Any complete measurement of the SoP consequently needs to solve the set of equations Eq. (5.8)-(5.11) by acquiring the intensities of at least four differently polarised components of the incoming wavefront – at least three of them must be linearly independent.

$$\boldsymbol{A = \frac{2}{N} \sum_{n=1}^{N=8} I_n} \tag{5.12}$$

$$\boldsymbol{B = \frac{4}{N} \sum_{n=1}^{N=8} I_n \, sin(2\gamma_n)} \tag{5.13}$$

$$\boldsymbol{C = \frac{4}{N} \sum_{n=1}^{N=8} I_n \, cos(4\gamma_n)} \tag{5.14}$$

$$\boldsymbol{D = \frac{4}{N} \sum_{n=1}^{N=8} I_n \, sin(4\gamma_n)} \tag{5.15}$$

The experimentally obtained intensity matrices I_n of Eq. (5.7) were used to determine the A, B, C and D matrices according to Eq. (5.12)-(5.15) [179]. Care had to be taken to calculate the partially polarised Stokes parameter S_0^* to S_3^* since the fixed polariser transmitted $|\mathrm{V}\rangle$ polarised light as opposed to the $|\mathrm{H}\rangle$ described in [179]. To correct for the polariser's 90º "misalignment", an additional $sgn(-)$ had to be inserted in Eq. (5.17), Eq. (5.18) and Eq. (5.19), as described by Eq. (7) of Flueraru et al. [469].

$$\boldsymbol{S_0^* = A - C} \tag{5.16}$$

$$\boldsymbol{S_1^* = -(2C)} \tag{5.17}$$

$$\boldsymbol{S_2^* = -(2D)} \tag{5.18}$$

$$\boldsymbol{S_3^* = -(B)} \tag{5.19}$$

After calculating the degree of polarisation (DOP) in Eq. (5.20), the fully polarised Stokes Parameter S_0 to S_3 (normalised by S_0) can be calculated in Eq. (5.21) to Eq. (5.24). In turn,

the characteristic angles of the PE can be calculated by Eq. (5.25) and Eq. (5.26), namely the orientation angle ψ and ellipticity angle χ, respectively.

$$\boldsymbol{DOP = \frac{\sqrt{S_1^{*\,2} + S_2^{*\,2} + S_3^{*\,2}}}{S_0^*}} \tag{5.20}$$

$$\boldsymbol{S_0 = \frac{S_0^*}{DOP} - \frac{(1 - DOP)}{DOP}} \tag{5.21}$$

$$\boldsymbol{S_1 = \frac{S_1^*}{DOP \cdot S_0}} \tag{5.22}$$

$$\boldsymbol{S_2 = \frac{S_2^*}{DOP \cdot S_0}} \tag{5.23}$$

$$\boldsymbol{S_3 = \frac{S_3^*}{DOP \cdot S_0}} \tag{5.24}$$

$$\boldsymbol{\Psi = \frac{1}{2} arctan\left(\frac{S_2}{S_1}\right) \quad (0 < \Psi \leq \pi)} \tag{5.25}$$

$$\boldsymbol{\chi = \frac{1}{2} arctan\left(\frac{S_3}{\sqrt{S_1^{\,2} + S_2^{\,2}}}\right) \quad \left(-\frac{\pi}{4} < \Psi \leq \frac{\pi}{4}\right)} \tag{5.26}$$

The resulting image matrices of Eq. (5.20) to Eq. (5.26) were consequently smoothened with a 3-by-3 median filter using the MATLAB function " medfilt2(Data,[3 3]) ".

5.3.4 Pseudo-Colour Images Depicting Polarimetric Information

Analysing the experimental image data for its Stokes parameter inevitably splits up the measured intensity contrast into different polarimetric contrast channel, especially if the incident probe beam shows a variable SoP as in the present case. For example, certain horizontal and vertical features may be clearly visible in the spatial $S_1(x, y)$ profile yet remain hidden in the $S_2(x, y)$ or $S_3(x, y)$ profiles. Furthermore, quantitative information on highly polarised image regions is lost for all parameter except $DOP(x, y)$, which describes the relative fraction of polarised radiation with respect to all detected intensity. Consequently, it would be of great benefit to merge and depict the entire information on both SoP and DOP within a single image with smooth transitions between adjacent states that shall be simple to interpret.

The perception of colour is hereby an inherently intuitive and powerful tool to merge several greyscale parameters into a single pseudo-colour image. The three parameters identified to convey polarimetric information are introduced below:

1. **The degree of polarisation $\boldsymbol{DOP}(\boldsymbol{x},\boldsymbol{y})$**, describing the detected fraction of polarised light relative to all detected light within the linear interval [0; 1], describing areas of highly polarised optical fields.
2. **The orientation angle $\boldsymbol{\Psi}(\boldsymbol{x},\boldsymbol{y})$ of the PE** within the periodic interval (-90º; 90º], describing the spatial orientation of the ellipse's strongest linearly polarised component (major axis).
3. **The ellipticity angle $\boldsymbol{\chi}(\boldsymbol{x},\boldsymbol{y})$ of the PE** within the linear interval [-45º; 45º], describing the ratio between major and minor axis of the PE, describing areas with circularly polarised components (+/- defines handedness)

The subsequent task was to find a tri-parametric colour space that was compatible with the structure of this greyscale data i.e., periodic interval for Ψ, linear intervals for both χ and DOP. The CIE's cylindric L^*C^*h colour space, which is derived from the CIE-$L^*a^*b^*$ colours by simple coordinate transformation, appears ideally suited for this task [470]:

a. The CIE-L^*C^*h colour space is based on relative prevalence of complementary colours, e.g., red vs. green, blue vs. yellow, white vs. black. This parametric structure fits perfectly to the Poincare sphere, which is based on relative prevalence of orthogonal SoPs, e.g., |H⟩ vs. |V⟩, |D⟩ vs. |A⟩, |R⟩ vs. |L⟩, respectively. In turn, the colour parameter hue h is periodic within (-180º; 180º] while Luminance L^* and chroma C^* are both defined within a linear interval of [0 ; 100], thereby perfectly matching to the polarisation parameters Ψ, χ and DOP, respectively.
b. The definition of CIE-L^*C^*h takes account to human vision to achieve near perpendicular dimensions throughout the colour space [470]. The result is perceptual uniformity, meaning that Euclidean distances between two arbitrary colour coordinates corresponding to their perceived colour difference within the entire colour space [207, 470]. This is an important property for the pseudo-colour images as it translates into a direct correlation between perceived colour change and measured SoP change throughout the entire Poincare sphere, making SoP changes intuitively quantifiable.

The spherical polarisation space with azimuth angle of (-2Ψ), latitude angle of $(2\chi + \pi/2)$ and radius of $(3/2\,\mathrm{DOP})$ was consequently linked to the cylindric $\mathrm{L^*C^*h}$ colour space (luminance, chroma, hue) according to Eq. (5.27), Eq. (5.28) and Eq. (5.29):

$$L^* = \left[-\left(\frac{3}{2}\cdot DOP\right)\cdot sin(2\chi)+1\right]\cdot 50 \quad (5.27)$$

$$C^* = \left|\left(\frac{3}{2}\cdot DOP\right)\cdot cos(2\chi)\right|\cdot 100 \quad (5.28)$$

$$h = -2\Psi \quad (5.29)$$

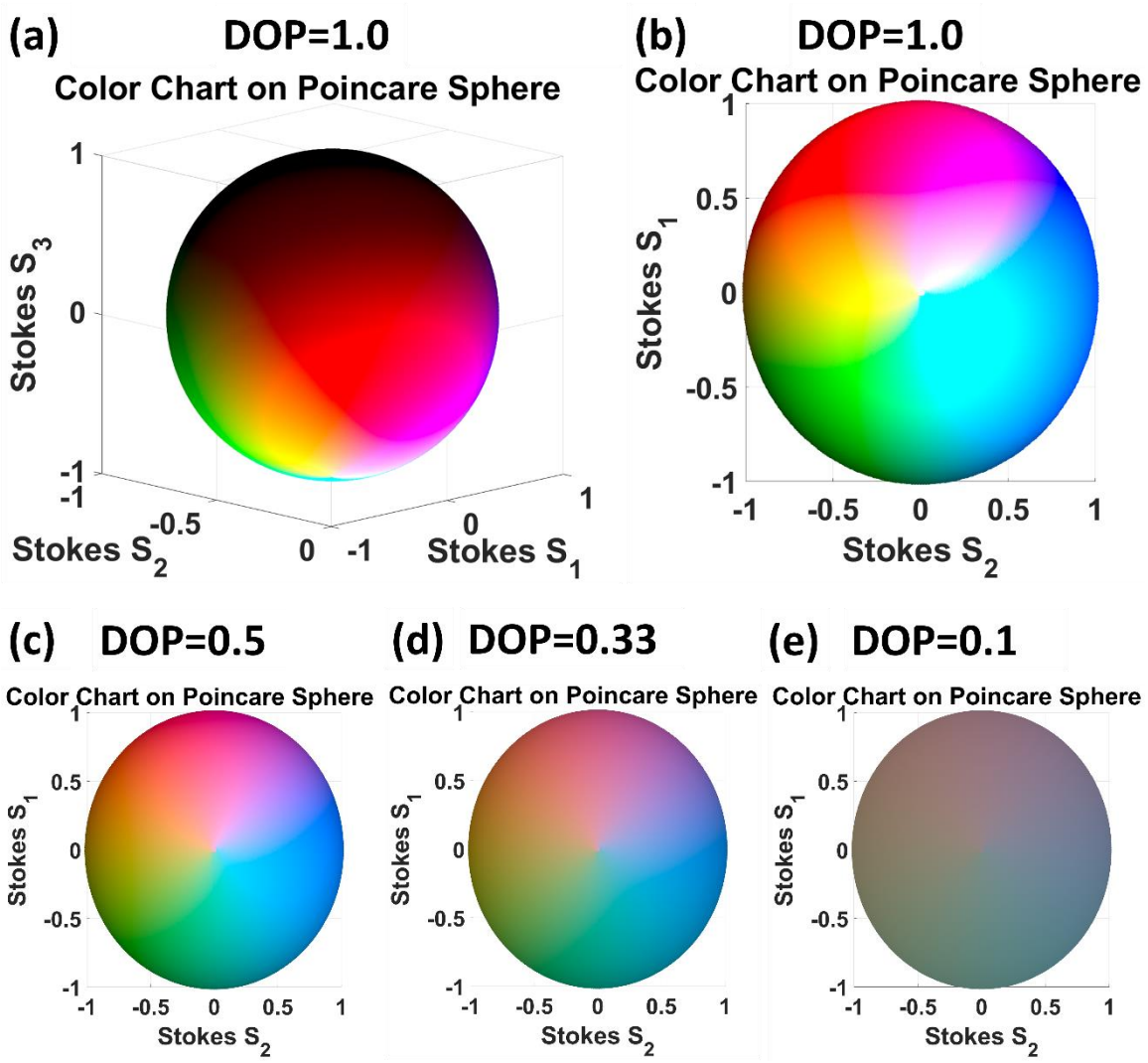

Figure 5.8: (a) 3D depiction of the pseudo-colour chart on the Poincare sphere and (b) a view of the southern hemisphere (prevalent $|L\rangle$ component, $S_3 \leq 0$) showing the equatorial S_1-S_2-plane (outermost circle). The colours at each point on the Poincare sphere were defined by their respective coordinate in the cylindric CIE-L^*C^*h colour space. The effect of decreasing DOP on the respectively encoded colours is shown for (a)-(b) 100 %, (c) 50 %, (d) 33 % and (e) 10 % polarised light. This clearly demonstrates that areas of low DOP will entail an increasing grey component in the final pseudo-colour images, whereas areas of highly polarised light will show pure colours with strong chroma.

Once the pseudo-colour images had been generated, they were converted into Cartesian CIE-$L^*a^*b^*$ colour space and RBG images for easier handling in subsequent software. The colour-encoded Poincare sphere shown in Figure 5.8 (a), (b) was obtained with this methodology for $\mathrm{DOP} = 1$, and respective results for diverse values of the DOP in (c)-(d). The azimuth angle on the Poincare sphere (-2ψ) is depicted as a colour's hue h. Viewing the respective S_1-S_2 plane from the southern side ($\mathrm{S}_3 \leq 0$) in Figure 5.8 (b)-(e) one can clearly identify the changing colour hue around the equator (outermost circle) with $|\mathrm{H}\rangle$ light ($\mathrm{S}_1 = 1$) appearing as magenta, $|\mathrm{V}\rangle$ ($\mathrm{S}_1 = -1$) as green, $|\mathrm{D}\rangle$ ($\mathrm{S}_2 = 1$) as blue and $|\mathrm{A}\rangle$ ($\mathrm{S}_2 = -1$) as yellow. The luminance L^* of a colour is connected to the latitude angle $(2\chi + \pi/2)$ on the Poincare sphere, resulting in increasingly bright colours in Figure 5.8 (a) from $|\mathrm{R}\rangle$ ($\mathrm{S}_3 = 1$, black) to $|\mathrm{L}\rangle$ ($\mathrm{S}_3 = -1$, white). Finally, chroma C^* is linked to the degree of polarisation since both describe the purity of a colour or detected SoP, respectively. The prefactor 3/2 was chosen to ensure colour purity ($\mathrm{C}^* \geq 100$) for highly polarised pixel with a DOP larger than 66.6 %, whereas areas with lower DOP values show an increasing grey component ($\mathrm{C}^* < 100$). The presented pseudo-colour encoded Poincare sphere can be regarded as "polarisation look-up table/illustration" to convert the depicted colours of the polarimetric images presented in Sections 5.4.4 and 5.4.5 into Stokes parameter of the SoP.

5.4 Experimental Results

5.4.1 Beam Calibration Measurements

Using the setup, the measurement methodology and data analysis presented in Section 5.3, a calibration scan of the metasurface's transverse and axial beam profiles was undertaken for two different metasurface designs:

I. A short-range (SR) design optimised for sensing applications with short oscillation length, hence high sensitivity to the RI of introduced samples:
OPB of $|\mathrm{L}\rangle/|\mathrm{R}\rangle$, $\mathrm{g}_1/\mathrm{g}_2 = 0.72\ \mathrm{mm}/0.39\ \mathrm{mm}$, α_1/α_2 = 9.5º/17.8º,
$\mathrm{z}_{\mathrm{max},1}/\mathrm{z}_{\mathrm{max},2}$ = 65.8 mm/34.2 mm, $\mathrm{w}_1/\mathrm{w}_2$ = 0.28 mm/0.15 mm, Λ_{theo} = 3.45 mm.

II. A long range (LR) design optimised for polarimetric imaging applications requiring a large illuminating central lobe and both longer range and oscillation period:
OPB of $|\mathrm{L}\rangle/|\mathrm{R}\rangle$, $\mathrm{g}_1/\mathrm{g}_2 = 2.4\ \mathrm{mm}/1.22\ \mathrm{mm}$, α_1/α_2 = 2.8º/5.6º,
$\mathrm{z}_{\mathrm{max},1}/\mathrm{z}_{\mathrm{max},2}$ = 221.9 mm/112.4 mm, $\mathrm{w}_1/\mathrm{w}_2$ = 0.92 mm/0.47 mm, Λ_{theo} = 33.7 mm.

Figure 5.9 (a) shows the experimentally obtained transverse intensity profile at a single axial scan position for the SR design and (b)-(e) its polarimetric analysis results including (f) their combined pseudo-colour depiction. The single raw intensity image exhibited a clear central lobe - the theoretical extends w_1, w_2 of which are shown as black dotted circles - with a faint surrounding structure of equidistant concentric rings typical for Bessel beams. The Stokes S_0 parameter obtained from Eq. (5.16) showed a similar result to the raw image albeit with a clearer distinction between the brighter inner central lobe of diameter w_2 (red) and the larger outer central lobe of diameter w_1 (green) that were in good agreement with their theoretical extent. The profile of the DOP confirmed that this beam centre and ring structure were highly polarised compared to the background. Looking at the characteristic angles of the PE's Ψ and χ in (d) and (e), respectively, the beam centre appears uniformly polarised with both angles close to 0º ($|H\rangle$). The ring structure of these Bessel beams alternates between $|V\rangle$ ($\Psi = \pm 90º$) polarised rings that corresponded to intensity minima and $|H\rangle$ polarised rings that corresponded to intensity maxima, each separated by thinner rings of highly circular polarisation ($|\chi| > 0º$) of alternating handedness in-between intensity minima and maxima and vice versa. This polarisation profile of the transverse plane was as expected for two superimposed circularly polarised Bessel beams of differing diffraction angles. Finally, the polarimetric information could be combined in the pseudo-colour image of Figure 5.9 (f) to show a compressed yet intuitive picture of the transverse polarisation profile.

The same analysis of the transverse plane was repeated in Figure 5.10 for the LR design that was used for imaging experiments. The previous observations remain true, but both central lobe diameters (black dotted circles) were significantly larger with a linearly polarised centre of Ψ_{max} = - 28.6º and surrounding rings of Ψ_{min} = 61.4º (orthogonal) polarisation.

We can hence conclude that the transverse beam and polarisation profile was well-understood and in line with the theoretical design. Hence, the central lobe polarisation was averaged at several axial beam positions to observe the on-axis SoP profile in Figure 5.11.

The orientation $\Psi(z_i)$ and ellipticity $\chi(z_i)$ angles at each axial position z_i of the metasurface that are shown as datapoints in Figure 5.11 were obtained by circular averaging measured pixel values within a circular aperture at the beam centre with diameter of (a)-(c) 0.18 mm for the SR design (1.23 w_2) and (d)-(f) 0.36 mm (1.29 w_2) for the LR design. For both metasurfaces, the experimentally observed on-axis progression of (a), (d) $\Psi(z_i)$ and (b), (e) $\chi(z_i)$ were in excellent agreement with the theoretical model introduced in Section 5.2.

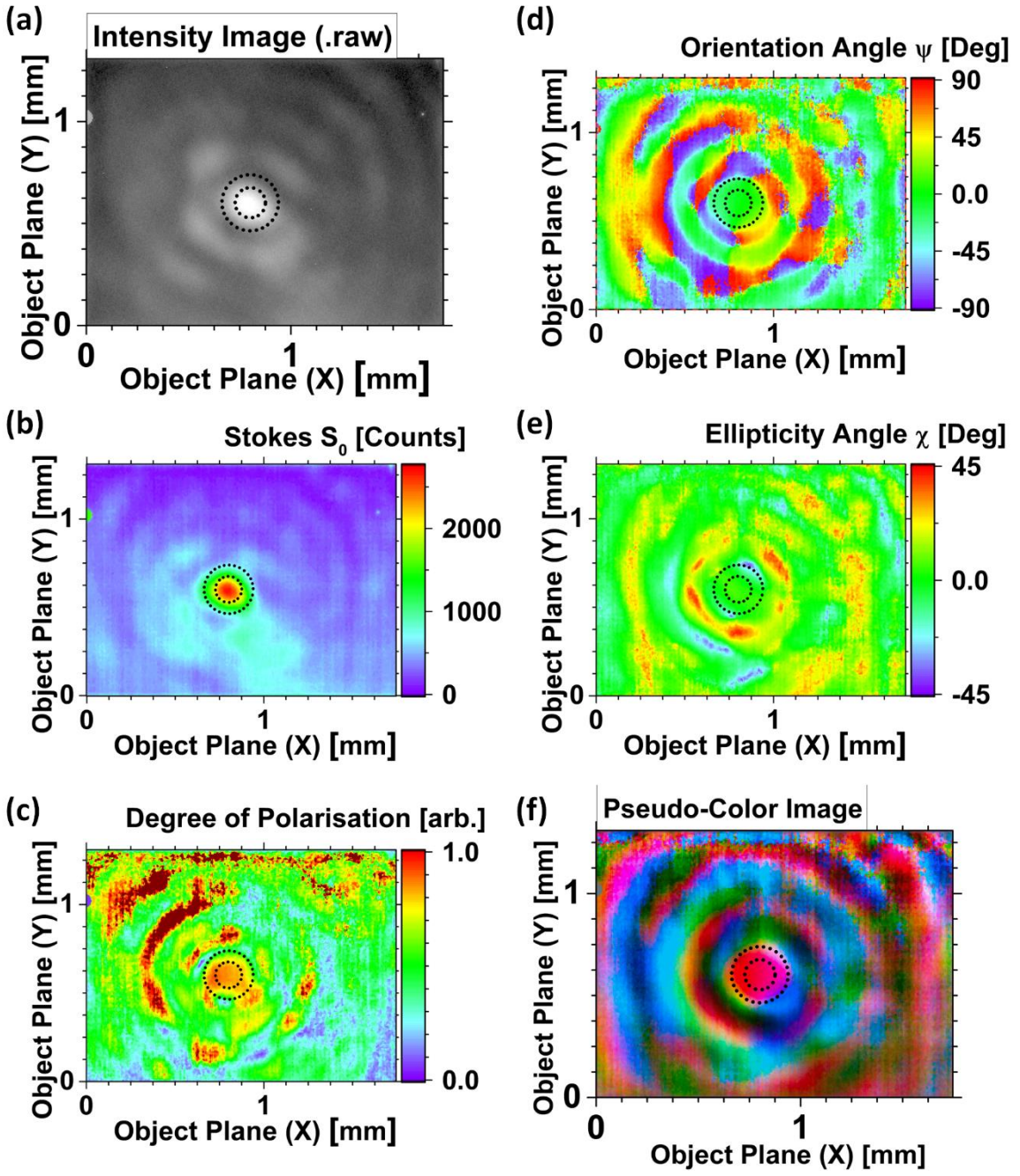

Figure 5.9: Transverse beam profile calibration of the "short range design" bi-axicon metasurface employed for sensing applications in Sections 5.4.2 and 5.4.3. The theoretical central lobe diameters w_1 and w_2 of each individual Bessel beam B_1 and B_2 obtained with Eq. (2.19) are shown in each image as black dotted circles with diameter of 0.28 mm and 0.15 mm, respectively. (a) Single intensity image as taken with the setup of Figure 5.6. Polarimetric analysis according to Section 5.3.3 resulted in the spatial profiles of (b) the Stokes S_0 parameter, (c) degree of polarisation, (d) the orientation angle Ψ and (e) ellipticity angle χ of the PE. Their combination in a pseudo-colour image shown in (f) was achieved as described in Section 5.3.4.

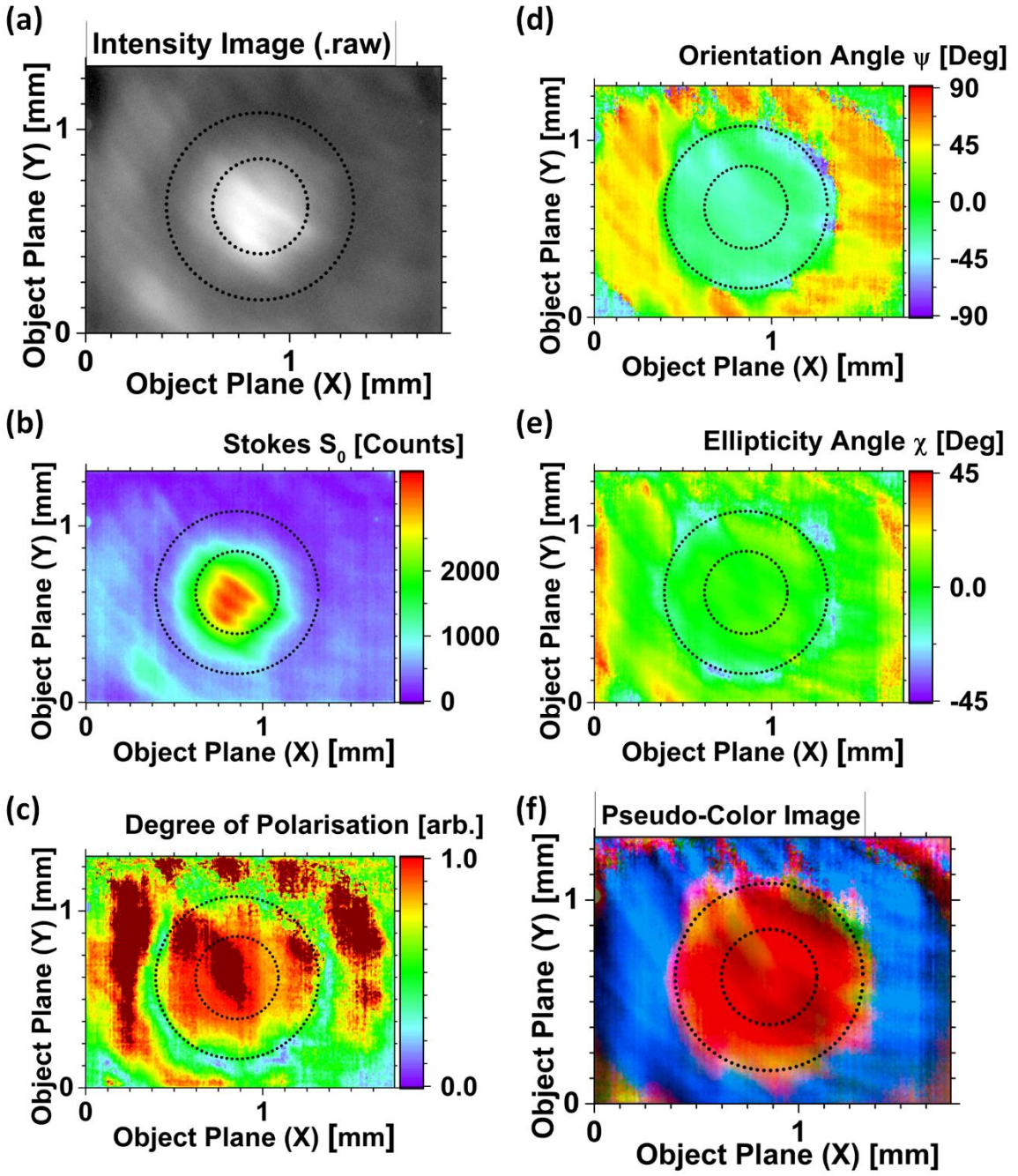

Figure 5.10: Transverse beam profile calibration of the "long range design" bi-axicon metasurface employed for imaging applications in Sections 5.4.4 and 5.4.5. The theoretical central lobe diameters w_1 and w_2 of each individual Bessel beam B_1 and B_2 obtained with Eq. (2.19) are shown in each image as black dotted circles with diameter of 0.92 mm and 0.47 mm, respectively. (a) Single intensity image as taken with the setup of Figure 5.6. Polarimetric analysis according to Section 5.3.3 resulted in the spatial profiles of (b) the Stokes S_0 parameter, (c) degree of polarisation, (d) the orientation angle Ψ and (e) ellipticity angle χ of the PE. Their combination in a pseudo-colour image shown in (f) was achieved as described in Section 5.3.4.

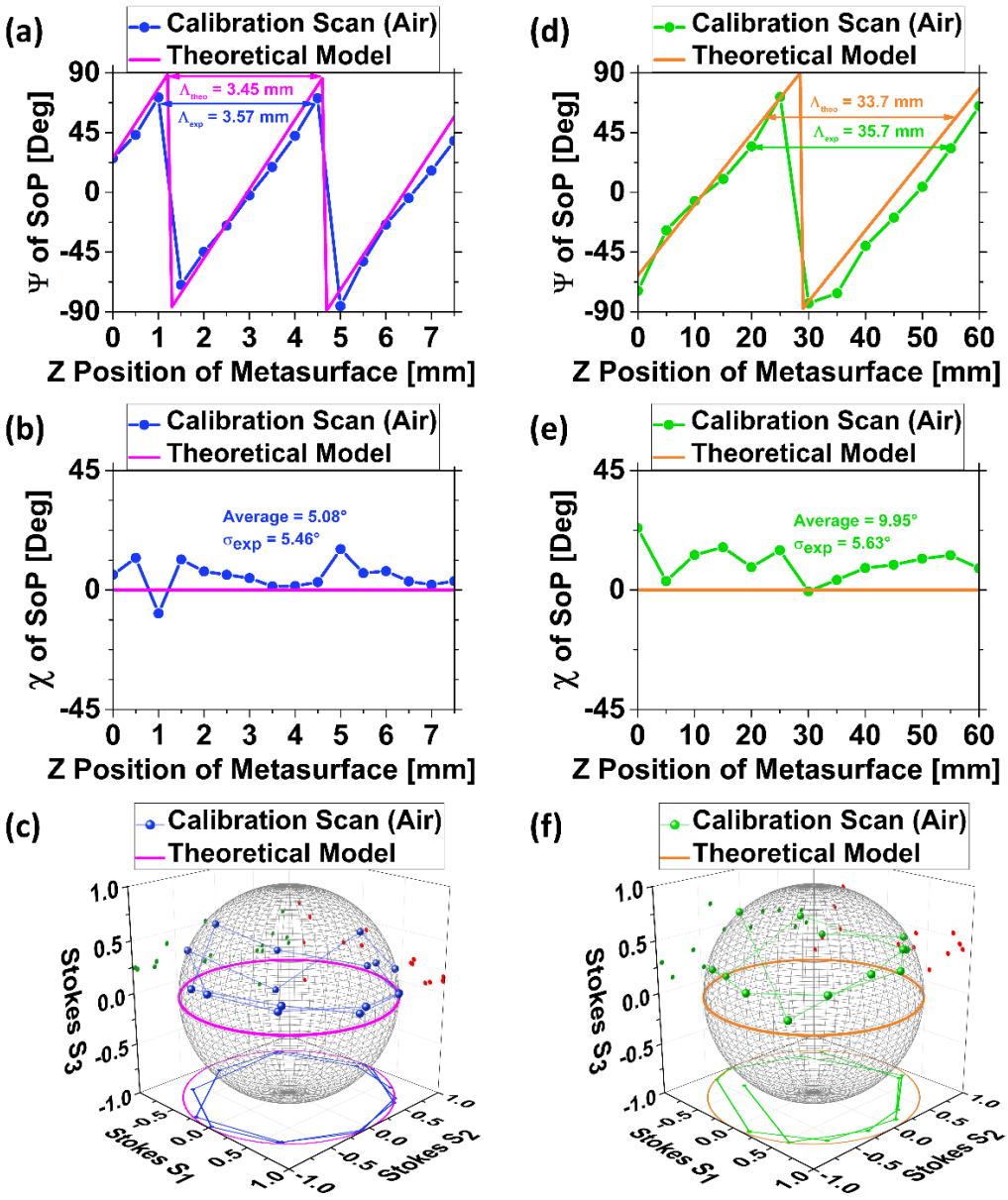

Figure 5.11: Experimentally obtained longitudinal beam calibration of the on-axis SoP along the central lobe for (left) the SR metasurface design and (right) the LR metasurface design. (a) The on-axis orientation angle $\Psi(z_i)$ exhibited the expected linear change with a experimentally observed periodicity Λ_{exp} of 3.45 mm, very close to the 3.57 mm predicted by the theoretical model of Eq. (5.3), whereas the (b) ellipticity angle $\chi(z_i)$ remained close to 0°. (c) The axial SoP change represented a circular path along the equator on the Poincare sphere. The LR design exhibited similar behaviour with (d) a longer oscillation period of 35.7 mm (theory: 33.7 mm). Again, the (e) ellipticity angle remained close to 0° while (f) the path on the Poincare sphere was described by an equatorial oscillation. Each datapoint was obtained by circular averaging of pixel values within a circular aperture at the beam centre with 40 pixels (0.18 mm) diameter for the SR design and 80 pixel (0.36 mm) for the LR design.

Depicted on the Poincare sphere in Figure 5.11 (c), (f), this axial change of the central lobe polarisation represented a circular path along the equator with an experimentally observed oscillation periodicity Λ_{exp} of 3.45 mm for the SR design and 35.7 mm for the LR design, very close to the predicted values of 3.57 mm and 33.7 mm using the analytical model.
We hence conclude that the presented probe beams were operating according to their intended function and were accurately described by the analytical model introduced in Section 5.2. Their axial polarisation profile was now calibrated for respective applications in sensing and imaging.

5.4.2 Sensing of Diattenuating Properties

In a first sensing experiment, a randomly oriented wire grid polariser (Ψ_{theo} = 25º) was introduced into the beam path of the SR bi-axicon's probe beam and compared to the calibration data of Figure 5.9 and Figure 5.11 (a)-(c).
Figure 5.12 (a)-(d) shows the transverse S_0 profile (polarised intensity) for (a), (b) the calibration without polariser and (c), (d) measurements with inserted polariser at axial positions that are polarised (a), (c) along the extinction or (b), (d) along the transmission axis of the inserted polariser.
As expected, the polarised intensity S_0 of the central lobe without polariser (calibration) remained more or less constant at both scan positions but a stark difference was observed after the polariser was inserted, with the beam centre polarised along the extinction axis in Figure 5.12 (c) completely absent yet nearly undisturbed along the transmission axis in (d) due to the polariser's diattenuation.
Examining the on-axis characteristic angles in (e) and (f), it is clear that the axial polarisation change observed in the calibration (blue datapoints) changed to a constant polarisation (red datapoints) that accurately described the polariser's transmission axis to 26.7º$\pm$4.1º compared to the know value of 25º ($\pm$5º). The centre beam ellipticity in Figure 5.12 (d) remained low with only minor non-systematic deviations from the calibration, thereby confirming reliable measurement quality as discussed in Section 5.2.1.
The on-axis polarisation oscillation with constant intensity of the calibration measurement was hence transformed by the polariser's diattenuation into a constant on-axis polarisation with sinusoidally oscillating intensity. This experiment hence demonstrated the ability of the presented setup to probe the diattenuating behaviour of samples introduced into the beam path, such as conductive fibres or wires.

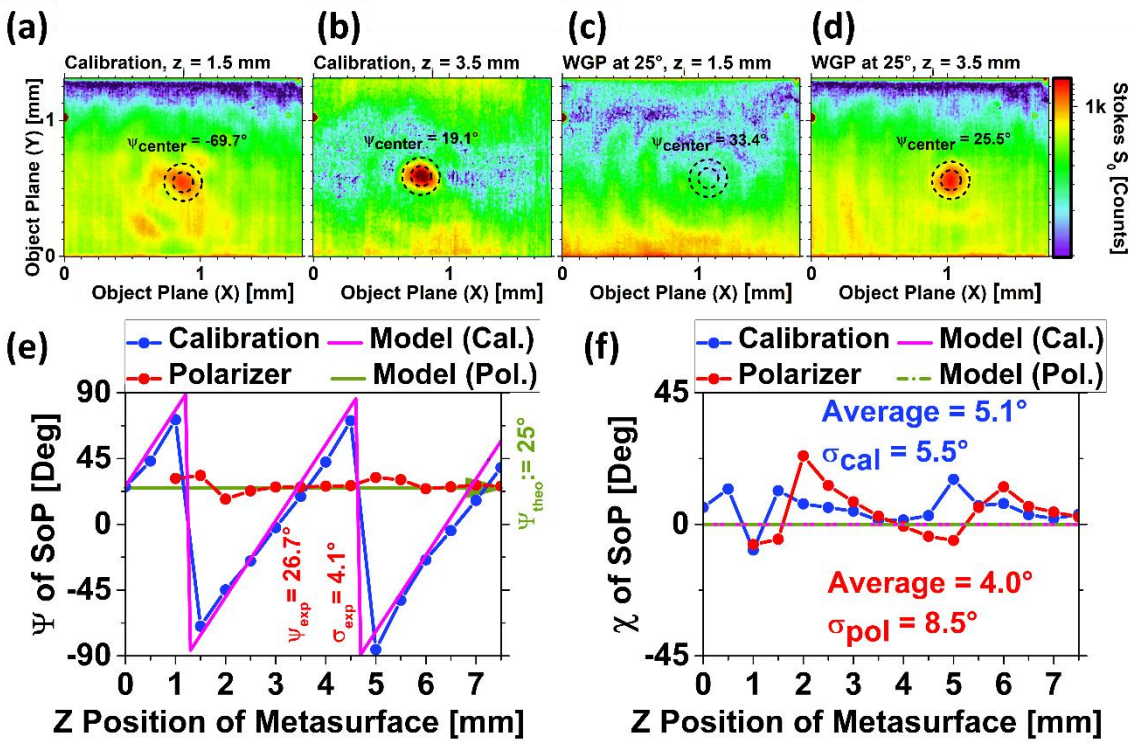

Figure 5.12: Effect of introducing a diattenuating medium (polariser with transmission axis at 25° ± 5°) into the bi-axicon's beam path. The theoretical central lobe diameters w_1 and w_2 obtained with Eq. (2.19) are shown in (a)-(d) as black dotted circles with diameter of 0.28 mm and 0.15 mm, respectively. The transverse polarised intensity (S_0) profile is shown for (a), (b) the calibration without inserted polariser at axial positions corresponding to the polariser's extinction and transmission axis, respectively, and (c), (d) again after inserting the polariser. The on-axis characteristic angles (e) $\Psi(z_i)$ and (f) $\chi(z_i)$ show that the axial polarisation oscillation of the calibration is transformed into a constant polarisation with sinusoidal intensity oscillation along the propagation direction due to the polariser's diattenuating behaviour.

5.4.3 Sensing of the Refractive Index

The setup's capability to measure the RI of a homogeneous sample of known thickness was experimentally confirmed with a 5.65 mm thick HDPE slab introduced into the beam path of the SR design calibrated in Figure 5.9 and Figure 5.11 (a)-(c).

The analytical model of Eq. (5.4) and Eq. (5.5), which was verified with large active area FDTD simulations in Section 5.2.2, was inverted to generate the coloured background in Figure 5.13 (a) that encoded the measured RI. Required input parameter for this were the

measured sample thickness and the Ψ-ordinate obtained from a linear fit though the unwrapped/linearised datapoints of the calibration scan (blue datapoints).

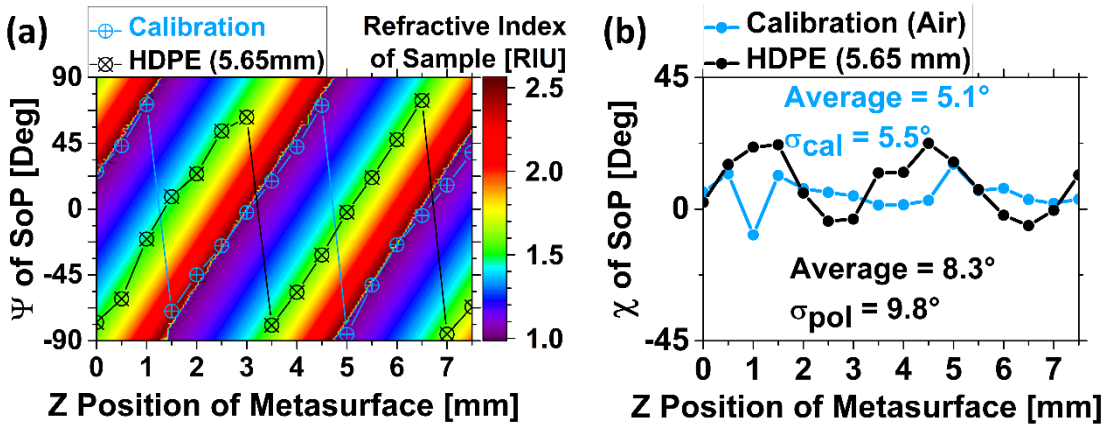

Figure 5.13: (a) RI measurement of a 5.65 mm thick HDPE sample inside the beam path (black data points) exploiting the measured orientation angle Ψ and its sample-induced shift ΔΨ = 76.9° ± 5.5° compared to the calibration (blue data points) as measurement channel. Using the analytical model of model of Eq. (5.4) and Eq. (5.5), shown as coloured background, the RI can be measured to 1.56 RIU ± 0.06 RIU, very close to its literature value of n_{Lit} = 1.58 RIU [29] at 2.52 THz. (b) The respective axial ellipticity angle χ(z_i) showed no significant or systematic deviation between both measurements.

One can clearly see that the measurement including the HDPE sample (black datapoints) exhibited a shifted orientation angle ΔΨ that was constant at 76.9°±5.5° compared to the calibration for each axial position of the metasurface, as expected from model and simulations. Relating this shift to the underlying RI (colour) resulted in a measured RI of 1.56 RIU ± 0.06 RIU averaged over all datapoints, which is in excellent agreement with the literature value for HDPE of 1.58 RIU at 2.52 THz [29].

The centre beam ellipticity in Figure 5.13 (b) remained low with only minor, non-systematic deviations from the calibration measurements, thereby confirming reliable measurement quality as discussed in Section 5.2.1.

We hence demonstrated the successful, accurate, repeatable and robust measurement of a sample's RI using the developed bi-axicon as a probe beam within a polarimetric microscope operating at 2.52 THz.

5.4.4 Polarimetric Image Resolution Gauged with the 1951 USAF Target

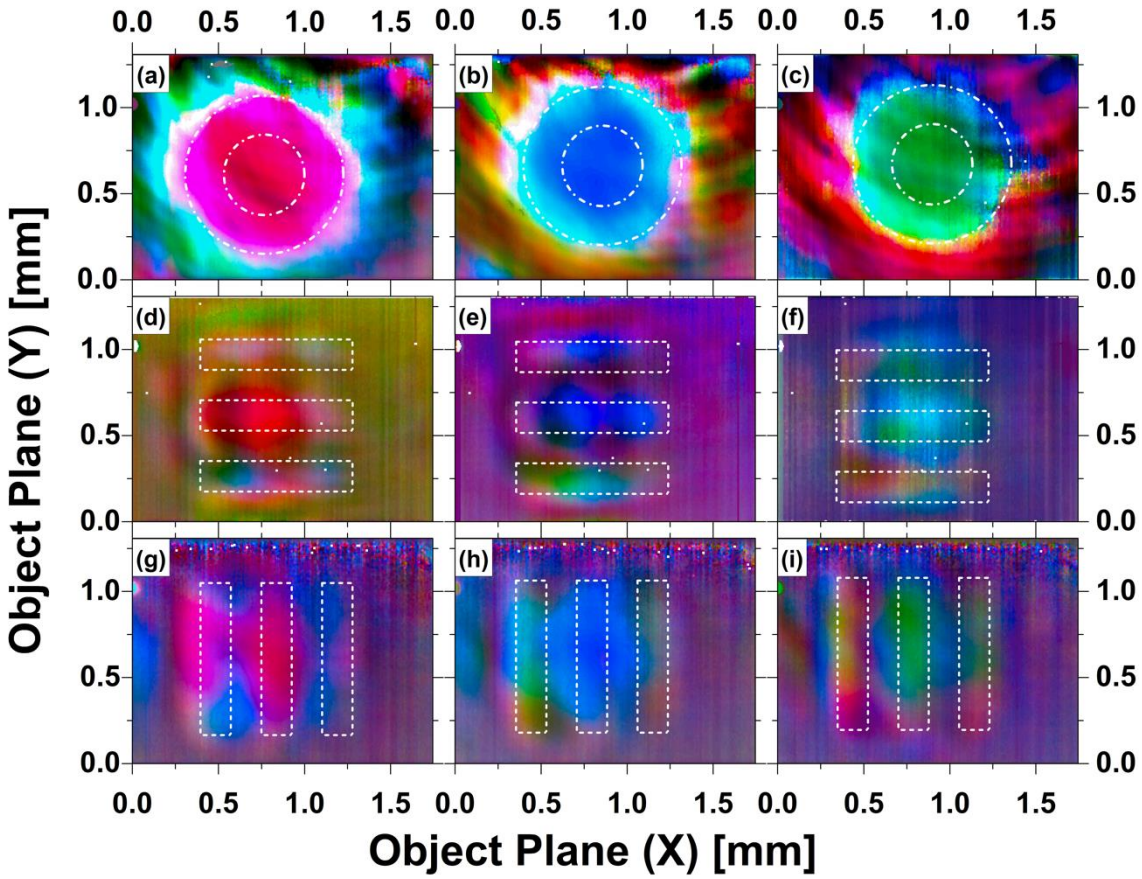

Figure 5.14: Imaging results showing the pseudo-colour encoded SoP at three different scan positions (columns), corresponding to a (from left to right) $|H\rangle$, $|D\rangle$ and $|V\rangle$ polarised beam centre. (a), (b) and (c) show the transverse beam profiles without sample (calibration) with the two white dash-dotted circles representing the beam's expected central lobes spanned by $w_{|L\rangle}$ and $w_{|R\rangle}$, see Eq. (2.19). *(d), (e), (f) show the respective result of introducing the USAF 1951 resolution target (group 1, element 4) of Figure 5.5 with three horizontally aligned lines (white dotted rectangles) that transmit light in contrast to their opaque surrounding. (g), (h), (i) show the results of the same target with the three vertically aligned lines (white dotted rectangles). The resolvable line width L is 176.78 µm (1.49 λ_0).*

For imaging experiments, it is desirable to evenly illuminate a larger sample area corresponding to larger central lobe diameters $w_{1,2}$. Consequently, the LR design introduced in Figure 5.10 with increased central lobe diameters $w_{|L\rangle}$ and $w_{|R\rangle}$ of 0.919 mm and 0.467 mm ($g_{|L\rangle}$ and $g_{|R\rangle}$ of 2.4 mm and 1.22 mm), respectively, was employed in the

subsequent imaging experiments. After the initial calibration scan without imaging target shown in Figure 5.11 (d), (e), (f), three axial positions (60 mm, 68.75 mm and 77.5 mm before the objective) of the metasurface corresponding to the central lobe polarisations |H⟩, |D⟩, |V⟩ were selected. The transverse beam profiles for these three axial positions are shown as pseudo-colour images in Figure 5.14 (a), (b), (c), respectively, with the two white circular dash-dotted lines in each image indicating the theoretic extend of the central lobes spanned by the diameters $w_{|L\rangle}$ and $w_{|R\rangle}$ determined with Eq. (2.19). For the colour map that aids to convert the depicted pseudo-colours into the Stokes polarisation parameter, the author refers to Figure 5.8. The beam's centre (dash-dotted white circles with $w_{1,2}$) retained its size, alignment and colour uniformity (representing the SoP uniformity) throughout the three scan positions, with changing hue (representing Ψ) between them.

The entire transverse beam profile was blocked by the USAF 1951 imaging target (see Figure 5.5) introduced at the object plane of the magnifying objective – except for the set of three cut-out lines that are represented (to scale) by the three white dashed rectangles in Figure 5.14 (d)-(i). As shown in Figure 5.14 (d), (e), (f) and (g), (h), (i), the three horizontal and vertical lines of group 1 element 4, respectively, can be identified for all three central lobe SoPs, corresponding to a remarkable resolvable line width *L*of 176.78 µm, or 1.49 λ_0. We can hence conclude that the developed polarimetric imaging microscope operates as intended with an accurately predicted magnification and beam centre size, a good polarimetric image contrast shown in pseudo-colour as well as a high spatial resolution of at least 1.49 λ, close to the diffraction limit (0.5 λ.).These results might well constitute the best image resolution thus far demonstrated at 2.52 THz.

5.4.5 Polarimetric Imaging of Carbon Fibres in Polymer Matrix

To assess the imaging performance for NDT, a composite sample consisting of randomly oriented carbon fibres (average diameter of 5.1 µm $\pm$ 1.4 µm, length of 3-8 mm) sandwiched between two thin PTFE discs (0.5 mm thick) that was previously shown in Figure 5.5 (c) and (d), was investigated with the same three incident beam polarisations in Figure 5.15. Compared to the respective calibration images in Figure 5.15 (a)-(c), the corresponding images using the PTFE composite sample clearly show the colour contrast of a vertically oriented fibre (white dotted rectangle as guide for the eye) in the beam centre of Figure 5.15 (e) for |D⟩ illumination and Figure 5.15 (f) for |V⟩ illumination, but not in Figure 5.15

(d) for |H⟩ illumination. This observation can be explained by the carbon fibre's linear diattenuation, stemming from its electric conductivity and anisotropic shape with subwavelength diameter. A vertically oriented fibre will reflect |V⟩ and transmit |H⟩ light therefore it will only create polarimetric image contrast if the incident SoP possesses a component of |V⟩ light. The carbon fibre therefore remains hidden in Figure 5.15 (d) since all incident |H⟩ light is transmitted without interaction with the fibre.

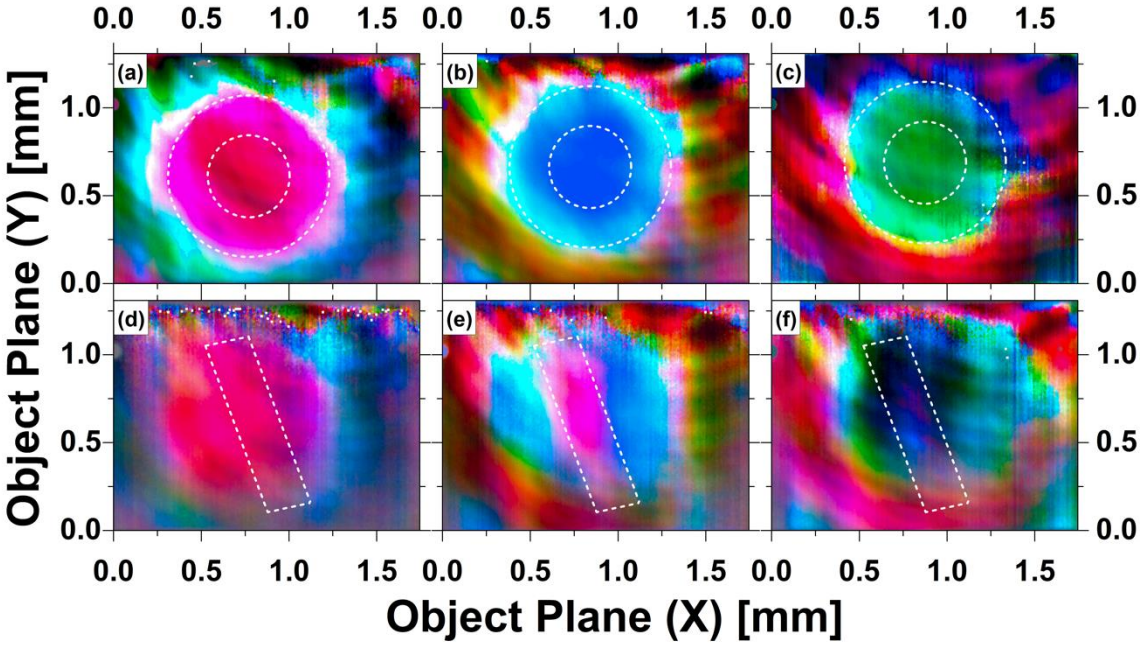

Figure 5.15: Imaging results showing the pseudo-colour encoded SoP at three different scan positions (columns) corresponding to (from left to right) |H⟩, |D⟩ and |V⟩ beam centres. (a), (b) and (c) show the respective beam profiles without sample (calibration). (d), (e), (f) The images produced with carbon fibres sandwiched between two PTFE slabs (0.5 mm). The polarisation contrast of the fibre (white dashed rectangle as guide for the eye) is evident for incident SoPs comprising a partial |V⟩ component owing to the fibre's diattenuation and orientation.

This result highlights the importance of both illuminating an unknown sample with several different polarisations, as well as polarimetric image analysis, validating the imaging approach chosen in this work. Although further work and optimisations are admittedly required for an industrially viable application in NDT imaging, these results nevertheless successfully outlined and demonstrated the capability to detect and quantify polarisation-dependent effects with high accuracy and resolution at terahertz frequencies by utilising

ultra-compact and efficient beam forming metasurface optic, hence substantiating the approach chosen within this work.

5.5 Conclusion and Future Work

This chapter demonstrated the capability of the presented metasurface optics to integrate complex beam forming capabilities into a single, ultra-compact and highly efficient optical layer to control both the transmitted phase front and polarisation front.

The generated probe beam consisted of two independently controlled and orthogonally polarised Bessel beams that caused a well-defined on-axis oscillation of the SoP. A simple set of design parameter – namely the two orthogonal grating periods $g_1$and g_2 and their respective OPB - was shown to control the important beam characteristics, such as focal length, central lobe diameter, the period of axial polarisation oscillation and its path along the Poincare sphere. An analytical model was developed to describe the physics behind the on-axis change of the SoP as function of these design parameter, which accurately described observed results of both numerical large active area simulations and experimental results.

The obtained probe beam was found to be robust against longitudinal and transverse misalignments, with previously reported self-healing capabilities after encountering an obstruction [358]. In particular, probe beams with circularly polarised OPB were found to exhibit an exceptionally robust and accurate axial correlation between the PE's orientation angle and the axial coordinate $\Psi \propto z_i$, which rendered Ψ ideally suited as accurate measurement channel. This was due to the special circumstance that deviations caused by transverse misalignment or intensity imbalances were exclusively concentrated in the axial relation of the ellipticity angle $\chi \propto z_i$, which was hence ideally suited to assess the image quality and setup alignment. This division between accurate measurement channel and tainted quality channel helped to achieve the remarkably accurate sensing results and aided the optimisation of the optical assembly later.

The probe beam's prospects in sensing applications were briefly outlined and experimentally confirmed by accurately determining the diattenuation and RI of respective samples introduced into the beam path of the experimental setup. This was achieved by designing an elaborate imaging setup that involved a custom-build telecentric objective which incorporated polarimetric capabilities via the rotating QWP method [179].

For polarimetric imaging, a pseudo-colour encoding routine was developed to intuitively depict the multi-dimensional SoP within a single image. An experimental image resolution of at least 1.49 λ_0 was demonstrated using the 1951 USAF target. Carbon fibres in a polymer matrix were then imaged at different incident SoPs to showcase the fibres diattenuating nature and the setup's capabilities for polarimetric microscopy of composite materials, thereby demonstrating the first setup towards an important industrial application.

Future work might extend investigations on the probe beam's ideal parametric design for RI measurements with high accuracy and/or dynamic range, or the theoretical description and experimental characterisation of a sample's birefringence. Extending the design to involve the more complex frozen wave method [33, 471, 472] would improve the control over the on-axis intensity profile of the probe beams and hence their uniformity. Further investigations to simultaneously characterise the fibre orientation and RI/thickness of the polymer matrix would underline the setup's value for NDT imaging.

While the presented experiments aimed to explore the absolute resolution limit of the developed technique, future work on polarimetric imaging will require larger FOV, either via point-by-point transverse scanning of the sample relative to the beam, or by interchangeable objectives with lower magnification. Such techniques to measure a 2D map of the sample's birefringence, diattenuation or RI would be invaluable for the characterisation of micro-crystallinity, micro-fibres or inclusions within the polymer.

Significant limiting factors for the image quality and resolution observed upon experiments were a small degree of beam wander upon rotation of the QWP, as well as fluctuations of the beam power encountered upon polarimetric image acquisition. To address these issues, a compact polarimeter that is capable of fast measurements of the entire polarimetric information within a single image while avoiding moving parts (except for the probe beam) would be of great benefit to simplify polarimetric measurements and improve the obtained polarimetric accuracy. Consequently, such a division-of aperture polarimeter (DoAP) that was integrated into a single metasurface layer was designed and tested in Chapter 6.

Chapter 6 : Polarimetry with a Beam analysing Metasurface

6.1 Motivation

The state of polarisation (SoP) is a fundamental property of electromagnetic radiation that can carry a rich set of important information imprinted in the light transmitted through a test sample, as has been shown in the previous Chapter 5. There are a wide range of polarisation-dependent material interactions (circular or linear) and polarising effects that can be observed including diattenuation [473], birefringence [181] and Brewster's law [189] to name a few. The ability to measure the SoP accurately and quickly is hence of significance to a wide range of applications in material characterisation such as ellipsometry [474], polarimetric imaging [32, 475, 476] and NDT [32, 474]. The technological significance of polarimetry is on par with spectroscopy and uncovers an independent dimension to carry information within light, e.g. for polarisation division multiplexing in wireless communication [477].

Despite the multitude of potential applications, the SoP remains difficult to exploit in practice since its measurement typically requires complex apparatus with multiple moving parts. Polarisation analysing instruments aim to determine the four Stokes parameter and require the quantitative measurement of at least four different SoPs that ideally form a tetrahedron within the Poincare sphere (octahedron for six measurements) [32]. Traditional instruments based on classical components perform these measurements either sequentially (division of time) e.g., via the rotating QWP method described in Section 5.3.3, or in parallel e.g., using a division of aperture polarimeter (DoAP) [473]. Each method has drawbacks since sequential measurements are time-consuming and prone to errors arising from fluctuations between individual measurements, while in parallel setups are typically complex, less efficient and more expensive [473].

Metasurface-based polarimeters (MSP) have considerable potential to overcome the mentioned drawbacks associated with the DoAP design while achieving ultra-fast measurements of the SoP in a single image. Thus, MSPs have recently been studied extensively to obtain improved performance, extreme compactness and straightforward integrability at the system-level [30, 32, 177, 222, 223, 284, 475, 478-480]. Some advanced designs demonstrated polarimetric imaging capabilities that allowed for video-rate polarimetric inspection and characterisation of large sample areas [32, 475].

This chapter presents work on the design of a metasurface polarimeter (MSP) that incorporated the entire functionality of a division-of-aperture-polarimeter (DoAP) with high efficiency into a single silicon layer without the need for moving parts. Section 6.2 will describe the design underlying the presented MSP based on three interlaced lattices and its inherent capabilities. Section 6.3.1 describes the experimental setup and measurement methodology employed for all polarisation measurements presented in this chapter. An automated calibration process and polarimetric analysis algorithm is described in Section 6.3.2, which was found to add considerable robustness to systematic error sources in practice. Section 6.4.1 presents experimentally obtained qualitative results of the six calibration measurements, which show perfect agreement with both respective collective simulations and the intended operation. The quantitative determination of the SoP from a single experimentally obtained image is shown in Section 6.4.2 for 64 individual measurements of 14 different SoPs, with an average experimental accuracy of 92.1 % $\pm$ 4.2 % that is on par with published results at 800 nm [479] and 1550 nm [284]. Extended collective simulations presented in Section 6.4.3 reveal prospects of our metasurface design for broadband operation and the measurement of partially polarised light. Section 6.5 will conclude this chapter and outline future avenues to employ the presented metasurface for spectral polarimetry and polarimetric imaging.

6.2 Interlaced Metasurface Design

The design of the MSP developed in this work divided the hexagonal arrangement of pillars into three hexagonal sub-lattices with individual (next-) nearest neighbour distance D_1 of 69.3 µm, known as interleaved spatial multiplexing [481, 482]. The pillars of each sub-lattice shown in Figure 6.1 (a) encoded a pair of independent phase functions on orthogonal SoPs as described in Section 3.3, namely linearly horizontal |H⟩ and vertical |V⟩ polarised (yellow square), linearly diagonal |D⟩ and anti-diagonal |A⟩ polarised (green triangle), and right |R⟩ and left |L⟩ circularly polarised (red circle). Phase functions of spherical off-axis lenses $\varphi_{1-6}(x,y)$ with the focal length f were chosen for these six SoPs, see Eq. (6.1).

$$\boldsymbol{\varphi_{1-6}(x,y) = \frac{2\pi}{\lambda_0}\left(f - \sqrt{[f^2 + (x - x_0)^2 + (y - y_0)^2]}\right)} \qquad \textbf{(6.1)}$$

Each of these six phase functions φ_{1-6} generated one of six differently polarised focal points observed at different off-axis positions in the focal plane. The individual off-axis

displacements $\Delta_{xy} = |(x_0, y_0)|$ were chosen to arrange the six focal points at the vertices of a regular hexagon around the optical axis to ensure equal amounts of aberrations for every focal point, with a spacing that spanned the camera's sensor area as shown in Figure 6.1 (b). The fabricated metasurface showed no significant fabrication defects, see Figure 6.1 (c).

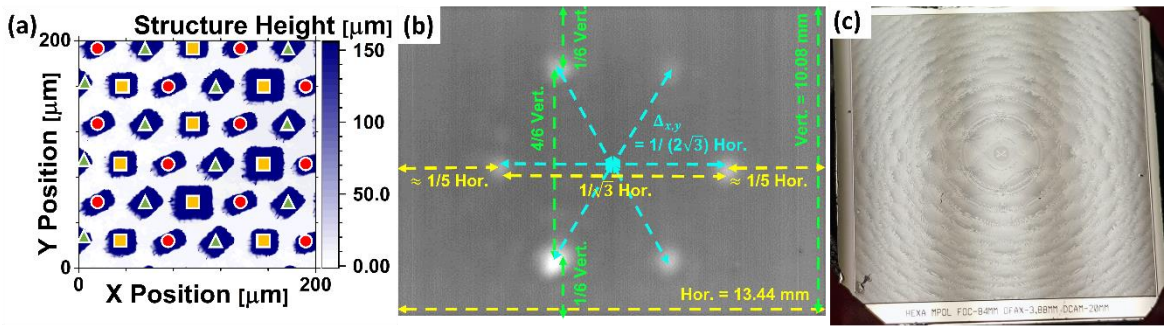

Figure 6.1: (a) The zoomed-in surface profile of the fabricated metasurface (pillar's top surface in blue, etch floor in white) obtained by WLI showing the three hexagonal sub-lattices (coloured symbols). (b) The off-axis displacements Δ_{xy} were optimised to arrange all six focal points along the vertices of a regular hexagon (cyan arrows) that spanned the camera's sensor area, as indicated by the green and yellow dimensions. (c) Optical image of the fabricated metasurface used to obtain the experimental results of this Chapter 6. The pattern was essentially free of defects - apart from dust particles that deposited after the fabrication was already completed and minor tweezer damage in the bottom left corner.

6.3 Experimental Setup and Data Analysis

6.3.1 Optical Setup and Measurement Methodology

The experimental setup for both the calibration and polarisation measurements is depicted in Figure 6.2. The terahertz source (FIRL 295, Edinburgh Instruments) delivered a collimated $|H\rangle$ polarised Gaussian CW beam (1/e diameter ca. 11 mm) of up to 150 mW at 2.52 THz. A combination of non-polarising beam splitter and power meter created a reference arm to monitor power fluctuations via $I_{ref,k}$ [223]. However, these fluctuations only had to be considered during the calibration process and not in subsequent SoP measurements since each image was self-referenced, which highlights a key advantage of this measurement method compared to the previously employed rotating QWP method described in Section 5.3.3. In the measurement arm, an initial pair of polarisers allowed for

dynamic adjustments of the beam intensity with WGP 1 while WGP 2 transmitted |H⟩ polarised light. The arbitrary polarisation generator (APG) consisted of a HWP (angle α) followed by a linear polariser (angle 2α) and QWP (angle β). The collimated beam incident on the MSP was split up into the hexagonal set of focal points 82 mm behind the MSP and imaged by the terahertz camera (INO MicroXCam-384-THz). Spatially resolved polarimetric images can be obtained in principle by placing the image sensor outside the focal plane – or by integration of the MSP into a magnifying objective as described in [32] - but this was beyond the scope of this work.

The experimental results presented in this chapter were obtained within a single measurement series. The camera sensor was initially calibrated and zeroed with blocked beam path before the first image was recorded. Every image thereafter was averaged over 60 frames at 50 Hz (1.2 s integration time) while the average beam power detected in the reference beam path $I_{ref,k}$ was noted. The first image was taken for $\alpha = 0°, \beta = 0°$, after which images with incrementally increasing QWP angle β in steps of 22.5° were obtained until the image for $\beta_{max} = 157.5°$ was recorded. Next, the HWP angle α was increased by 22.5° and the next set of 8 images were taken with β increasing again incrementally from 0° to 157.5° until all 64 images were recorded ($\alpha_{max} = 157.5°, \beta_{max} = 157.5°$).

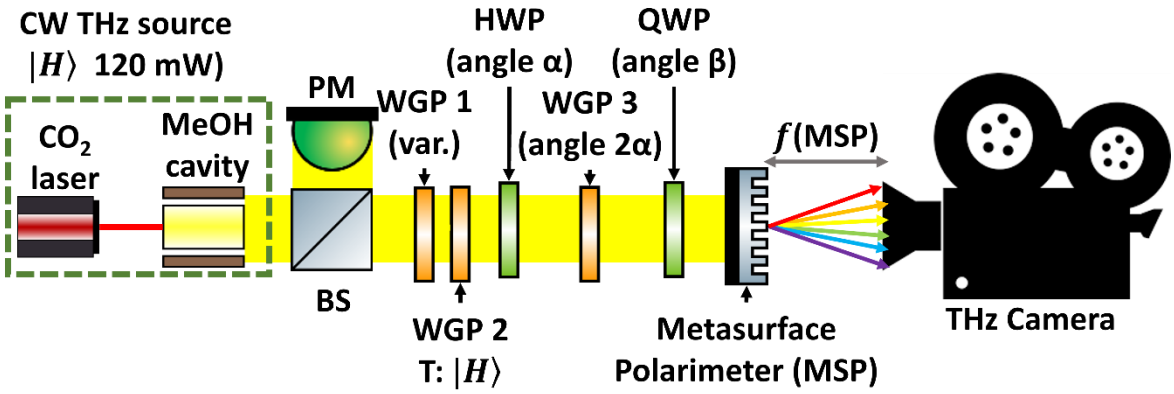

Figure 6.2: Schematic of the setup employed for the calibration and SoP measurements. BS: non-polarising beam splitter, PM: power meter, WGP: (linear) wire grid polariser, HWP/QWP: Half/Quarter wave plate.

6.3.2 Calibration Process and Polarimetric Analysis

The theoretically expected Stokes vector $\vec{S}_t$ of each image was calculated with Eq. (6.2) using the Mueller Matrices M_i of each optical element i shown in Figure 6.2 with their respective orientation angles α, β and the Stokes vector $\vec{S}_{in} = (1 \quad 1 \quad 0 \quad 0)^T$ for the incident $|H\rangle$ polarised light. The Mueller matrix of a linear polariser is given by Eq. (6.3), whereas linear retarders are described by Eq. (6.4) (QWP for $\Delta=\pi/2$, HWP for $\Delta=\pi$) both with a generic orientation angle γ [483].

$$\vec{S}_t = M_{QWP}(\beta) \cdot M_{LP}(2\alpha) \cdot M_{HWP}(\alpha) \cdot \vec{S}_{in} \tag{6.2}$$

$$M_{LP}(\gamma) = \frac{1}{2}\begin{pmatrix} 1 & \cos 2\gamma & \sin 2\gamma & 0 \\ \cos 2\gamma & \cos^2 2\gamma & \sin 2\gamma \cos 2\gamma & 0 \\ \sin 2\gamma & \sin 2\gamma \cos 2\gamma & \sin^2 2\gamma & 0 \\ 0 & 0 & 0 & 0 \end{pmatrix} \tag{6.3}$$

$$M_{Ret}(\gamma) = \frac{1}{2}\begin{pmatrix} 1 & 0 & 0 & 0 \\ 0 & \cos^2 2\gamma + \cos\Delta \sin^2 2\gamma & (1-\cos\Delta)\sin 2\gamma \cos 2\gamma & \sin\Delta \cos 2\gamma \\ 0 & (1-\cos\Delta)\sin 2\gamma \cos 2\gamma & \sin^2 2\gamma + \cos\Delta \cos^2 2\gamma & -\sin\Delta \cos 2\gamma \\ 0 & -\sin\Delta \sin 2\gamma & \sin\Delta \cos 2\gamma & \cos\Delta \end{pmatrix} \tag{6.4}$$

Table 6.1: Summary of the six degenerate SoP measurements selected for the calibration of the MSP, including their Stokes vectors $\vec{S}_t$, HWP/QWP angles α / β and reference intensity $I_{ref,n}$. The intensity distribution at their focal plane is shown in Figure 6.5.

SoP	Theoretical Stokes vector $\vec{S}_t$	HWP angle α [°]	QWP angle β [°]	$I_{ref,n}$ [mW]
$\|H\rangle$	$(1 \quad 1 \quad 0 \quad 0)^T$	90	90	7.8
$\|V\rangle$	$(1 \quad -1 \quad 0 \quad 0)^T$	135	90	7.8
$\|D\rangle$	$(1 \quad 0 \quad 1 \quad 0)^T$	112.5	135	8.2
$\|A\rangle$	$(1 \quad 0 \quad -1 \quad 0)^T$	157.5	135	7.6
$\|R\rangle$	$(1 \quad 0 \quad 0 \quad 1)^T$	157.5	90	8.0
$\|L\rangle$	$(1 \quad 0 \quad 0 \quad -1)^T$	157.5	0	7.4

Calibration measurements including an automated analysis script were necessary to calibrate the entire setup prior to measurements of arbitrary SoPs [223, 284, 484]. This calibration required six images with incident light of the six degenerate SoPs, which were deliberately

selected from the 2nd half of the recorded measurement series to include the effect of a spatially uneven increase of the dark count throughout the calibration process. This deviation was presumably caused by a combination of thermal heating upon prolonged operation and an unideal gain correction table of the camera, which further highlights the robustness of the chosen calibration method to systematic sources of errors. Table 6.1 summarises the calibration measurements with their respective SoPs and Stokes vectors. The flowchart of the algorithms used to calibrate the setup and perform polarimetric measurements from a single image are summarised in Figure 6.3 (a) and (b), respectively.

For each (calibration) image k, the script zeroed the measured intensity column wise (col) with the minimum raw pixel value $Min\ [I_{raw,k}(col)]$ of each respective column because the employed bolometric sensor showed a column-dependent increase of its dark count over time. Every pixel of an calibration image k was then scaled by a factor accounting for power fluctuation of the reference beam $I_{ref,k}$ relative to the maximum power detected during all calibration images $Max[I_{ref,K}]$, as shown in Eq. (6.5).

$$\boldsymbol{I_k = \left(I_{raw,\mathbf{k}}(col) - Min\ [I_{raw,\mathbf{k}}(col)]\right) \cdot \frac{Max\ [I_{ref,\mathbf{K}}]}{I_{ref,\mathbf{k}}}} \qquad \textbf{(6.5)}$$

For each (calibration) image k, the script then located the peak positions of each focal point l and performed an individual background correction with subsequent 2D Gaussian fit to quantify the integrated intensities $I(k,l)$ of each respective focal point. The background correction was performed by subtracting the averaged value of pixels that formed a circular path (R = 25pixel) around the peak position. These integrated intensities were arranged within a 6×6 intensity matrix I_C in Eq.(6.6), while the respective theoretically expected Stokes vectors $\vec{S}_t(k)$ of each image's incident SoP formed the columns of the 4×6 Stokes Matrix S_C, see Eq. (6.7). Finally, the 6×4 calibration matrix C was generated in Eq. (6.8) with the pseudo-inverse of S_C.

$$\boldsymbol{I_C = \begin{bmatrix} I(1,1) & \dots & I(6,1) \\ \vdots & I(k,l) & \vdots \\ I(1,6) & \dots & I(6,6) \end{bmatrix}} \qquad \textbf{(6.6)}$$

$$\boldsymbol{S_C = \begin{bmatrix} \vec{S}_t(\mathbf{k}=1) & \dots & \vec{S}_t(\mathbf{k}=6) \end{bmatrix}} \qquad \textbf{(6.7)}$$

$$\boldsymbol{C = I_C \cdot pinv(S_C)} \qquad \textbf{(6.8)}$$

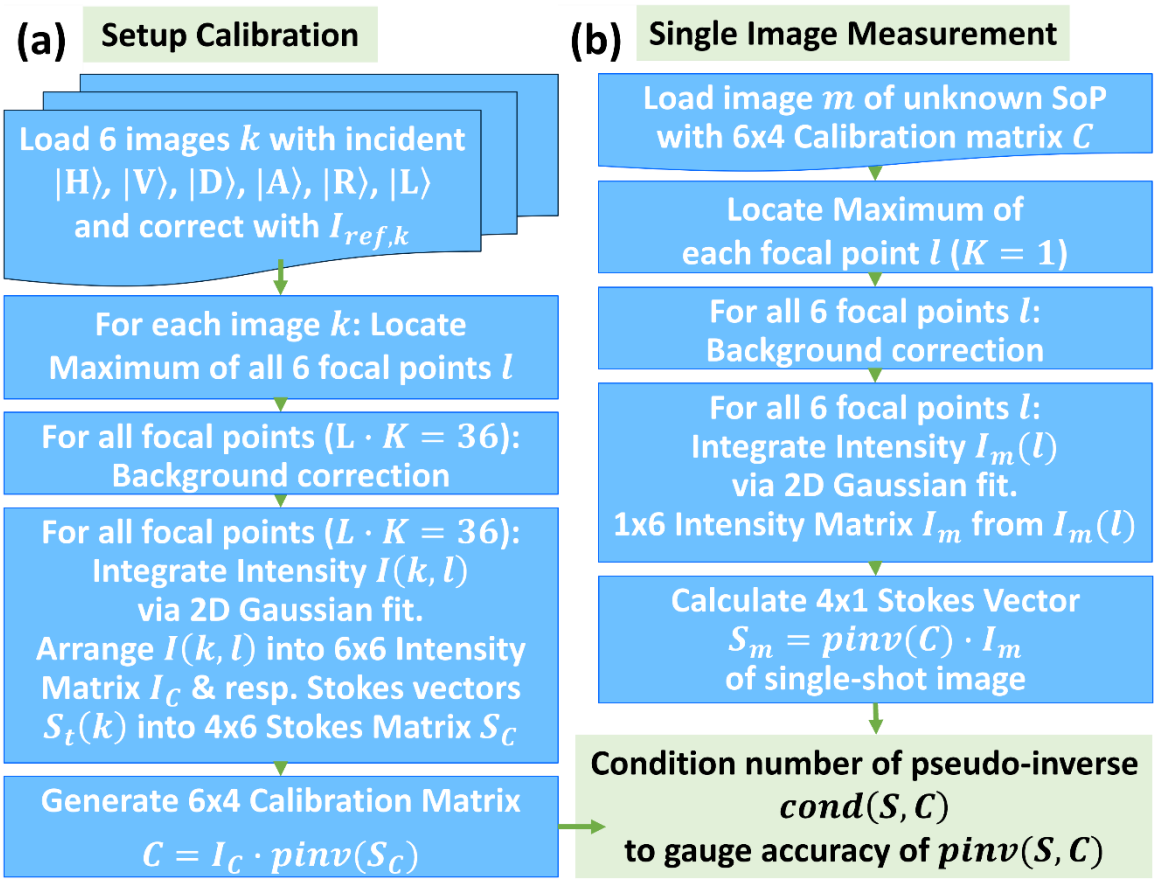

Figure 6.3: Flow-chart of the algorithms to (a) calculate the calibration matrix C from six calibration measurements of degenerate SoPs and (b) determine the Stokes vector S_m of an arbitrary incident SoP from a single image.

Once the calibration matrix was obtained, individual SoP measurements were analysed by obtaining the 1×6 intensity vector I_m of an individual image of unknown SoP as described above (for K = 1). The SoP was subsequently identified via its 4×1 Stokes vector $\vec{S}_m$ calculated according to Eq. (6.9) using the pseudo-inverse of the calibration matrix.

$$\vec{S}_m = pinv(C) \cdot I_m \tag{6.9}$$

Within the grayscale range of the camera's sensor, each pixel's recorded signal should respond to thermal heating with the same linear relation that is also observed for a respectively increased influx of terahertz radiation due to the underlying bolometric detection. As such, the effects of heating and an uneven gain correction table should be accounted for by the calibration method of the MSP. Nevertheless, a recalibration before every new set of measurements or upon every restart of the setups is advisable.

6.4 Collective Simulations and Experimental Results

6.4.1 Calibration Measurements compared to Collective Simulations

The six degenerate SoPs incident on the MSP that were required for the calibration process were chosen as summarised in the previously shown Table 6.1.

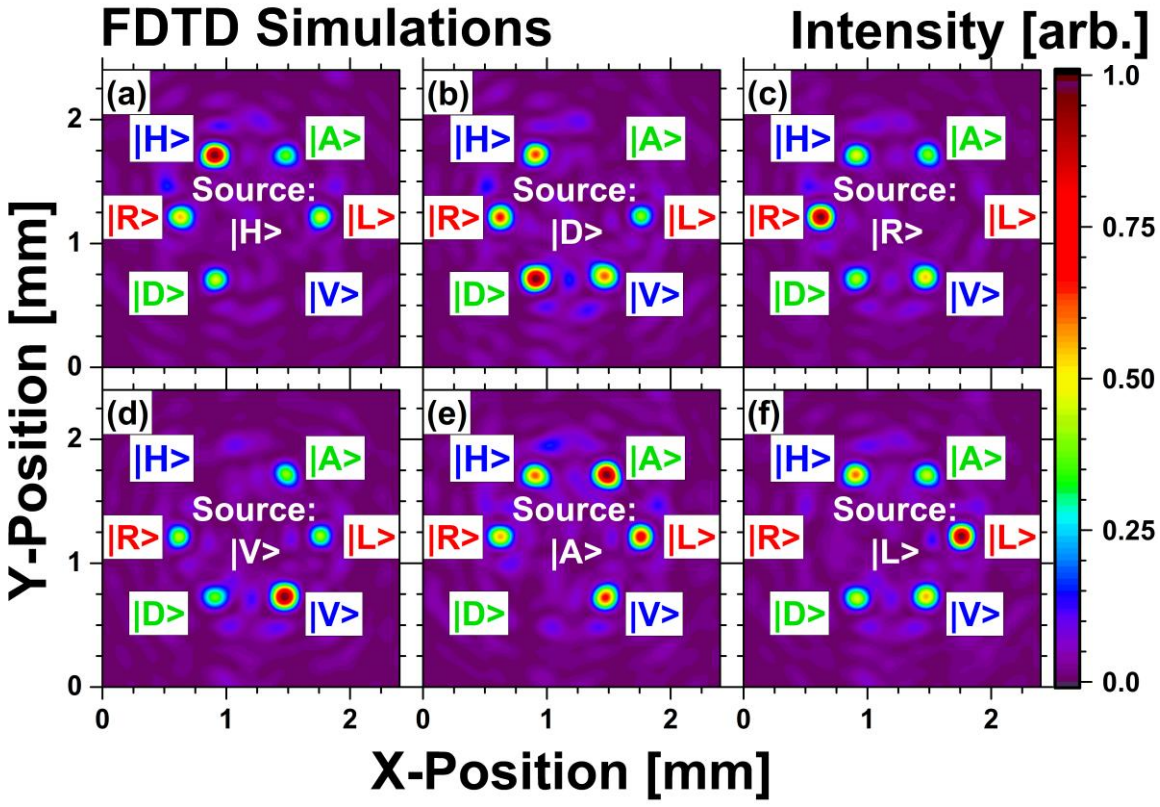

Figure 6.4: Collective simulations of the MSP in Lumerical FDTD solutions for six incident SoPs: (a) |H⟩, (b) |D⟩, (c) |R⟩, (d) |V⟩, (e) |A⟩ and (f) |L⟩ polarised light. Each image shows the transverse spatial distribution of the normalised intensity (E^2) at the focal plane f = 3.2 mm behind the metasurface. In each image, the focal spots originating from the six phase functions are labelled with their respective SoP with a designed off-axis displacement Δ_{xy} of 0.6 mm. The intensity distribution between these six focal spots changes as function of the incident SoP, as intended by the chosen interlaced design.

Collective simulations of a downscaled metasurface in Lumerical FDTD Solutions confirmed the intended operation of the MSP in Figure 6.4, exhibiting a hexagonal set of six differently polarised focal points. The intensity distribution between these six focal points changed as a function of the SoP incident to the metasurface in Figure 6.4. For example,

incident |H⟩ polarised light in Figure 6.4 (a) resulted in equal intensities of the |D⟩, |A⟩, |R⟩ and |L⟩ focal points, but a dominant |H⟩ and absent |V⟩ focal point.

The respective experimentally obtained calibration measurements are depicted in Figure 6.5 and show excellent agreement with the simulations of Figure 6.4, thereby confirming the intended operation of both the fabricated metasurface and experimental setup. The normalisation of each individual image I shown in Figure 6.5 included the subtraction of the average pixel value $Avg(I)$ according to Eq. (6.10) in order to take account to the increasing dark count caused by heating.

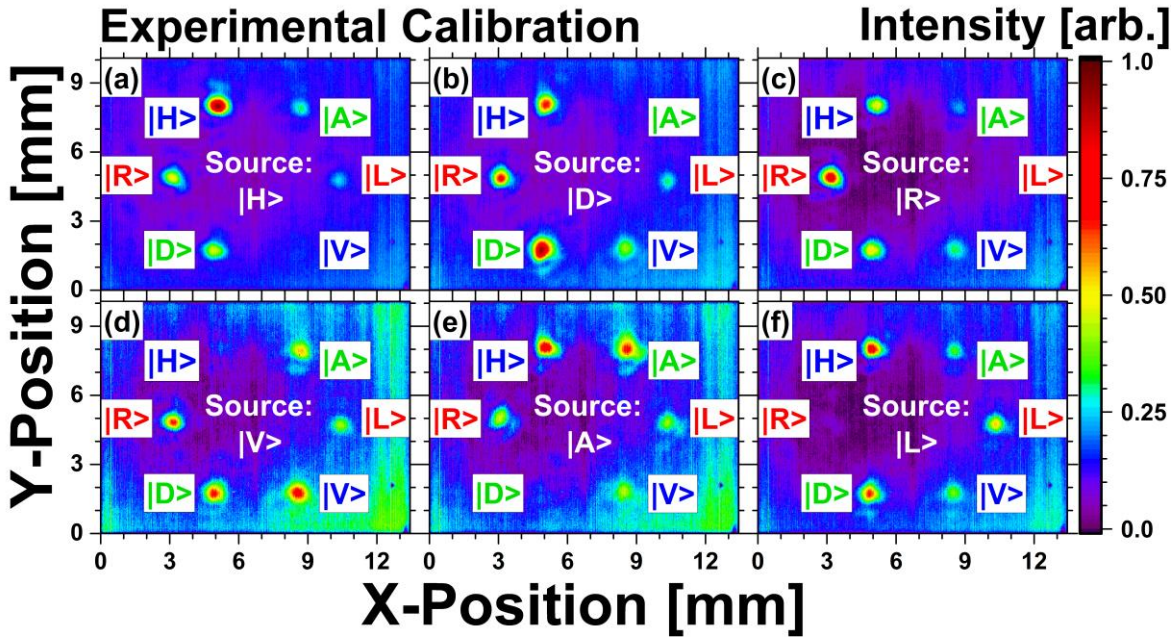

Figure 6.5: Experimentally obtained calibration images of the MSP with incident light of the six degenerate SoPs: (a) |H⟩, (b) |D⟩, (c) |R⟩, (d) |V⟩, (e) |A⟩ and (f) |L⟩. Each image shows the detected intensity at the focal plane f = 82 mm behind the metasurface. In each image, the focal spots originating from the six phase functions are labelled with their respective SoP with a designed off-axis displacement Δ_{xy} of 3.88 mm. The intensity distribution between these six focal spots changes as function of the incident SoP, in excellent agreement with the simulations of Figure 6.4.

$$I_{norm} = \frac{I - Min(I) - Avg(I)}{Max(I) - Min(I)} \qquad (6.10)$$

Despite this subtraction, one can still clearly see an increased dark count at the (bottom) right side of each image, indicating a spatially uneven gain or heating effect. As mentioned previously, the dark signal – observed as average pixel count in Figure 6.5 – increased during prolonged experiments due to heat generation from both the FIRL and image sensor. In the analysis algorithm, this was accounted for by including the background correction for each focal spot. Another important benefit of the employed calibration was that systematic non-uniformities of the setup were accounted for as well, such as the systematically lower intensity detected at the sensor's right side e.g., the |L⟩ and |A⟩ focal points should be as bright as their opposing |R⟩ and|D⟩ focal points in Figure 6.5 (a), etc.

6.4.2 Single-Shot Polarimetric Measurements

Using the calibration matrix C obtained as described by Eq. (6.8) from the six calibration images that were summarised in Table 6.1 and shown in Figure 6.5, the Stokes vectors $\vec{S}_m$ of each of the 64 individual images m could be retrieved with Eq. (6.9), which included the calibration images itself. These 64 experimentally obtained Stokes vectors $\vec{S}_m$ using the MSP could then be compared to their 14 theoretically expected[8] Stokes vectors $\vec{S}_t$ obtained from Eq. (6.2) with the known orientation angles α and β of the APG.

Figure 6.6 (a) shows the expected SoP ($\vec{S}_t$) as coloured cubes with their measured SoP ($\vec{S}_m$) as points of respective colour on the Poincare sphere. To simplify the graphic illustration into a 2D format, the azimuth angle 2Ψ and latitude angle 2χ were calculated for each datapoint from the Stokes vector's three parameter S_1-S_3 according to Eq. (6.11) and Eq. (6.12), respectively, and plotted in the equirectangular projection of Figure 6.6 (b).

$$2\Psi = \arctan\left(\frac{S_2}{S_1}\right) \qquad (0 < \Psi \leq \pi) \tag{6.11}$$

$$2\chi = \arctan\left(\frac{S_3}{\sqrt{{S_1}^2 + {S_2}^2}}\right) \qquad (-\frac{\pi}{4} < \Psi \leq \frac{\pi}{4}) \tag{6.12}$$

[8] The 64 measurements included duplicate SoPs e.g., $\alpha = 0°$, $\beta = 0°$ is in the same SoP as $\alpha = 90°$, $\beta = 0°$ or $\alpha = 0°$, $\beta = 90°$ or $\alpha = 90°$, $\beta = 90°$. As such, 12 different SoPs were measured 4 times each while the two circular SoPs were measured 8 times each, amounting to 14 different SoPs measured.

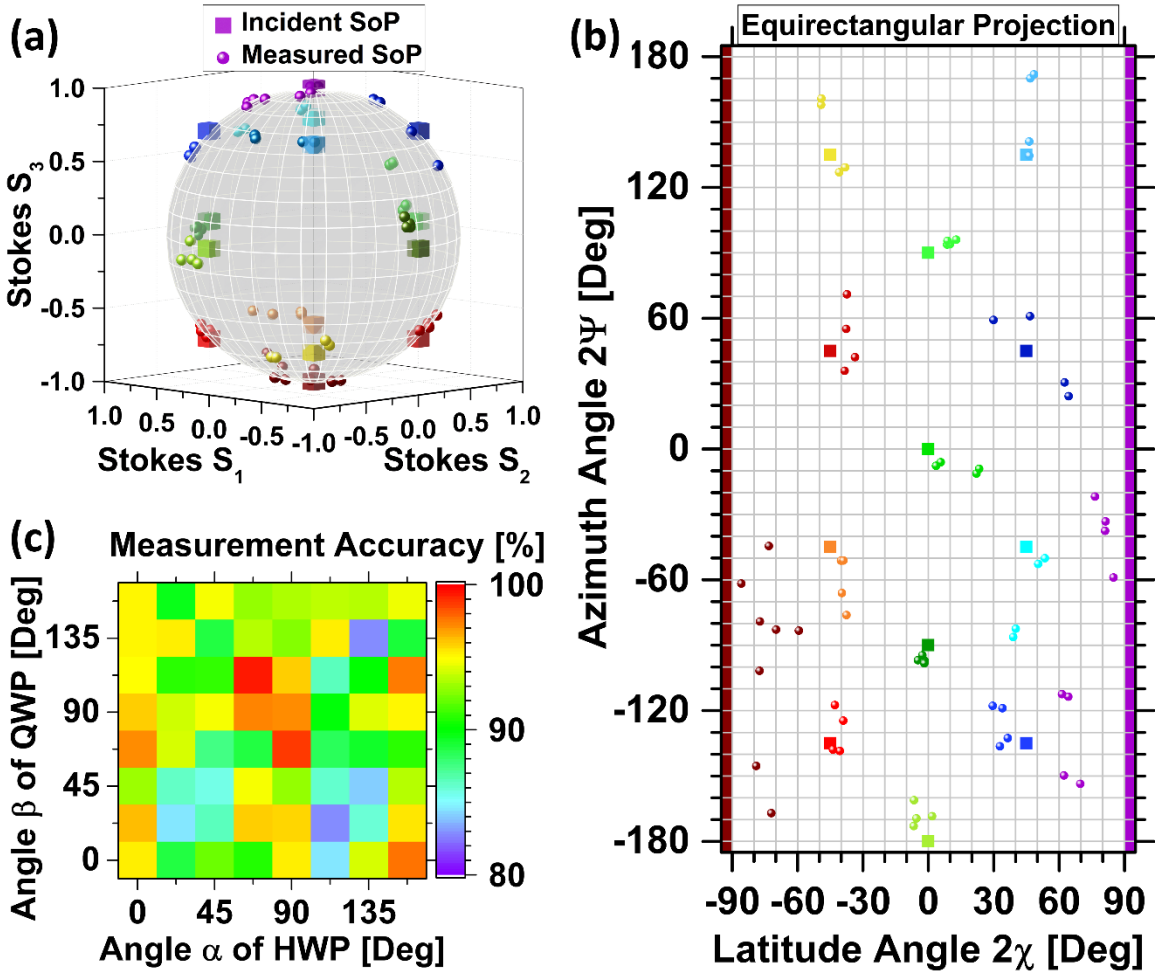

Figure 6.6: (a) Illustration of the Poincare sphere showing the theoretically expected SoP $\vec{S}_t$ incident on the MSP calculated from the known orientation angles α (HWP) and β (QWP) of the APG (14 coloured cubes) compared to the SoP retrieved from the measured images $\vec{S}_m$ (64 respectively coloured spherical markers) using the measurement and analysis methodology presented in Section 6.3. These results are easier to interpret in the (b) equirectangular 2D projection using the azimuth and latitude angles 2Ψ and 2χ, respectively. (c) The measurement accuracy as defined by Eq. (6.13) and Eq. (6.14) for the different orientation angles α and β of the APG.

It is qualitatively apparent from these results that the calibrated setup employing the MSP accurately and reproducibly predicted the incident SoP from a single image of the focal plane. The measurement accuracy η_{exp} was defined in Eq. (6.13) to quantify the results using the normalised orthodromic distance d_{circ} (radius = 1) between theoretically expected (subscript t) and experimentally measured (subscript m) SoP in Eq. (6.14). Figure 6.6 (c)

shows this measurement accuracy for each setting of the APG's orientation angles α, β, which seemingly followed an arbitrary pattern.

$$\boldsymbol{\eta_{exp} = (1 - d_{circ}) \cdot 100\ \%} \quad \textbf{(6.13)}$$

$$\boldsymbol{d_{circ} = \frac{1}{\pi} a\cos[\cos(2\Psi_t)\cos(2\Psi_e)\cos(2\chi_t - 2\chi_e) + \sin(2\Psi_t)\sin(2\Psi_e)]} \quad \textbf{(6.14)}$$

The averaged measurement accuracy of all 64 measurements was 92.1 % $\pm$ 4.2 % with a minimum value of 82.8 %. This accuracy is on par with published results of comparable MSPs obtained at technologically less challenging spectral ranges, e.g. 92.4 % $\pm$ 4.2 % from 48 measurements at 800 nm [479] and 97.2 % $\pm$ 2.5 % from 18 measurements at 1550 nm [284]. It can thus be concluded that the MSP presented in this chapter successfully measured the SoP at terahertz frequencies with high precision and repeatability, even in comparison to respective MSPs operating with more mature equipment at different wavelengths.

6.4.3 Simulation of broadband behaviour and (partially) unpolarised light

The performance of the MSP under broadband illumination and with incident (partially) unpolarised light was qualitatively explored with adapted FDTD simulations in Figure 6.7. Figure 6.7 (a), (b) indicate a good operational bandwidth for the MSP (ν_{opt} = 2.52 THz) between ca. 3.53 THz and 2.24 THz, respectively, if the shifted focal length f due to negative chromatic aberration [255] was considered. The lower frequency boundary shown in Figure 6.7 (b) is expected to be limited by the small focal length chosen in the presented simulations, which was further compressed towards increasingly inefficient diffraction angles, i.e. high NA [283, 483]. Designs with a larger chosen focal length are expected to show acceptable operation below 2.0 THz, extending the already impressive potential operational range $\Delta\nu$ from 1.29 THz to beyond 2 THz. Unfortunately, such designs with large focal length could not be simulated due to the immense computational costs associated with increased simulation volumes when using the FDTD algorithm [483]. These preliminary broadband simulations assumed a negligibly small dispersion of silicon within the simulated spectral region from 1.5 THz to 3.5 THz, supported by literature [126].

Unpolarised light, which can be regarded as superposition of any pair of orthogonal SoPs with equal intensity, led to all six focal spots excited with equal intensity in Figure 6.7 (c). The analysis of partially polarised light is hence also possible as shown in Figure 6.7 (d) for $|\mathrm{H}\rangle$ polarised light with DOP of 0.5. The $|H\rangle$ polarised spot is dominant (100 % intensity)

while the |D⟩, |A⟩, |R⟩, |L⟩ spots are of equal intermediate intensity (50 % intensity). However, a weak |V⟩ polarised spot was observed with approx. 25% intensity, which had previously been absent (0 % intensity) under fully |H⟩ polarised incidence (DOP=1) in Figure 6.4 (a). These preliminary results are hence encouraging, albeit more work is needed.

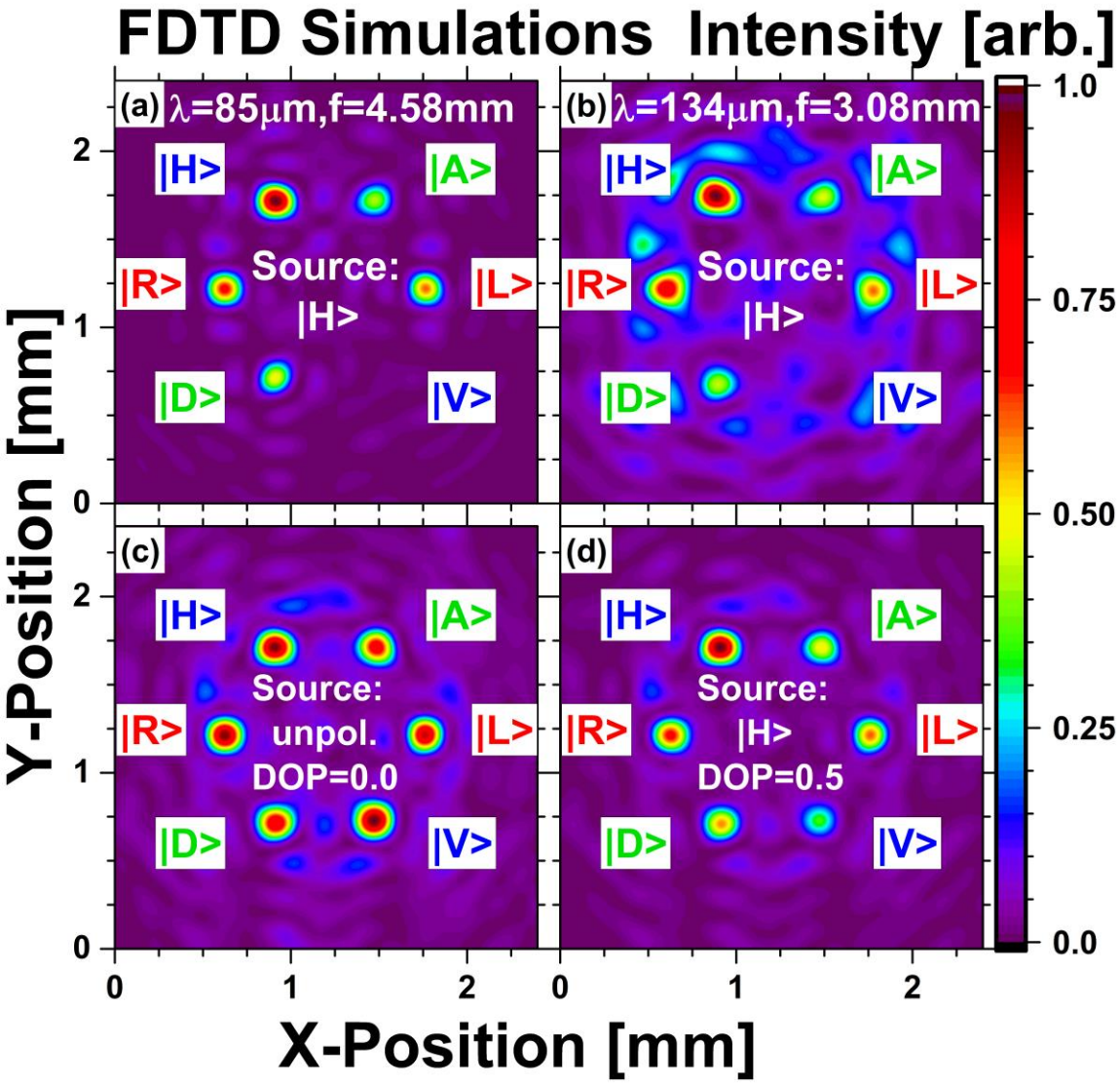

Figure 6.7: Collective simulations of the MSP in Lumerical FDTD solutions. Adjusted focal plane under |H⟩ incidence of radiation with (a) 3.54 THz (85 μm) at f = 4.58 mm and (b) 2.24 THz (134 μm) at f = 3.08 mm behind the metasurface. (c) Focal plane at f = 3.2 mm with unpolarised (DOP = 0.0) incident light and (d) partially |H⟩ polarised light (DOP = 0.5) of ν_{opt} = 2.52 THz. Each image shows the transverse spatial distribution of the normalised intensity (E^2). In each image, the focal spots originating from the six phase functions are labelled with their respective SoP.

6.5 Conclusion and Future Work

In conclusion, the design and experimental verification of a metasurface functioning as division of aperture polarimeter (DoAP) at terahertz frequencies was presented. The anisotropic meta-pillars were grouped into three interlaced sub-lattices that enabled the choice of independent phase functions for all six degenerate SoPs. The equidistant off-axis focusing of all six phase functions on to the vertices of a regular hexagon ensured approx. equal aberrations for each focal point. Interleaving the sub-lattices throughout the entire active area ensured an operation that was invariant to small transverse or longitudinal misalignments of the metasurface while providing a large aperture to collect incident radiation, unlike earlier designs based on segmented aperture division [481, 482, 485]. The intended operation was confirmed with collective simulations that were found to be in excellent agreement with experimental results.

To quantify the SoP from each individual image using the Stokes parameter, a calibration-based measurement methodology was developed and automated with a self-written analysis algorithm. The calibration took account of systematic error sources, such as increasing dark signal owing to uneven sensor heating, spatially varying pixel sensitivity and slight axial misalignments of the metasurface. The SoP determined from the obtained images consistently agreed with the known SoP, with an experimentally obtained accuracy of 92.1 % $\pm$ 4.2 % obtained from 64 measurements. Notably, this accuracy and repeatability is on par with published results of comparable MSPs obtained at technologically less challenging spectral ranges, e.g. 92.4 % $\pm$ 4.2 % from 48 measurements at 800 nm [479] and 97.2 % $\pm$ 2.5 % from 18 measurements at 1550 nm [284].

Preliminary broadband simulations indicate an exceptionally large operation bandwidth of at least 1.29 THz thanks to the very low dispersion of Silicon around the design frequency of 2.52 THz [126], and the analysis of (partially) unpolarised light appears feasible as well.

We expect the proposed MSP to be of considerable interest for applications in polarimetric terahertz imaging and sensing for NDT owing to the straight-forward integrability of the metasurface as silicon window of the employed terahertz camera. Of particular interest for future work would be to test the broadband operation of the presented MSP within a THz-TDS or integrate the metasurface within an objective to explore polarimetric imaging capabilities as described in [32, 486]. Extending the experimental setup of Figure 6.2 to explore the MSP's capability to characterise partially polarised light including the degree of

polarisation with an APG as described in [487] would be of great interest as well. At last, it shall be mentioned that initial plans aimed to combine both, the beam forming metasurfaces introduced in Chapter 5 and the beam analysing metasurface introduced in this chapter within a single demonstrator system for NDT and polarimetric imaging, which was supposed to be solely based on metasurface optics. However, the final steps towards this goal were unfortunately outwith the scope of this work i.e., due to delays caused by the COVID-19 pandemic.

Chapter 7 : Summary, Discussion and Future Work

7.1 Introduction

This chapter aims to summarise the achievements and findings that were presented throughout this thesis and evaluate them in the broader context of their significance to both the scientific community and industrial applications. Furthermore, scientific and technological limitations of the presented work shall be highlighted to derive suggestions for future work that builds up on the capabilities and insight gained from this project. Concluding remarks will comment on the attainment of project deliverables and scientific expectations, as well as on the encompassing TeraApps project and the impact of the COVID-19 pandemic on the ability to conduct research throughout the funded period.

7.2 Summary of this Thesis

Within this thesis, I outlined and pursued the concept of novel optical setups that combined the advantages of terahertz imaging with the added information provided by polarimetry and the advanced capabilities of dielectric metasurface optics. The combination of these three scientific topics was intended to be mutually beneficial by mitigating constraints and obstacles commonly encountered by the individual topics, as discussed in Section 1.4. The scientific achievements of this thesis can be summarised into five key contributions, which approximately follow the chapter structure of this thesis.

1) The design of anisotropic metasurface optics operating at terahertz frequency was presented in Chapter 3. Elaborate optimisation simulations of the anisotropic meta-pillars resulted in a collection of highly transmissive pillar geometries that allowed for simultaneous and independent control over the transmitted phase profiles for terahertz radiation polarised along the two in-plane pillar dimensions. Purpose-written code arrayed individual meta-pillars into large metasurfaces that replicated user-defined phase and polarisation functions upon transmission based on the combined principles of acquired propagation phase and geometric phase. This enabled the independent encoding of two different phase functions on to two orthogonal SoPs and in turn versatile alterations of the transmitted spatial polarisation profile. Collective FDTD simulations of downscaled metasurfaces were conducted for the rapid confirmation and optimisation of the intended operation of each metasurface design.

Such simulation results also successfully served as reference frame for both the development of descriptive analytical models and the evaluation of obtained experimental results.

2) The monolithic fabrication of dielectric metasurfaces presented in Chapter 4 was optimised based on fast and simple i-line photolithography in hard contact mode with a chromium photomask that contained the metasurface pattern. A Bosch process was optimised to dry-etch the meta-pillars monolithically into readily available silicon substrates within a single lithography step. Notably, a quality assurance step was developed based on WLI in which the spatial etch profile, the average etch depth and its standard deviation could be reproducibly measured over large areas without the need to strip the protective photoresist.

3) The Bessel beams with axial SoP variations were investigated in Chapter 5 for their beam forming capabilities that allowed for well-defined 3D variations of the SoP, including their potential use as polarised probe beams for various applications. Such non-diffracting probe beams were generated from a single metasurface and maintained their focus over a long distance with a depth-varying polarisation profile that acted as information channel. Design parameter that controlled the beam's intensity and polarisation profiles were explored in simulations and experiments, both of which were accurately described by the developed analytical model.

4) The beam analysing metasurface polarimeter (MSP) presented in Chapter 6 was designed to act as highly integrated division-of-aperture polarimeter (DoAP) to capture quantitative information on the incident SoP instantaneously within a single image. The experimental characterisation of the optical performance was in excellent agreement with both the analytical model and simulation data. The automated analysis script reliably and reproducibly determined the SoP incident on to the MSP with a very high prediction accuracy of over 90 % after initial calibration measurements.

5) The system-level demonstration of terahertz applications in sensing, imaging and polarimetry was based around the two types of metasurface optics presented before. Two setups targeted industrially attractive applications that demonstrated the straightforward integrability of metasurface optics to form compact systems with advanced optical capabilities. The beam forming metasurface of Chapter 5 demonstrated its potential for polarimetric sensing and imaging applications via the NDT of polymers and composite materials, whereas the beam analysing metasurface of Chapter 6 successfully operated as DoAP with high precision and repeatability.

7.3 Discussion of Results, Limitations and Future Work

7.3.1 Design of Anisotropic Metasurface Optics

Although there has been previously reported work on dielectric metasurfaces operating within the terahertz spectrum [305, 311-315], this thesis nevertheless constitutes one of the first demonstrations that explored the polarisation altering capabilities of an anisotropic meta-pillar design in a systematic and application-driven manner. Especially the ability to combine propagation phase and geometric phase to independently address orthogonal circular polarisations was often overlooked by other publications due to the added complexity of the underlying theory and pattern generation compared to the manipulation of orthogonal linear polarisations. Furthermore, the impact of expected fabrication tolerances on the optical performance i.e., the etch depth deviation caused by ARDE, was already considered upon optimising the design of meta-pillars to render the final metasurfaces more robust against such tolerances. As a result, the experimentally obtained estimate for the optical transmission of the fabricated metasurface $\bar{T}_{exp} = 76.0 \pm 0.4\,\%$ was close to the simulated average of all meta-pillar geometries of $\bar{T}_{sim} = 86.9\,\% \pm 6.4\,\%$, and more generally comparable to values reported for other dielectric metasurfaces [30-33]. A few publications achieved even higher total transmission by incorporating (broadband) anti-reflective metasurface layers on the substrate's backside [313, 325, 488]. Such anti-reflective layers could be adopted in a future step to improve the efficiency of the metasurface design presented in this thesis as well, albeit at the expense of added fabrication complexity. A clear deficit of the presented design process was the deliberate decision to restrict the meta-pillar optimisation to the design wavelength of 118.8 µm instead of considering broadband operation. This decision greatly simplified and accelerated the design process and was justified by the monochromatic nature of the FIRL employed for optical experiments. However, reports on dispersion-engineered metasurface optics [198, 255, 489] in combination with negligible dispersion of silicon around the design wavelength [126] offer high prospects for the design of virtually dispersion-free optics that is optimised towards ultra-broadband operation covering the majority of the terahertz spectrum. Such ultra-broadband metasurface optics would be of great benefit to both lab-based and industry-scale optical terahertz setups alike and therefore a compelling avenue for future work. At last, it shall be emphasised that the metasurface design developed in this thesis can be easily adapted and extended to explore a rich set of other optical functions and phenomena of

interest for academic research upon future projects, such as vortex beams, multi-focal lenses, lens arrays or arbitrary polarisation filter, to name a few.

7.3.2 Monolithic Fabrication and Quality Assurance

This thesis reported one of the first demonstrations of dielectric metasurface optics that was fabricated monolithically into cheap and widely available silicon substrates using a single-step photolithographic process that employed dry etching. The monolithic fabrication process offered significant advantages in terms of speed and simplicity when compared to previous lithographic processes that employed either an etch-stop layer [305, 490] or additive layer depositions [278, 282]. Instead of such attempts to prevent fabrication tolerances by employing expensive custom-made substrates or time-consuming fabrication sequences, the strategy pursued in this thesis was to quantify the tolerances encountered upon a fast and simple fabrication process, uncover the underlying mechanisms, and reduce the impact on the optical performance towards acceptable limits. The ability to measure the average etch depth with resist atop meta-pillars using WLI allowed for the quantification of fabrication tolerances and their reduction via a subsequent fine etch step thus ensuring a certain degree of process control and granting insights on the mechanisms underlying deviations of the spatial etch depth profile. To the best of my knowledge, these efforts to gain process control and develop a control model for quality assurance are the first of its kind, with previous work on monolithic fabrication uncritically accepting performance deviations associated to ARDE [293, 304, 312, 491, 492]. In principle, these results can be extended to any other wavelength or structure size. The reported fabrication technique including quality assurance are thus expected to benefit efforts towards upscaling and industrialisation of metasurface optics. In the future, the quality assurance can be extended with a theoretical investigation on the impact of deviating sidewall verticality or roughness on the optical performance, which was outside the scope of this work. Another previously mentioned extension that would enhance efficiency, compactness, and capabilities of the presented metasurface optics would be the development of a bi-layer patterning process that allows for the fabrication of metasurface layers on both substrate sides. Compared to other fabrication processes such as 3D printing [298, 427-429, 493] or laser ablation [431, 432, 494, 495], the lithography-based process excels in terms of achievable minimum feature sizes and uniformity of both structures and material, resulting in superior performance for metasurfaces operating particularly at high terahertz frequencies above ca. 1 THz. However,

attempts to scale the developed fabrication technique towards operation at low terahertz frequencies (i.e., 0.3 THz) were unfavourable due to large associated structure sizes (i.e., pillar height ≈ 800 µm) at which dry-etching became increasingly inefficient and inaccurate. Thus, alternative fabrication techniques like 3D printing or laser ablation are more promising candidates for low-frequency terahertz optics, which might be developed and optimised in future work.

7.3.3 Bessel Beams with Axial Variation of the State of Polarisation

Bessel beams with well-defined axial variations of the SoP are a fairly recent development that was first demonstrated by Moreno et al. in 2015 [350]. Thus far, experimental demonstrations of such beams were limited to a simple proof-of-concept in the visible spectrum, with most setups relying on complicated assemblies that involve spatial light modulators (SLM) and reflectors to independently address two orthogonal SoPs [350, 360, 362, 374, 418, 496, 497]. One advantage of SLM-based setups is their dynamic tunability of the optical function [418], which is only possible with more sophisticated metasurface designs [498, 499].

Only after my own research on this topic was already underway, Dorrah et al. demonstrated axial polarisation control of Bessel beams generated by a single metasurface, which vastly simplified the involved setup [33]. A major novelty of their sophisticated metasurface design based on dual matrix holography was the ability to superimpose five (or more) Bessel beams with individual SoP and intensity profile to create arbitrary on-axis SoP profiles that were independent of the SoP incident on their metasurface. Although their approach resulted in improved control over the on-axis intensity profile compared to the design presented in this thesis, this came at several disadvantages. Their metasurface required spatial interlacing of the unit cells and a 4-f spatial filtering stage behind the metasurface, both of which further complicated the design and optical assembly while reducing the transmitted intensity to less than 1/5 of the incident value. Furthermore, their design process and its underlying theoretical model were vastly more complex and less intuitive to understand, complicating the analysis of obtained results. Arguably, the simple but efficient design of this thesis better suited the application-driven research at terahertz frequencies as it maintained high transmitted intensity levels and a more compact setup, together with an intuitive theoretical model. Especially the fact that the employed terahertz source (FIRL) emitted a well-known and constant SoP rendered the gimmick of a Beam profile that was independent of the

incident SoP obsolete. At last, Dorrah's work was once again restricted to an experimental proof-of-concept rather than demonstrating a practical application, with future applications as probe beam of a refractometer only considered in theory within their supplement [418]. Consequently, the experimental exploitation of Bessel beams with axially varying SoP for applications in sensing and polarimetric were the first of its kind and should inspire subsequent work. As such, further exploration of the design parameters such as grating constants, polarisation basis, oscillation length or orbital angular momentum is desirable to better understand their limits and impact on potential applications. Furthermore, the design of the Bessel beams could be improved in the future by implementing the "frozen wave method" to gain control over the on-axis intensity profile [388, 471, 472, 500, 501]. Of high interest would also be the exploration of avenues to employ the presented Bessel beams for terahertz (6G) communication and OAM-based encryption techniques [502].

7.3.4 Metasurface Polarimeter

The design of the metasurface polarimeter (MSP) based on spatial interleaving of sub-lattices throughout the entire active area rendered the MSP particularly robust against misalignments and improved the signal power due to its large aperture that focussed the incident radiation into a single set of focal points, in contrast to previously reported MSP that applied segmented aperture division [481, 482, 485]. While the increased intensity of the focal points was crucial to boost the SNR at terahertz frequencies, it also deterred a prospective application for beam profiling as demonstrated by Yang et al. [284]. An impressive measurement accuracy of 92.1 % $\pm$ 4.2 % was obtained from 64 measurements after an initial calibration that effectively reduced the impact of sources of (thermal) noise. The obtained accuracy is in line with published results of comparable MSPs obtained at technologically less challenging spectral ranges, e.g. 92.4 % $\pm$ 4.2 % from 48 measurements at 800 nm [479] and 97.2 % $\pm$ 2.5 % from 18 measurements at 1550 nm [284]. The MSP design presented in this thesis offers adaptable design parameters together with a straightforward integration of the MSP as front-window of commercial terahertz cameras, such as the INO MicroXCam-384-THz used within this thesis, since the entire beam forming functionality was compressed into a single metasurface layer. From a commercial point of view, this is highly desirable compared to current polarimeter based on multiple (moving) optical components. Initial simulation studies on the capabilities of the presented MSP to analyse partially polarised light as showcased in [487] and accurately operate throughout a

broad spectral range (> 1 THz) showed promising results, but experimental demonstrations are subject to future work. Another promising task in the future would be to engineer spectral dispersion of a follow-up design to achieve dispersion-free operation or even tailored chromatic dispersion, potentially resulting in the extended analytical capabilities of a spectropolarimeter [222]. Furthermore, off-focus placement of the image sensor would in principle enable spatially resolved imaging polarimetry as demonstrated by [32, 486], which was explored in initial experiments with encouraging result that require further work.

7.3.5 System-level Demonstration of Terahertz Applications

The optical setups to characterise and utilise the presented metasurface optics were another significant contribution of this thesis. The design, assembly, and testing of custom-built terahertz setups was conducted from the initial idea towards the envisioned application, as opposed to a big portion of publications on terahertz imaging that solely employ pre-build or even commercial setups to simply characterise interchangeable samples.

As such, the experimental setup to test and utilise the Bessel metasurfaces presented in Chapter 5 included the meticulous design and optimisation of a -7.7x magnifying telecentric objective that included polarisation analysing capabilities based on the rotating QWP method [179], which has not yet been demonstrated at terahertz frequencies by other groups. The obtained resolution limit was ca. 1.5 λ_0, which was slightly worse than the 0.6 λ_0 reported by Minkevicius et al. [495] for imaging with Bessel beams at 0.6 THz. However, their work was restricted to intensity contrast and applied special deconvolution algorithms that would also benefit the resolution of the polarimetric images presented in this thesis. While the high -7.7x magnification was well-suited to explore the absolute resolution limit of the presented setup, it somewhat hindered practical applications due to the comparably small associated FOV. Furthermore, initial plans to image the reflected Bessel beams off a sample had to be cancelled due to the objective's small working distance (≈10 mm), which did not leave enough space for an angled sample. Such reflection experiments would have been interesting since the sample's topography would be imprinted in the reflected polarisation front thus in principle allowing for the retrieval of depth information from the detected SoP. In turn, 3D images of the sample topography comparable to phase contrast imaging could be obtained in principle e.g., to analyse the fibre weave of commercial carbon fibre composites. Future work would hence benefit from new telecentric objectives with smaller magnifications of ca. 1.5x or 3x and increased working distance, which have already

been designed. It was unfortunately realised too late that the FIRL employed as terahertz source throughout most of the measurements involving the Bessel beam metasurface of Chapter 5 was not properly aligned and optimised, which resulted in sub-optimal power levels (ca. 100-80 mW) and small beam divergence that further restricted the usable optical power and in turn the signal strength. Future experiments are hence expected to achieve higher signal strength and a lowered noise floor.

All presented experiments were conducted an exceptionally powerful monochromatic terahertz source (FIRL). Showcasing the reliable operation of the presented metasurfaces with a more economic source, such as a THz-TDS setup or QCL, would have underlined the maturity for industrial applications of the approach taken in this thesis. Particularly broadband characterisations within a THz-TDS setup would have been compelling since preliminary simulation results indicated exceptional prospects for broadband operation of the developed metasurfaces. Such experiments with a THz-TDS setup were initially planned within a secondment with Prof. Feiginov at the Vienna University of Technology but had to be cancelled due to prolonged travel restrictions throughout the COVID-19 pandemic.

At last, it shall be mentioned that initial plans aimed to combine both the beam forming metasurface introduced in Chapter 5 and the beam analysing metasurface introduced in Chapter 6 within a single demonstrator system for NDT and polarimetric imaging applications, which was supposed to be solely based on metasurface optics. Such an imaging setup would have highlighted the maturity and capabilities of metasurface optics in enabling compact and efficient setups for polarimetric applications at terahertz frequencies.

7.4 Concluding Remarks

7.4.1 Connection to the Innovative Training Network ‘TeraApps’

This PhD research project filled one of 15 positions, namely ESR #12, within the European Union’s Marie Skłodowska-Curie Innovative Training Network (MSCA-ITN) in “Terahertz Technologies for Imaging, Radar and Communication Applications” (abbreviated to ‘TeraApps’), which was funded by the European Commission under the Horizon 2020 programme. Consequently, each public dissemination resulting from this PhD - including this thesis - is required to acknowledge the following:

This work has received funding from the European Union's Horizon 2020 research and innovation programme under the Marie Skłodowska-Curie grant agreement No. 765426 (TeraApps).

Our research was therefore subject to guidelines and deliverables outlined within the TeraApps grant agreement, for which regular reporting both in written and oral format were required. Several in-person progress meetings, workshops and summer schools took place throughout this project, as listed in the Section "Outcomes of the Research Activity". Personal and professional connections to partner institutes and the work of fellow ESRs were fostered with collaborative work strongly encouraged i.e., in the format of 'secondments' hosted by both academic and industrial members of the TeraApps consortium.

In this framework, the research of this thesis was part of the work package "demonstrator systems" and consequently aimed to innovate terahertz imaging and sensing on a system level in a scientifically novel and technologically feasible manner that demonstrates industrially viable applications. This work targeted innovations on optical components associated with terahertz imaging and their system-level operation, thereby complementing the work of other ESRs that focussed on the improvement of terahertz radiation sources (most notably the Resonant Tunnelling Diodes - RTD) and detectors (e.g., graphene-based detection, nanowire detectors, triple barrier RTD-transceivers, etc.). Secondments were planned that targeted the testing of the developed optical components with both commercial sources and detectors and the ones produced by fellow ESRs or industrial collaborators. Unfortunately, the planned collaborative secondments of this PhD project were made impossible by travel restrictions imposed by the COVID-19 pandemic, as discussed in Section 7.4.2.

7.4.2 Impact of the Covid-19 Pandemic

A significant period of this PhD was unfortunately subject to considerable disruptions caused by the COVID-19 pandemic. Particularly severe was the impact on the working conditions in the second and third year of the 3-year long TeraApps project, which was extended by another 6 months as a result.

International and national travel restrictions imposed by most nations, including the United Kingdom, prohibited or limited work-related travel for almost 2 years. As a consequence, anticipated attendance at several conferences was either cancelled, postponed or shifted

online, which negatively impacted the ability to disseminate results to a broader audience and network with colleagues. Even worse, all secondments and on-site collaborations that were planned for this PhD project within the TeraApps consortium, as outlined in Section 7.4.1, were not possible until the last 6 months of the project, at which point such work had become redundant. Unfortunately, a shift towards digital secondments did not appear feasible due to the experimental focus of this PhD's research objectives.

Even within the University of Glasgow, the pandemic inevitably caused disruptions and delays to practical work. Notably, the fabrication of metasurfaces and execution of optical experiments were significantly delayed due to the closure of both the James Watt Nanofabrication Centre and the laser laboratory for ca. 4 months, including a significantly lowered capacity thereafter due to social distancing rules. This consequently also impacted the timeline for scientific dissemination, e.g., delayed submission of manuscripts and conference presentations. Wherever possible, meetings and conferences were attended online.

Another consequence of lowered on-site staff and maintenance during the lockdown was a flood within the laser laboratory (Room 120 in Rankine building) in June 2020, which severely contaminated the custom-built experimental setup, see Figure 7.1. Optical components had to be cleaned or reordered, the room dehumidified and the experimental setup rebuilt. Furthermore, the air-conditioning of the laser laboratory was broken from early March 2021 until late April, inhibiting laser experiments due to potential overheating.

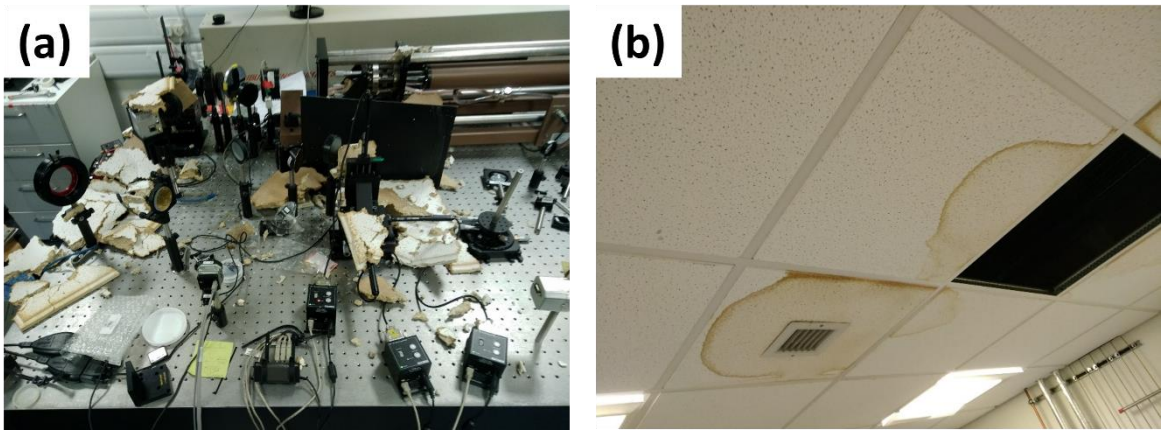

Figure 7.1: (a) Damages and contaminations of the optical setup found after the lockdown in June 2020 caused by (b) a flood originating from the ceiling that collapsed a ceiling tile right on to the optical laser setup. Sensitive cleaning, drying and restocking of the components and Laboratory 120 (Rankine building) required significant effort and time.

Apart from these incidents of higher force, the PhD student and his supervisory team successfully adapted the outline and work undertaken throughout the pandemic to the ‘new normal’ and restricted the detrimental impact of the pandemic to external factors. Immediate measures taken during the lockdowns were a shift towards theoretical and simulation-based work, (re-)design of improved metasurfaces, and participation in the government’s furlough scheme to save funding for a project extension. The impact of reduced lab capacity was mitigated by effective planning of work schedules including late working hours. The PhD student’s internal and external supervisory board remarked at several instances that the PhD student’s efforts and success in mitigating the impact of the pandemic were exemplary.

7.4.3 Conclusion on the conducted Research Activity

The work conducted throughout this thesis successfully designed, assembled, and tested highly specialised demonstrator systems that showcased applications in polarimetry, NDT and polarimetric imaging at terahertz frequencies. These setups were based on a novel design approach that rigorously tailored highly integrated and efficient metasurface optics towards their intended operation rather than combining pre-designed optics into complex and less efficient optical assemblies. As such, the main task outlined within the grant agreement was achieved and all deliverables were successfully fulfilled and reported on.

The experimentally obtained data was thoroughly documented, analysed and backed up by both analytical models and numerical simulation results whenever possible. Unfavourable results were openly discussed, and acknowledgement was given to the work of others wherever necessary. The author is therefore confident that the standards of the University of Glasgow on quality of work scientific rigour were upheld.

Scientific results were openly shared with both colleagues and the public at regular meetings within the TeraApps consortium, various prestigious conferences and via publication within high-profile peer-reviewed scientific journals, as has been summarised in the Section “Outcomes of the Research Activity”. Consequently, the conducted research withstood international scrutiny, benefitted the work of fellow researcher and will continue to do so.

The author strongly believes that the complexity of the work conducted throughout this project, the quality of obtained results and their significance to the scientific community will qualify for the award of the degree *doctor of philosophy* by research in “Electronics and Electrical Engineering” in accordance with the University of Glasgow’s postgraduate guidelines.

Appendix

Throughout this PhD project, a rich and extensive set of data was collected from experiments, simulations and theoretical models, which includes the code of several scripts to analyse or generate said data. Although most of this data can be considered fundamental to the obtained results shown in this thesis, it is simply too vast and extensive to be reasonably included within this appendix. For this reason, the below appendix is limited to supplementing a few key aspects that were discussed in the main body of this thesis, whereas the remaining data and files are provided separately in their native file format within the "Dataset & Code" repository that accompanies this thesis.

A. Step-by-step Derivation of Geometric Phase introduced in Chapter 2

The below calculation shows a step-by-step derivation of Eq. (2.5) in Section 2.3.1.

$$\vec{J}_{out} = A_{HWP}(\theta)\cdot\vec{J}_R = \begin{bmatrix}\cos^2\theta-\sin^2\theta & 2\cos\theta\sin\theta\\ 2\cos\theta\sin\theta & \sin^2\theta-\cos^2\theta\end{bmatrix}\cdot\frac{1}{\sqrt{2}}\begin{pmatrix}1\\ i\end{pmatrix}$$

$$= \frac{1}{\sqrt{2}}\begin{pmatrix}\cos^2\theta-\sin^2\theta+i\,2\cos\theta\sin\theta\\ 2\cos\theta\sin\theta-i\,(\cos^2\theta-\sin^2\theta)\end{pmatrix}$$

$$= \frac{1}{\sqrt{2}}\begin{pmatrix}\cos 2\theta+i\,\sin 2\theta\\ \sin 2\theta-i\,\cos 2\theta\end{pmatrix} = \frac{1}{\sqrt{2}}\begin{pmatrix}\exp(i\,2\theta)\\ -i\exp(i\,2\theta)\end{pmatrix}$$

$$= \frac{1}{\sqrt{2}}\begin{pmatrix}1\\ -i\end{pmatrix}\cdot exp(i\,2\theta) = \vec{J}_L\cdot\underbrace{exp(i\,2\theta)}_{:=\varphi_{geo}(2\theta)}$$

B. Python Code for the Metasurface Pattern presented in Chapter 5

The below python code was used to generate the metasurface patterns employed for the simulation and experimental results presented in Chapter 5 using the meta-pillar and unit cell geometries introduced in Section 3.2 as discussed in detail in Section 3.3.

```
# Note: Within this script, all length units are given in micrometre, or converted into micrometre after import
# All angular Units are given in Degree, or converted into degree after their calculation
# Import required packages
from gdsCAD import *
import numpy
import shapely
from shapely.geometry import Polygon
from gdsii.library import Library
from gdsii.elements import *
import csv

# Define functions for later use

def cart2pol(x, y):        # Transforms 2D cartesian to polar coordinates
    rho = numpy.sqrt(x**2 + y**2)
```

```
    phi = numpy.arctan2(y, x)
    return(rho, phi)

def pol2cart(rho, phi):          # Transforms polar coordinates to 2D cartesian coordinates
    x = rho * numpy.cos(phi)
    y = rho * numpy.sin(phi)
    return(x, y)

def round_1(x, base=1):          # Rounds a floating number to full integer
    return int(base*numpy.round(float(x)/base))

def round_05(x, base=0.5):          # Rounds a floating number to multiples of 0.5
    return int(base*numpy.round(float(x)/base))

def interval_360(x, base=360):          # Wraps continuous Phase into periodic interval [0, 360] rounded to full degree [°]
    P = (float(x)/base)
    i, d = divmod(P, 1)
    return round_1(int(float(x) - (i*base) ))
# Create meta-atom Library from previous Simulations (directly loaded from associated csv-file with "," as seperator)
library = numpy.loadtxt(open("R-P-T-Tuples_aniso_H150um_PureSi-15-30_row.csv", "rb"), delimiter=",", skiprows=1)
# Input fundamental pattern parameter
nnd = float(40)          # Nearest Neighbour Distance between adjacent lattice Points (Meta-pillar Seperattion)
# Next: Code asked to input the diameter of the metasurface in [mm], converted to microns
size = 1000 * float(input("Which size (diameter in mm)?:" ))
# Next: Axicon Period for Polarisation #1
axicon_1 = float(input("Which radial axicon period g1 (in micrometre) for RCP component?:" ))
# Next: Additional Axicon Period for Polarisation #2
axicon_2 = float(input("Additional radial period g_ad (in micrometre) for LCP component?:" ))
# Next: Calculates the number of full Lattice Periods within the selecetd Pattern Extent rounded to full Integers
periods = int(size/(nnd))
# Define some running Variables and set to 0
i_x = (0)
i_y = (0)
n = int(0)
# Define Imaginary Unit
j= 0 + 1j
# Create Cells, Lists & Containers
Unit_cell = core.Cell('Rectangles')
topcell=core.Cell('TOP')
layout = core.Layout('LIBRARY')
COMs = []          # Empty List for "Center Of Meta-atoms"
# Generate 2D hexagonal lattice points within List of (x,y)-Tuples to fill List "Center Of Meta-atoms (COM)"
while i_y < (periods/numpy.sqrt(3)):          # Loop over the y-dimension of the Pillar Extent, skipping every 2nd row
    while i_x < periods:                    # Loop over the x-dimension of the Pillar Extent
        coord1 = ((-0.5*size +(i_x*nnd)),(-0.5*size +(i_y*nnd*numpy.sqrt(3))))          # COM Coordinates of row 1 pillar
        coord2 = ((-0.5*size +((0.5+i_x)*nnd)),((-0.5*size +(0.5+i_y)*nnd*numpy.sqrt(3)))) # COM Coordinates of row 2 pillar
        COMs.append(coord1)     # Save COM Coordinates of row 1 into List "Center Of Meta-atoms"
        COMs.append(coord2)     # Save COM Coordinates of row 1 into List "Center Of Meta-atoms"
        i_x = i_x+1     # Advance running Variable for inner Loop (x-Position)
    i_x = 0            # Zero running Variable for inner Loop (x-Position)
    i_y = i_y+1        # Advance running Variable for outer Loop (y-Position)
# Loop over Lattice Points, select the optimised Meta-Pillar and place it into TopCell
for COM in COMs:          # Loop over each Lattice Point COM
    polar = cart2pol(COM[0],COM[1])          # Polar Coordinates of the new Lattice Point
    if polar[0] <= size/2:          # Circular Aperture: Lattice Points outside a circle of pattern dimension are discarded
        # Next: Chosen Phase delay at lattice point for |R> polarised Light
        Phase_R = (numpy.rad2deg(-( 2*numpy.pi*polar[0]/axicon_1 ) ) )
        # Next: Chosen Phase delay at lattice point for |L> polarised Light
        Phase_L = (numpy.rad2deg(-( 2*numpy.pi*polar[0]/axicon_1 ) -( 2*numpy.pi*polar[0]/axicon_2 ) ) )
        # Next: Required x-pol. Phase shift of Pillar at lattice point
        Phase_req_x = (180 - interval_360(round_1(0.5* (Phase_R+Phase_L) ) ))
        # Next: Required y-pol. Phase shift of Pillar at lattice point
        Phase_req_y = (180 - interval_360(round_1(-180 + 0.5* (Phase_R+Phase_L) ) ))
        # Next: Required in-plane Rotation Angle of Pillar at lattice point
        angle = round_05(45+(((0.25*(Phase_R-Phase_L)) )))
        delta = 180          # Define/Set Benchmark Error of optimisation to 180 [°] for the new Lattice Point
        W_opt_x = 0          # Define/Set Optimised Pillar Width along x to 0 for the new Lattice Point
        W_opt_y = 0          # Define/Set Optimised Pillar Width along y to 0 for the new Lattice Point
        for tup in library:          # Loop trough the Meta-Pillar Library
            # Next: Calculate Complex Error for x-pol. between required properties and Pillar properties
            delta_new_x = ( numpy.square(numpy.absolute(tup[2]*(numpy.exp(j*numpy.radians(tup[1]))) - numpy.exp(j*numpy.radians(Phase_req_x) )))) )
            # Next: Calculate Complex Error for y-pol. between required properties and Pillar properties
            delta_new_y = ( numpy.square(numpy.absolute(tup[5]*(numpy.exp(j*numpy.radians(tup[4]))) - numpy.exp(j*numpy.radians(Phase_req_y)))) )
            # Next: Optimisation Condition: Does current Pillar have smaller RMS error for x- & y-polarised light than the current benchmark Error?
            if numpy.sqrt(0.5*(delta_new_x + delta_new_y)) < delta:
                # Next: Update the benchmark RMS Error to the current Pillar's value
                delta = numpy.sqrt(0.5*(delta_new_x + delta_new_y))
                # Next: Update the optimised Pillar Width in x to the current Pillar's value
                W_opt_x = tup[0]
                # Next: Update the optimised Pillar's Phase Shift along x to the current Pillar's value
                Phase_opt_x = tup[1]
                # Next: Update the optimised Pillar's Transmission along x to the current Pillar's value
                Trans_opt_x = tup[2]
                # Next: Update the optimised Pillar Width in y to the current Pillar's value
                W_opt_y = tup[3]
                # Next: Update the optimised Pillar's Phase Shift along y to the current Pillar's value
```

```
            Phase_opt_y = tup[4]
            # Next: Update the optimised Pillar's Transmission along y to the current Pillar's value
            Trans_opt_y = tup[5]
        rectangle = shapes.Rectangle( ( ((COM[0]+W_opt_x/2)), (COM[1] + (W_opt_y)/2) ) , ( ((COM[0]-W_opt_x/2)), (COM[1] - (W_opt_y)/2) ) ) # After Loop over all Pillars:
Create Rectangle with optimal Dimensions at its Lattice Point
        struc = rectangle.rotate(angle, center=(COM[0],COM[1]))         # Rotate Optimised Rectangle by the required Angle
        topcell.add(struc)                                      # Add optimised Pillar Structure into TopCell
layout.add(topcell)         #Add the final TopCell filled with all Meta-Pillars to the Layout ...
layout.save('MetasurfaceName.gds')          # ... and save it as .gds File
```

C. Python Code for the Metasurface Pattern presented in Chapter 6

The below python code was used to generate the metasurface patterns employed for the simulation and experimental results presented in Chapter 6 using the meta-pillar and unit cell geometries introduced in Section 3.2 as discussed in detail in Section 3.3.

```
# Note: Within this script, all length units are given in micrometre, or converted into micrometre after import
# All angular Units are given in Degree, or converted into degree after their calculation
# Import required packages
from gdsCAD import *
import numpy
import shapely
from shapely.geometry import Polygon
from gdsii.library import Library
from gdsii.elements import *
import csv

# Define functions for later use
def cart2pol(x, y):          # Transforms 2D cartesian to polar coordinates
    rho = numpy.sqrt(x**2 + y**2)
    phi = numpy.arctan2(y, x)
    return(rho, phi)

def pol2cart(rho, phi):          # Transforms polar coordinates to 2D cartesian coordinates
    x = rho * numpy.cos(phi)
    y = rho * numpy.sin(phi)
    return(x, y)

def round_1(x, base=1):          # Rounds a floating number to full integer
    return int(base*numpy.round(float(x)/base))

def round_05(x, base=0.5):          # Rounds a floating number to multiples of 0.5
    return int(base*numpy.round(float(x)/base))

def interval_360(x, base=360):          # Wraps continuous Phase into periodic interval [0, 360] rounded to full degree [°]
    P = (float(x)/base)
    i, d = divmod(P, 1)
    return round_1(int(float(x) - (i*base) ))

def interval_1(x, base=1):          # Returns full integers of a input float
    P = (float(x)/base)
    i, d = divmod(P, 1)
    return (int(i*base) )

# Create meta-atom Library from previous Simulations (directly loaded from associated csv-file with "," as seperator)
library = numpy.loadtxt(open("R-P-T-Tuples_aniso_H150um_PureSi-15-30_row.csv", "rb"), delimiter=",", skiprows=1)

# Input fundamental pattern parameter
nnd = float(40)          # Nearest Neighbour Distance between adjacent lattice Points (Meta-pillar Seperattion)
# Next: Code asked to input the diameter of the metasurface in [mm], converted to microns
size = 1000 * float(input("Which size (diameter in mm)?:" ))
periods = int(size/(nnd)) # Pattern Extent in Unit Cell Periods
# Next: Code asked to input the focal length of the metasurface in [mm], converted to microns
f = 1000*float(input("Which focal length for all Stokes-Points (in mm)?:" ))
# Next: Code asked to input the off-axis length of the metasurface in [mm], converted to microns
df = 1000*float(input("Which transversal off-axis length (from center) of the focal spot for all Stokes-Points (in mm)?:" ))
wl = float(118.8) # Design Wavelength in microns

# Define some running Variables and set to 0
i_x = (0)
i_y = (0)
n = int(0)
# Define Imaginary Unit
j= 0 + 1j

# Create Cells, Lists & Containers
Unit_cell = core.Cell('Rectangles')
topcell=core.Cell('TOP')
layout = core.Layout('LIBRARY')
LAT1 = []     # Empty List for Points of "Sub-Lattice 1"
LAT2 = []     # Empty List for Points of "Sub-Lattice 2"
LAT3 = []     # Empty List for Points of "Sub-Lattice 3"

# Generate 2D hexagonal lattice points within List of (x,y)-Tuples to fill List of Sub-Lattices
resc_y = 0.5*nnd*numpy.sqrt(3)*interval_1((periods/numpy.sqrt(3)))     # Define Rescale factor of y-Coordinate
while i_y < (periods/numpy.sqrt(3)):          # Loop over the y-dimension of the Pillar Extent, skipping every 2nd row
    while i_x < periods/3:                  # Loop over the x-dimension of the Pillar Extent
        lat1_1 = ((-0.5*size +(i_x*3*nnd)),(-resc_y +(i_y*nnd*numpy.sqrt(3))))     # Coordinates of Lattice 1 row 1 pillar
        lat1_2 = ((-0.5*size +((1.5*nnd+i_x*3*nnd))),((-resc_y +(0.5+i_y)*nnd*numpy.sqrt(3)))) # Coordinates of Lattice 1 row 2 pillar
```

```
        LAT1.append(lat1_1)     # Save Coordinates of Lattice 1 row 1 pillar into List "Sub-Lattice 1"
        LAT1.append(lat1_2)     # Save Coordinates of Lattice 1 row 2 pillar into List "Sub-Lattice 1"
        lat2_1 = ((-0.5*size +((nnd+i_x*3*nnd))),(-resc_y +(i_y*nnd*numpy.sqrt(3))))     # Coordinates of Lattice 2 row 1 pillar
        lat2_2 = ((-0.5*size +((2.5*nnd+i_x*3*nnd))),((-resc_y +(0.5+i_y)*nnd*numpy.sqrt(3)))) # Coordinates of Lattice 2 row 2 pillar
        LAT2.append(lat2_1)     # Save Coordinates of Lattice 2 row 1 pillar into List "Sub-Lattice 2"
        LAT2.append(lat2_2)     # Save Coordinates of Lattice 2 row 2 pillar into List "Sub-Lattice 2"
        lat3_1 = ((-0.5*size +((2*nnd+i_x*3*nnd))),(-resc_y +(i_y*nnd*numpy.sqrt(3))))     # Coordinates of Lattice 3 row 1 pillar
        lat3_2 = ((-0.5*size +((0.5*nnd+i_x*3*nnd))),((-resc_y +(0.5+i_y)*nnd*numpy.sqrt(3))))     # Coordinates of Lattice 3 row 2 pillar
        LAT3.append(lat3_1)     # Save Coordinates of Lattice 3 row 1 pillar into List "Sub-Lattice 3"
        LAT3.append(lat3_2)     # Save Coordinates of Lattice 3 row 2 pillar into List "Sub-Lattice 3"
        i_x = i_x+1     # Advance running Variable for inner Loop (x-Position)
    i_x = 0           # Zero running Variable for inner Loop (x-Position)
    i_y = i_y+1       # Advance running Variable for outer Loop (y-Position)

# Loop over Lattice Points of Lattice 1 (|H> vs. |V>), select the optimised Meta-Pillar and place it into TopCell
for lat in LAT1:    # Loop over each Lattice Point lat in LAT1
    polar = cart2pol(lat[0],lat[1])         # Polar Coordinates of the new Lattice Point
    angle_1 = 0                             # Required in-plane Rotation Angle of Pillar at lattice point
    # Next: Required x-pol. Phase shift of Pillar at lattice point
    Phase_req_x = (180 - interval_360(round_1(numpy.rad2deg(-(2*numpy.pi/wl)*(-f + numpy.sqrt( numpy.square(f) + numpy.square( lat[0]-(0.5*df) ) + numpy.square(
lat[1]+(numpy.sqrt(3)*0.5*df) ) ) ) ) ) ) )
    # Next: Required y-pol. Phase shift of Pillar at lattice point
    Phase_req_y = (180 - interval_360(round_1(numpy.rad2deg(-(2*numpy.pi/wl)*(-f + numpy.sqrt( numpy.square(f) + numpy.square(lat[0]+(0.5*df)) +
numpy.square(lat[1]-(numpy.sqrt(3)*0.5*df) ) ) ) ) ) ) )
    delta = 180         # Define/Set Benchmark Error of optimisation to 180 [°] for the new Lattice Point
    W_opt_x = 0         # Define/Set Optimised Pillar Width along x to 0 for the new Lattice Point
    W_opt_y = 0         # Define/Set Optimised Pillar Width along y to 0 for the new Lattice Point
    for tup in library:         # Loop trough the Meta-Pillar Library
        # Next: Calculate Complex Error for x-pol. between required properties and Pillar properties
        delta_new_x = ( numpy.square(numpy.absolute(tup[2]*(numpy.exp(j*numpy.radians(tup[1])))) - numpy.exp((j*numpy.radians(Phase_req_x) )))) )
        # Next: Calculate Complex Error for y-pol. between required properties and Pillar properties
        delta_new_y = ( numpy.square(numpy.absolute(tup[5]*(numpy.exp(j*numpy.radians(tup[4])))) - numpy.exp(j*numpy.radians(Phase_req_y)))) )
        # Next: Optimisation Condition: Does current Pillar have smaller RMS error for x- & y-polarised light than the current benchmark Error?
        if numpy.sqrt(0.5*(delta_new_x + delta_new_y)) < delta:
            # Next: Update the benchmark RMS Error to the current Pillar's value
            delta = (delta_new_x + delta_new_y)
            # Next: Update the optimised Pillar Width in x to the current Pillar's value
            W_opt_x = tup[0]
            # Next: Update the optimised Pillar's Phase Shift along x to the current Pillar's value
            Phase_opt_x = tup[1]
            # Next: Update the optimised Pillar's Transmission along x to the current Pillar's value
            Trans_opt_x = tup[2]
            # Next: Update the optimised Pillar Width in y to the current Pillar's value
            W_opt_y = tup[3]
            # Next: Update the optimised Pillar's Phase Shift along y to the current Pillar's value
            Phase_opt_y = tup[4]
            # Next: Update the optimised Pillar's Transmission along y to the current Pillar's value
            Trans_opt_y = tup[5]
    rectangle = shapes.Rectangle( ( ((lat[0]+W_opt_x/2)), (lat[1] + (W_opt_y)/2) ) , ( ((lat[0]-W_opt_x/2)), (lat[1] - (W_opt_y)/2) ) ) # After Loop over all Pillars: Create
Rectangle with optimal Dimensions at its Lattice Point
    topcell.add(rectangle)          # Add optimised Pillar Structure into TopCell

# Loop over Lattice Points of Lattice 2 (|D> vs. |A>), select the optimised Meta-Pillar and place it into TopCell
for lat in LAT2:    # Loop over each Lattice Point lat in LAT2
    polar = cart2pol(lat[0],lat[1])         # Polar Coordinates of the new Lattice Point
    angle_2 = 45                            # Required in-plane Rotation Angle of Pillar at lattice point
    # Next: Required x-pol. Phase shift of Pillar at lattice point
    Phase_req_x = (180 - interval_360(round_1(numpy.rad2deg(-(2*numpy.pi/wl)*(-f + numpy.sqrt( numpy.square(f) + numpy.square(lat[0]-(0.5*df)) +
numpy.square(lat[1]-(numpy.sqrt(3)*0.5*df) ) ) ) ) ) ) )
    # Next: Required y-pol. Phase shift of Pillar at lattice point
    Phase_req_y = (180 - interval_360(round_1(numpy.rad2deg(-(2*numpy.pi/wl)*(-f + numpy.sqrt( numpy.square(f) + numpy.square(lat[0]+(0.5*df)) +
numpy.square(lat[1]+(numpy.sqrt(3)*0.5*df)) ) ) ) ) ) )
    delta = 180         # Define/Set Benchmark Error of optimisation to 180 [°] for the new Lattice Point
    W_opt_x = 0         # Define/Set Optimised Pillar Width along x to 0 for the new Lattice Point
    W_opt_y = 0         # Define/Set Optimised Pillar Width along y to 0 for the new Lattice Point
    for tup in library:         # Loop trough the Meta-Pillar Library
        # Next: Calculate Complex Error for x-pol. between required properties and Pillar properties
        delta_new_x = ( numpy.square(numpy.absolute(tup[2]*(numpy.exp(j*numpy.radians(tup[1])))) - numpy.exp((j*numpy.radians(Phase_req_x) )))) )
        # Next: Calculate Complex Error for y-pol. between required properties and Pillar properties
        delta_new_y = ( numpy.square(numpy.absolute(tup[5]*(numpy.exp(j*numpy.radians(tup[4])))) - numpy.exp(j*numpy.radians(Phase_req_y)))) )
        # Next: Optimisation Condition: Does current Pillar have smaller RMS error for x- & y-polarised light than the current benchmark Error?
        if numpy.sqrt(0.5*(delta_new_x + delta_new_y)) < delta:
            # Next: Update the benchmark RMS Error to the current Pillar's value
            delta = (delta_new_x + delta_new_y)
            # Next: Update the optimised Pillar Width in x to the current Pillar's value
            W_opt_x = tup[0]
            # Next: Update the optimised Pillar's Phase Shift along x to the current Pillar's value
            Phase_opt_x = tup[1]
            # Next: Update the optimised Pillar's Transmission along x to the current Pillar's value
            Trans_opt_x = tup[2]
            # Next: Update the optimised Pillar Width in y to the current Pillar's value
            W_opt_y = tup[3]
            # Next: Update the optimised Pillar's Phase Shift along y to the current Pillar's value
            Phase_opt_y = tup[4]
            # Next: Update the optimised Pillar's Transmission along y to the current Pillar's value
            Trans_opt_y = tup[5]
```

```
    rectangle = shapes.Rectangle( ( ((lat[0]+W_opt_x/2)), (lat[1] + (W_opt_y)/2) ) , ( ((lat[0]-W_opt_x/2)), (lat[1] - (W_opt_y)/2) ) ) # After Loop over all Pillars: Create
Rectangle with optimal Dimensions at its Lattice Point
    struc = rectangle.rotate(angle_2, center=(lat[0],lat[1]))        # Rotate Optimised Rectangle by the required Angle
    topcell.add(struc)        # Add optimised Pillar Structure into TopCell

# Loop over Lattice Points of Lattice 3 (|R> vs. |L>), select the optimised Meta-Pillar and place it into TopCell
for lat in LAT3:    # Loop over each Lattice Point lat in LAT3
    polar = cart2pol(lat[0],lat[1])        # Polar Coordinates of the new Lattice Point
    # Next: Chosen Phase delay at lattice point for |R> polarised Light
    Phase_R = ((numpy.rad2deg(-(2*numpy.pi/wl)*(-f + numpy.sqrt( numpy.square(f) + numpy.square(lat[0]-(df)) + numpy.square(lat[1]) ) ) ) ) )
    # Next: Chosen Phase delay at lattice point for |L> polarised Light
    Phase_L = ((numpy.rad2deg(-(2*numpy.pi/wl)*(-f + numpy.sqrt( numpy.square(f) + numpy.square(lat[0]+(df)) + numpy.square(lat[1]) ) ) ) ) )
    # Next: Required x-pol. Phase shift of Pillar at lattice point
    Phase_req_x = (180 - interval_360(round_1(0.5* (Phase_R+Phase_L) ) ))
    # Next: Required y-pol. Phase shift of Pillar at lattice point
    Phase_req_y = (180 - interval_360(round_1(-180 + 0.5* (Phase_R+Phase_L) ) ))
    angle_3 = round_05((((0.25*(Phase_R-Phase_L)) )))    # Required in-plane Rotation Angle of Pillar at lattice point
    delta = 180        # Define/Set Benchmark Error of optimisation to 180 [°] for the new Lattice Point
    W_opt_x = 0        # Define/Set Optimised Pillar Width along x to 0 for the new Lattice Point
    W_opt_y = 0        # Define/Set Optimised Pillar Width along y to 0 for the new Lattice Point
    for tup in library:        # Loop trough the Meta-Pillar Library
        # Next: Calculate Complex Error for x-pol. between required properties and Pillar properties
        delta_new_x = ( numpy.square(numpy.absolute(tup[2]*(numpy.exp(j*numpy.radians(tup[1]))) - numpy.exp((j*numpy.radians(Phase_req_x) )))) )
        # Next: Calculate Complex Error for y-pol. between required properties and Pillar properties
        delta_new_y = ( numpy.square(numpy.absolute(tup[5]*(numpy.exp(j*numpy.radians(tup[4]))) - numpy.exp(j*numpy.radians(Phase_req_y)))) )
        if numpy.sqrt(0.5*(delta_new_x + delta_new_y)) < delta:
            # Next: Update the benchmark RMS Error to the current Pillar's value
            delta = (delta_new_x + delta_new_y)
            # Next: Update the optimised Pillar Width in x to the current Pillar's value
            W_opt_x = tup[0]
            # Next: Update the optimised Pillar's Phase Shift along x to the current Pillar's value
            Phase_opt_x = tup[1]
            # Next: Update the optimised Pillar's Transmission along x to the current Pillar's value
            Trans_opt_x = tup[2]
            # Next: Update the optimised Pillar Width in y to the current Pillar's value
            W_opt_y = tup[3]
            # Next: Update the optimised Pillar's Phase Shift along y to the current Pillar's value
            Phase_opt_y = tup[4]
            # Next: Update the optimised Pillar's Transmission along y to the current Pillar's value
            Trans_opt_y = tup[5]
    rectangle = shapes.Rectangle( ( ((lat[0]+W_opt_x/2)), (lat[1] + (W_opt_y)/2) ) , ( ((lat[0]-W_opt_x/2)), (lat[1] - (W_opt_y)/2) ) ) # After Loop over all Pillars: Create
Rectangle with optimal Dimensions at its Lattice Point
    struc = rectangle.rotate(angle_3, center=(lat[0],lat[1]))        # Rotate Optimised Rectangle by the required Angle
    topcell.add(struc)        # Add optimised Pillar Structure into TopCell


layout.add(topcell)        #Add the final TopCell filled with all Meta-Pillars to the Layout ...
layout.save('Metasurface_DOAPolarimeter.gds')        # ... and save it as .gds File
```

D. Detailed Settings of the spin coating of substrates presented in Chapter 4

Table D.1 summarises the parameters used for the spin coating of silicon substrates with the primer MCC80/20 and the photoresist SPR220.7.

Table D.1: Summary of parameters used to apply primer (program 1) and photoresist (program 2) to the silicon substrates via spin coating.

Program	Step 1	Step 2	Step 3	Step 4
1: Applying Primer (MCC80/20)	**30 s at 3'000 rpm with 20'000 rpm/s (spin-up & spin off)**	**0 s at 0 rpm with 20'000 rpm/s (spin down)**	/	/
2: Applying Photoresist (SPR 220.7)	**5 s at 500 rpm with 100 rpm/s (slow spin-up)**	**22 s at 3'500 rpm with 20'000 rpm/s (spin off)**	**3 s at 6'000 rpm with 20'000 rpm/s (edge bead removal)**	**0 s at 0 rpm with 6'000 rpm/s (spin down)**

E. Detailed Settings of the Bosch process presented in Chapter 4

Table E.2 summarises the parameters used for the optimised Bosch process to dry etch the silicon substrates around the resist-covered meta-pillars as described in Section 4.2.3.

Table E.2: Process parameters employed for the dry etching of silicon within the Bosch process (PlasmaPro 100 Estrelas, Oxford Instruments) using C_4F_8/SF_6 plasma chemistry. 3 Sub-recipes with adapted durations of etch and deposition cycles were used sequentially to maintain a sidewall verticality close to 90° throughout the etch. The base pressure and table temperature were held constant at $7.5 \cdot 10^{-9}$ Torr and 5 °C, respectively.

STEP NAME	PROCESS TIME [s]	APC PRESSURE [mTorr]	HF POWER [W]	ICP POWER [W]	LF POWER [W]	HELIUM BACKING [Torr]	GAS7 O2 [sccm]	GAS8 SF6 [sccm]	GAS11 C4F8 [sccm]
Plasma Strike below (Start)									
CLAMP STABLE	10	0	0	0	0	0	0	0	0
He Check 25C	20	0	0	0	0	10	0	0	0
gas on	2	20	0	0	0	10	50	10	50
strike1	5	20	10	1750	0	10	100	10	100
strike2	2	40	0	1750	10	10	0	10	200
pre dep	2	40	0	1600	10	10	0	10	200
Sub-Recipe 1: 152 repetitions [cycles] resulting in an average etch dept of ca. 65-70 µm									
DEPa	1.45	50	0	1500	0	10	0	10	200
DEPb	0.3	15	0	1500	10	10	0	200	10
ETCH1	0.9	30	0	1800	60	10	0	200	10
ETCH2a	2.2	35	0	1800	0	10	0	200	10
ETCH2b	0.3	70	0	1800	0	10	0	10	200
Sub-Recipe 2: 152 repetitions [cycles] resulting in an average (cumulative) etch dept of ca. 120 -130 µm									
DEPa	1.55	50	0	1500	0	10	0	10	200
DEPb	0.3	15	0	1500	10	10	0	200	10
ETCH1	0.95	30	0	1800	60	10	0	200	10
ETCH2a	2.2	35	0	1800	0	10	0	200	10
ETCH2b	0.3	70	0	1800	0	10	0	10	200
Sub-Recipe 3: ca. 80 (+/- X) repetitions [cycles] resulting in an average (cumulative) etch dept of ca. 145-155 µm									
DEPa	1.65	50	0	1500	0	10	0	10	200
DEPb	0.3	15	0	1500	10	10	0	200	10
ETCH1	1.0	30	0	1800	60	10	0	200	10
ETCH2a	2.2	35	0	1800	0	10	0	200	10
ETCH2b	0.3	70	0	1800	0	10	0	10	200
PUMP DOWN	30	0	0	0	0	0	0	0	0

References

[1] T. S. Nowack *et al.*, "Terahertz polarimetry with a monolithic metasurface," *Optics Letters*, vol. 47, no. 16, 2022, doi: 10.1364/ol.463143.

[2] A. C. D. Yash D. Shah, James P. Grant, David R. S. Cumming, Charles Altuzarra, Thomas S. Nowack, Ashley Lyons, Matteo Clerici, Daniele Faccio, "An All-dielectric Metasurface Polarimeter," *ACS Photonics (Accepted Manuscript)*, 2022, doi: 10.48550/arXiv.2203.05590.

[3] T. S. Nowack *et al.*, "Metasurface Optics with on-axis Polarization Control for Terahertz Sensing Applications," *submitted to IEEE Transactions on Terahertz Science and Technology on 21.12.22*, 2022.

[4] S. S. Dhillon *et al.*, "The 2017 terahertz science and technology roadmap," *Journal of Physics D: Applied Physics*, vol. 50, no. 4, 2017, doi: 10.1088/1361-6463/50/4/043001.

[5] K. Sengupta, T. Nagatsuma, and D. M. Mittleman, "Terahertz integrated electronic and hybrid electronic–photonic systems," *Nature Electronics*, vol. 1, no. 12, pp. 622-635, 2018, doi: 10.1038/s41928-018-0173-2.

[6] H. Guerboukha, K. Nallappan, and M. Skorobogatiy, "Toward real-time terahertz imaging," *Advances in Optics and Photonics*, vol. 10, no. 4, 2018, doi: 10.1364/aop.10.000843.

[7] G. Valusis, A. Lisauskas, H. Yuan, W. Knap, and H. G. Roskos, "Roadmap of Terahertz Imaging 2021," *Sensors (Basel)*, vol. 21, no. 12, Jun 14 2021, doi: 10.3390/s21124092.

[8] Y. Cheng, Y. Wang, Y. Niu, and Z. Zhao, "Concealed object enhancement using multi-polarization information for passive millimeter and terahertz wave security screening," *Opt Express*, vol. 28, no. 5, pp. 6350-6366, Mar 2 2020, doi: 10.1364/OE.384029.

[9] H. Feng *et al.*, "A passive video-rate terahertz human body imager with real-time calibration for security applications," *Applied Physics B*, vol. 126, no. 8, 2020, doi: 10.1007/s00340-020-07496-3.

[10] A. V. Shchepetilnikov *et al.*, "New Ultra-Fast Sub-Terahertz Linear Scanner for Postal Security Screening," *Journal of Infrared, Millimeter, and Terahertz Waves*, vol. 41, no. 6, pp. 655-664, 2020, doi: 10.1007/s10762-020-00692-4.

[11] M. Kato, S. R. Tripathi, K. Murate, K. Imayama, and K. Kawase, "Non-destructive drug inspection in covering materials using a terahertz spectral imaging system with injection-seeded terahertz parametric generation and detection," *Opt Express*, vol. 24, no. 6, pp. 6425-32, Mar 21 2016, doi: 10.1364/OE.24.006425.

[12] Y. Peng, C. Shi, Y. Zhu, M. Gu, and S. Zhuang, "Terahertz spectroscopy in biomedical field: a review on signal-to-noise ratio improvement," *PhotoniX*, vol. 1, no. 1, 2020, doi: 10.1186/s43074-020-00011-z.

[13] A. I. Nikitkina *et al.*, "Terahertz radiation and the skin: a review," *J Biomed Opt*, vol. 26, no. 4, Feb 2021, doi: 10.1117/1.JBO.26.4.043005.

[14] K. Lee *et al.*, "Measuring water contents in animal organ tissues using terahertz spectroscopic imaging," *Biomed Opt Express*, vol. 9, no. 4, pp. 1582-1589, Apr 1 2018, doi: 10.1364/BOE.9.001582.

[15] K. Akiyama *et al.*, "First M87 Event Horizon Telescope Results. II. Array and Instrumentation," *The Astrophysical Journal*, vol. 875, no. 1, 2019, doi: 10.3847/2041-8213/ab0c96.

[16] N. Siegler *et al.*, "Origins Space Telescope: the far infrared imager and polarimeter FIP," in *Space Telescopes and Instrumentation 2018: Optical, Infrared, and Millimeter Wave*, 2018, doi: 10.1117/12.2312626.

[17] C. Kulesa, "Terahertz Spectroscopy for Astronomy: From Comets to Cosmology," *IEEE Transactions on Terahertz Science and Technology*, vol. 1, no. 1, pp. 232-240, 2011, doi: 10.1109/tthz.2011.2159648.

[18] D.-H. Han and L.-H. Kang, "Nondestructive evaluation of GFRP composite including multi-delamination using THz spectroscopy and imaging," *Composite Structures*, vol. 185, pp. 161-175, 2018, doi: 10.1016/j.compstruct.2017.11.012.

[19] Y. H. Tao, A. J. Fitzgerald, and V. P. Wallace, "Non-Contact, Non-Destructive Testing in Various Industrial Sectors with Terahertz Technology," *Sensors (Basel)*, vol. 20, no. 3, Jan 28 2020, doi: 10.3390/s20030712.

[20] J. Dong *et al.*, "Visualization of subsurface damage in woven carbon fiber-reinforced composites using polarization-sensitive terahertz imaging," *NDT & E International*, vol. 99, pp. 72-79, 2018, doi: 10.1016/j.ndteint.2018.07.001.

[21] P. Fosodeder, S. Hubmer, A. Ploier, R. Ramlau, S. van Frank, and C. Rankl, "Phase-contrast THz-CT for non-destructive testing," *Opt Express*, vol. 29, no. 10, pp. 15711-15723, May 10 2021, doi: 10.1364/OE.422961.

[22] J. Dong, B. Kim, A. Locquet, P. McKeon, N. Declercq, and D. S. Citrin, "Nondestructive evaluation of forced delamination in glass fiber-reinforced composites by terahertz and ultrasonic waves," *Composites Part B: Engineering*, vol. 79, pp. 667-675, 2015, doi: 10.1016/j.compositesb.2015.05.028.

[23] P. Han, X. Wang, and Y. Zhang, "Time-Resolved Terahertz Spectroscopy Studies on 2D Van der Waals Materials," *Advanced Optical Materials*, vol. 8, no. 3, 2019, doi: 10.1002/adom.201900533.

[24] D. Zhao and E. E. M. Chia, "Free Carrier, Exciton, and Phonon Dynamics in Lead-Halide Perovskites Studied with Ultrafast Terahertz Spectroscopy," *Advanced Optical Materials*, vol. 8, no. 3, 2019, doi: 10.1002/adom.201900783.

[25] P. Kužel and H. Němec, "Terahertz Spectroscopy of Nanomaterials: a Close Look at Charge-Carrier Transport," *Advanced Optical Materials*, vol. 8, no. 3, 2019, doi: 10.1002/adom.201900623.

[26] L. Afsah-Hejri, E. Akbari, A. Toudeshki, T. Homayouni, A. Alizadeh, and R. Ehsani, "Terahertz spectroscopy and imaging: A review on agricultural applications," *Computers and Electronics in Agriculture*, vol. 177, 2020, doi: 10.1016/j.compag.2020.105628.

[27] M. S. Vitiello and A. Tredicucci, "Physics and technology of Terahertz quantum cascade lasers," *Advances in Physics: X*, vol. 6, no. 1, 2021, doi: 10.1080/23746149.2021.1893809.

[28] V. S. Philipp Kuehne, Nerijus Armakavicius, Mathias Schubert, and Vanya Darakchieva, "Stealth technology-based Terahertz frequency-domain ellipsometry instrumentation," *IEEE Transactions on Terahertz Science and Technology*, 2017, doi: 10.48550/arXiv.1712.05283.

[29] P. D. Cunningham *et al.*, "Broadband terahertz characterization of the refractive index and absorption of some important polymeric and organic electro-optic materials," *Journal of Applied Physics*, vol. 109, no. 4, pp. 043505-043505-5, 2011, doi: 10.1063/1.3549120.

[30] J. P. Balthasar Mueller, N. A. Rubin, R. C. Devlin, B. Groever, and F. Capasso, "Metasurface Polarization Optics: Independent Phase Control of Arbitrary

Orthogonal States of Polarization," *Phys Rev Lett,* vol. 118, no. 11, p. 113901, Mar 17 2017, doi: 10.1103/PhysRevLett.118.113901.

[31] A. Arbabi, Y. Horie, M. Bagheri, and A. Faraon, "Dielectric metasurfaces for complete control of phase and polarization with subwavelength spatial resolution and high transmission," *Nat Nanotechnol,* vol. 10, no. 11, pp. 937-43, Nov 2015, doi: 10.1038/nnano.2015.186.

[32] N. A. Rubin, G. D'Aversa, P. Chevalier, Z. Shi, W. T. Chen, and F. Capasso, "Matrix Fourier optics enables a compact full-Stokes polarization camera," *Science,* vol. 365, no. 6448, Jul 5 2019, doi: 10.1126/science.aax1839.

[33] A. H. Dorrah, N. A. Rubin, A. Zaidi, M. Tamagnone, and F. Capasso, "Metasurface optics for on-demand polarization transformations along the optical path," *Nature Photonics,* vol. 15, no. 4, pp. 287-296, 2021, doi: 10.1038/s41566-020-00750-2.

[34] M. Reid and R. Fedosejevs, "Terahertz birefringence and attenuation properties of wood and paper," *Appl Opt,* vol. 45, no. 12, pp. 2766-72, Apr 20 2006, doi: 10.1364/ao.45.002766.

[35] E. Castro-Camus, "Polarization-Resolved Terahertz Time-Domain Spectroscopy," *Journal of Infrared, Millimeter, and Terahertz Waves,* vol. 33, no. 4, pp. 418-430, 2011, doi: 10.1007/s10762-011-9856-8.

[36] M. Kashima, S. Tsuchikawa, and T. Inagaki, "Simultaneous detection of density, moisture content and fiber direction of wood by THz time-domain spectroscopy," *Journal of Wood Science,* vol. 66, no. 1, 2020, doi: 10.1186/s10086-020-01874-3.

[37] M. B. Johnston, E. Castro-Camus, J. Lloyd-Hughes, M. D. Fraser, H. H. Tan, and C. Jagadish, "Polarisation-sensitive terahertz detectors," presented at the 2005 Joint 30th International Conference on Infrared and Millimeter Waves and 13th International Conference on Terahertz Electronics, 2005.

[38] S. Watanabe, "Terahertz Polarization Imaging and Its Applications," *Photonics,* vol. 5, no. 4, 2018, doi: 10.3390/photonics5040058.

[39] E. R. Brown, "Fundamentals of Terrestrial Millimeter-Wave and THz Remote Sensing," *International Journal of High Speed Electronics and Systems,* vol. 13, no. 04, pp. 995-1097, 2011, doi: 10.1142/s0129156403002125.

[40] D. V. Mifsud, P. A. Hailey, A. Traspas Muiña, O. Auriacombe, N. J. Mason, and S. Ioppolo, "The Role of Terahertz and Far-IR Spectroscopy in Understanding the Formation and Evolution of Interstellar Prebiotic Molecules," *Frontiers in Astronomy and Space Sciences,* vol. 8, 2021, doi: 10.3389/fspas.2021.757619.

[41] A. Li, "The Warm, Cold and Very Cold Dusty Universe," in *Penetrating Bars Through Masks of Cosmic Dust*, Johannesburg, South Afrika, 2004.

[42] J. M. Marr and F. P. Wilkin, "A better presentation of Planck's radiation law," *American Journal of Physics,* vol. 80, no. 5, pp. 399-405, 2012, doi: 10.1119/1.3696974.

[43] C. M. Armstrong, "The truth about terahertz," *IEEE Spectrum,* vol. 49, no. 9, pp. 36-41, 2012, doi: 10.1109/mspec.2012.6281131.

[44] C. Eiroa *et al.,* "Herschel discovery of a new class of cold, faint debris discs," *Astronomy & Astrophysics,* vol. 536, 2011, doi: 10.1051/0004-6361/201117797.

[45] K. Akiyama *et al.,* "First M87 Event Horizon Telescope Results. IV. Imaging the Central Supermassive Black Hole," *The Astrophysical Journal,* vol. 875, no. 1, 2019, doi: 10.3847/2041-8213/ab0e85.

[46] X. Yang *et al.,* "Biomedical Applications of Terahertz Spectroscopy and Imaging," *Trends Biotechnol,* vol. 34, no. 10, pp. 810-824, Oct 2016, doi: 10.1016/j.tibtech.2016.04.008.

[47] K. Ajito and Y. Ueno, "THz Chemical Imaging for Biological Applications," *IEEE Transactions on Terahertz Science and Technology,* vol. 1, no. 1, pp. 293-300, 2011, doi: 10.1109/tthz.2011.2159562.

[48] M. Naftaly, "Broadband terahertz measurements of optical properties of materials," in *2022 Microwave Mediterranean Symposium (MMS)*, 2022, pp. 1-4, doi: 10.1109/mms55062.2022.9825577.

[49] M. Naftaly, N. Vieweg, and A. Deninger, "Industrial Applications of Terahertz Sensing: State of Play," *Sensors (Basel),* vol. 19, no. 19, Sep 27 2019, doi: 10.3390/s19194203.

[50] D. Ye *et al.*, "Characterization of thermal barrier coatings microstructural features using terahertz spectroscopy," *Surface and Coatings Technology,* vol. 394, 2020, doi: 10.1016/j.surfcoat.2020.125836.

[51] J. A. Spies *et al.*, "Terahertz Spectroscopy of Emerging Materials," *The Journal of Physical Chemistry C,* vol. 124, no. 41, pp. 22335-22346, 2020, doi: 10.1021/acs.jpcc.0c06344.

[52] A. V. Ewing and S. G. Kazarian, "Recent advances in the applications of vibrational spectroscopic imaging and mapping to pharmaceutical formulations," *Spectrochim Acta A Mol Biomol Spectrosc,* vol. 197, pp. 10-29, May 15 2018, doi: 10.1016/j.saa.2017.12.055.

[53] P. Bawuah *et al.*, "Terahertz study on porosity and mass fraction of active pharmaceutical ingredient of pharmaceutical tablets," *Eur J Pharm Biopharm,* vol. 105, pp. 122-33, Aug 2016, doi: 10.1016/j.ejpb.2016.06.007.

[54] M. O. AlNabooda, R. M. Shubair, N. R. Rishani, and G. Aldabbagh, "Terahertz Spectroscopy and Imaging for the Detection and Identification of Illicit Drugs," (in English), *2017 Sensors Networks Smart and Emerging Technologies (Senset)*, pp. 1-4, 2017, doi: 10.1109/SENSET.2017.8125065.

[55] J. F. Federici *et al.*, "THz imaging and sensing for security applications—explosives, weapons and drugs," *Semiconductor Science and Technology,* vol. 20, no. 7, pp. S266-S280, 2005, doi: 10.1088/0268-1242/20/7/018.

[56] J. S. Melinger, Y. Yang, M. Mandehgar, and D. Grischkowsky, "THz detection of small molecule vapors in the atmospheric transmission windows," *Opt Express,* vol. 20, no. 6, pp. 6788-807, Mar 12 2012, doi: 10.1364/OE.20.006788.

[57] A. D'Arco *et al.*, "Terahertz continuous wave spectroscopy: a portable advanced method for atmospheric gas sensing," *Optics Express,* vol. 30, no. 11, 2022, doi: 10.1364/oe.456022.

[58] A. Cuisset *et al.*, "Terahertz Rotational Spectroscopy of Greenhouse Gases Using Long Interaction Path-Lengths," *Applied Sciences,* vol. 11, no. 3, 2021, doi: 10.3390/app11031229.

[59] X. Yang *et al.*, "Terahertz spectroscopy for the isothermal detection of bacterial DNA by magnetic bead-based rolling circle amplification," *Analyst,* vol. 142, no. 24, pp. 4661-4669, Dec 4 2017, doi: 10.1039/c7an01438d.

[60] L. Wei, L. Yu, H. Jiaoqi, H. Guorong, Z. Yang, and F. Weiling, "Application of terahertz spectroscopy in biomolecule detection," *Frontiers in Laboratory Medicine,* vol. 2, no. 4, pp. 127-133, 2018, doi: 10.1016/j.flm.2019.05.001.

[61] I. F. Akyildiz, C. Han, Z. Hu, S. Nie, and J. M. Jornet, "Terahertz Band Communication: An Old Problem Revisited and Research Directions for the Next Decade," *IEEE Transactions on Communications,* vol. 70, no. 6, pp. 4250-4285, 2022, doi: 10.1109/tcomm.2022.3171800.

[62] H. Cheon, H. J. Yang, S. H. Lee, Y. A. Kim, and J. H. Son, "Terahertz molecular resonance of cancer DNA," *Sci Rep,* vol. 6, p. 37103, Nov 15 2016, doi: 10.1038/srep37103.

[63] M. Danciu *et al.*, "Terahertz Spectroscopy and Imaging: A Cutting-Edge Method for Diagnosing Digestive Cancers," *Materials (Basel),* vol. 12, no. 9, May 9 2019, doi: 10.3390/ma12091519.

[64] K. Wang, D.-W. Sun, and H. Pu, "Emerging non-destructive terahertz spectroscopic imaging technique: Principle and applications in the agri-food industry," *Trends in Food Science & Technology,* vol. 67, pp. 93-105, 2017, doi: 10.1016/j.tifs.2017.06.001.

[65] A. Ren *et al.*, "State-of-the-art in terahertz sensing for food and water security – A comprehensive review," *Trends in Food Science & Technology,* vol. 85, pp. 241-251, 2019, doi: 10.1016/j.tifs.2019.01.019.

[66] B. You, C. Y. Chen, C. P. Yu, P. H. Wang, and J. Y. Lu, "Frequency-dependent skin penetration depth of terahertz radiation determined by water sorption-desorption," *Opt Express,* vol. 26, no. 18, pp. 22709-22721, Sep 3 2018, doi: 10.1364/OE.26.022709.

[67] R. A. Lewis, "A review of terahertz sources," *Journal of Physics D: Applied Physics,* vol. 47, no. 37, 2014, doi: 10.1088/0022-3727/47/37/374001.

[68] A. Siemion, "Terahertz Diffractive Optics—Smart Control over Radiation," *Journal of Infrared, Millimeter, and Terahertz Waves,* vol. 40, no. 5, pp. 477-499, 2019, doi: 10.1007/s10762-019-00581-5.

[69] E. Castro-Camus, M. Koch, and A. I. Hernandez-Serrano, "Additive manufacture of photonic components for the terahertz band," *Journal of Applied Physics,* vol. 127, no. 21, 2020, doi: 10.1063/1.5140270.

[70] M. Naftaly, S. Chick, G. Matmon, and B. Murdin, "Refractive Indices of Ge and Si at Temperatures between 4–296 K in the 4–8 THz Region," *Applied Sciences,* vol. 11, no. 2, 2021, doi: 10.3390/app11020487.

[71] A. Siemion, "The Magic of Optics-An Overview of Recent Advanced Terahertz Diffractive Optical Elements," *Sensors (Basel),* vol. 21, no. 1, Dec 26 2020, doi: 10.3390/s21010100.

[72] R. Kohler *et al.*, "Terahertz semiconductor-heterostructure laser," *Nature,* vol. 417, no. 6885, pp. 156-9, May 9 2002, doi: 10.1038/417156a.

[73] M. S. Vitiello, G. Scalari, B. Williams, and P. De Natale, "Quantum cascade lasers: 20 years of challenges," *Opt Express,* vol. 23, no. 4, pp. 5167-82, Feb 23 2015, doi: 10.1364/OE.23.005167.

[74] G. Liang, T. Liu, and Q. J. Wang, "Recent Developments of Terahertz Quantum Cascade Lasers," *IEEE Journal of Selected Topics in Quantum Electronics,* vol. 23, no. 4, pp. 1-18, 2017, doi: 10.1109/jstqe.2016.2625982.

[75] M. A. Belkin and F. Capasso, "New frontiers in quantum cascade lasers: high performance room temperature terahertz sources," *Physica Scripta,* vol. 90, no. 11, 2015, doi: 10.1088/0031-8949/90/11/118002.

[76] L. Bosco, M. Franckié, G. Scalari, M. Beck, A. Wacker, and J. Faist, "Thermoelectrically cooled THz quantum cascade laser operating up to 210 K," *Applied Physics Letters,* vol. 115, no. 1, 2019, doi: 10.1063/1.5110305.

[77] A. Khalatpour, A. K. Paulsen, C. Deimert, Z. R. Wasilewski, and Q. Hu, "High-power portable terahertz laser systems," *Nature Photonics,* vol. 15, no. 1, pp. 16-20, 2020, doi: 10.1038/s41566-020-00707-5.

[78] Q. Y. Lu, S. Slivken, N. Bandyopadhyay, Y. Bai, and M. Razeghi, "Widely tunable room temperature semiconductor terahertz source," *Applied Physics Letters*, vol. 105, no. 20, 2014, doi: 10.1063/1.4902245.

[79] A. Al-Khalidi *et al.*, "Resonant Tunneling Diode Terahertz Sources With up to 1 mW Output Power in the J-Band," *IEEE Transactions on Terahertz Science and Technology*, vol. 10, no. 2, pp. 150-157, 2020, doi: 10.1109/tthz.2019.2959210.

[80] S. Rout and S. Sonkusale, "Introduction," in *Active Metamaterials: Terahertz Modulators and Detectors*. Cham: Springer International Publishing, 2017, pp. 1-25.

[81] J. Sun, *Field-effect Self-mixing Terahertz Detectors* (Springer Theses). Springer, 2016.

[82] A. Crocker, H. A. Gebbie, M. F. Kimmitt, and L. E. S. Mathias, "Stimulated Emission in the Far Infra-Red," *Nature*, vol. 201, no. 4916, pp. 250-251, 1964, doi: 10.1038/201250a0.

[83] P. Chevalier *et al.*, "Widely tunable compact terahertz gas lasers," *Science*, vol. 366, no. 6467, pp. 856-860, Nov 15 2019, doi: 10.1126/science.aay8683.

[84] F. Wang *et al.*, "A high-efficiency regime for gas-phase terahertz lasers," *Proc Natl Acad Sci U S A*, vol. 115, no. 26, pp. 6614-6619, Jun 26 2018, doi: 10.1073/pnas.1803261115.

[85] S. L. Chua *et al.*, "Spatio-temporal theory of lasing action in optically-pumped rotationally excited molecular gases," *Opt Express*, vol. 19, no. 8, pp. 7513-29, Apr 11 2011, doi: 10.1364/OE.19.007513.

[86] M.-H. Mammez *et al.*, "Optically Pumped Terahertz Molecular Laser: Gain Factor and Validation up to 5.5 THz," *Advanced Photonics Research*, vol. 3, no. 4, 2022, doi: 10.1002/adpr.202100263.

[87] S. R. Kasjoo, M. B. M. Mokhar, N. F. Zakaria, and N. J. Juhari, "A brief overview of detectors used for terahertz imaging systems," in *The 2nd International Conference on Applied Photonics and Electronics 2019 (InCAPE 2019)*, 2020, doi: 10.1063/1.5142112.

[88] M. Chen, Y. Wang, X. Wang, and L. Li, "Editorial: Advances in Terahertz Detection and Imaging," *Frontiers in Physics*, vol. 10, 2022, doi: 10.3389/fphy.2022.855623.

[89] F. Simoens, "Buyer's guide for a terahertz (THz) camera," *Photoniques Special EOS Issue*, no. 2, pp. 58-62, 2018.

[90] F. Sizov and A. Rogalski, "THz detectors," *Progress in Quantum Electronics*, vol. 34, no. 5, pp. 278-347, 2010, doi: 10.1016/j.pquantelec.2010.06.002.

[91] M. Hangyo, "Development and future prospects of terahertz technology," *Japanese Journal of Applied Physics*, vol. 54, no. 12, 2015, doi: 10.7567/jjap.54.120101.

[92] N. Oda, "Uncooled bolometer-type Terahertz focal plane array and camera for real-time imaging," *Comptes Rendus Physique*, vol. 11, no. 7-8, pp. 496-509, 2010, doi: 10.1016/j.crhy.2010.05.001.

[93] D. Dufour *et al.*, "Review of terahertz technology development at INO," *Journal of Infrared, Millimeter, and Terahertz Waves*, vol. 36, no. 10, pp. 922-946, 2015, doi: 10.1007/s10762-015-0181-5.

[94] F. Simoens, J. Meilhan, and J.-A. Nicolas, "Terahertz Real-Time Imaging Uncooled Arrays Based on Antenna-Coupled Bolometers or FET Developed at CEA-Leti," *Journal of Infrared, Millimeter, and Terahertz Waves*, vol. 36, no. 10, pp. 961-985, 2015, doi: 10.1007/s10762-015-0197-x.

[95] Q. Li, S. H. Ding, R. Yao, and Q. Wang, "Real-time terahertz scanning imaging by use of a pyroelectric array camera and image denoising," *J Opt Soc Am A Opt Image Sci Vis*, vol. 27, no. 11, pp. 2381-6, Nov 1 2010, doi: 10.1364/JOSAA.27.002381.

[96] S. H. Ding, Q. Li, Y. D. Li, and Q. Wang, "Continuous-wave terahertz digital holography by use of a pyroelectric array camera," *Opt Lett,* vol. 36, no. 11, pp. 1993-5, Jun 1 2011, doi: 10.1364/OL.36.001993.

[97] E. Hack, L. Valzania, G. Gaumann, M. Shalaby, C. P. Hauri, and P. Zolliker, "Comparison of Thermal Detector Arrays for Off-Axis THz Holography and Real-Time THz Imaging," *Sensors (Basel),* vol. 16, no. 2, p. 221, Feb 6 2016, doi: 10.3390/s16020221.

[98] M. J. Golay, "The theoretical and practical sensitivity of the pneumatic infra-red detector," *Rev Sci Instrum,* vol. 20, no. 11, pp. 816-20, Nov 1949, doi: 10.1063/1.1741396.

[99] A. Fernandez Olvera *et al.*, "International System of Units (SI) Traceable Noise-Equivalent Power and Responsivity Characterization of Continuous Wave ErAs:InGaAs Photoconductive Terahertz Detectors," *Photonics,* vol. 6, no. 1, 2019, doi: 10.3390/photonics6010015.

[100] R. A. Lewis, "A review of terahertz detectors," *Journal of Physics D: Applied Physics,* vol. 52, no. 43, 2019, doi: 10.1088/1361-6463/ab31d5.

[101] D. H. Auston, K. P. Cheung, and P. R. Smith, "Picosecond photoconducting Hertzian dipoles," *Applied Physics Letters,* vol. 45, no. 3, pp. 284-286, 1984, doi: 10.1063/1.95174.

[102] P. R. Smith, D. H. Auston, and M. C. Nuss, "Subpicosecond photoconducting dipole antennas," *IEEE Journal of Quantum Electronics,* vol. 24, no. 2, pp. 255-260, 1988, doi: 10.1109/3.121.

[103] C. Fattinger and D. Grischkowsky, "Terahertz beams," *Applied Physics Letters,* vol. 54, no. 6, pp. 490-492, 1989, doi: 10.1063/1.100958.

[104] X. C. Zhang and D. H. Auston, "Optoelectronic measurement of semiconductor surfaces and interfaces with femtosecond optics," *Journal of Applied Physics,* vol. 71, no. 1, pp. 326-338, 1992, doi: 10.1063/1.350710.

[105] X. C. Zhang and D. H. Auston, "Optically Induced THz Electromagnetic Radiation From Planar Photoconducting Structures," *Journal of Electromagnetic Waves and Applications,* vol. 6, no. 1-4, pp. 85-106, 2012, doi: 10.1163/156939392x01039.

[106] P. U. Jepsen, R. H. Jacobsen, and S. R. Keiding, "Generation and detection of terahertz pulses from biased semiconductor antennas," *Journal of the Optical Society of America B,* vol. 13, no. 11, 1996, doi: 10.1364/josab.13.002424.

[107] Y. C. Shen, P. C. Upadhya, E. H. Linfield, H. E. Beere, and A. G. Davies, "Ultrabroadband terahertz radiation from low-temperature-grown GaAs photoconductive emitters," *Applied Physics Letters,* vol. 83, no. 15, pp. 3117-3119, 2003, doi: 10.1063/1.1619223.

[108] R. J. Hwu, D. H. Wu, D. L. Woolard, and J. R. Meyer, "Terahertz emission, detection, and military applications," presented at the Terahertz for Military and Security Applications II, 2004.

[109] W. Qi and Z. Xi-Cheng, "Design and characterization of traveling-wave electrooptic terahertz sensors," *IEEE Journal of Selected Topics in Quantum Electronics,* vol. 2, no. 3, pp. 693-700, 1996, doi: 10.1109/2944.571769.

[110] Q. Wu and X. C. Zhang, "Free-space electro-optic sampling of terahertz beams," *Applied Physics Letters,* vol. 67, no. 24, pp. 3523-3525, 1995, doi: 10.1063/1.114909.

[111] P. U. Jepsen, C. Winnewisser, M. Schall, V. V. Schyja, S. R. Keiding, and H. Helm, "Detection of THz pulses by phase retardation in lithium tantalate," *Phys Rev E Stat*

Phys Plasmas Fluids Relat Interdiscip Topics, vol. 53, no. 4, pp. R3052-R3054, Apr 1996, doi: 10.1103/physreve.53.r3052.

[112] A. Nahata, D. H. Auston, T. F. Heinz, and C. Wu, "Coherent detection of freely propagating terahertz radiation by electro-optic sampling," *Applied Physics Letters*, vol. 68, no. 2, pp. 150-152, 1996, doi: 10.1063/1.116130.

[113] Q. Wu, T. D. Hewitt, and X. C. Zhang, "Two-dimensional electro-optic imaging of THz beams," *Applied Physics Letters*, vol. 69, no. 8, pp. 1026-1028, 1996, doi: 10.1063/1.116920.

[114] Z. G. Lu, P. Campbell, and X. C. Zhang, "Free-space electro-optic sampling with a high-repetition-rate regenerative amplified laser," *Applied Physics Letters*, vol. 71, no. 5, pp. 593-595, 1997, doi: 10.1063/1.119803.

[115] X. Lu and X. C. Zhang, "Balanced terahertz wave air-biased-coherent-detection," *Applied Physics Letters*, vol. 98, no. 15, 2011, doi: 10.1063/1.3574535.

[116] J. Dai, X. Xie, and X. C. Zhang, "Detection of broadband terahertz waves with a laser-induced plasma in gases," *Phys Rev Lett*, vol. 97, no. 10, p. 103903, Sep 8 2006, doi: 10.1103/PhysRevLett.97.103903.

[117] J. Dai, J. Liu, and X.-C. Zhang, "Terahertz Wave Air Photonics: Terahertz Wave Generation and Detection With Laser-Induced Gas Plasma," *IEEE Journal of Selected Topics in Quantum Electronics*, vol. 17, no. 1, pp. 183-190, 2011, doi: 10.1109/jstqe.2010.2047007.

[118] R. Han *et al.*, "Active Terahertz Imaging Using Schottky Diodes in CMOS: Array and 860-GHz Pixel," *IEEE Journal of Solid-State Circuits*, vol. 48, no. 10, pp. 2296-2308, 2013, doi: 10.1109/jssc.2013.2269856.

[119] S. P. Han *et al.*, "Real-time continuous-wave terahertz line scanner based on a compact 1 x 240 InGaAs Schottky barrier diode array detector," *Opt Express*, vol. 22, no. 23, pp. 28977-83, Nov 17 2014, doi: 10.1364/OE.22.028977.

[120] R. Tauk *et al.*, "Plasma wave detection of terahertz radiation by silicon field effects transistors: Responsivity and noise equivalent power," *Applied Physics Letters*, vol. 89, no. 25, 2006, doi: 10.1063/1.2410215.

[121] W. Knap *et al.*, "Field Effect Transistors for Terahertz Detection: Physics and First Imaging Applications," *Journal of Infrared, Millimeter, and Terahertz Waves*, 2009, doi: 10.1007/s10762-009-9564-9.

[122] R. Al Hadi *et al.*, "A 1 k-Pixel Video Camera for 0.7–1.1 Terahertz Imaging Applications in 65-nm CMOS," *IEEE Journal of Solid-State Circuits*, vol. 47, no. 12, pp. 2999-3012, 2012, doi: 10.1109/jssc.2012.2217851.

[123] M. Naftaly and R. Dudley, "Terahertz reflectivities of metal-coated mirrors," *Appl Opt*, vol. 50, no. 19, pp. 3201-4, Jul 1 2011, doi: 10.1364/AO.50.003201.

[124] S. Sung, "Terahertz Imaging and Remote Sensing Design for Applications in Medical Imaging," University of California, 2013.

[125] V. E. Rogalin, I. A. Kaplunov, and G. I. Kropotov, "Optical Materials for the THz Range," *Optics and Spectroscopy*, vol. 125, no. 6, pp. 1053-1064, 2019, doi: 10.1134/s0030400x18120172.

[126] J. Dai, J. Zhang, W. Zhang, and D. Grischkowsky, "Terahertz time-domain spectroscopy characterization of the far-infrared absorption and index of refraction of high-resistivity, float-zone silicon," (in English), *Journal of the Optical Society of America B*, vol. 21, no. 7, pp. 1379-1386, Jul 2004, doi: 10.1364/josab.21.001379.

[127] T. S. Hartwick, D. T. Hodges, D. H. Barker, and F. B. Foote, "Far infrared imagery," *Appl Opt*, vol. 15, no. 8, pp. 1919-22, Aug 1 1976, doi: 10.1364/AO.15.001919.

[128] D. M. Mittleman, "Perspective: Terahertz science and technology," *Journal of Applied Physics*, vol. 122, no. 23, 2017, doi: 10.1063/1.5007683.
[129] D. M. Mittleman, "Twenty years of terahertz imaging [Invited]," *Opt Express*, vol. 26, no. 8, pp. 9417-9431, Apr 16 2018, doi: 10.1364/OE.26.009417.
[130] B. B. Hu and M. C. Nuss, "Imaging with terahertz waves," *Opt Lett*, vol. 20, no. 16, p. 1716, Aug 15 1995, doi: 10.1364/ol.20.001716.
[131] J.-H. Son, S. J. Oh, and H. Cheon, "Potential clinical applications of terahertz radiation," *Journal of Applied Physics*, vol. 125, no. 19, 2019, doi: 10.1063/1.5080205.
[132] J. H. Son, "Principle and applications of terahertz molecular imaging," *Nanotechnology*, vol. 24, no. 21, p. 214001, May 31 2013, doi: 10.1088/0957-4484/24/21/214001.
[133] Q. Sun, Y. He, K. Liu, S. Fan, E. P. J. Parrott, and E. Pickwell-MacPherson, "Recent advances in terahertz technology for biomedical applications," *Quant Imaging Med Surg*, vol. 7, no. 3, pp. 345-355, Jun 2017, doi: 10.21037/qims.2017.06.02.
[134] A. Redo-Sanchez, N. Laman, B. Schulkin, and T. Tongue, "Review of Terahertz Technology Readiness Assessment and Applications," *Journal of Infrared, Millimeter, and Terahertz Waves*, vol. 34, no. 9, pp. 500-518, 2013, doi: 10.1007/s10762-013-9998-y.
[135] A. D'Arco *et al.*, "Characterization of volatile organic compounds (VOCs) in their liquid-phase by terahertz time-domain spectroscopy," *Biomed Opt Express*, vol. 11, no. 1, pp. 1-7, Jan 1 2020, doi: 10.1364/BOE.11.000001.
[136] H. Zhang *et al.*, "An Infrared-Induced Terahertz Imaging Modality for Foreign Object Detection in a Lightweight Honeycomb Composite Structure," *IEEE Transactions on Industrial Informatics*, vol. 14, no. 12, pp. 5629-5636, 2018, doi: 10.1109/tii.2018.2832244.
[137] J. Zhao, Y. E, K. Williams, X. C. Zhang, and R. W. Boyd, "Spatial sampling of terahertz fields with sub-wavelength accuracy via probe-beam encoding," *Light Sci Appl*, vol. 8, p. 55, 2019, doi: 10.1038/s41377-019-0166-6.
[138] L. Olivieri, J. S. Totero Gongora, A. Pasquazi, and M. Peccianti, "Time-Resolved Nonlinear Ghost Imaging," *ACS Photonics*, vol. 5, no. 8, pp. 3379-3388, 2018, doi: 10.1021/acsphotonics.8b00653.
[139] R. I. Stantchev, X. Yu, T. Blu, and E. Pickwell-MacPherson, "Real-time terahertz imaging with a single-pixel detector," *Nat Commun*, vol. 11, no. 1, p. 2535, May 21 2020, doi: 10.1038/s41467-020-16370-x.
[140] N. V. Petrov, M. S. Kulya, A. N. Tsypkin, V. G. Bespalov, and A. Gorodetsky, "Application of Terahertz Pulse Time-Domain Holography for Phase Imaging," *IEEE Transactions on Terahertz Science and Technology*, vol. 6, no. 3, pp. 464-472, 2016, doi: 10.1109/tthz.2016.2530938.
[141] M. Karaliunas *et al.*, "Non-destructive inspection of food and technical oils by terahertz spectroscopy," *Sci Rep*, vol. 8, no. 1, p. 18025, Dec 21 2018, doi: 10.1038/s41598-018-36151-3.
[142] J. Neu and C. A. Schmuttenmaer, "Tutorial: An introduction to terahertz time domain spectroscopy (THz-TDS)," *Journal of Applied Physics*, vol. 124, no. 23, 2018, doi: 10.1063/1.5047659.
[143] A. D'Arco, M. D. Di Fabrizio, V. Dolci, M. Petrarca, and S. Lupi, "THz Pulsed Imaging in Biomedical Applications," *Condensed Matter*, vol. 5, no. 2, 2020, doi: 10.3390/condmat5020025.

[144] M. Haaser, K. C. Gordon, C. J. Strachan, and T. Rades, "Terahertz pulsed imaging as an advanced characterisation tool for film coatings - a review," *Int J Pharm*, vol. 457, no. 2, pp. 510-20, Dec 5 2013, doi: 10.1016/j.ijpharm.2013.03.053.

[145] M. Bernier, F. Garet, and J.-L. Coutaz, "Determining the Complex Refractive Index of Materials in the Far-Infrared from Terahertz Time-Domain Data," in *Terahertz Spectroscopy - A Cutting Edge Technology*, 2017, ch. 7.

[146] M. Naftaly and R. E. Miles, "Terahertz Time-Domain Spectroscopy for Material Characterization," *Proceedings of the IEEE*, vol. 95, no. 8, pp. 1658-1665, 2007, doi: 10.1109/jproc.2007.898835.

[147] S. Augustin and H.-W. Hubers, "Phase-Sensitive Passive Terahertz Imaging at 5-m Stand-Off Distance," *IEEE Transactions on Terahertz Science and Technology*, vol. 4, no. 4, pp. 418-424, 2014, doi: 10.1109/tthz.2014.2327388.

[148] F. Xiang *et al.*, "Terahertz ptychography using a long-distance diffraction-free beam as the probe," *Opt Lett*, vol. 47, no. 2, pp. 238-241, Jan 15 2022, doi: 10.1364/OL.442964.

[149] L. Rong *et al.*, "Continuous-wave terahertz reflective ptychography by oblique illumination," *Opt Lett*, vol. 45, no. 16, pp. 4412-4415, Aug 15 2020, doi: 10.1364/OL.400506.

[150] L. Valzania, T. Feurer, P. Zolliker, and E. Hack, "Terahertz ptychography," *Opt Lett*, vol. 43, no. 3, pp. 543-546, Feb 1 2018, doi: 10.1364/OL.43.000543.

[151] L. Valzania, P. Zolliker, and E. Hack, "Coherent reconstruction of a textile and a hidden object with terahertz radiation," *Optica*, vol. 6, no. 4, 2019, doi: 10.1364/optica.6.000518.

[152] D. Wang *et al.*, "Multi-layered full-field phase imaging using continuous-wave terahertz ptychography," *Opt Lett*, vol. 45, no. 6, pp. 1391-1394, Mar 15 2020, doi: 10.1364/OL.384589.

[153] M. Locatelli *et al.*, "Real-time terahertz digital holography with a quantum cascade laser," *Sci Rep*, vol. 5, p. 13566, Aug 28 2015, doi: 10.1038/srep13566.

[154] J. B. Perraud, J. P. Guillet, O. Redon, M. Hamdi, F. Simoens, and P. Mounaix, "Shape-from-focus for real-time terahertz 3D imaging," *Opt Lett*, vol. 44, no. 3, pp. 483-486, Feb 1 2019, doi: 10.1364/OL.44.000483.

[155] Y. Shang *et al.*, "Terahertz image reconstruction based on compressed sensing and inverse Fresnel diffraction," *Opt Express*, vol. 27, no. 10, pp. 14725-14735, May 13 2019, doi: 10.1364/OE.27.014725.

[156] G. Klatt *et al.*, "High-Resolution Terahertz Spectrometer," *IEEE Journal of Selected Topics in Quantum Electronics*, vol. 17, no. 1, pp. 159-168, 2011, doi: 10.1109/jstqe.2010.2047635.

[157] A. Bartels *et al.*, "Ultrafast time-domain spectroscopy based on high-speed asynchronous optical sampling," *Rev Sci Instrum*, vol. 78, no. 3, p. 035107, Mar 2007, doi: 10.1063/1.2714048.

[158] Q. Wang, L. Xie, and Y. Ying, "Overview of imaging methods based on terahertz time-domain spectroscopy," *Applied Spectroscopy Reviews*, vol. 57, no. 3, pp. 249-264, 2021, doi: 10.1080/05704928.2021.1875480.

[159] A. S. Bendada, S.; Ibarra-Castanedo, C.; Akhloufi, M.; Caumes, J.P.; Pradere, C.; Batsale, J.C.; Maldague, X., "Subsurface imaging for panel paintings inspection: A comparative study of the ultraviolet, the visible, the infrared and the terahertz spectra," *Opto-Electron. Rev.*, vol. 23, pp. 88-99, 2015, doi: 10.1515/oere−2015−0013.

[160] M. Humphreys *et al.*, "Video-rate terahertz digital holographic imaging system," *Opt Express*, vol. 26, no. 20, pp. 25805-25813, Oct 1 2018, doi: 10.1364/OE.26.025805.
[161] H. Zhang *et al.*, "Non-destructive Investigation of Paintings on Canvas by Continuous Wave Terahertz Imaging and Flash Thermography," *Journal of Nondestructive Evaluation*, vol. 36, no. 2, 2017, doi: 10.1007/s10921-017-0414-8.
[162] S. Yeom *et al.*, "Real-time outdoor concealed-object detection with passive millimeter wave imaging," *Opt Express*, vol. 19, no. 3, pp. 2530-6, Jan 31 2011, doi: 10.1364/OE.19.002530.
[163] I. N. Dolganova, K. I. Zaytsev, A. A. Metelkina, and S. O. Yurchenko, "The active-passive continuous-wave terahertz imaging system," *Journal of Physics: Conference Series*, vol. 735, 2016, doi: 10.1088/1742-6596/735/1/012075.
[164] C. Mann, "Real Time Passive Imaging at 250GHz for Security: Technology and Phenomenology," in *2009 International Conference on Electromagnetics in Advanced Applications*, 2009: IEEE, pp. 1013-1015, doi: 10.1109/ICEAA.2009.5297813.
[165] T. Yang *et al.*, "Towards industrial applications of terahertz real-time imaging," in *Terahertz, RF, Millimeter, and Submillimeter-Wave Technology and Applications XI*, 2018, doi: 10.1117/12.2287709.
[166] P. Doradla, K. Alavi, C. Joseph, and R. Giles, "Detection of colon cancer by continuous-wave terahertz polarization imaging technique," *Journal of Biomedical Optics*, vol. 18, no. 9, 2013, doi: 10.1117/1.Jbo.18.9.090504.
[167] C. S. Joseph, R. Patel, V. A. Neel, R. H. Giles, and A. N. Yaroslavsky, "Imaging of ex vivo nonmelanoma skin cancers in the optical and terahertz spectral regions optical and terahertz skin cancers imaging," *J Biophotonics*, vol. 7, no. 5, pp. 295-303, May 2014, doi: 10.1002/jbio.201200111.
[168] Y. A. Garcia-Jomaso, D. L. Hernandez-Roa, J. Garduno-Mejia, C. G. Trevino-Palacios, O. V. Kolokoltsev, and N. Qureshi, "Sub-wavelength continuous THz imaging system based on interferometric detection," *Opt Express*, vol. 29, no. 12, pp. 19120-19125, Jun 7 2021, doi: 10.1364/OE.424163.
[169] M. Neshat and N. P. Armitage, "Terahertz time-domain spectroscopic ellipsometry: instrumentation and calibration," *Opt Express*, vol. 20, no. 27, pp. 29063-75, Dec 17 2012, doi: 10.1364/OE.20.029063.
[170] M. Fusco, "FDTD algorithm in curvilinear coordinates (EM scattering)," *IEEE Transactions on Antennas and Propagation*, vol. 38, no. 1, pp. 76-89, 1990, doi: 10.1109/8.43592.
[171] P. G. Huray, *Maxwell's Equations*. John Wiley & Sons, 2010.
[172] M. Zamboni-Rached, L. A. Ambrosio, A. H. Dorrah, and M. Mojahedi, "Structuring light under different polarization states within micrometer domains: exact analysis from the Maxwell equations," *Opt Express*, vol. 25, no. 9, pp. 10051-10056, May 1 2017, doi: 10.1364/OE.25.010051.
[173] I. Nadeem *et al.*, "A comprehensive survey on ‘circular polarized antennas’ for existing and emerging wireless communication technologies," *Journal of Physics D: Applied Physics*, vol. 55, no. 3, 2021, doi: 10.1088/1361-6463/ac2c36.
[174] G. P. Misson, "A Mueller matrix model of Haidinger's brushes," *Ophthalmic Physiol Opt*, vol. 23, no. 5, pp. 441-7, Sep 2003, doi: 10.1046/j.1475-1313.2003.00138.x.
[175] W. Haidinger, "Ueber das directe Erkennen des polarisierten Lichts und der Lage der Polarisationsebene," *Annalen der Physik und Chemie*, vol. 139, no. 9, pp. 29-39, 1844, doi: 10.1002/andp.18441390903.

[176] S. Rossel and R. Wehner, "Polarization Vision in Bees," (in English), *Nature,* vol. 323, no. 6084, pp. 128-131, Sep 11 1986, doi: 10.1038/323128a0.
[177] A. Basiri *et al.*, "Nature-inspired chiral metasurfaces for circular polarization detection and full-Stokes polarimetric measurements," *Light Sci Appl,* vol. 8, p. 78, 2019, doi: 10.1038/s41377-019-0184-4.
[178] Z. Chen, T. Zeng, B. Qian, and J. Ding, "Complete shaping of optical vector beams," *Opt Express,* vol. 23, no. 14, pp. 17701-10, Jul 13 2015, doi: 10.1364/OE.23.017701.
[179] B. Schaefer, E. Collett, R. Smyth, D. Barrett, and B. Fraher, "Measuring the Stokes polarization parameters," (in English), *American Journal of Physics,* vol. 75, no. 2, pp. 163-168, Feb 2007, doi: 10.1119/1.2386162.
[180] M. V. Berry, "The Adiabatic Phase and Pancharatnam's Phase for Polarized Light," *Journal of Modern Optics,* vol. 34, no. 11, pp. 1401-1407, 1987, doi: 10.1080/09500348714551321.
[181] C. Lane, D. Rode, and T. Rosgen, "Two-dimensional birefringence measurement technique using a polarization camera," *Appl Opt,* vol. 60, no. 27, pp. 8435-8444, Sep 20 2021, doi: 10.1364/AO.433066.
[182] M. Usman, "Studies of Ferroelectric and Multiferroic Behavior in [Ba(Zr,Ti)O3]1-y: [CoFe2O4]y System," PhD, Quaid-i-Azam University, Islamabad, 2015.
[183] A. Emoto *et al.*, "Form birefringence in intrinsic birefringent media possessing a subwavelength structure," *Appl Opt,* vol. 49, no. 23, pp. 4355-61, Aug 10 2010, doi: 10.1364/AO.49.004355.
[184] S. Kruk and Y. Kivshar, "Functional Meta-Optics and Nanophotonics Governed by Mie Resonances," *ACS Photonics,* vol. 4, no. 11, pp. 2638-2649, 2017, doi: 10.1021/acsphotonics.7b01038.
[185] Z. Zhu and T. G. Brown, "Stress-induced birefringence in microstructured optical fibers," *Opt Lett,* vol. 28, no. 23, pp. 2306-8, Dec 1 2003, doi: 10.1364/ol.28.002306.
[186] A. Adhikari, T. Bourgade, and A. Asundi, "Residual stress measurement for injection molded components," *Theoretical and Applied Mechanics Letters,* vol. 6, no. 4, pp. 152-156, 2016, doi: 10.1016/j.taml.2016.04.004.
[187] D. Stifter, P. Burgholzer, O. Hglinger, E. Gtzinger, and C. K. Hitzenberger, "Polarisation-sensitive optical coherence tomography for material characterisation and strain-field mapping," *Applied Physics A: Materials Science & Processing,* vol. 76, no. 6, pp. 947-951, 2003, doi: 10.1007/s00339-002-2065-5.
[188] J. Kaneshiro, T. M. Watanabe, H. Fujita, and T. Ichimura, "Full control of polarization state with a pair of electro-optic modulators for polarization-resolved optical microscopy," *Appl Opt,* vol. 55, no. 5, pp. 1082-9, Feb 10 2016, doi: 10.1364/AO.55.001082.
[189] S. Ding, Q. Li, R. Yao, and Q. Wang, "Brewster's angle method for absorption coefficient measurement of high-resistivity silicon based on CW THz laser," *Applied Physics B,* vol. 98, no. 1, pp. 119-124, 2009, doi: 10.1007/s00340-009-3611-z.
[190] X. Lu, J. Yang, W. Jin, L. Li, X. Wang, and S. Qiu, "Polarization properties of reflected light with natural light incidence and elimination of angle of incidence ambiguity," *Appl Opt,* vol. 57, no. 29, pp. 8549-8556, Oct 10 2018, doi: 10.1364/AO.57.008549.
[191] B. A. Wallace, "The role of circular dichroism spectroscopy in the era of integrative structural biology," *Curr Opin Struct Biol,* vol. 58, pp. 191-196, Oct 2019, doi: 10.1016/j.sbi.2019.04.001.

[192] A. J. Miles, R. W. Janes, and B. A. Wallace, "Tools and methods for circular dichroism spectroscopy of proteins: a tutorial review," *Chem Soc Rev,* vol. 50, no. 15, pp. 8400-8413, Aug 7 2021, doi: 10.1039/d0cs00558d.

[193] M. Vorlickova, I. Kejnovska, K. Bednarova, D. Renciuk, and J. Kypr, "Circular dichroism spectroscopy of DNA: from duplexes to quadruplexes," *Chirality,* vol. 24, no. 9, pp. 691-8, Sep 2012, doi: 10.1002/chir.22064.

[194] G. Gottarelli, S. Lena, S. Masiero, S. Pieraccini, and G. P. Spada, "The use of circular dichroism spectroscopy for studying the chiral molecular self-assembly: an overview," *Chirality,* vol. 20, no. 3-4, pp. 471-85, Mar 2008, doi: 10.1002/chir.20459.

[195] Y. Luo, L. Wu, B. Yang, Y. Jin, K. Zheng, and Z. He, "A novel potential primary method for quantification of enantiomers by high performance liquid chromatography-circular dichroism," *Sci Rep,* vol. 8, no. 1, p. 7390, May 9 2018, doi: 10.1038/s41598-018-25682-4.

[196] L. T. McDonald, E. D. Finlayson, B. D. Wilts, and P. Vukusic, "Circularly polarized reflection from the scarab beetle Chalcothea smaragdina: light scattering by a dual photonic structure," *Interface Focus,* vol. 7, no. 4, p. 20160129, Aug 6 2017, doi: 10.1098/rsfs.2016.0129.

[197] F. Zhang *et al.*, "All-Dielectric Metasurfaces for Simultaneous Giant Circular Asymmetric Transmission and Wavefront Shaping Based on Asymmetric Photonic Spin-Orbit Interactions," *Advanced Functional Materials,* vol. 27, no. 47, 2017, doi: 10.1002/adfm.201704295.

[198] M. Kenney *et al.*, "Pancharatnam-Berry Phase Induced Spin-Selective Transmission in Herringbone Dielectric Metamaterials," *Adv Mater,* vol. 28, no. 43, pp. 9567-9572, Nov 2016, doi: 10.1002/adma.201603460.

[199] J. Li *et al.*, "Active controllable spin-selective terahertz asymmetric transmission based on all-silicon metasurfaces," *Applied Physics Letters,* vol. 118, no. 22, 2021, doi: 10.1063/5.0053236.

[200] S. Wang *et al.*, "Arbitrary polarization conversion dichroism metasurfaces for all-in-one full Poincare sphere polarizers," *Light Sci Appl,* vol. 10, no. 1, p. 24, Jan 27 2021, doi: 10.1038/s41377-021-00468-y.

[201] D. H. Goldstein, *Polarized Light*. Boca Raton: CRC Press, 2017.

[202] D. B. Chenault *et al.*, "An overview of polarimetric sensing techniques and technology with applications to different research fields," in *Polarization: Measurement, Analysis, and Remote Sensing XI*, 2014: SPIE, doi: 10.1117/12.2053245.

[203] Y. Zhang, H. Zhao, P. Song, S. Shi, W. Xu, and X. Liang, "Ground-based full-sky imaging polarimeter based on liquid crystal variable retarders," *Opt Express,* vol. 22, no. 7, pp. 8749-64, Apr 7 2014, doi: 10.1364/OE.22.008749.

[204] P. Y. Deschamps *et al.*, "The POLDER mission: instrument characteristics and scientific objectives," *IEEE Transactions on Geoscience and Remote Sensing,* vol. 32, no. 3, pp. 598-615, 1994, doi: 10.1109/36.297978.

[205] F. J. García-Haro *et al.*, "Derivation of global vegetation biophysical parameters from EUMETSAT Polar System," *ISPRS Journal of Photogrammetry and Remote Sensing,* vol. 139, pp. 57-74, 2018, doi: 10.1016/j.isprsjprs.2018.03.005.

[206] J. A. Shaw, D. A. LeMaster, T. Marbach, J. Riedi, A. Lacan, and P. Schlüssel, "The 3MI mission: multi-viewing-channel-polarisation imager of the EUMETSAT polar system: second generation (EPS-SG) dedicated to aerosol and cloud monitoring," in *Polarization Science and Remote Sensing VII*, 2015, doi: 10.1117/12.2186978.

[207] C.-Y. Chiang, K.-S. Chen, C.-Y. Chu, Y.-L. Chang, and K.-C. Fan, "Color Enhancement for Four-Component Decomposed Polarimetric SAR Image Based on a CIE-Lab Encoding," *Remote Sensing,* vol. 10, no. 4, 2018, doi: 10.3390/rs10040545.

[208] J. Qu, X. Qiu, W. Wang, Z. Wang, B. Lei, and C. Ding, "A Comparative Study on Classification Features between High-Resolution and Polarimetric SAR Images through Unsupervised Classification Methods," *Remote Sensing,* vol. 14, no. 6, 2022, doi: 10.3390/rs14061412.

[209] C. a. B. Neumann, Michael, "Polarimetric Target Detection on SAR Images," *2019 20th International Radar Symposium (IRS),* 2019, doi: 10.23919/IRS.2019.8767463.

[210] J. Liang, L. Ren, H. Ju, W. Zhang, and E. Qu, "Polarimetric dehazing method for dense haze removal based on distribution analysis of angle of polarization," *Opt Express,* vol. 23, no. 20, pp. 26146-57, Oct 5 2015, doi: 10.1364/OE.23.026146.

[211] K. Akiyama *et al.*, "First M87 Event Horizon Telescope Results. VII. Polarization of the Ring," *The Astrophysical Journal Letters,* vol. 910, no. 1, 2021, doi: 10.3847/2041-8213/abe71d.

[212] T. Laskar *et al.*, "ALMA Detection of a Linearly Polarized Reverse Shock in GRB 190114C," *The Astrophysical Journal,* vol. 878, no. 1, 2019, doi: 10.3847/2041-8213/ab2247.

[213] S. V. Vadawale *et al.*, "Phase-resolved X-ray polarimetry of the Crab pulsar with the AstroSat CZT Imager," *Nature Astronomy,* vol. 2, no. 1, pp. 50-55, 2017, doi: 10.1038/s41550-017-0293-z.

[214] J. F. Wardle and D. C. Homan, "The nature of jets: Evidence from circular polarization observations," *arXiv preprint astro-ph/0011515,* 2000, doi: 10.48550/arXiv.astro-ph/0011515.

[215] R. Siebenmorgen, N. V. Voshchinnikov, and S. Bagnulo, "Dust in the diffuse interstellar medium," *Astronomy & Astrophysics,* vol. 561, 2014, doi: 10.1051/0004-6361/201321716.

[216] D. C. J. Larry Pezzaniti, "Detection of Obscured Targets with IR Polarimetric Imaging," *Detection and Sensing of Mines, Explosive Objects, and Obscured Targets XIX,* vol. 9072, pp. 347-358, 2014, doi: 10.1117/12.2053076.

[217] X. Li, Y. Han, H. Wang, T. Liu, S.-C. Chen, and H. Hu, "Polarimetric Imaging Through Scattering Media: A Review," *Frontiers in Physics,* vol. 10, 2022, doi: 10.3389/fphy.2022.815296.

[218] M. Ballesta-Garcia, S. Peña-Gutiérrez, A. Val-Martí, and S. Royo, "Polarimetric Imaging vs. Conventional Imaging: Evaluation of Image Contrast in Fog," *Atmosphere,* vol. 12, no. 7, 2021, doi: 10.3390/atmos12070813.

[219] K. Usmani, G. Krishnan, T. O'Connor, and B. Javidi, "Deep learning polarimetric three-dimensional integral imaging object recognition in adverse environmental conditions," *Opt Express,* vol. 29, no. 8, pp. 12215-12228, Apr 12 2021, doi: 10.1364/OE.421287.

[220] K. Usmani *et al.*, "Three-dimensional polarimetric integral imaging in photon-starved conditions: performance comparison between visible and long wave infrared imaging," *Opt Express,* vol. 28, no. 13, pp. 19281-19294, Jun 22 2020, doi: 10.1364/OE.395301.

[221] M. Pertenais, C. Neiner, P. Bernardi, J. M. Reess, and P. Petit, "Static spectropolarimeter concept adapted to space conditions and wide spectrum constraints," *Appl Opt,* vol. 54, no. 24, pp. 7377-86, Aug 20 2015, doi: 10.1364/AO.54.007377.

[222] F. Ding, A. Pors, Y. Chen, V. A. Zenin, and S. I. Bozhevolnyi, "Beam-Size-Invariant Spectropolarimeters Using Gap-Plasmon Metasurfaces," *ACS Photonics,* vol. 4, no. 4, pp. 943-949, 2017, doi: 10.1021/acsphotonics.6b01046.

[223] W. T. Chen *et al.*, "Integrated plasmonic metasurfaces for spectropolarimetry," *Nanotechnology,* vol. 27, no. 22, p. 224002, Jun 3 2016, doi: 10.1088/0957-4484/27/22/224002.

[224] T. Mu, S. Pacheco, Z. Chen, C. Zhang, and R. Liang, "Snapshot linear-Stokes imaging spectropolarimeter using division-of-focal-plane polarimetry and integral field spectroscopy," *Sci Rep,* vol. 7, p. 42115, Feb 13 2017, doi: 10.1038/srep42115.

[225] P. Braeuninger-Weimer *et al.*, "Fast, Noncontact, Wafer-Scale, Atomic Layer Resolved Imaging of Two-Dimensional Materials by Ellipsometric Contrast Micrography," *ACS Nano,* vol. 12, no. 8, pp. 8555-8563, Aug 28 2018, doi: 10.1021/acsnano.8b04167.

[226] U. Wurstbauer *et al.*, "Imaging ellipsometry of graphene," *Applied Physics Letters,* vol. 97, no. 23, 2010, doi: 10.1063/1.3524226.

[227] D. H. Kim, Y. H. Yun, and K.-N. Joo, "LASIE: Large Area Spectroscopic Imaging Ellipsometry for Characterizing Multi-Layered Film Structures," *International Journal of Precision Engineering and Manufacturing,* vol. 19, no. 8, pp. 1125-1132, 2018, doi: 10.1007/s12541-018-0133-9.

[228] X. Chen *et al.*, "Development of a spectroscopic Mueller matrix imaging ellipsometer for nanostructure metrology," *Rev Sci Instrum,* vol. 87, no. 5, p. 053707, May 2016, doi: 10.1063/1.4952385.

[229] T.-F. Li *et al.*, "Terahertz faraday rotation of magneto-optical films enhanced by helical metasurface," *Applied Physics Letters,* vol. 116, no. 25, 2020, doi: 10.1063/5.0009704.

[230] A. N. Grebenchukov, V. I. Ivanova, G. I. Kropotov, and M. K. Khodzitsky, "Terahertz Faraday rotation of aluminum-substituted barium hexaferrite," *Applied Physics Letters,* vol. 118, no. 19, 2021, doi: 10.1063/5.0048604.

[231] X. Han, A. Markou, J. Stensberg, Y. Sun, C. Felser, and L. Wu, "Giant intrinsic anomalous terahertz Faraday rotation in the magnetic Weyl semimetal Co2MnGa at room temperature," *Physical Review B,* vol. 105, no. 17, 2022, doi: 10.1103/PhysRevB.105.174406.

[232] V. Balos, G. Bierhance, M. Wolf, and M. Sajadi, "Terahertz-Magnetic-Field Induced Ultrafast Faraday Rotation of Molecular Liquids," *Phys Rev Lett,* vol. 124, no. 9, p. 093201, Mar 6 2020, doi: 10.1103/PhysRevLett.124.093201.

[233] W. J. Choi, G. Cheng, Z. Huang, S. Zhang, T. B. Norris, and N. A. Kotov, "Terahertz circular dichroism spectroscopy of biomaterials enabled by kirigami polarization modulators," *Nat Mater,* vol. 18, no. 8, pp. 820-826, Aug 2019, doi: 10.1038/s41563-019-0404-6.

[234] J. Hu, M. Lawrence, and J. A. Dionne, "High Quality Factor Dielectric Metasurfaces for Ultraviolet Circular Dichroism Spectroscopy," *ACS Photonics,* vol. 7, no. 1, pp. 36-42, 2019, doi: 10.1021/acsphotonics.9b01352.

[235] H. He *et al.*, "Mueller Matrix Polarimetry—An Emerging New Tool for Characterizing the Microstructural Feature of Complex Biological Specimen," *Journal of Lightwave Technology,* vol. 37, no. 11, pp. 2534-2548, 2019, doi: 10.1109/jlt.2018.2868845.

[236] A. Van Eeckhout *et al.*, "Polarimetric imaging microscopy for advanced inspection of vegetal tissues," *Sci Rep,* vol. 11, no. 1, p. 3913, Feb 16 2021, doi: 10.1038/s41598-021-83421-8.

[237] S.-X. Huang *et al.*, "Terahertz Multi-Spectral Mueller Matrix Polarimetry on Leaf Using Only Orthogonal-Polarization Measurements," *IEEE Transactions on Terahertz Science and Technology*, vol. 11, no. 6, pp. 609-619, 2021, doi: 10.1109/tthz.2021.3090111.

[238] G.-H. Oh, J.-H. Jeong, S.-H. Park, and H.-S. Kim, "Terahertz time-domain spectroscopy of weld line defects formed during an injection moulding process," *Composites Science and Technology*, vol. 157, pp. 67-77, 2018, doi: 10.1016/j.compscitech.2018.01.030.

[239] Q. Wang *et al.*, "Nondestructive imaging of hidden defects in aircraft sandwich composites using terahertz time-domain spectroscopy," *Infrared Physics & Technology*, vol. 97, pp. 326-340, 2019, doi: 10.1016/j.infrared.2019.01.013.

[240] S. Rout and S. Sonkusale, "Introduction," in *Active Metamaterials*: Springer, Cham., 2017, ch. Chapter 1, pp. 1-25.

[241] J. Wang and J. Du, "Metasurfaces for Spatial Light Manipulation," in *Metamaterials - Devices and Applications*, 2017, ch. 3.

[242] P. Cheben *et al.*, "Refractive index engineering with subwavelength gratings for efficient microphotonic couplers and planar waveguide multiplexers," *Opt Lett*, vol. 35, no. 15, pp. 2526-8, Aug 1 2010, doi: 10.1364/OL.35.002526.

[243] H. Kikuta, Y. Ohira, H. Kubo, and K. Iwata, "Effective medium theory of two-dimensional subwavelength gratings in the non-quasi-static limit," *Journal of the Optical Society of America A*, vol. 15, no. 6, 1998, doi: 10.1364/josaa.15.001577.

[244] R. Halir *et al.*, "Waveguide sub-wavelength structures: a review of principles and applications," *Laser & Photonics Reviews*, vol. 9, no. 1, pp. 25-49, 2014, doi: 10.1002/lpor.201400083.

[245] B. Lee, I.-M. Lee, S. Kim, D.-H. Oh, and L. Hesselink, "Review on subwavelength confinement of light with plasmonics," *Journal of Modern Optics*, vol. 57, no. 16, pp. 1479-1497, 2010, doi: 10.1080/09500340.2010.506985.

[246] Q. Wang *et al.*, "Broadband metasurface holograms: toward complete phase and amplitude engineering," *Sci Rep*, vol. 6, p. 32867, Sep 12 2016, doi: 10.1038/srep32867.

[247] G. Y. Lee *et al.*, "Complete amplitude and phase control of light using broadband holographic metasurfaces," *Nanoscale*, vol. 10, no. 9, pp. 4237-4245, Mar 1 2018, doi: 10.1039/c7nr07154j.

[248] S. L. Jia, X. Wan, P. Su, Y. J. Zhao, and T. J. Cui, "Broadband metasurface for independent control of reflected amplitude and phase," *AIP Advances*, vol. 6, no. 4, 2016, doi: 10.1063/1.4948513.

[249] A. C. Overvig *et al.*, "Dielectric metasurfaces for complete and independent control of the optical amplitude and phase," *Light Sci Appl*, vol. 8, p. 92, 2019, doi: 10.1038/s41377-019-0201-7.

[250] A. Zaidi, N. A. Rubin, A. H. Dorrah, J. S. Park, and F. Capasso, "Generalized polarization transformations with metasurfaces," *Opt Express*, vol. 29, no. 24, pp. 39065-39078, Nov 22 2021, doi: 10.1364/OE.442844.

[251] J. P. Balthasar Mueller, K. Leosson, and F. Capasso, "Ultracompact metasurface in-line polarimeter," *Optica*, vol. 3, no. 1, 2016, doi: 10.1364/optica.3.000042.

[252] E. Hasman, V. Kleiner, G. Biener, and A. Niv, "Polarization dependent focusing lens by use of quantized Pancharatnam–Berry phase diffractive optics," *Applied Physics Letters*, vol. 82, no. 3, pp. 328-330, 2003, doi: 10.1063/1.1539300.

[253] M. Khorasaninejad *et al.*, "Multispectral Chiral Imaging with a Metalens," *Nano Lett*, vol. 16, no. 7, pp. 4595-600, Jul 13 2016, doi: 10.1021/acs.nanolett.6b01897.

[254] W. Zhao *et al.*, "Dielectric Huygens' Metasurface for High-Efficiency Hologram Operating in Transmission Mode," *Sci Rep*, vol. 6, p. 30613, Jul 26 2016, doi: 10.1038/srep30613.
[255] E. Arbabi, A. Arbabi, S. M. Kamali, Y. Horie, and A. Faraon, "Controlling the sign of chromatic dispersion in diffractive optics with dielectric metasurfaces," *Optica*, vol. 4, no. 6, 2017, doi: 10.1364/optica.4.000625.
[256] M. Khorasaninejad *et al.*, "Achromatic Metalens over 60 nm Bandwidth in the Visible and Metalens with Reverse Chromatic Dispersion," *Nano Lett*, vol. 17, no. 3, pp. 1819-1824, Mar 8 2017, doi: 10.1021/acs.nanolett.6b05137.
[257] S. Wang *et al.*, "Broadband achromatic optical metasurface devices," *Nat Commun*, vol. 8, no. 1, p. 187, Aug 4 2017, doi: 10.1038/s41467-017-00166-7.
[258] S. Shrestha, A. C. Overvig, M. Lu, A. Stein, and N. Yu, "Broadband achromatic dielectric metalenses," *Light Sci Appl*, vol. 7, p. 85, 2018, doi: 10.1038/s41377-018-0078-x.
[259] C. Guo, M. Xiao, M. Orenstein, and S. Fan, "Structured 3D linear space-time light bullets by nonlocal nanophotonics," *Light Sci Appl*, vol. 10, no. 1, p. 160, Aug 2 2021, doi: 10.1038/s41377-021-00595-6.
[260] C. Schlickriede, S. S. Kruk, L. Wang, B. Sain, Y. Kivshar, and T. Zentgraf, "Nonlinear Imaging with All-Dielectric Metasurfaces," *Nano Lett*, vol. 20, no. 6, pp. 4370-4376, Jun 10 2020, doi: 10.1021/acs.nanolett.0c01105.
[261] S. Kruk *et al.*, "Nonlinear light generation in topological nanostructures," *Nat Nanotechnol*, vol. 14, no. 2, pp. 126-130, Feb 2019, doi: 10.1038/s41565-018-0324-7.
[262] G. Zograf *et al.*, "High-Harmonic Generation from Resonant Dielectric Metasurfaces Empowered by Bound States in the Continuum," *ACS Photonics*, vol. 9, no. 2, pp. 567-574, 2022, doi: 10.1021/acsphotonics.1c01511.
[263] M. Khorasaninejad and F. Capasso, "Broadband Multifunctional Efficient Meta-Gratings Based on Dielectric Waveguide Phase Shifters," *Nano Lett*, vol. 15, no. 10, pp. 6709-15, Oct 14 2015, doi: 10.1021/acs.nanolett.5b02524.
[264] M. Schmitz, R. Bräuer, and O. Bryngdahl, "Phase gratings with subwavelength structures," *Journal of the Optical Society of America A*, vol. 12, no. 11, 1995, doi: 10.1364/josaa.12.002458.
[265] E. Hasman, Z. e. Bomzon, A. Niv, G. Biener, and V. Kleiner, "Polarization beam-splitters and optical switches based on space-variant computer-generated subwavelength quasi-periodic structures," *Optics Communications*, vol. 209, no. 1-3, pp. 45-54, 2002, doi: 10.1016/s0030-4018(02)01598-5.
[266] J. B. Pendry, A. J. Holden, D. J. Robbins, and W. J. Stewart, "Magnetism from conductors and enhanced nonlinear phenomena," *IEEE Transactions on Microwave Theory and Techniques*, vol. 47, no. 11, pp. 2075-2084, 1999, doi: 10.1109/22.798002.
[267] D. R. Smith, D. C. Vier, W. Padilla, S. C. Nemat-Nasser, and S. Schultz, "Loop-wire medium for investigating plasmons at microwave frequencies," *Applied Physics Letters*, vol. 75, no. 10, pp. 1425-1427, 1999, doi: 10.1063/1.124714.
[268] D. Schurig, J. J. Mock, and D. R. Smith, "Electric-field-coupled resonators for negative permittivity metamaterials," *Applied Physics Letters*, vol. 88, no. 4, 2006, doi: 10.1063/1.2166681.
[269] R. A. Shelby, D. R. Smith, S. C. Nemat-Nasser, and S. Schultz, "Microwave transmission through a two-dimensional, isotropic, left-handed metamaterial," *Applied Physics Letters*, vol. 78, no. 4, pp. 489-491, 2001, doi: 10.1063/1.1343489.

[270] D. R. Smith, W. J. Padilla, D. C. Vier, S. C. Nemat-Nasser, and S. Schultz, "Composite medium with simultaneously negative permeability and permittivity," *Phys Rev Lett,* vol. 84, no. 18, pp. 4184-7, May 1 2000, doi: 10.1103/PhysRevLett.84.4184.

[271] R. A. Shelby, D. R. Smith, and S. Schultz, "Experimental verification of a negative index of refraction," *Science,* vol. 292, no. 5514, pp. 77-9, Apr 6 2001, doi: 10.1126/science.1058847.

[272] J. Sun, L. Kang, R. Wang, L. Liu, L. Sun, and J. Zhou, "Low loss negative refraction metamaterial using a close arrangement of split-ring resonator arrays," *New Journal of Physics,* vol. 12, no. 8, 2010, doi: 10.1088/1367-2630/12/8/083020.

[273] E. Ozbay, K. Guven, and K. Aydin, "Metamaterials with negative permeability and negative refractive index: experiments and simulations," *Journal of Optics A: Pure and Applied Optics,* vol. 9, no. 9, pp. S301-S307, 2007, doi: 10.1088/1464-4258/9/9/s04.

[274] N. Yu *et al.*, "Light propagation with phase discontinuities: generalized laws of reflection and refraction," *Science,* vol. 334, no. 6054, pp. 333-7, Oct 21 2011, doi: 10.1126/science.1210713.

[275] J. Zhang, M. ElKabbash, R. Wei, S. C. Singh, B. Lam, and C. Guo, "Plasmonic metasurfaces with 42.3% transmission efficiency in the visible," *Light Sci Appl,* vol. 8, p. 53, 2019, doi: 10.1038/s41377-019-0164-8.

[276] Y. D. Shah *et al.*, "Ultralow-light-level color image reconstruction using high-efficiency plasmonic metasurface mosaic filters," *Optica,* vol. 7, no. 6, 2020, doi: 10.1364/optica.389905.

[277] S. M. Kamali, E. Arbabi, A. Arbabi, and A. Faraon, "A review of dielectric optical metasurfaces for wavefront control," *Nanophotonics,* vol. 7, no. 6, pp. 1041-1068, 2018, doi: 10.1515/nanoph-2017-0129.

[278] M. Kenney *et al.*, "Large area metasurface lenses in the NIR region," in *Modeling Aspects in Optical Metrology VII*, 2019, doi: 10.1117/12.2527157.

[279] M. Khorasaninejad and F. Capasso, "Metalenses: Versatile multifunctional photonic components," *Science,* vol. 358, no. 6367, Dec 1 2017, doi: 10.1126/science.aam8100.

[280] E. Maguid, I. Yulevich, M. Yannai, V. Kleiner, L. B. M, and E. Hasman, "Multifunctional interleaved geometric-phase dielectric metasurfaces," *Light Sci Appl,* vol. 6, no. 8, p. e17027, Aug 2017, doi: 10.1038/lsa.2017.27.

[281] Q. Chen *et al.*, "High numerical aperture multifocal metalens based on Pancharatnam-Berry phase optical elements," *Appl Opt,* vol. 57, no. 27, pp. 7891-7894, Sep 20 2018, doi: 10.1364/AO.57.007891.

[282] R. C. Devlin, M. Khorasaninejad, W. T. Chen, J. Oh, and F. Capasso, "Broadband high-efficiency dielectric metasurfaces for the visible spectrum," *Proc Natl Acad Sci U S A,* vol. 113, no. 38, pp. 10473-8, Sep 20 2016, doi: 10.1073/pnas.1611740113.

[283] H. Liang *et al.*, "Ultrahigh Numerical Aperture Metalens at Visible Wavelengths," *Nano Lett,* vol. 18, no. 7, pp. 4460-4466, Jul 11 2018, doi: 10.1021/acs.nanolett.8b01570.

[284] Z. Yang *et al.*, "Generalized Hartmann-Shack array of dielectric metalens sub-arrays for polarimetric beam profiling," *Nat Commun,* vol. 9, no. 1, p. 4607, Nov 2 2018, doi: 10.1038/s41467-018-07056-6.

[285] L. Wang, S. Kruk, K. Koshelev, I. Kravchenko, B. Luther-Davies, and Y. Kivshar, "Nonlinear Wavefront Control with All-Dielectric Metasurfaces," *Nano Lett,* vol. 18, no. 6, pp. 3978-3984, Jun 13 2018, doi: 10.1021/acs.nanolett.8b01460.

[286] K. Fan, I. V. Shadrivov, and W. J. Padilla, "Dynamic bound states in the continuum," *Optica*, vol. 6, no. 2, 2019, doi: 10.1364/optica.6.000169.
[287] K. Koshelev, Y. Tang, K. Li, D.-Y. Choi, G. Li, and Y. Kivshar, "Nonlinear Metasurfaces Governed by Bound States in the Continuum," *ACS Photonics*, vol. 6, no. 7, pp. 1639-1644, 2019, doi: 10.1021/acsphotonics.9b00700.
[288] K. Koshelev, S. Lepeshov, M. Liu, A. Bogdanov, and Y. Kivshar, "Asymmetric Metasurfaces with High-Q Resonances Governed by Bound States in the Continuum," *Phys Rev Lett*, vol. 121, no. 19, p. 193903, Nov 9 2018, doi: 10.1103/PhysRevLett.121.193903.
[289] K. Du, H. Barkaoui, X. Zhang, L. Jin, Q. Song, and S. Xiao, "Optical metasurfaces towards multifunctionality and tunability," *Nanophotonics*, vol. 11, no. 9, pp. 1761-1781, 2022, doi: 10.1515/nanoph-2021-0684.
[290] F. Aieta *et al.*, "Aberration-free ultrathin flat lenses and axicons at telecom wavelengths based on plasmonic metasurfaces," *Nano Lett*, vol. 12, no. 9, pp. 4932-6, Sep 12 2012, doi: 10.1021/nl302516v.
[291] Z. B. Fan *et al.*, "A broadband achromatic metalens array for integral imaging in the visible," *Light Sci Appl*, vol. 8, p. 67, 2019, doi: 10.1038/s41377-019-0178-2.
[292] Q. Zhang *et al.*, "High-Numerical-Aperture Dielectric Metalens for Super-Resolution Focusing of Oblique Incident Light," *Advanced Optical Materials*, vol. 8, no. 9, 2020, doi: 10.1002/adom.201901885.
[293] T. Y. Huang *et al.*, "A monolithic immersion metalens for imaging solid-state quantum emitters," *Nat Commun*, vol. 10, no. 1, p. 2392, Jun 3 2019, doi: 10.1038/s41467-019-10238-5.
[294] K. Wu, P. Coquet, Q. J. Wang, and P. Genevet, "Modelling of free-form conformal metasurfaces," *Nat Commun*, vol. 9, no. 1, p. 3494, Aug 28 2018, doi: 10.1038/s41467-018-05579-6.
[295] Metalenz, "World's first metasurface for consumer electronics makes commercial debut," 2022. [Online]. Available: https://www.metalenz.com/worlds-first-metasurface-for-consumer-electronics-makes-commercial-debut/ (last accessed 11.09.2022)
[296] S. Xu *et al.*, "High-Efficiency Fabrication of Geometric Phase Elements by Femtosecond-Laser Direct Writing," *Nanomaterials (Basel)*, vol. 10, no. 9, Sep 1 2020, doi: 10.3390/nano10091737.
[297] M. J. Qu, W. Y. Li, T. Zeng, J. X. Su, and W. L. Song, "3D printed metasurface for generating a Bessel beam with arbitrary focusing directions," *Opt Lett*, vol. 46, no. 21, pp. 5441-5444, Nov 1 2021, doi: 10.1364/OL.440977.
[298] S. Banerji and B. Sensale-Rodriguez, "A Computational Design Framework for Efficient, Fabrication Error-Tolerant, Planar THz Diffractive Optical Elements," *Sci Rep*, vol. 9, no. 1, p. 5801, Apr 9 2019, doi: 10.1038/s41598-019-42243-5.
[299] J. Cheng, Y. Yang, F. Fan, X. Wang, and S. Chang, "Terahertz tight-focused Bessel beam generation and point-to-point focusing based on nonlocal diffraction engineering," *Opt Lett*, vol. 47, no. 11, pp. 2879-2882, Jun 1 2022, doi: 10.1364/OL.460747.
[300] Y. Intaravanne and X. Chen, "Recent advances in optical metasurfaces for polarization detection and engineered polarization profiles," *Nanophotonics*, vol. 9, no. 5, pp. 1003-1014, 2020, doi: 10.1515/nanoph-2019-0479.
[301] Z. Shi *et al.*, "Continuous angle-tunable birefringence with freeform metasurfaces for arbitrary polarization conversion," *Sci Adv*, vol. 6, no. 23, p. eaba3367, Jun 2020, doi: 10.1126/sciadv.aba3367.

[302] E. Cohen, H. Larocque, F. Bouchard, F. Nejadsattari, Y. Gefen, and E. Karimi, "Geometric phase from Aharonov–Bohm to Pancharatnam–Berry and beyond," *Nature Reviews Physics,* vol. 1, no. 7, pp. 437-449, 2019, doi: 10.1038/s42254-019-0071-1.

[303] Z. Bomzon, G. Biener, V. Kleiner, and E. Hasman, "Space-variant Pancharatnam-Berry phase optical elements with computer-generated subwavelength gratings," *Opt Lett,* vol. 27, no. 13, pp. 1141-3, Jul 1 2002, doi: 10.1364/ol.27.001141.

[304] Y. Xu *et al.*, "Generation of terahertz vector beams using dielectric metasurfaces via spin-decoupled phase control," *Nanophotonics,* vol. 9, no. 10, pp. 3393-3402, 2020, doi: 10.1515/nanoph-2020-0112.

[305] X. Jiang *et al.*, "All-dielectric metalens for terahertz wave imaging," *Opt Express,* vol. 26, no. 11, pp. 14132-14142, May 28 2018, doi: 10.1364/OE.26.014132.

[306] X. Ling *et al.*, "Giant photonic spin Hall effect in momentum space in a structured metamaterial with spatially varying birefringence," *Light: Science & Applications,* vol. 4, no. 5, pp. e290-e290, 2015, doi: 10.1038/lsa.2015.63.

[307] Y. Ke, Y. Liu, J. Zhou, Y. Liu, H. Luo, and S. Wen, "Photonic spin filter with dielectric metasurfaces," *Opt Express,* vol. 23, no. 26, pp. 33079-86, Dec 28 2015, doi: 10.1364/OE.23.033079.

[308] Y. Qiu, S. Tang, T. Cai, H. Xu, and F. Ding, "Fundamentals and applications of spin-decoupled Pancharatnam—Berry metasurfaces," *Frontiers of Optoelectronics,* vol. 14, no. 2, pp. 134-147, 2021, doi: 10.1007/s12200-021-1220-6.

[309] R. C. Devlin *et al.*, "Spin-to-orbital angular momentum conversion in dielectric metasurfaces," *Opt Express,* vol. 25, no. 1, pp. 377-393, Jan 9 2017, doi: 10.1364/OE.25.000377.

[310] Y. Hu *et al.*, "All-dielectric metasurfaces for polarization manipulation: principles and emerging applications," *Nanophotonics,* vol. 9, no. 12, pp. 3755-3780, 2020, doi: 10.1515/nanoph-2020-0220.

[311] Z. Ma *et al.*, "Terahertz All-Dielectric Magnetic Mirror Metasurfaces," *ACS Photonics,* vol. 3, no. 6, pp. 1010-1018, 2016, doi: 10.1021/acsphotonics.6b00096.

[312] H. Zhang *et al.*, "Polarization-independent all-silicon dielectric metasurfaces in the terahertz regime," *Photonics Research,* vol. 6, no. 1, 2017, doi: 10.1364/prj.6.000024.

[313] H. Zhang *et al.*, "High-Efficiency Dielectric Metasurfaces for Polarization-Dependent Terahertz Wavefront Manipulation," *Advanced Optical Materials,* vol. 6, no. 1, 2018, doi: 10.1002/adom.201700773.

[314] D. Headland *et al.*, "Dielectric Resonator Reflectarray as High-Efficiency Nonuniform Terahertz Metasurface," *ACS Photonics,* vol. 3, no. 6, pp. 1019-1026, 2016, doi: 10.1021/acsphotonics.6b00102.

[315] D. Jia *et al.*, "Transmissive terahertz metalens with full phase control based on a dielectric metasurface," *Opt Lett,* vol. 42, no. 21, pp. 4494-4497, Nov 1 2017, doi: 10.1364/OL.42.004494.

[316] Z. Wang, Q. Li, and F. Yan, "Broadband generation of abruptly autofocusing terahertz ring-Airy beams with all-silicon metasurface," *Optics & Laser Technology,* vol. 150, 2022, doi: 10.1016/j.optlastec.2022.107924.

[317] X. Zang *et al.*, "Polarization-Insensitive Metalens with Extended Focal Depth and Longitudinal High-Tolerance Imaging," *Advanced Optical Materials,* vol. 8, no. 2, 2019, doi: 10.1002/adom.201901342.

[318] Z. Zhang *et al.*, "Multifunctional Light Sword Metasurface Lens," *ACS Photonics,* vol. 5, no. 5, pp. 1794-1799, 2018, doi: 10.1021/acsphotonics.7b01536.

[319] X. Zang *et al.*, "A Multi-Foci Metalens with Polarization-Rotated Focal Points," *Laser & Photonics Reviews,* vol. 13, no. 12, 2019, doi: 10.1002/lpor.201900182.
[320] Q. Cheng *et al.*, "Broadband achromatic metalens in terahertz regime," *Science Bulletin,* vol. 64, no. 20, pp. 1525-1531, 2019, doi: 10.1016/j.scib.2019.08.004.
[321] H. Chen *et al.*, "Sub-wavelength tight-focusing of terahertz waves by polarization-independent high-numerical-aperture dielectric metalens," *Opt Express,* vol. 26, no. 23, pp. 29817-29825, Nov 12 2018, doi: 10.1364/OE.26.029817.
[322] S.-G. Park, K. Lee, D. Han, J. Ahn, and K.-H. Jeong, "Subwavelength silicon through-hole arrays as an all-dielectric broadband terahertz gradient index metamaterial," *Applied Physics Letters,* vol. 105, no. 9, 2014, doi: 10.1063/1.4894054.
[323] S. Y. Zhu, G. B. Wu, S. W. Pang, and C. H. Chan, "Compact Terahertz Dielectric Folded Metasurface," *Advanced Optical Materials,* vol. 10, no. 3, 2021, doi: 10.1002/adom.202101663.
[324] Q. Yu *et al.*, "All-Dielectric Meta-lens Designed for Photoconductive Terahertz Antennas," *IEEE Photonics Journal,* vol. 9, no. 4, pp. 1-9, 2017, doi: 10.1109/jphot.2017.2721503.
[325] P. Chen, B. Fang, J. Li, X. Jing, M. Kong, and Z. Hong, "Enhancement of efficiency on the Pancharatnam-Berry geometric phase metalens in the terahertz region," *Appl Opt,* vol. 60, no. 26, pp. 7849-7857, Sep 10 2021, doi: 10.1364/AO.433115.
[326] J. Tian, F. Laurell, V. Pasiskevicius, M. Qiu, and H. Jang, "Demonstration of terahertz ferroelectric metasurface using a simple and scalable fabrication method," *Opt Express,* vol. 26, no. 21, pp. 27917-27930, Oct 15 2018, doi: 10.1364/OE.26.027917.
[327] R. Dharmavarapu *et al.*, "Dielectric cross-shaped-resonator-based metasurface for vortex beam generation at mid-IR and THz wavelengths," *Nanophotonics,* vol. 8, no. 7, pp. 1263-1270, 2019, doi: 10.1515/nanoph-2019-0112.
[328] W. S. L. Lee *et al.*, "Dielectric-resonator metasurfaces for broadband terahertz quarter- and half-wave mirrors," *Opt Express,* vol. 26, no. 11, pp. 14392-14406, May 28 2018, doi: 10.1364/OE.26.014392.
[329] J. Zi *et al.*, "Dual-Functional Terahertz Waveplate Based on All-Dielectric Metamaterial," *Physical Review Applied,* vol. 13, no. 3, 2020, doi: 10.1103/PhysRevApplied.13.034042.
[330] J. Zi *et al.*, "Antireflection-assisted all-dielectric terahertz metamaterial polarization converter," *Applied Physics Letters,* vol. 113, no. 10, 2018, doi: 10.1063/1.5042784.
[331] S. Li *et al.*, "Polarization-insensitive tunable terahertz polarization rotator," *Opt Express,* vol. 27, no. 12, pp. 16966-16974, Jun 10 2019, doi: 10.1364/OE.27.016966.
[332] X. Zang *et al.*, "Metasurface for multi-channel terahertz beam splitters and polarization rotators," *Applied Physics Letters,* vol. 112, no. 17, 2018, doi: 10.1063/1.5028401.
[333] Q. Yang *et al.*, "Broadband terahertz rotator with an all-dielectric metasurface," *Photonics Research,* vol. 6, no. 11, 2018, doi: 10.1364/prj.6.001056.
[334] Y. Xu *et al.*, "Spin-Decoupled Multifunctional Metasurface for Asymmetric Polarization Generation," *ACS Photonics,* vol. 6, no. 11, pp. 2933-2941, 2019, doi: 10.1021/acsphotonics.9b01047.
[335] Y. Rao *et al.*, "Asymmetric transmission of linearly polarized waves based on Mie resonance in all-dielectric terahertz metamaterials," *Opt Express,* vol. 28, no. 20, pp. 29855-29864, Sep 28 2020, doi: 10.1364/OE.404912.

[336] Z. Ma, Y. Li, Y. Li, Y. Gong, S. A. Maier, and M. Hong, "All-dielectric planar chiral metasurface with gradient geometric phase," *Opt Express,* vol. 26, no. 5, pp. 6067-6078, Mar 5 2018, doi: 10.1364/OE.26.006067.

[337] J. Peng, J. Hou, T. Tang, J. Li, and Z. Chen, "All-Dielectric Terahertz Metasurface with Giant Extrinsic Chirality for Dual-Mode Sensing," *physica status solidi (b),* 2022, doi: 10.1002/pssb.202200114.

[338] C. Qin *et al.,* "Enhanced asymmetric transmission of linearly polarized light based on all-dielectric stereometamaterial," *Journal of Optics,* vol. 23, no. 3, 2021, doi: 10.1088/2040-8986/abd9df.

[339] D. P. Tsai, T. Tanaka, W. Kubo, N. Green, J. Frame, and X. Fang, "Plasmonic vanadium dioxide microbolometers with wavelength and polarisation sensitivity," in *Plasmonics: Design, Materials, Fabrication, Characterization, and Applications XVI*, 2018, doi: 10.1117/12.2320554.

[340] K. Fan, J. Y. Suen, X. Liu, and W. J. Padilla, "All-dielectric metasurface absorbers for uncooled terahertz imaging," *Optica,* vol. 4, no. 6, 2017, doi: 10.1364/optica.4.000601.

[341] W. Withayachumnankul *et al.,* "Terahertz Localized Surface Plasmon Resonances in Coaxial Microcavities," *Advanced Optical Materials,* vol. 1, no. 6, pp. 443-448, 2013, doi: 10.1002/adom.201300021.

[342] S. Yin *et al.,* "High-performance terahertz wave absorbers made of silicon-based metamaterials," *Applied Physics Letters,* vol. 107, no. 7, 2015, doi: 10.1063/1.4929151.

[343] Y. Z. Cheng *et al.,* "Ultrabroadband Plasmonic Absorber for Terahertz Waves," *Advanced Optical Materials,* vol. 3, no. 3, pp. 376-380, 2015, doi: 10.1002/adom.201400368.

[344] S. M. Hanham *et al.,* "Broadband terahertz plasmonic response of touching InSb disks," *Adv Mater,* vol. 24, no. 35, pp. OP226-30, Sep 11 2012, doi: 10.1002/adma.201202003.

[345] J. Wang, K. Guo, and Z. Guo, "THz filter based on the Si microdisk array," *AIP Advances,* vol. 9, no. 4, 2019, doi: 10.1063/1.5083004.

[346] J. Li *et al.,* "All-silicon metasurfaces for polarization multiplexed generation of terahertz photonic orbital angular momentum superposition states," *Journal of Materials Chemistry C,* vol. 9, no. 16, pp. 5478-5485, 2021, doi: 10.1039/d1tc00594d.

[347] B. Fang *et al.,* "Continuous scattering angle control of transmission terahertz wave by convolution manipulation of all-dielectric encoding metasurfaces," *Applied Physics A,* vol. 126, no. 8, 2020, doi: 10.1007/s00339-020-03720-1.

[348] D. McGloin and K. Dholakia, "Bessel beams: Diffraction in a new light," *Contemporary Physics,* vol. 46, no. 1, pp. 15-28, 2005, doi: 10.1080/0010751042000275259.

[349] H. D. Nguyen *et al.,* "Non-Diffractive Bessel Beams for Ultrafast Laser Scanning Platform and Proof-Of-Concept Side-Wall Polishing of Additively Manufactured Parts," *Micromachines (Basel),* vol. 11, no. 11, Oct 30 2020, doi: 10.3390/mi11110974.

[350] I. Moreno, J. A. Davis, M. M. Sanchez-Lopez, K. Badham, and D. M. Cottrell, "Nondiffracting Bessel beams with polarization state that varies with propagation distance," *Opt Lett,* vol. 40, no. 23, pp. 5451-4, Dec 1 2015, doi: 10.1364/OL.40.005451.

[351] C. Rosales-Guzmán, B. Ndagano, and A. Forbes, "A review of complex vector light fields and their applications," *Journal of Optics,* vol. 20, no. 12, 2018, doi: 10.1088/2040-8986/aaeb7d.

[352] P. Li *et al.*, "Three-dimensional modulations on the states of polarization of light fields," *Chinese Physics B,* vol. 27, no. 11, 2018, doi: 10.1088/1674-1056/27/11/114201.

[353] A. V. a. S. B. Raghu Dharmavarapu, "Design and fabrication of holographic optical elements for the generation of tilted and accelerating Airy beams," *Asian J. Phys,* vol. 24, no. 10, pp. 1363-1372, 2015.

[354] G. S. Sokolovskii *et al.*, "Bessel beams from semiconductor light sources," *Progress in Quantum Electronics,* vol. 38, no. 4, pp. 157-188, 2014, doi: 10.1016/j.pquantelec.2014.07.001.

[355] G. Di Domenico, G. Ruocco, C. Colosi, E. DelRe, and G. Antonacci, "Cancellation of Bessel beam side lobes for high-contrast light sheet microscopy," *Sci Rep,* vol. 8, no. 1, p. 17178, Nov 21 2018, doi: 10.1038/s41598-018-35006-1.

[356] H. He *et al.*, "Background-Free Volumetric Two-Photon Microscopy by Side-Lobes-Cancelled Bessel Beam," *IEEE Journal of Selected Topics in Quantum Electronics,* vol. 27, no. 4, pp. 1-7, 2021, doi: 10.1109/jstqe.2021.3054892.

[357] T. Meinert and A. Rohrbach, "Light-sheet microscopy with length-adaptive Bessel beams," *Biomed Opt Express,* vol. 10, no. 2, pp. 670-681, Feb 1 2019, doi: 10.1364/BOE.10.000670.

[358] P. Li *et al.*, "Generation and self-healing of vector Bessel-Gauss beams with variant state of polarizations upon propagation," *Opt Express,* vol. 25, no. 5, pp. 5821-5831, Mar 6 2017, doi: 10.1364/OE.25.005821.

[359] C. Gohn-Kreuz and A. Rohrbach, "Light needles in scattering media using self-reconstructing beams and the STED principle," *Optica,* vol. 4, no. 9, 2017, doi: 10.1364/optica.4.001134.

[360] J. A. Davis, I. Moreno, K. Badham, M. M. Sanchez-Lopez, and D. M. Cottrell, "Nondiffracting vector beams where the charge and the polarization state vary with propagation distance," *Opt Lett,* vol. 41, no. 10, pp. 2270-3, May 15 2016, doi: 10.1364/OL.41.002270.

[361] Y. Liu *et al.*, "Generation of perfect vortex and vector beams based on Pancharatnam-Berry phase elements," *Sci Rep,* vol. 7, p. 44096, Mar 9 2017, doi: 10.1038/srep44096.

[362] S. Fu, S. Zhang, and C. Gao, "Bessel beams with spatial oscillating polarization," *Sci Rep,* vol. 6, p. 30765, Aug 4 2016, doi: 10.1038/srep30765.

[363] E. Otte, C. Rosales-Guzman, B. Ndagano, C. Denz, and A. Forbes, "Entanglement beating in free space through spin-orbit coupling," *Light Sci Appl,* vol. 7, p. 18009, 2018, doi: 10.1038/lsa.2018.9.

[364] A. H. Dorrah, N. A. Rubin, M. Tamagnone, A. Zaidi, and F. Capasso, "Structuring total angular momentum of light along the propagation direction with polarization-controlled meta-optics," *Nat Commun,* vol. 12, no. 1, p. 6249, Oct 29 2021, doi: 10.1038/s41467-021-26253-4.

[365] J. Wang and Y. Liang, "Generation and Detection of Structured Light: A Review," *Frontiers in Physics,* vol. 9, 2021, doi: 10.3389/fphy.2021.688284.

[366] H. Rubinsztein-Dunlop *et al.*, "Roadmap on structured light," *Journal of Optics,* vol. 19, no. 1, 2017, doi: 10.1088/2040-8978/19/1/013001.

[367] O. V. Angelsky, A. Y. Bekshaev, S. G. Hanson, C. Y. Zenkova, I. I. Mokhun, and Z. Jun, "Structured Light: Ideas and Concepts," *Frontiers in Physics,* vol. 8, 2020, doi: 10.3389/fphy.2020.00114.

[368] D. Naidoo *et al.*, "Controlled generation of higher-order Poincaré sphere beams from a laser," *Nature Photonics,* vol. 10, no. 5, pp. 327-332, 2016, doi: 10.1038/nphoton.2016.37.

[369] F. Cardano, E. Karimi, S. Slussarenko, L. Marrucci, C. de Lisio, and E. Santamato, "Polarization pattern of vector vortex beams generated by q-plates with different topological charges," *Appl Opt,* vol. 51, no. 10, pp. C1-6, Apr 1 2012, doi: 10.1364/AO.51.0000C1.

[370] Y. Kozawa and S. Sato, "Generation of a radially polarized laser beam by use of a conical Brewster prism," *Opt Lett,* vol. 30, no. 22, pp. 3063-5, Nov 15 2005, doi: 10.1364/ol.30.003063.

[371] W. J. Lai, B. C. Lim, P. B. Phua, K. S. Tiaw, H. H. Teo, and M. H. Hong, "Generation of radially polarized beam with a segmented spiral varying retarder," *Opt Express,* vol. 16, no. 20, pp. 15694-9, Sep 29 2008, doi: 10.1364/oe.16.015694.

[372] M. M. Sanchez-Lopez *et al.*, "Performance of a q-plate tunable retarder in reflection for the switchable generation of both first- and second-order vector beams," *Opt Lett,* vol. 41, no. 1, pp. 13-6, Jan 1 2016, doi: 10.1364/OL.41.000013.

[373] M. A. Cox, C. Rosales-Guzman, M. P. Lavery, D. J. Versfeld, and A. Forbes, "On the resilience of scalar and vector vortex modes in turbulence," *Opt Express,* vol. 24, no. 16, pp. 18105-13, Aug 8 2016, doi: 10.1364/OE.24.018105.

[374] M. Corato-Zanarella, A. H. Dorrah, M. Zamboni-Rached, and M. Mojahedi, "Arbitrary Control of Polarization and Intensity Profiles of Diffraction-Attenuation-Resistant Beams along the Propagation Direction," *Physical Review Applied,* vol. 9, no. 2, 2018, doi: 10.1103/PhysRevApplied.9.024013.

[375] R.-P. Chen, Z. Chen, Y. Gao, J. Ding, and S. He, "Flexible Manipulation of the Polarization Conversions in a Structured Vector Field in Free Space," *Laser & Photonics Reviews,* vol. 11, no. 6, 2017, doi: 10.1002/lpor.201700165.

[376] S. N. Khonina and S. A. Degtyarev, "Analysis of the formation of a longitudinally polarized optical needle by a lens and axicon under tightly focused conditions," *Journal of Optical Technology,* vol. 83, no. 4, 2016, doi: 10.1364/jot.83.000197.

[377] Y. Saito *et al.*, "z-Polarization sensitive detection in micro-Raman spectroscopy by radially polarized incident light," *Journal of Raman Spectroscopy,* vol. 39, no. 11, pp. 1643-1648, 2008, doi: 10.1002/jrs.1953.

[378] J. Zhao *et al.*, "Specially shaped Bessel-like self-accelerating beams along predesigned trajectories," *Science Bulletin,* vol. 60, no. 13, pp. 1157-1169, 2015, doi: 10.1007/s11434-015-0792-1.

[379] L. Gong *et al.*, "Controllable light capsules employing modified Bessel-Gauss beams," *Sci Rep,* vol. 6, p. 29001, Jul 8 2016, doi: 10.1038/srep29001.

[380] Q. Zhan, "Cylindrical vector beams: from mathematical concepts to applications," *Advances in Optics and Photonics,* vol. 1, no. 1, 2009, doi: 10.1364/aop.1.000001.

[381] S. N. Khonina, N. L. Kazanskiy, S. V. Karpeev, and M. A. Butt, "Bessel Beam: Significance and Applications-A Progressive Review," *Micromachines (Basel),* vol. 11, no. 11, Nov 11 2020, doi: 10.3390/mi11110997.

[382] R. Grunwald and M. Bock, "Needle beams: a review," *Advances in Physics: X,* vol. 5, no. 1, 2020, doi: 10.1080/23746149.2020.1736950.

[383] N. Weber, D. Spether, A. Seifert, and H. Zappe, "Highly compact imaging using Bessel beams generated by ultraminiaturized multi-micro-axicon systems," (in

English), *J Opt Soc Am A,* vol. 29, no. 5, pp. 808-816, May 2012, doi: 10.1364/Josaa.29.000808.

[384] D. G. Grier, "A revolution in optical manipulation," *Nature,* vol. 424, no. 6950, pp. 810-6, Aug 14 2003, doi: 10.1038/nature01935.

[385] M. Padgett and R. Bowman, "Tweezers with a twist," *Nature Photonics,* vol. 5, no. 6, pp. 343-348, 2011, doi: 10.1038/nphoton.2011.81.

[386] K. E. Ballantine, J. F. Donegan, and P. R. Eastham, "There are many ways to spin a photon: Half-quantization of a total optical angular momentum," *Sci Adv,* vol. 2, no. 4, p. e1501748, Apr 2016, doi: 10.1126/sciadv.1501748.

[387] T. A. Nieminen, N. R. Heckenberg, and H. Rubinsztein-Dunlop, "Forces in optical tweezers with radially and azimuthally polarized trapping beams," *Opt Lett,* vol. 33, no. 2, pp. 122-4, Jan 15 2008, doi: 10.1364/ol.33.000122.

[388] M. Zamboni-Rached, "Stationary optical wave fields with arbitrary longitudinal shape by superposing equal frequency Bessel beams: Frozen Waves," *Opt Express,* vol. 12, no. 17, pp. 4001-6, Aug 23 2004, doi: 10.1364/opex.12.004001.

[389] J. Arlt, V. Garces-Chavez, W. Sibbett, and K. Dholakia, "Optical micromanipulation using a Bessel light beam," *Optics Communications,* vol. 197, no. 4-6, pp. 239-245, 2001, doi: 10.1016/s0030-4018(01)01479-1.

[390] T. Du, T. Wang, and F. Wu, "Generation of three-dimensional optical bottle beams via focused non-diffracting Bessel beam using an axicon," *Optics Communications,* vol. 317, pp. 24-28, 2014, doi: 10.1016/j.optcom.2013.11.059.

[391] V. Shvedov, A. R. Davoyan, C. Hnatovsky, N. Engheta, and W. Krolikowski, "A long-range polarization-controlled optical tractor beam," *Nature Photonics,* vol. 8, no. 11, pp. 846-850, 2014, doi: 10.1038/nphoton.2014.242.

[392] A. B. Kashekodi, T. Meinert, R. Michiels, and A. Rohrbach, "Miniature scanning light-sheet illumination implemented in a conventional microscope," *Biomed Opt Express,* vol. 9, no. 9, pp. 4263-4274, Sep 1 2018, doi: 10.1364/BOE.9.004263.

[393] F. O. Fahrbach, P. Simon, and A. Rohrbach, "Microscopy with self-reconstructing beams," *Nature Photonics,* vol. 4, no. 11, pp. 780-785, 2010, doi: 10.1038/nphoton.2010.204.

[394] X. Xie, Y. Chen, K. Yang, and J. Zhou, "Harnessing the point-spread function for high-resolution far-field optical microscopy," *Phys Rev Lett,* vol. 113, no. 26, p. 263901, Dec 31 2014, doi: 10.1103/PhysRevLett.113.263901.

[395] J. Tang, J. Ren, and K. Y. Han, "Fluorescence imaging with tailored light," *Nanophotonics,* vol. 8, no. 12, pp. 2111-2128, Dec 2019, doi: 10.1515/nanoph-2019-0227.

[396] W. Yu *et al.,* "Super-resolution deep imaging with hollow Bessel beam STED microscopy," *Laser & Photonics Reviews,* vol. 10, no. 1, pp. 147-152, 2016, doi: 10.1002/lpor.201500151.

[397] F. Courvoisier, J. Zhang, M. K. Bhuyan, M. Jacquot, and J. M. Dudley, "Applications of femtosecond Bessel beams to laser ablation," *Applied Physics A,* vol. 112, no. 1, pp. 29-34, 2012, doi: 10.1007/s00339-012-7201-2.

[398] C. Hnatovsky, V. G. Shvedov, N. Shostka, A. V. Rode, and W. Krolikowski, "Polarization-dependent ablation of silicon using tightly focused femtosecond laser vortex pulses," *Opt Lett,* vol. 37, no. 2, pp. 226-8, Jan 15 2012, doi: 10.1364/OL.37.000226.

[399] Y. Ito, R. Yoshizaki, N. Miyamoto, and N. Sugita, "Ultrafast and precision drilling of glass by selective absorption of fiber-laser pulse into femtosecond-laser-induced filament," *Applied Physics Letters,* vol. 113, no. 6, 2018, doi: 10.1063/1.5027421.

[400] R. Meyer *et al.*, "Extremely high-aspect-ratio ultrafast Bessel beam generation and stealth dicing of multi-millimeter thick glass," *Applied Physics Letters*, vol. 114, no. 20, 2019, doi: 10.1063/1.5096868.
[401] S. Matsusaka, Y. Kozawa, and S. Sato, "Micro-hole drilling by tightly focused vector beams," *Opt Lett*, vol. 43, no. 7, pp. 1542-1545, Apr 1 2018, doi: 10.1364/OL.43.001542.
[402] M. Erhard, R. Fickler, M. Krenn, and A. Zeilinger, "Twisted photons: new quantum perspectives in high dimensions," *Light Sci Appl*, vol. 7, p. 17146, 2018, doi: 10.1038/lsa.2017.146.
[403] A. E. Willner *et al.*, "Optical communications using orbital angular momentum beams," *Advances in Optics and Photonics*, vol. 7, no. 1, 2015, doi: 10.1364/aop.7.000066.
[404] G. Molina-Terriza, J. P. Torres, and L. Torner, "Twisted photons," *Nature Physics*, vol. 3, no. 5, pp. 305-310, 2007, doi: 10.1038/nphys607.
[405] J. Wang *et al.*, "Terabit free-space data transmission employing orbital angular momentum multiplexing," *Nature Photonics*, vol. 6, no. 7, pp. 488-496, 2012, doi: 10.1038/nphoton.2012.138.
[406] G. Milione, T. A. Nguyen, J. Leach, D. A. Nolan, and R. R. Alfano, "Using the nonseparability of vector beams to encode information for optical communication," *Opt Lett*, vol. 40, no. 21, pp. 4887-90, Nov 1 2015, doi: 10.1364/OL.40.004887.
[407] L. Zhu and J. Wang, "Demonstration of obstruction-free data-carrying N-fold Bessel modes multicasting from a single Gaussian mode," *Opt Lett*, vol. 40, no. 23, pp. 5463-6, Dec 1 2015, doi: 10.1364/OL.40.005463.
[408] Q. Tian, L. Zhu, Y. Wang, Q. Zhang, B. Liu, and X. Xin, "The Propagation Properties of a Longitudinal Orbital Angular Momentum Multiplexing System in Atmospheric Turbulence," *IEEE Photonics Journal*, vol. 10, no. 1, pp. 1-16, 2018, doi: 10.1109/jphot.2017.2778238.
[409] A. Dudley *et al.*, "Efficient sorting of Bessel beams," *Opt Express*, vol. 21, no. 1, pp. 165-71, Jan 14 2013, doi: 10.1364/OE.21.000165.
[410] N. Ahmed *et al.*, "Mode-Division-Multiplexing of Multiple Bessel-Gaussian Beams Carrying Orbital-Angular-Momentum for Obstruction-Tolerant Free-Space Optical and Millimetre-Wave Communication Links," *Sci Rep*, vol. 6, p. 22082, Mar 1 2016, doi: 10.1038/srep22082.
[411] Q. Yang *et al.*, "Ultra-secure optical encryption based on tightly focused perfect optical vortex beams," *Nanophotonics*, vol. 11, no. 5, pp. 1063-1070, 2022, doi: 10.1515/nanoph-2021-0786.
[412] H. Zhou *et al.*, "Polarization-Encrypted Orbital Angular Momentum Multiplexed Metasurface Holography," *ACS Nano*, vol. 14, no. 5, pp. 5553-5559, May 26 2020, doi: 10.1021/acsnano.9b09814.
[413] Y. Xie, T. Lei, C. Yang, L. Du, and X. Yuan, "Beam wander relieved optical switch using Bessel beams in turbulent atmosphere," *Chinese Optics Letters*, vol. 17, no. 9, 2019, doi: 10.3788/col201917.090602.
[414] R. Feng *et al.*, "Flexible Manipulation of Bessel-Like Beams with a Reconfigurable Metasurface," *Advanced Optical Materials*, vol. 8, no. 23, 2020, doi: 10.1002/adom.202001084.
[415] G.-B. Wu, K. F. Chan, K. M. Shum, and C. H. Chan, "Millimeter-Wave and Terahertz OAM Discrete-Lens Antennas for 5G and Beyond," *IEEE Communications Magazine*, vol. 60, no. 1, pp. 34-39, 2022, doi: 10.1109/mcom.001.2100523.

[416] H. J. Meyer, S. Mamani, and R. R. Alfano, "Steady-state stimulated Raman generation and filamentation using complex vector vortex beams," *Appl Opt,* vol. 59, no. 21, pp. 6245-6251, Jul 20 2020, doi: 10.1364/AO.393973.
[417] Y. Qin, Y. Li, D. Deng, Y. Liu, and M. Sun, "Ultracompact biosensor based on a metalens with a longitudinally structured vector beam," *Appl Opt,* vol. 58, no. 16, pp. 4438-4442, Jun 1 2019, doi: 10.1364/AO.58.004438.
[418] A. H. Dorrah, M. Zamboni-Rached, and M. Mojahedi, "Experimental demonstration of tunable refractometer based on orbital angular momentum of longitudinally structured light," *Light Sci Appl,* vol. 7, p. 40, 2018, doi: 10.1038/s41377-018-0034-9.
[419] F. K. Fatemi, "Cylindrical vector beams for rapid polarization-dependent measurements in atomic systems," *Opt Express,* vol. 19, no. 25, pp. 25143-50, Dec 5 2011, doi: 10.1364/OE.19.025143.
[420] Z. Guo, S. Liu, P. Li, B. Wei, and J. Zhao, "Tightly autofocusing beams along the spherical surface," *Optics Express,* vol. 30, no. 15, 2022, doi: 10.1364/oe.461986.
[421] C. Pfeiffer and A. Grbic, "Controlling Vector Bessel Beams with Metasurfaces," *Physical Review Applied,* vol. 2, no. 4, 2014, doi: 10.1103/PhysRevApplied.2.044012.
[422] R. C. Devlin, A. Ambrosio, N. A. Rubin, J. P. B. Mueller, and F. Capasso, "Arbitrary spin-to-orbital angular momentum conversion of light," *Science,* vol. 358, no. 6365, pp. 896-901, Nov 17 2017, doi: 10.1126/science.aao5392.
[423] R. T. Ako, A. Upadhyay, W. Withayachumnankul, M. Bhaskaran, and S. Sriram, "Dielectrics for Terahertz Metasurfaces: Material Selection and Fabrication Techniques," *Advanced Optical Materials,* vol. 8, no. 3, 2019, doi: 10.1002/adom.201900750.
[424] A. G. Mark. "gdsCAD's documentation." https://pythonhosted.org/gdsCAD/ (accessed 11 September, 2022).
[425] S. Kruk, B. Hopkins, I. I. Kravchenko, A. Miroshnichenko, D. N. Neshev, and Y. S. Kivshar, "Invited Article: Broadband highly efficient dielectric metadevices for polarization control," *APL Photonics,* vol. 1, no. 3, 2016, doi: 10.1063/1.4949007.
[426] Z. Wang, Q. Li, and F. Yan, "Theoretical study on 2.52 terahertz beam shaping and polarization conversion based on the transmissive all-dielectric metasurface," *Optics Communications,* vol. 460, 2020, doi: 10.1016/j.optcom.2019.125131.
[427] X. P. Dong, J. R. Cheng, F. Fan, S. T. Xu, X. H. Wang, and S. J. Chang, "Wideband sub-THz half-wave plate using 3D-printed low-index metagratings with superwavelength lattice," *Opt Express,* vol. 27, no. 1, pp. 202-211, Jan 7 2019, doi: 10.1364/OE.27.000202.
[428] W. D. Furlan, V. Ferrando, J. A. Monsoriu, P. Zagrajek, E. Czerwinska, and M. Szustakowski, "3D printed diffractive terahertz lenses," *Opt Lett,* vol. 41, no. 8, pp. 1748-51, Apr 15 2016, doi: 10.1364/OL.41.001748.
[429] S. Banerji, B. Sensale-Rodriguez, M. S. Islam, and T. George, "3D-printed diffractive terahertz optical elements through computational design," *Micro- and Nanotechnology Sensors, Systems, and Applications XI,* 2019, doi: 10.1117/12.2518805.
[430] R. A. Ovanesyan, E. A. Filatova, S. D. Elliott, D. M. Hausmann, D. C. Smith, and S. Agarwal, "Atomic layer deposition of silicon-based dielectrics for semiconductor manufacturing: Current status and future outlook," *Journal of Vacuum Science & Technology A,* vol. 37, no. 6, 2019, doi: 10.1116/1.5113631.

[431] M. J. O. Laakso, S. Pagliano, U. Shah, G. E. Martensson, G. Stemme, and F. Niklaus, "Water in contact with the backside of a silicon substrate enables drilling of high-quality holes through the substrate using ultrashort laser pulses," *Opt Express*, vol. 28, no. 2, pp. 1394-1407, Jan 20 2020, doi: 10.1364/OE.377256.

[432] M. Chambonneau, D. Grojo, O. Tokel, F. Ö. Ilday, S. Tzortzakis, and S. Nolte, "In-Volume Laser Direct Writing of Silicon—Challenges and Opportunities," *Laser & Photonics Reviews*, vol. 15, no. 11, 2021, doi: 10.1002/lpor.202100140.

[433] M. V. Gorkunov, O. Y. Rogov, A. V. Kondratov, V. V. Artemov, R. V. Gainutdinov, and A. A. Ezhov, "Chiral visible light metasurface patterned in monocrystalline silicon by focused ion beam," *Sci Rep*, vol. 8, no. 1, p. 11623, Aug 2 2018, doi: 10.1038/s41598-018-29977-4.

[434] A. M. Baracu *et al.*, "Metasurface Fabrication by Cryogenic and Bosch Deep Reactive Ion Etching," *Micromachines (Basel)*, vol. 12, no. 5, Apr 29 2021, doi: 10.3390/mi12050501.

[435] F. Stöhr *et al.*, "Sacrificial structures for deep reactive ion etching of high-aspect ratio kinoform silicon x-ray lenses," *Journal of Vacuum Science & Technology B, Nanotechnology and Microelectronics: Materials, Processing, Measurement, and Phenomena*, vol. 33, no. 6, 2015, doi: 10.1116/1.4931622.

[436] C. Mack, *Fundamental Principles of Optical Lithography*. John Wiley & Sons, 2007.

[437] MicroChem, "Materials Safety Data Sheet for MCC Primer 80/20 (Product #: P021020)," 11 October 2005. [Online]. Available: https://uwaterloo.ca/giga-to-nanoelectronics-centre/sites/ca.giga-to-nanoelectronics-centre/files/uploads/files/mccprimer_80_20_0.pdf (last accessed 11.09.2022)

[438] F. Chiarella, M. Barra, L. Ricciotti, A. Aloisio, and A. Cassinese, "Morphology, Electrical Performance and Potentiometry of PDIF-CN2 Thin-Film Transistors on HMDS-Treated and Bare Silicon Dioxide," *Electronics*, vol. 3, no. 1, pp. 76-86, 2014, doi: 10.3390/electronics3010076.

[439] Micro_Resist_Technology, "Distribution Products (Part 1) - Product Datasheet for SPR220 Photoresist ", 30 March 2009. [Online]. Available: https://www.nanophys.kth.se/nanolab/resists/mrt-pdfs/optical-res-overv.pdf (last accessed 11.09.22)

[440] T. Baëtens and S. Arscott, "Planarization and edge bead reduction of spin-coated polydimethylsiloxane," *Journal of Micromechanics and Microengineering*, vol. 29, no. 11, 2019, doi: 10.1088/1361-6439/ab3b18.

[441] H. Lee, K. Lee, B. Ahn, J. Xu, L. Xu, and K. W. Oh, "A new fabrication process for uniform SU-8 thick photoresist structures by simultaneously removing edge bead and air bubbles," *Journal of Micromechanics and Microengineering*, vol. 21, no. 12, 2011, doi: 10.1088/0960-1317/21/12/125006.

[442] Megaposit, "Material Safety Data Sheet for SPR220.7 Photoresist," 4 February 2004. [Online]. Available: https://louisville.edu/micronano/files/documents/safety-data-sheets-sds/SPR2207.0.pdf (last accessed 11.09.22)

[443] Rohm_and_Haas_Electronic, "Specification Datasheet: Megaposit™ SPR™ 220 Series photoresist for i-line applications," July 2004. [Online]. Available: https://static1.squarespace.com/static/57b26cc76b8f5b7524bf9ed2/t/5b02febc0e2e72164d99295b/1526922940515/SPR_220_Photoresist.pdf (last accessed 11.09.2022)

[444] G. B. Gill, "3.9 The Wolff Rearrangement," in *Comprehensive Organic Synthesis*, I. F. Barry M. Trost Ed., 1991, ch. 3, pp. 887-912.

[445] DOW, "Material Safety Datasheet for MICROPOSIT™ MF™ -CD-26 DEVELOPER," 20 August 2012. [Online]. Available:

https://www.nanofab.utah.edu/wp-content/uploads/2018/08/MICROPOSIT%E2%84%A2-MF%E2%84%A2-CD-26-DEVELOPER-Dow-20Aug12_v1.1.pdf (last accessed 11.09.22).

[446] J. J. Li, "Wolff Rearrangement," in *Name Reactions*, 2021, ch. Chapter 160, pp. 580-582.

[447] Shipley, "Datasheet for SVC-14 positive photoresist stripper." [Online]. Available: https://kayakuam.com/wp-content/uploads/2020/10/svc-14-datasheet.pdf (last accessed 11.09.2022)

[448] Kayaku, "Technical data sheet for SU-8 Permanent Negative Epoxy Photoresist (Formulations 2-25)," September 2020. [Online]. Available: https://kayakuam.com/wp-content/uploads/2020/09/KAM-SU-8-2-25-Datasheet-9.3.20-final.pdf (last accessed: 11.09.22)

[449] X. Huikai and G. K. Fedder, "Fabrication, characterization, and analysis of a DRIE CMOS-MEMS gyroscope," *IEEE Sensors Journal*, vol. 3, no. 5, pp. 622-631, 2003, doi: 10.1109/jsen.2003.817901.

[450] G. Gattere, F. Rizzini, L. Corso, A. Alessandri, F. Tripodi, and I. Gelmi, "Experimental investigation of MEMS DRIE etching dimensional loss," *IEEE*, 2018, doi: 10.1109/ISISS.2018.8358123.

[451] R. R. Reddy, Y. Okamoto, and Y. Mita, "An On-Chip Micromachined Test Structure to Study the Tribological Behavior of Deep-RIE MEMS Sidewall Surfaces," *IEEE Transactions on Semiconductor Manufacturing*, vol. 33, no. 2, pp. 187-195, 2020, doi: 10.1109/tsm.2020.2982659.

[452] R. Mukhiya *et al.*, "Design, modelling and system level simulations of DRIE-based MEMS differential capacitive accelerometer," *Microsystem Technologies*, vol. 25, no. 9, pp. 3521-3532, 2019, doi: 10.1007/s00542-018-04292-0.

[453] G. B. Loozen, A. Karuna, M. M. R. Fanood, E. Schreuder, and J. Caro, "Integrated photonics multi-waveguide devices for optical trapping and Raman spectroscopy: design, fabrication and performance demonstration," *Beilstein J Nanotechnol*, vol. 11, pp. 829-842, 2020, doi: 10.3762/bjnano.11.68.

[454] M. François *et al.*, "Photonic band gap material for integrated photonic application: technological challenges," *Microelectronic Engineering*, vol. 61-62, pp. 537-544, 2002, doi: 10.1016/s0167-9317(02)00526-9.

[455] S. Hönl, H. Hahn, Y. Baumgartner, L. Czornomaz, and P. Seidler, "Highly selective dry etching of GaP in the presence of AlxGa1–xP with a SiCl4/SF6plasma," *Journal of Physics D: Applied Physics*, vol. 51, no. 18, 2018, doi: 10.1088/1361-6463/aab8b7.

[456] H. V. Jansen, M. J. de Boer, S. Unnikrishnan, M. C. Louwerse, and M. C. Elwenspoek, "Black silicon method: X. A review on high speed and selective plasma etching of silicon with profile control: an in-depth comparison between Bosch and cryostat DRIE processes as a roadmap to next generation equipment," *Journal of Micromechanics and Microengineering*, vol. 19, no. 3, 2009, doi: 10.1088/0960-1317/19/3/033001.

[457] B. Chang, P. Leussink, F. Jensen, J. Hübner, and H. Jansen, "DREM: Infinite etch selectivity and optimized scallop size distribution with conventional photoresists in an adapted multiplexed Bosch DRIE process," *Microelectronic Engineering*, vol. 191, pp. 77-83, 2018, doi: 10.1016/j.mee.2018.01.034.

[458] B. Wu, A. Kumar, and S. Pamarthy, "High aspect ratio silicon etch: A review," *Journal of Applied Physics*, vol. 108, no. 5, 2010, doi: 10.1063/1.3474652.

[459] O. Ertl and S. Selberherr, "Three-dimensional level set based Bosch process simulations using ray tracing for flux calculation," *Microelectronic Engineering*, vol. 87, no. 1, pp. 20-29, 2010, doi: 10.1016/j.mee.2009.05.011.
[460] S. L. Lai, D. Johnson, and R. Westerman, "Aspect ratio dependent etching lag reduction in deep silicon etch processes," *Journal of Vacuum Science & Technology A: Vacuum, Surfaces, and Films*, vol. 24, no. 4, pp. 1283-1288, 2006, doi: 10.1116/1.2172944.
[461] Ted_Pella_Inc., "Safety Data Sheet Product No. 891-50 Santovac® 5, Diffusion Pump Oil," 31 August 2017. [Online]. Available: https://www.tedpella.com/SDS_html/891-50_sds.pdf (last accessed 14.09.22)
[462] J. Schmit and A. Pakuła, "White Light Interferometry," in *Handbook of Advanced Nondestructive Evaluation*, 2019, ch. 14, pp. 421-467.
[463] P. de Groot, "Principles of interference microscopy for the measurement of surface topography," *Advances in Optics and Photonics*, vol. 7, no. 1, 2015, doi: 10.1364/aop.7.000001.
[464] Bruker, "ContourGT-X 3D Optical Profilometer," 2021. [Online]. Available: https://www.bruker.com/en/products-and-solutions/test-and-measurement/3d-optical-profilers/contourgt-x.html (last accessed 11.09.2022)
[465] W. Zhou, R. Apkarian, Z. L. Wang, and D. Joy, "Fundamentals of Scanning Electron Microscopy (SEM)," in *Scanning Microscopy for Nanotechnology*: Springer science & business media, 2006, ch. 1, pp. 1-40.
[466] C. Ni, "Scanning Electron Microscopy (SEM)," in *Encyclopedia of Tribology*: Springer, Boston, MA, 2013, ch. 1217, pp. 2977-2982.
[467] A. A. Ayón, K. Ishihara, R. A. Braff, H. H. Sawin, and M. A. Schmidt, "Microfabrication and testing of suspended structures compatible with silicon-on-insulator technology," *Journal of Vacuum Science & Technology B: Microelectronics and Nanometer Structures*, vol. 17, no. 4, 1999, doi: 10.1116/1.590794.
[468] R. M. Azzam, "Stokes-vector and Mueller-matrix polarimetry [Invited]," *J Opt Soc Am A Opt Image Sci Vis*, vol. 33, no. 7, pp. 1396-408, Jul 1 2016, doi: 10.1364/JOSAA.33.001396.
[469] C. Flueraru, S. Latoui, J. Besse, and P. Legendre, "Error Analysis of a Rotating Quarter-Wave Plate Stokes' Polarimeter," *IEEE Transactions on Instrumentation and Measurement*, vol. 57, no. 4, pp. 731-735, 2008, doi: 10.1109/tim.2007.913752.
[470] B. Hill, T. Roger, and F. W. Vorhagen, "Comparative analysis of the quantization of color spaces on the basis of the CIELAB color-difference formula," (in English), *Acm T Graphic*, vol. 16, no. 2, pp. 109-154, Apr 1997, doi: 10.1145/248210.248212.
[471] P. Li *et al.*, "Polarization oscillating beams constructed by copropagating optical frozen waves," *Photonics Research*, vol. 6, no. 7, 2018, doi: 10.1364/prj.6.000756.
[472] A. H. Dorrah, M. Zamboni-Rached, and M. Mojahedi, "Frozen Waves following arbitrary spiral and snake-like trajectories in air," *Applied Physics Letters*, vol. 110, no. 5, 2017, doi: 10.1063/1.4975593.
[473] J. S. Tyo, D. L. Goldstein, D. B. Chenault, and J. A. Shaw, "Review of passive imaging polarimetry for remote sensing applications," *Appl Opt*, vol. 45, no. 22, pp. 5453-69, Aug 1 2006, doi: 10.1364/ao.45.005453.
[474] Z. Mrazkova *et al.*, "In-situ Mueller matrix ellipsometry of silicon nanowires grown by plasma-enhanced vapor-liquid-solid method for radial junction solar cells," *Applied Surface Science*, vol. 421, pp. 667-673, 2017, doi: 10.1016/j.apsusc.2016.12.199.

[475] E. Arbabi, S. M. Kamali, A. Arbabi, and A. Faraon, "Full-Stokes Imaging Polarimetry Using Dielectric Metasurfaces," *ACS Photonics,* vol. 5, no. 8, pp. 3132-3140, 2018, doi: 10.1021/acsphotonics.8b00362.

[476] Y. Dai *et al.*, "Multifunctional geometric phase optical element for high-efficiency full Stokes imaging polarimetry," *Photonics Research,* vol. 7, no. 9, 2019, doi: 10.1364/prj.7.001066.

[477] N. Oshima, K. Hashimoto, S. Suzuki, and M. Asada, "Terahertz Wireless Data Transmission With Frequency and Polarization Division Multiplexing Using Resonant-Tunneling-Diode Oscillators," *IEEE Transactions on Terahertz Science and Technology,* vol. 7, no. 5, pp. 593-598, 2017, doi: 10.1109/tthz.2017.2720470.

[478] F. Ding, S. Tang, and S. I. Bozhevolnyi, "Recent Advances in Polarization-Encoded Optical Metasurfaces," *Advanced Photonics Research,* vol. 2, no. 6, 2021, doi: 10.1002/adpr.202000173.

[479] A. Pors, M. G. Nielsen, and S. I. Bozhevolnyi, "Plasmonic metagratings for simultaneous determination of Stokes parameters," *Optica,* vol. 2, no. 8, 2015, doi: 10.1364/optica.2.000716.

[480] L. Li *et al.*, "Monolithic Full-Stokes Near-Infrared Polarimetry with Chiral Plasmonic Metasurface Integrated Graphene-Silicon Photodetector," *ACS Nano,* Nov 16 2020, doi: 10.1021/acsnano.0c00724.

[481] E. Arbabi, A. Arbabi, S. M. Kamali, Y. Horie, and A. Faraon, "Multiwavelength metasurfaces through spatial multiplexing," *Sci Rep,* vol. 6, p. 32803, Sep 6 2016, doi: 10.1038/srep32803.

[482] E. Maguid, I. Yulevich, D. Veksler, V. Kleiner, M. L. Brongersma, and E. Hasman, "Photonic spin-controlled multifunctional shared-aperture antenna array," *Science,* vol. 352, no. 6290, pp. 1202-6, Jun 3 2016, doi: 10.1126/science.aaf3417.

[483] S. J. Byrnes, A. Lenef, F. Aieta, and F. Capasso, "Designing large, high-efficiency, high-numerical-aperture, transmissive meta-lenses for visible light," *Opt Express,* vol. 24, no. 5, pp. 5110-5124, Mar 7 2016, doi: 10.1364/OE.24.005110.

[484] A. Cofré *et al.*, "Quantitative performance of a polarization diffraction grating polarimeter encoded onto two liquid-crystal-on-silicon displays," *Optics & Laser Technology,* vol. 96, pp. 219-226, 2017, doi: 10.1016/j.optlastec.2017.05.027.

[485] F. Ding, B. Chang, Q. Wei, L. Huang, X. Guan, and S. I. Bozhevolnyi, "Versatile Polarization Generation and Manipulation Using Dielectric Metasurfaces," *Laser & Photonics Reviews,* vol. 14, no. 11, 2020, doi: 10.1002/lpor.202000116.

[486] N. A. Rubin, P. Chevalier, M. Juhl, M. Tamagnone, R. Chipman, and F. Capasso, "Imaging polarimetry through metasurface polarization gratings," *Opt Express,* vol. 30, no. 6, pp. 9389-9412, Mar 14 2022, doi: 10.1364/OE.450941.

[487] A. Lizana, I. Estevez, F. A. Torres-Ruiz, A. Peinado, C. Ramirez, and J. Campos, "Arbitrary state of polarization with customized degree of polarization generator," *Opt Lett,* vol. 40, no. 16, pp. 3790-3, Aug 15 2015, doi: 10.1364/OL.40.003790.

[488] X. Li, Z. Shen, Q. Tan, and W. Hu, "High Efficient Metadevices for Terahertz Beam Shaping," *Frontiers in Physics,* vol. 9, 2021, doi: 10.3389/fphy.2021.659747.

[489] X. Li and Z. Fan, "Mid-infrared dielectric metasurfaces with desired chromatic dispersion," *Optik,* vol. 257, 2022, doi: 10.1016/j.ijleo.2022.168838.

[490] D. Wang, S. Sun, Z. Feng, and W. Tan, "Complete Terahertz Polarization Control with Broadened Bandwidth via Dielectric Metasurfaces," *Nanoscale Res Lett,* vol. 16, no. 1, p. 157, Oct 19 2021, doi: 10.1186/s11671-021-03614-y.

[491] S. Zhou, Z. Shen, X. Li, S. Ge, Y. Lu, and W. Hu, "Liquid crystal integrated metalens with dynamic focusing property," *Opt Lett,* vol. 45, no. 15, pp. 4324-4327, Aug 1 2020, doi: 10.1364/OL.398601.

[492] C. Liu, Y. Li, X. Feng, X. Zhang, J. Han, and W. Zhang, "Dual non-diffractive terahertz beam generators based on all-dielectric metasurface," *Frontiers of Optoelectronics,* vol. 14, no. 2, pp. 201-210, 2020, doi: 10.1007/s12200-020-1098-8.

[493] X. Li *et al.*, "Experimental demonstration of 3D printed terahertz polarization-insensitive flat devices based on low-index meta-gratings," *Journal of Physics D: Applied Physics,* vol. 53, no. 50, 2020, doi: 10.1088/1361-6463/abb272.

[494] H. Wang, F. Zhang, K. Ding, and J. a. Duan, "Non-diffraction-length Bessel-beam femtosecond laser drilling of high-aspect-ratio microholes in PMMA," *Optik,* vol. 229, 2021, doi: 10.1016/j.ijleo.2021.166295.

[495] L. Minkevicius, D. Jokubauskis, I. Kasalynas, S. Orlov, A. Urbas, and G. Valusis, "Bessel terahertz imaging with enhanced contrast realized by silicon multi-phase diffractive optics," *Opt Express,* vol. 27, no. 25, pp. 36358-36367, Dec 9 2019, doi: 10.1364/OE.27.036358.

[496] V. S. Ilchenko *et al.*, "Arbitrary control of the polarization state and intensity of non-diffracting beams along their propagation direction," in *Laser Resonators, Microresonators, and Beam Control XX*, 2018, doi: 10.1117/12.2289225.

[497] A. H. Dorrah, M. Zamboni-Rached, and M. Mojahedi, "Controlling the topological charge of twisted light beams with propagation," *Physical Review A,* vol. 93, no. 6, 2016, doi: 10.1103/PhysRevA.93.063864.

[498] Y. Che, X. Wang, Q. Song, Y. Zhu, and S. Xiao, "Tunable optical metasurfaces enabled by multiple modulation mechanisms," *Nanophotonics,* vol. 9, no. 15, pp. 4407-4431, 2020, doi: 10.1515/nanoph-2020-0311.

[499] Q. He, S. Sun, and L. Zhou, "Tunable/Reconfigurable Metasurfaces: Physics and Applications," *Research (Wash D C)*, vol. 2019, p. 1849272, 2019, doi: 10.34133/2019/1849272.

[500] M. Zamboni-Rached, E. Recami, and H. E. Hernandez-Figueroa, "Theory of "frozen waves": modeling the shape of stationary wave fields," *J Opt Soc Am A Opt Image Sci Vis,* vol. 22, no. 11, pp. 2465-75, Nov 2005, doi: 10.1364/josaa.22.002465.

[501] A. H. Dorrah, "Longitudinal Patterning of Structured Light and its Applications in Sensing," University of Toronto (Canada), 2019.

[502] N. Mphuthi, L. Gailele, I. Litvin, A. Dudley, R. Botha, and A. Forbes, "Free-space optical communication link with shape-invariant orbital angular momentum Bessel beams," *Appl Opt,* vol. 58, no. 16, pp. 4258-4264, Jun 1 2019, doi: 10.1364/AO.58.004258.